Development of Functional Titanate and Titanium Oxide Mesocrystal Materials and Their Applications

Dengwei Hu

Kagawa University

September 2014

Contents

Chapter I General Introduction

The study of nanocrystals has increasingly become an intense and major interdisciplinary research area because nanocrystals with distinct properties can serve as building units to construct hierarchically structured materials.[1,2] The electronic, optical, transport and magnetic properties of the nanomaterials depend on not only the characteristics of individual nanocrystals, but also the coupling and interaction among the aligned nanocrystals with the same orientational crystal-axis.[3] Ordered self-assembly or directed assembly of nanocrystals to polycrystal with superstructures, and polycrystals with nanocrystal-axis-orientation are particularly eye-catching. In this field, mesocrystals, a new class of material, which are polycrystals constructed from oriented nanocrystals or microcrystals. In particular for materials chemistry, mesocrystals can offer unique new opportunities for materials design, and be applied to catalysis, sensing, and energy storage and conversion.[4] Therefore, they have attracted considerable attention of chemists and physicists in recent decade, and are becoming a hotspot research field. However, the understanding mesocrystals are very limited, such as the preparation approaches, the formation processes, microstructures and characteristics, and the developments of the various types and high performance applications.

In this chapter, some reviews on the synthesis, the formation mechanisms, characterizations, and the applications of conventional mesocrystals, the general introduction for the topochemical synthesis, the layered protonated titanate as a precursor for topochemical synthesis of the mesocrystals, and the fabrication of oriented ceramics materials are described. Furthermore, the purposes of this dissertation are clarified.

1.1 Overview on mesocrystals

1.1.1 Mesocrystals and their formation mechanisms

Ordered alignment of nanocrystals into polycrystals constructed from oriented submicro/nanocrystals by bottom-up approaches opens up the possibilities of fabricating new materials and devices, which is one of the key topics of modern materials science. [5] The obtained assemblies not only have properties based on the individual nanocrystal, but also exhibit unique collective properties and advanced tunable functions.[6-8] It is also well known that, in classical crystallization process, the thermodynamic driving force for crystallization is the supersaturation of the solution, and the crystallization starts from dissolved atoms or molecules, or in case of salts from different ions. [9] However, in the formation processes of the crystalline assemblies, some mesoscopic transformations, and metastable or amorphous precursor nanocrystals into polycrystals can take place.[4] The manner of some assembled crystallizations is obviously different from the classical crystallization.

Based on not only the detailed investigations of the nanostructures and possible formation mechanisms of the crystalline assemblies, but also the various crystallization pathways as well as the necessary analytics of the experimental evidence, H. Cölfen and S. Mann brought forward that the crystal growth mechanisms of the crystalline assemblies may be an aggregation-based process via a mesoscale transformation.[10] Before long, a cogitative concept of mesocrystal was proposed and developed to explain the whole crystallization process by H. Cölfen and M. Antonietti in 2005.[4] Mesocrystal is deemed to an abbreviation for a mesoscopically structured crystal. Mesocrystal is defined as an orientational superstructure of crystalline assembly, a polycrystal constructed and formed from crystallographically well-aligned and oriented submicro/nanocrystals with mesoscopic size (1–1000 nm).[2,9,10,11]

In this case, the formation of the crystalline assemblies is contrasting with the classical atom/ion/molecule mediated crystallization pathway. A nonclassical crystallization theory to explain the formation of the crystalline assemblies, that is, crystal-unit mediated crystallization pathway, was suggested by H. Cölfen.[4] Based on the crystalline theory proposed by H. Cölfen etc., the different possible formation mechanisms of mesocrystals were well summarized with a schematic diagram by some reviews, [2,12] as shown in Figure 1.1. In the description below, the different nanocrystals, mesocrystals, single crystals, and original ions or/and molecules are abbreviated to N-x, M-x, S-x, and O-x, respectively, where x corresponds to the ordinal number. In the schematic diagram, firstly, nanocrystals are formed via a classical nucleation and crystal growth from original ions or/and molecules (Figure 1.1, O-1 and O-2). These nanocrystals are temporarily stabilized by the organic additives, or original ions or/and molecules and partly organic substances, or original ions or/and molecules only (Figure 1.1, N-1, N-2, and N-3, respectively). Secondly, the stabilized nanocrystals undergo a nonclassical crystallization (a mesoscale oriented self-assembly process of nanocrystals) (Figure 1.1, N-1→M-1, N-2→M-2, and N-3→M-3, respectively), or a classical crystal growth of the formation of bridged nanocrystals (Figure 1.1, N-2→M-2, N-3→M-2) to form the different possible mesocrystals. In these processes, the organic additives may preferentially attach onto the specific surfaces of nanocrystals and therefore give rise to strongly anisotropic mutual interactions between nanocrystals. If the lattice energy of the formed mesocrystals is high, these metastable intermediates can be gradually transformed into the single crystals finally via the crystallographic fusion approach (process of mesocrystal→single crystal-1 in Figure 1.1). In addition, a single crystal can be transformed into mesocrystal via the topochemical conversion reaction (processes of single crystal-1→M-3, single crystal-1→M-4, and single crystal-1→M-4→M-5 in

Figure 1.1), and the transformation of the mesocrystal into the single crystal can be also realized by the topochemical conversion reaction (processes of M-4→single crystal-2, M-4→M-5→single crystal-2 in Figure 1.1). All the different kinds of the mesocrystals of the detailed formation mechanisms have been described as clear as possible by the L. Zhou and P. O'Brien.[2]

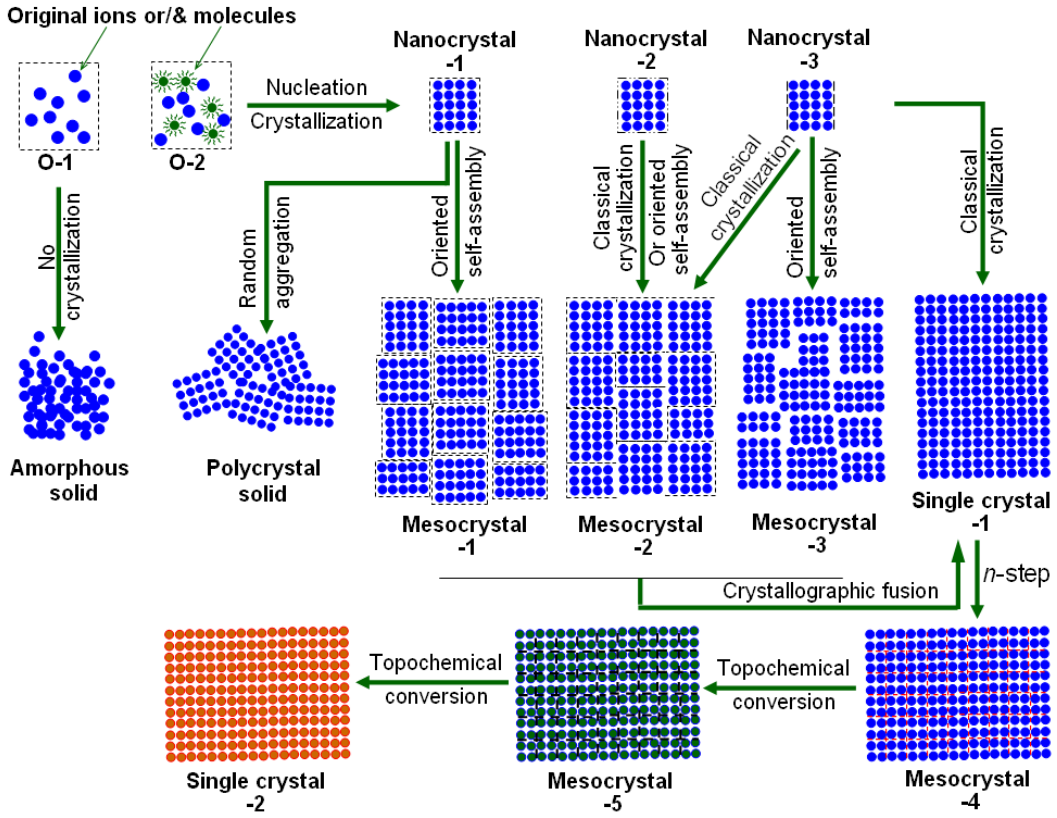

Figure 1.1 Schematic diagrams of different possible formation mechanisms of mesocrystals. O-1 and O-2 show possible original states: O-1, organic substances are not existent; O-2, organic substances are existent. N-1, N-2, and N-3 correspond to nanocrystalline intermediates: N-1, fully covered by organic substances; N-2, partly covered by organic substances; N-3, not covered by organic substances.[2] M-1, M-2, M-3, M-4, and M-5 correspond to possible forms of mesocrystals: M-1, the component nanocrystals are isolated and bridged by the organic substances; M-2, the component nanocrystals are connected partly by themselves and partly by organic substance; M-3, M-4, and M-5, the component bridged nanocrystals are only connected by themselves. The transformation of M-4 into M-5 maybe process directly or pass multiple steps. The formation of porous mesocrystal: O-2→N-3→M-2→M-3; the formation of sponge mesocrystal: O-1→N-3→M-3, or single crystal-1→M-4 (→M-5); the formation of microporous or nonporous

mesocrystal: single crystal-1→M-4(→M-5); the formation of microporous or nonporous single crystal: M-1 or M-2 to single crystal-1, M-4→(or M-5→) single crystal-II.

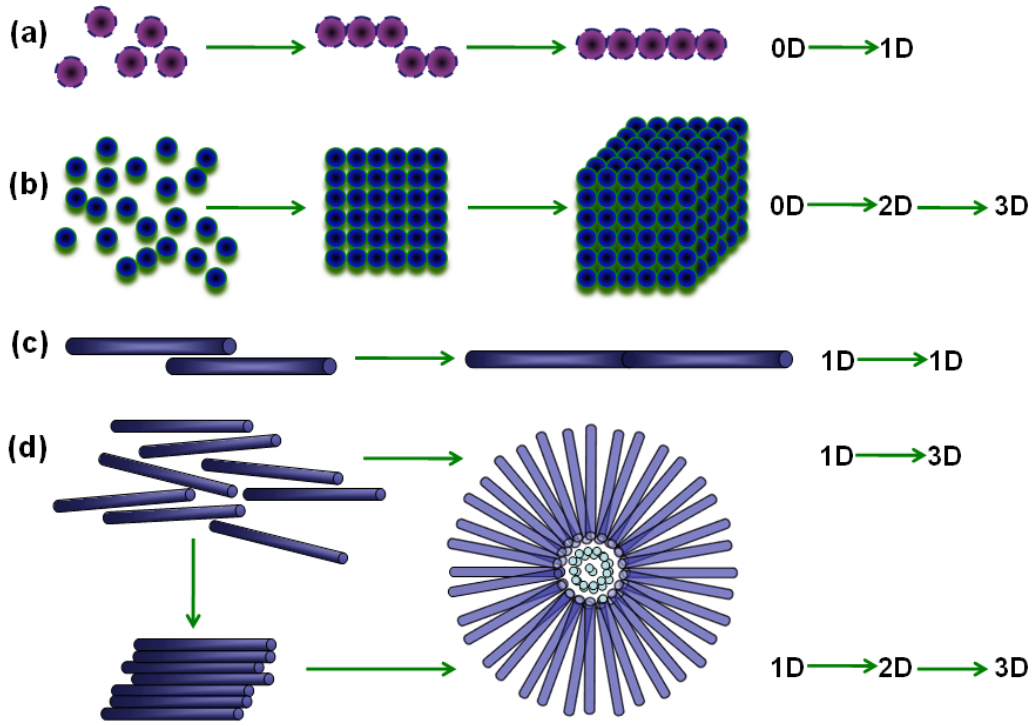

Figure 1.2 Various organizing dimensional schemes for self-construction of nanostructures by possible oriented attachment or assembly mechanisms.

Figure 1.1 only shows some plane graphs for the explanations of the formation mechanisms of the mesocrystals. In order to further understand the formation mechanisms of the mesocrystals, the possible formation mechanisms of the self-attachment or assembly of the mesocrystals with different dimensions and morphologies can be visually illustrated in Figure 1.2. The targeted mesocrystals with different dimensions can be formed by the transformation of the zero-dimensional (0D) or one-dimensional (1D) original crystalline units into the 1D, 2D, or three-dimensional (3D) assembles depending on the self-construction. In addition, a schematic illustration of the formation mechanism for the desired mesocrystals with different dimensions formed by the *in situ* topochemical conversion reaction from original designed precursors is shown in Figure 1.3. The formation mesocrystals can

still maintain the morphologies of the original precursors after one or multiple-step transformations, suggesting the morphologies of the mesocrystals are decided by the original precursors. Usually, this reaction occurs via accompanying the ion exchange, intercalation, deintercalation, and topochemical micro/nanocrystal conversion (TMC).

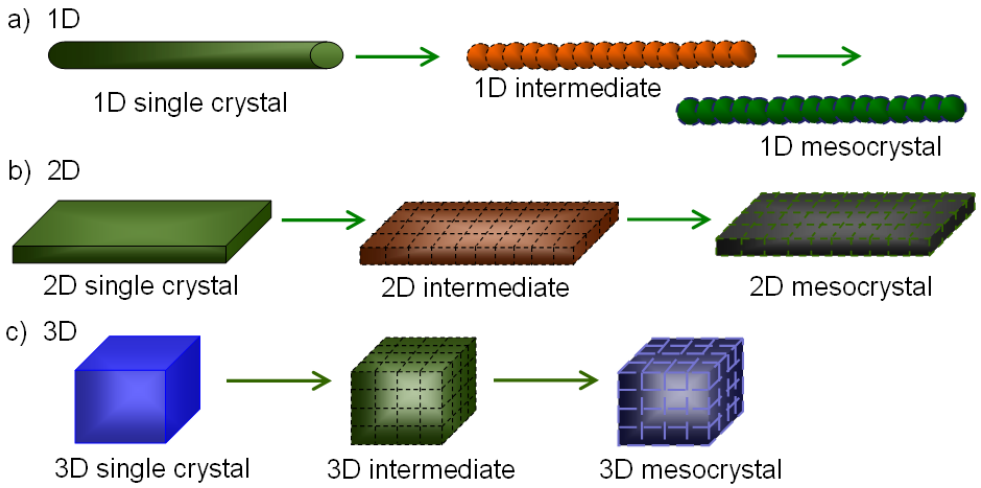

Figure 1.3 Various dimensional schemes for 1 and/or n-step *in situ* topochemical conversion reaction for formations of mesocrystals from original precursors.

1.1.2 Properties characteristic of mesocrystals

It is well known that the nanocrystal building units with the structural multiplicity and nanoscale size can provide additional opportunities for self-assembly. A variety of self-assemblies or topochemical bridge connections for the formations of the mesocrystals can offer new possibilities for superstructure formations, resulting in the mesocrystals present some different characteristic properties. The mesocrystals from functional materials are highly attractive due to the emergent properties of mesocrystalline materials, such as single crystal-like behavior, high crystallinity, high porosity and inner connection bridged by organic components and/or inorganic nanocrystals.[11] The mesocrystals can exhibit the following characteristic properties.

Firstly, the mesocrystals are polycrystals, but they present a single crystal behavior

in electron diffraction and X-ray scattering. For example, the $(NH_4)_3PW_{12}O_{40}$ dodecahedron mesocrystal shows a single crystal-like SAED pattern as shown in Figure 1.4.[13] In addition, all the submicro/nanocrystal units for the construction of the mesocrystal present the same direction of the interplanar spacing. These are due to that the mesocrystals are constructed from submicro/nanocrystals, and each submicro/nanocrystal is crystal-axis-oriented each other.

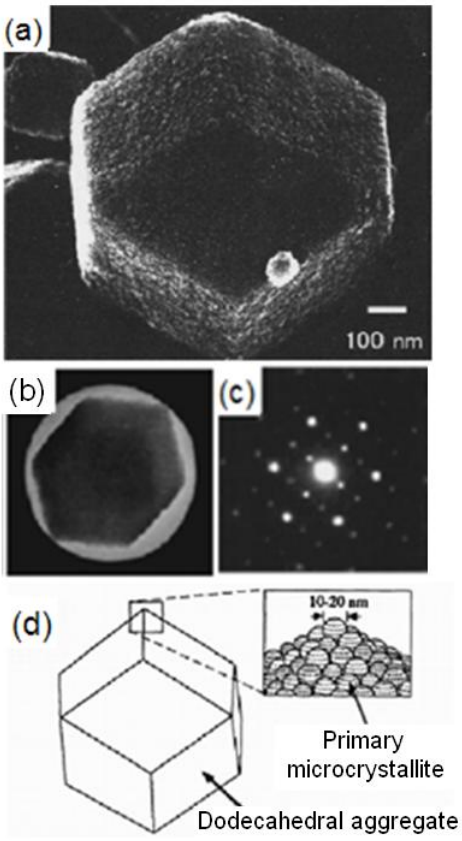

Figure 1.4 (a) SEM image, (b) TEM image, and (c) SAED pattern of $(NH_4)_3PW_{12}O_{40}$ dodecahedron mesocrystal. (d) Schematic illustration of $(NH_4)_3PW_{12}O_{40}$ dodecahedron mesocrystal shown in (a). Reproduced and adapted with permission from Reference [13]. Copyright @ 1996 The Chemical Society of Japan.

Secondly, the mesocrystals show some special properties of well-aligned and oriented crystalline assembly, which is unrivalled for single-crystalline, normal polycrystalline, and amorphous materials. Namely, some of desired properties can be

satisfied by using the mesocrystal superstructure rather than using the same material in single-crystalline, unordered polycrystalline aggregate, and amorphous.

Thirdly, the mechanical properties of the mesocrystals are unusual because of the primary crystallites sharing a common crystallographic orientation.[14] They can exhibit higher ductility and toughness than the corresponding single crystalline materials, and almost all the mesocrystals exhibit the fracture surfaces like amorphous glasses, but unlike the single crystals. [15]

Finally, the composite mesocrystal simultaneously present over two kinds of the functional properties, and prevail on the materials having a large improvement in some application areas. For instance, mechanical toughness and dielectric dissipation in one film, or optical and magnetic properties can be combined in one system. It is said that these properties would never mix on this nanoscale.[9] They combine the high crystallinity with small crystal size, high surface area and high porosity of the mesocrystal as well as good handling since the mesocrystal has a size in the nanometer to micrometer range. The existence of the superlattice structure is also the main reason and is highly attractive due to causing the emergent properties of mesocrystalline materials.

A mesocrystalline assembly process does not occur by an ion-by-ion manner, however, ionic strength and ionic species of the solution are still important variables in controlling crystallization to form mesocrystals. In particular for surfactant phases and microemulsion involved crystallization processes, phase equilibrium and physical characteristics of the product can strongly depend on ionic species and ionic strength especially if the catanionic lyotropic phases are applied.[11]

1.1.3 Recent advances in mesocrystal materials

In recent years, the optimization of synthetic strategies to synthesize

mesocrystalline materials has been developed,[2] and an increasing number of the mesocrystals preparations for applications to a wide range of the functional materials have been reported. A variety of mesocrystals have been developed. The progresses have led to an increasing understanding of the formation mechanism and expanding of the potential applications of mesocrystals. In the research area of the formation mechanism, the carbonates mesocrystals were studied at the earliest and most. The initial eclaircissement of the mesocrystalline formation was derived from the mesocrystalline carbonates chemistry, which is primary source of the mesocrystal theory today. [4,10,16———31] But one of the most early referring the indications of the mesocrystal intermediates was not derived from $CaCO_3$ but the investigation of the $BaSO_4$ crystal with the porous structure.[32] After exploration of some intermediate metal oxides mesocrystals, the mesocrystals with even higher definition were reported for $CaCO_3$ made in silica gels in 1986.[33] Henceforth, $CaCO_3$ mesocrystals are increasingly studied and developed via controlling the polymorph and morphology. But it is little-known that all the carbonate mesocrystals are involved with the high performance applications. Next, the study on the metal oxides mesocrystals not only becomes increasingly but also becomes the hottest. Especially in ZnO and TiO_2 mesocrystals, the preparation approaches, the formation mechanisms, microstructures, and the high performance applications have been getting increased attention. At present, the ZnO and TiO_2 mesocrystals have been used to catalysis, sensing, and energy storage and conversion.[11,34] The perovskite metal oxides mesocrystals have been also developed unsubstantially, but they are likely to widely apply the high performance electro-optic field, ferroelectric materials, and other functional composite materials.

Although some mesocrystals have been developed, and some formation mechanisms of the mesocrystals have been exposed, the mesocrystals are still a new

study field for the solid material. The metal oxide and carbonate mesocrystals are predominantly investigated, and there are still understood limitedly, some formation mechanisms are still very difficult to be clear. The varieties of the mesocrystals are not enough, the application studies of the other mesocrystals are hardly found out. In the following, the carbonates, metal oxides, and perovskite mesocrystals are briefly introduced and summarized, respectively. The goal is to further understand the approach, formation mechanism, and functional application of the mesocrystals, and is ready for the development and application of new kinds of functional mesocrystals.

1.2 Carbonates and simple metal oxides mesocrystals

1.2.1 $CaCO_3$ mesocrystals

$CaCO_3$ (calcium carbonate) is one of the most abundant minerals in nature existing in such as the sedimentary rocks [35] and the biological skeletons and tissues. [36] It includes three kinds of crystalline polymorphs: calcite (dominated phase at lower temperature), aragonite (dominated phase at higher temperature), and vaterite (usually at higher supersaturation). [37] Some new strategies of $CaCO_3$ chemistry have been developed and further extended for the controlling morphologies and crystallization, the various inorganic or organic–inorganic composite materials, superstructure materials, and improved functional materials. [38,39] Many studies on $CaCO_3$ materials have effectively promoted the development of the mesocrystal chemistry and provided theoretical basis of the mesocrystal chemistry. Almost all the $CaCO_3$ mesocrystals were prepared by a similar gel-sol reaction or a block copolymerization reaction.[29] Several representatives are described below.

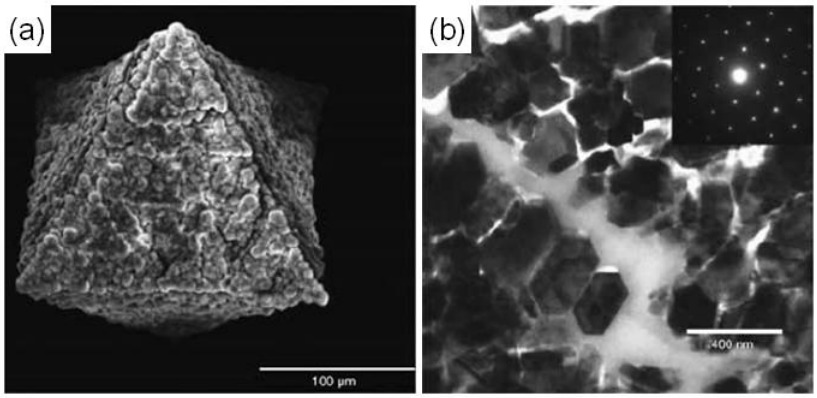

Figure 1.5 (a) SEM and (b) TEM images of calcite ($CaCO_3$) aggregate with characteristic pseudooctahedral morphology obtained from polyacrylamide gel. (Inserted in (b): SAED pattern of calcite mesocrystal). Reproduced and adapted with permission from Reference [40]. Copyright @ 2003 Mineralogical Society of American.

For calcite mesocrystals, some specific synthesis processes have been carried out by the following researches. A typical calcite mesocrystal with a pseudo-octahedron morphology constructed from rhombohedral nanocrystals has been prepared by the self-assemble in a polyacrylamide gel, as shown in Figure 1.5.[40] This calcite mesocrystal was formed by a precipitation process from an aqueous solution containing Ca^{2+} and sulfide. The aggregate and crystallographic block with rough surfaces are constructed from well-aligned nanocrystalline building units. The tightly packed nanocrystals and the organic matrix between the individual nanocrystal interspaces can be observed from the TEM image (Figure 1.5b). The inserted SAED pattern reveals a high orientation of the crystallographic block, suggesting a mesocrystal structure. The calcite mesocrystal can be also prepared by applying the CO_2 vapor diffusion into a $Ca(OH)_2$ solution.[20] Compared to the other approaches for the preparation of $CaCO_3$ crystals, the CO_2 vapor diffusion approach has the advantage of avoiding the interference of the extraneous ions, minimizing ionic strength and approaching a pH close to biological conditions at the end of the crystallization reaction. This approach is beneficial to the growth of calcite

mesocrystals. The vapor diffusion approach allows for further investigation of the driving forces for the oriented and/or self-assembling of nanocrystals toward mesocrystals.

And in general, the metastable mesocrystalline $CaCO_3$ polymorphs can be easily synthesized. The vaterite mesocrystals with hexagonal morphology could be synthesized from a metastable phase transformation by using a gas diffusion approach and an N-trimethylammonium derivative of hydroxyethyl cellulose as additive.[19] The microstructure characterizations of the obtained vaterite mesocrystal is shown in Figure 1.6, revealing the obtained hexagonal vaterite mesocrystal is constructed from vaterite nanoparticles and presents a [001] zone axis. The formation mechanism of the vaterite mesocrystal is promising for controlling the assembling formation of complex, highly oriented structured materials, and also provides some evidence for the mesocrystallization processes.

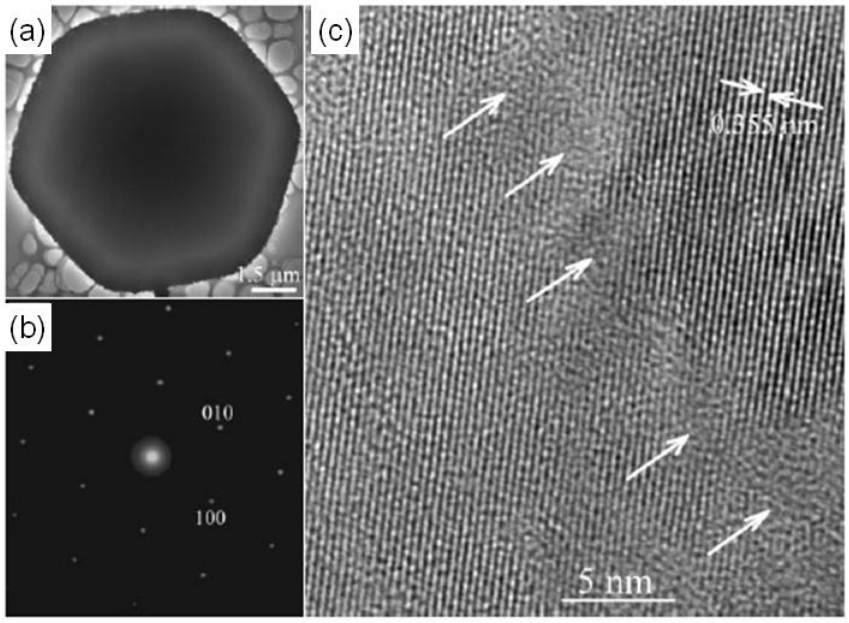

Figure 1.6 (a) TEM image and (b) corresponding SAED pattern recorded from [001] zone axis of hexagonal vaterite ($CaCO_3$) mesocrystal. (c) HRTEM image of vaterite plate with clearly resolved lattice fringe of (110) plane (d = 0.355 nm). Two vaterite nanoparticles have the same orientation but are separated by the crystal boundary (indicated by arrows). Reproduced with permission from

Reference [19]. Copyright © 2006 WILEY-VCH Verlag GmbH & Co. KGaA, Weinheim.

Very recently, a medicinal $CaCO_3$ mesocrystal as small drug carriers has been synthesized by a facile binary solvent approach under the normal temperature and pressure.[41] This kind of medicinal $CaCO_3$ mesocrystal is a new highly ordered hierarchical mesoporous $CaCO_3$ nanospheres (CCNSs). The hierarchical structure was constructed by multistage self-assembled strategy. Due to the large fraction of the voids inside the CCNSs which provides the space for physical absorption, the CCNSs can stably encapsulate the anticancer drug with the high drug loading efficiency, and the component $CaCO_3$ nanoparticles can be dispersed well in the cell culture. The CCNSs can enhance the delivery efficiencies of the drug to achieve an improved inhibition effect on the diseased cell growth. This research implies that the CCNSs are a promising drug delivery system for the certain medications in cancer therapy, and also expands the applications of the mesocrystals.

1.2.2 $BaCO_3$ mesocrystals

Comparing with $CaCO_3$ mesocrystals, the studies of the $BaCO_3$ (barium carbonate) mesocrystals are relatively less. Typical helices $BaCO_3$ mesocrystals composed of the nanorods can be structured by a face selective adsorption of a stiff polymer and subsequent self-assembly of nanocrystal building units.[29] In this block copolymerization process, the helices $BaCO_3$ mesocrystals were formed from a self-assembly process of the elongated orthorhombic $BaCO_3$ nanorods. The combined surface-active agents were utilized to produce the mesocrystalline $BaCO_3$ helices from $BaCO_3$ nanorods (Figure 1.7). The participant stiff polymer leads to form helix arrangement via a selective self-assembly. Firstly, the selective adsorption of the stiff polymer onto the favorable (110) planes of the $CaCO_3$ nanocrystalline rod occurs,

giving rise to a staggered arrangement of the aggregate nanocrystals which are controlled according to helix direction. Secondly, a nanocrystalline rod approaches an aggregate in the other directions and presents with favorable and unfavorable adsorption sites. The favorable adsorption sites only match with the (011) planes are required and the unfavorable adsorption sites match the other planes, such as (020) and (011) planes (Figure 1.7c). This selective adsorption process results in a twist for the formation of the helices of the mesocrystalline aggregate.[9] This is a classic example that the 3D mesocrystal is formed from 1D nanocrystalline building units.

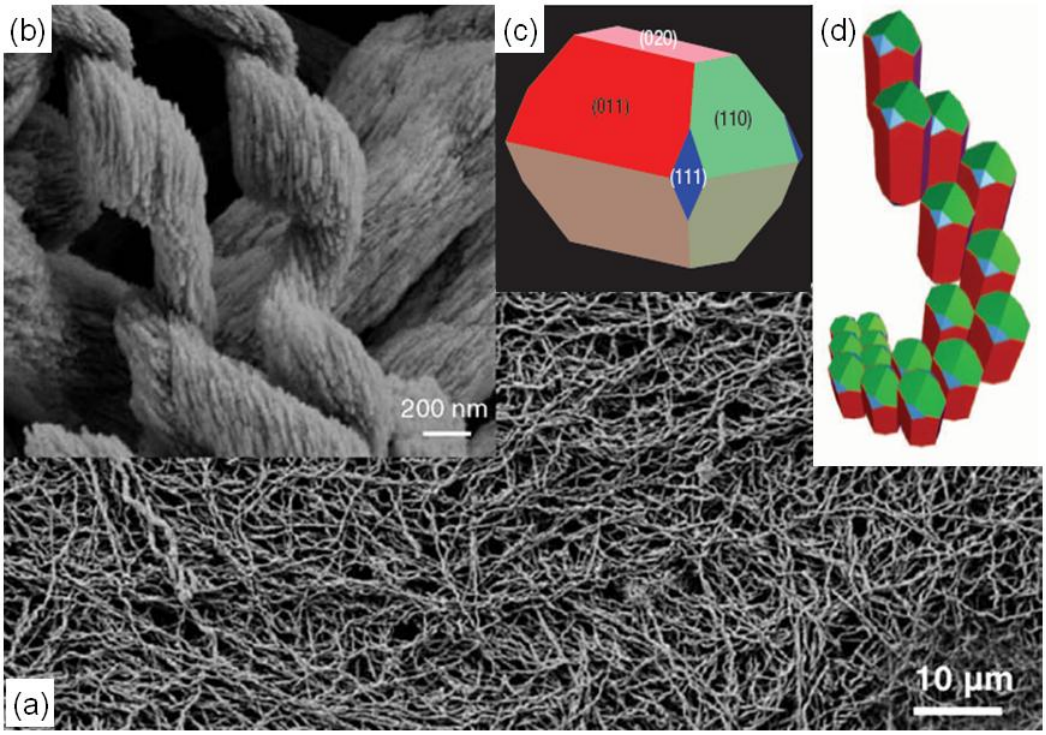

Figure 1.7 (a) SEM and (b) high-expanded SEM images of helical $BaCO_3$ mesocrystals formed by programmed self-assembly of elongated nanoparticles as template. (c) Relevant planes of nanocrystalline $BaCO_3$ block. (d) Proposed formation mechanism of helical superstructure. Reproduced with permission from [29]. Copyright @ 2005 Nature Publishing Group.

The spherical and dumbbell-like $BaCO_3$ mesocrystals can be prepared from a dynamic growth program by self-assembly processes and gelation reactions. [42] Nanocrystalline $BaCO_3$ superstructures exhibit unusual morphologies are obtained by

the CO_2 vapor diffusion technique in the presence of poly(ethylene oxide)-block-eicosa aspartate (PEO-b-Asp(20)) bioconjugate.[27] This formation process is also a block copolymerization reaction. In this formation reaction, the highly effective bioconjugate acts as a crystal growth modifier, which can lead Ba^{2+} and PEO-b-Asp(20) to form the poly(ethylene oxide)-block polyaspartate block copolymer. In this case, a well-defined mesocrystal yielded. Different from the commonly mesocrystals, the morphology of $BaCO_3$ mesocrystals can be systematically controlled along different twinned growth patterns by conditioning a broad range of the concentrations of polymer and Ba^{2+}.

1.2.3 ZnO mesocrystals

ZnO (zinc oxide) has attracted many attentions, and is a promising metal oxides material for the applications to the optical, electronic, piezoelectric, pyroelectric, and photocatalysis fields due to its wide band gap (3.37 eV at room temperature) and large exciton energy (60 meV).[43,44] ZnO single crystals normally prefers to grow along the [0001] direction because of its noncentrosymmetric structural anisotropy.[45] Some approaches in which the growth along the [0001] direction of ZnO crystals may be substantially suppressed are through the introduction of organic additives as stabilizing agent, or the adjusting of the pH value of the reaction solution.[46,47] But these approaches are no guarantee of success, and easily give rise to the formation of the ZnO mesocrystals with {0001} facet sometimes.[48] The conventional synthesis of the ZnO mesocrystals in the organic additives or solvent does not get rid of the bondage of the exposed {0001} facet. Therefore, the plentiful organic additives or solvents are usually used for the preparation of the ZnO mesocrystals via a block polymerization reaction. Some typical examples are enumerated in the sections below.

The microtubular ZnO mesocrystals were developed by using poly[(acrylic acid)-

co-(maleic acid)] sodium salt (PAMS) as template molecule via a typical block polymerization reaction.[49] In the formation process, initially, ZnO nanoclusters can be spawned by thermolysis of a zinc citrate-ethylenediamine composite and by hydrothermal treatment of natural water-oxidation of zinc foil. Then, the ZnO composite nanoclusters with rod-like micellar aggregates were formed by the self-assembly of ZnO nanoclusters and PAMS mixture. The ZnO composite nanoclusters subsequently coagulated to generate some metastable composite multimers. At last, the metastable composite multimers were coaxed into self-assembled nanoplates to form the mesocrystalline ZnO microtubes via the layer-by-layer approach. The formed microtubular ZnO mesocrystals are constructed from the well-assembled nanoplates growing along the [0001] direction, suggesting a [0001]-axis directional self-assembly of building units. The mesocrystalline ZnO microtubular with distinctive hollow interstices may allow using as microcarriers or microreactors for drug and catalyst.

For another example, ZnO mesocrystals with ellipsoidal superstructures can be formed via the zinc hydroxyl double salt (Zn-HDS) mesocrystals as intermediate.[48] The Zn-HDS mesocrystals are formed from self-assembly of Zn-HDS nanocrystals existing in cetyltrimethyl ammonium bromide (CTAB) at room temperature. The ZnO mesocrystals were formed through vertical attachment on (0001) planes of basic Zn-HDS nanocrystals. ZnO nanoplatelets and nanorings were subsequently formed from the assembly of ZnO mesocrystals through vertical attachment on (0001) planes. ZnO ellipsoidal superstructures were finally formed from the further assembly of the ZnO nanoplatelets and nanorings also through vertical attachment on (0001) facets. The formed ZnO mesocrystal has not still gotten rid of growing along the [0001] direction. The polar Zn-(0001) planes with high population of the obtained ZnO materials are likely to present high photocatalytic activity.

Rather than using organic additives, a facile and green room temperature ionic liquid as deep eutectic solvent was investigated to prepare the ultrafast formation of ZnO mesocrystals growing along the [0001] direction also.[50] The prepared ZnO mesocrystals are mesoporous materials with high specific surface areas. They present excellent photocatalytic activities which are comparable with that of the commercial photocatalyst P25. The present approach is convenient, and can be readily extended to develop the other functional mesocrystals with a wide range of applications.

Recently, ZnO mesocrystalline microspheres have been prepared on a large scale via a nonclassical crystallization pathway by a facile solution-based approach.[51] On account of no any template additives in the reaction system, the butanol solvent plays an important role for the formation of the spherical mesocrystal morphology. In the formation process, firstly, under the inhibitory effects of butanol, the Zn^{2+}-terminated (0001) plane is suppressed along the c-axis, a large number of ZnO clusters nucleate and produce the primary ZnO hexagonal nanoplates. Secondly, the positive and negative charges of the ZnO hexagonal nanoplates produce dipolar moments, resulting in the stacking of the hexagonal nanoplates. Such a hexagonal nanoplate structure has a strong dipole moment along the *c*-axis. Finally, a sphere mesocrystal with two concaves on the poles along the c-axis is evolved. The as-prepared ZnO mesocrystals with microsphere morphology show stable and intense yellow fluorescence, which can be expected to have potential in microscale photonic or electronic applications.[51]

It is noteworthy that the utilization of the large surface area of doped ZnO mesocrystal precursor was developed for biosensor very recently.[52] In this investigation, Ru (ruthenium) polypyridyl functionalized ZnO mesocrystals as bionanolabels were prepared. A solid mixture containing $Zn(NO_3)_2 \cdot 6H_2O$, 1-octadecene and dodecylamine as starting material were heated to obtain the ZnO

mesocrystals before the dispersed solution and wash of the crude product. Although some unique planes of the obtained ZnO mesocrystals can be observed from SEM and TEM images, the report does not give that these planes belong to which crystal plane. The large surface area of ZnO mesocrystals was beneficial for loading a high content Ru polypyridyl composite, giving rise to the excellent improvement of the electrochemiluminescence. It is worth to propose that the biological recognition and biosensing platform are expected to the application of Ru polypyridyl functionalized ZnO mesocrystals. This investigation provides a novel reference and a promising prospect for the development of the ZnO mesocrystals.

These studies on ZnO mesocrystals could provide an example for better understanding the formation mechanisms of other simple metal oxides mesocrystals in the presence of organic additives.

1.2.4 TiO_2 mesocrystals

TiO_2 (titanium dioxide) is among the most widely investigated metal oxides materials for its unique properties and many promising applications in environment, energy, photocatalysis, and sensing areas.[53-56] It has several kinds of crystal structures which have been reported,[57,58] including anatase, rutile, TiO_2(B), brookite, TiO_2(II), TiO_2 (H), etc. In these titanium dioxide polymorphs, rutile is a thermodynamic stable phase, and the others are metastable phases. Anatase is the most stable phase in the metastable phases.

TiO_2 nanocrystals have increasingly investigated and developed in functional metal oxides material fields because of their many outstanding physicochemical properties and wide application in electrical, optical, mechanical, catalytic, and sensing areas.[59,60] At present, many TiO_2 mesocrystals, such as nanorod-like,[61—64] cable-like,[65] hollow spheres,[66] nanowires,[67] ellipsoid,[34] and bipyramid-like[68,69] mesocrystals have

been synthesized. The differences in lattice structures and morphologies cause different electronic band structures and different surface geometric structures, which determine the performance and the chemical activity of TiO_2. The reported anatase TiO_2 mesocrystals with the [010] zone axis have potential application in lithium ion batteries because of their potential advantages in porous mesocrystalline structure, current rate capability, and safety.[34] The aligned [001] oriented rutile nanorods present excellent broadband and quasi-omnidirectional antireflective properties as electrode material for dye-sensitized solar cells (DSSCs),[64] and show a large reversible charge–discharge capacity and excellent cycling stability as anode material for lithium ion batteries.[62] Anatase mesocrystal-like porous nanostructures exhibit a multifunctional response, including good electrochemical performance and good capabilities for photocatalytic degradation and enzyme immobilization.[70] TiO_2 mesocrystals usually exhibit excellent photocatalytic performance due to their high surface area, high porosity, and oriented subunit alignment.[65,70−72] It is noteworthy that the efficient flexible dye-sensitized solar cells (DSSCs) have been fabricated by the growth of the aligned anatase TiO_2 nanorods on a Ti-foil substrate for using as a photo-anode.[73] These mesocrystalline TiO_2 nanorod arrays on Ti substrates with excellent antireflective properties could become a promising candidate as the photo-anode in flexible DSSCs with enhanced light harvesting performance.

Just the same to the other mesocrystals, there also have three kinds of approaches, including direct synthesis, oriented topochemical conversion, and crystal growth on support, for the acquisition of the TiO_2 mesocrystals.[74,75] In this section, some classical formation processes and the applications of the TiO_2 mesocrystals are enumerated.

The direct synthesis approach is the most common process for the preparation of the TiO_2 mesocrystals in an organic solvent or gel-sol system. The organic additives

played an important role in the self-assembly process for the formation of TiO_2 mesocrystals. The unique spindle-shaped nanoporous anatase TiO_2 mesocrystals with tunable sizes were directly developed on a large scale through mesoscale assembly in the tetrabutyl titanate-acetic acid system without any additives under the solvothermal conditions.[34] A complex mesoscale assembly process was put forward for the formation of the anatase mesocrystals, as shown in Figure 1.8.[34] In this formation program, organic titanium firstly reacts with organic acid by a hydrolytic/nonhydrolytic condensation reaction to from amorphous fiber-like titanium acetate complex precursors with Ti-O-Ti bonds. After two times of continuing condensation processes, the other crystalline spherical-like precursors come into being at the expense of the amorphous precursor. Subsequently, the crystalline spherical-like precursors gradually release soluble titanium including the nucleation and growth of anatase nanocrystals. Subsequently, the formed anatase nanocrystals assemble along the [001] direction, accompanying with the entrapment of *in situ* produced butyl acetate, leading to the formation of the spindle shaped anatase mesocrystals elongated along the [001] direction. The acetic acid molecules played multiple key roles during the nonhydrolytic processing of the [001]-oriented anatase mesocrystals. The obtained anatase mesocrystals with nanoporous exhibits remarkable crystalline stability and improved performance as anode materials for lithium ion batteries.

Also, the stable rutile mesocrystalline hollow spheres were developed by a direct hydrothermal synthesis approach simply.[66] The presence of N,N′-dicyclohexylcarbodiimide (DCC) and serine and their synergistic effects is essential for the formation of rutile mesocrystalline hollow spheres from a transparent $TiCl_4$ solution. An oriented attachment process with side-by-side and end-to-end ways was carried out for mesocrystallization of rutile. It can be concluded that the obtained rutile mesocrystalline hollow spheres were formed by self-assembly of rutile nanorods

growing along the [1-10] direction. This kind of rutile mesocrystals can be stable for longer time at lower temperature. The stability of mesocrystals at higher temperature in the solution can be enhanced also when some organic additives are properly utilized.

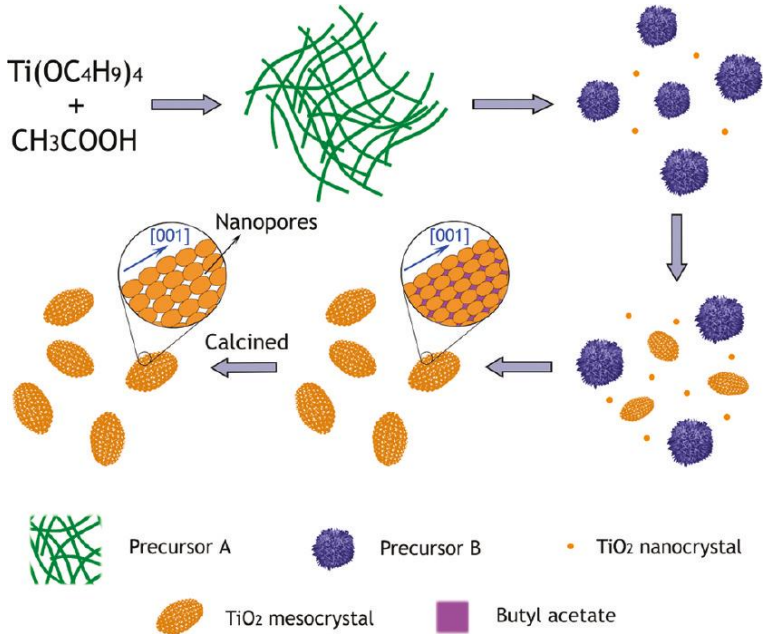

Figure 1.8 Schematic illustration of formation mechanism of nanoporous anatase mesocrystals without any additives. Reproduced with permission from Reference [34]. Copyright @ 2008 American Chemical Society.

In addition, Wulff-shaped and nanorod-like nanoporous rutile mesocrystals with a [010] zone axis constructed from ultrathin rutile nanowires were directly prepared in the surfactant sodium dodecyl benzene sulfonate (SDBS). [76] In the preparation program, SDBS played an important role in the homoepitaxial self-assembly process, in which titanate nanowires as the primary building units were assembled to mesocrystals. The obtained rutile mesocrystals were applied as the electrode materials in rechargeable lithium-ion batteries and demonstrated a large reversible charge–discharge capacity, excellent cycling stability and high rate performance. These

favourable properties are attributed to the intrinsic characteristic of the prepared mesocrystalline rutile with nanoporous nature and larger surface area.

For oriented topochemical conversion approach, a mesocrystal of ferroelectric NH_4TiOF_3 exhibiting a sandwich crystal structure with layers of corner sharing octahedra of $(TiOF_3)^-$ stacked and sandwiched by $(NH_4)^+$ tetrahedra along the *c*-direction, was used as precursor to prepare the first anatase TiO_2 mesocrystals.[77,78] Before the formation of the anatase mesocrystals, it is necessary to prepare a precursor of NH_4TiOF_3 mesocrystal. An aqueous solution containing $(NH_4)_2TiF_6$, H_3BO_3, and some present surfactants were firstly prepared. These present surfactants play an important role in both the controlling hydrolysis of $(NH_4)_2TiF_6$ and the self-assembly processes. The NH_4TiOF_3 mesocrystals can be obtained after stirring and subsequent thermal treatment of the aqueous solution. The anatase mesocrystals can be formed from the oriented topochemical conversion of the NH_4TiOF_3 mesocrystals by not only washing the NH_4TiOF_3 mesocrystals using a H_3BO_3 solution but also annealing 450 ^oC for 2 h in air. The anatase mesocrystals yield via the oriented topochemical conversion because NH_4TiOF_3 and anatase TiO_2 have similar critical parameters in the {001} facets with a very small average lattice mismatch. In the {001} facets of the two mesocrystals, the titanium atoms locating in octahedra centers of crystal spaces have same arrangements. The {100}, {010}, and {001} facets of the NH_4TiOF_3 nanocrystals corresponds to the obtained anatase nanocrystals, and their several electric diffractions from one particle present the same directions of the facets and same [001] zone axis, as illustrated in Figure 1.9. It has been implied that the similarities in crystal structures between NH_4TiOF_3 and TiO_2 provide the possibility for the oriented topochemical conversion.[75,79,80]

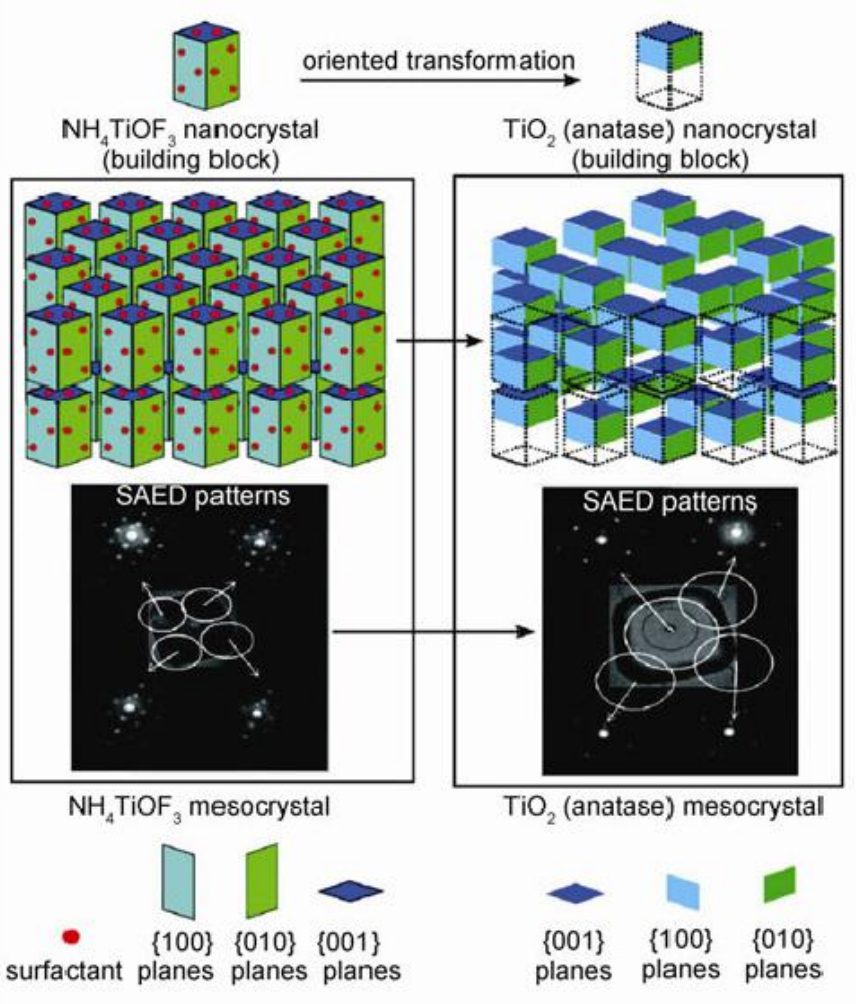

Figure 1.9 Schematic illustration of topochemical conversion of NH_4TiOF_3 mesocrystal to anatase mesocrystal. The SAED patterns show the single crystal diffraction behavior of both systems. Reproduced with permission from Reference [78]. Copyright @ 2008 American Chemical Society.

In addition to the direct synthesis approach and oriented topochemical conversion approach, the TiO_2 mesocrystals can also be developed by the crystal growth on support approach. The crystal growth on support approach may be beneficial to construct of the heterostructure surfaces/interfaces, mesocrystalline assemblies, and formation composite. The anatase mesocrystals with petallike morphology have been classically prepared on multiwalled carbon nanotubes (MCNTs) with controllable surface area and crystalline orientation.[65] In the prepared process, the MCNTs were firstly added to a TiF_4 aqueous solution, and then carried out an ultrasonic water bath. After thermal treatment at low temperature, the MCNTs supports were covered by

petallike TiO_2 crystals constructed tiny TiO_2 nanocrystals. Each petal grows along the [001] direction and has a single-crystal diffraction, suggesting that the petallike anatase is mesocrystalline. The obtained MCNTs supported mesocrystals of anatase mesocrystals were used as composite catalysts, and proved to be highly active and robust for photocatalytic degradation of methyl orange.

Very recently, the development of efficient photocatalysts based on anatase TiO_2 microcrystals with {101} facets was processed. A new approach has been carried out for improving the photooxidation activity of photocatalysts by combining metal oxide superstructures and oxygen/hydrogen-evolving co-catalysts support. Cobalt phosphate complexes (CoPi) and Pt nanoparticles as supports were selected as model co-catalysts and photochemically deposited on anatase mesocrystals.[81] It was found that the photogenerated holes in anatase mesocrystals are transferred to the Co species in CoPi under the ultra violet light irradiation, and the CoPi-doped anatase mesocrystals have higher activity than standard anatase mesocrystals. The approximately 300 times for photooxidation activity of the anatase mesocrystals can be further enhanced by introducing Pt nanoparticles on specific surfaces. The site-specific modification of co-catalyst supports tailored by anisotropic electron flow in the mesocrystal superstructures significantly can retard the charge recombination between the holes and electrons. Such developed strategy is very promising for developing novel photocatalytic materials for the applications of environmental renovation and water splitting.

1.3 Metal oxide perovskites mesocrystals

Metal oxide perovskites have a general formula ABO_3, where the large cations locate at A-site, while small cations locate at B-site. The properties of the perovskites

are influenced by the sizes and valences of the cations in the A-site and B-site.[82] Consequently, the perovskites exhibit outstanding chemical and physical properties, which include catalytic, oxygen-transport, ferroelectric, pyroelectric, piezoelectric, and dielectric behavior.[83,84,85] However, only a handful of the investigations on the perovskite mesocrystals have been reported, and almost none of application studies on the perovskite mesocrystals have been carried out, especially in titanate and niobate.

1.3.1 $PbTiO_3$ mesocrystals

$PbTiO_3$ (lead titanate) is one of important piezoelectric materials with high piezoelectric constant although it is not attracted considerable attention today because of the consideration of environmental pollution. Study on the $PbTiO_3$ mesocrystals is a little-known. As we all know, only two reports investigated the $PbTiO_3$ mesocrystals prepared using the SDBS surfactant process. Similar to the case of the preparation of rutile mesocrystals,[76] the SDBS surfactant also played an important role for the self-assembly of the nanoscale building units in the $PbTiO_3$ mesocrystals. The nanoscale $PbTiO_3$ mesocrystals with bur-like and affluent porosity were synthesized by self-assembly of $PbTiO_3$ nanocrystals under hydrothermal conditions using SDBS surfactant.[86] The bur-like mesocrystalline nanostructures exhibit a novel geometrical shape with cores of agglomerated nanocrystals and outershells of nanorods. In the formation process, firstly, the $PbTiO_3$ nanocrystals agglomerate into the nascent nanocrystal with the cube morphology. Secondly, the nascent nanocrystal assembles to form the $PbTiO_3$ mesocrystal. Finally, the nanocrystals in $PbTiO_3$ mesocrystal continuously grow up into $PbTiO_3$ nanorod. The $PbTiO_3$ nanorods with diameters in 30−100 nm are expected to be used as a template for the development of the oriented piezoelectric ceramics.

In addition, a $PbTiO_3$ mesocrystal layer with a thickness of 3−6 μm has been

prepared on $PbTiO_3$ and $SrTiO_3$ substrates by using this SDBS surfactant process also.[87] The prepared mesocrystal layer is constructed from three parts. The lower part of the mesocrystal layer is relatively porous, the middle part is more dense, and the surface part consists of nanorods growing along the [001] direction. In the prepared $PbTiO_3$ mesocrystal program, an epitaxial layer is firstly formed on the $PbTiO_3$ and $SrTiO_3$ substrates by ion-by-ion growth method, subsequently, by the self-assembly of nanocrystals into a mesocrystalline layer. The mesocrystalline layer can further grow up and ripen into arrays of single crystalline nanorods via a redissolution/ reprecipitation mechanism.

1.3.2 $SrTiO_3$ mesocrystals

$SrTiO_3$ (strontium titanate, ST) is often used as a dielectric and photoelectric material, and also is widely used as a substrate for epitaxial growth of other oxides films.[88] Only a few of ST mesocrystals have been reported. The ST mesocrystals with cubic morphology have been prepared by precipitation approach from a suspension of hydrolyzed $TiOCl_2$ aqueous gel.[89] The obtained ST mesocrystals was formed via an epitaxial self-assembly of nanocrystals with a size of 4−5 nm. The formation process is a spontaneous process and not inducing any additives. In addition, ST mesocrystals with a [010] zone axis along the direction of the wire-like morphology can be prepared by an oriented topochemical conversion approach.[90] In this formation process, the $H_2Ti_3O_7$ nanowire as a precursor was thermally treated to form anatase nanowire firstly. The solvothermal and hydrothermal treatments of the anatase nanowire in $Sr(OH)_2$ solutions were carried out to form the mesocrystalline ST. The formation of mesocrystals is resulted from a topochemical reaction between anatase single crystal particles as the templates suspended in a liquid phase and ionic/molecular species in solution. This formation mechanism of the mesocrystals is

very general and likely applicable to a variety of compounds encountered in precipitation processes, solvothermal and hydrothermal reactions, molten salt synthesis, and liquid-phase sintering.

Very recently, the other ST mesocrystals with cubic morphology were prepared via sol–precipitation coupled with a hydrothermal process using oleic acid ($CH_3(CH_2)_7CH=CH(CH_2)_7COOH$) as a capping agent.[91] In the formation process, initially, selective adsorption of oleic acid causes Sr–Ti–O nanorods to grow along the [100] direction from the Ti-based sol. Then these nanorods aggregate with a similar orientation to form the small crystalline ST particles. Finally, the crystallographic fusion takes place in the small crystalline ST particles along the [001] direction of ST crystal structure. The prepared ST mesocrystals with edge length of about 10 nm size show a [001] zone axis. The mesocrystal structure forms from the oriented fusion of these small crystalline units. The selective absorption of oleic acid probably limits the formation of single crystals from the fused particles. The band-gap energies values of the obtained ST mesocrystals are considerably larger than the non-oriented band-gap energy of pure ST. Although the band-gap energy typically increases as the particle size decreases, the ST mesocrystals with a larger particle size yield a higher band-gap energy, which may be related to the characteristic mesocrystalline structure.[91]

1.3.3 $BaTiO_3$ mesocrystals

$BaTiO_3$ (barium titanate, BT) is an important dielectric, piezoelectric, and ferroelectric materials, and attracted much attention because of its potential commercial applications in ceramic capacitors, chemical sensors, and nonvolatile memories.[92] At present, the BT mesocrystals with platelike or spherical morphologies can be prepared by a hydrothermal soft chemical process via an *in situ* topochemical conversion reaction in our previous works.[93—95] In the prepared processes, a

protonated layered titanate of $H_{1.07}Ti_{1.73}O_4 \cdot H_2O$ (HTO) crystal with a lepidocrocite-like layered structure was used as a precursor. For the preparation of the platelike BT mesocrystals, the protonated layered titanate was treated in a $Ba(OH)_2$ water solution under the hydrothermal conditions to transform the layered titanate to BT. The obtained platelike BT particles constructed from nanocrystals, and each nanocrystal presents the same [110]-direction orientation, suggesting the formation of platelike BT mesocrystal. There are two simultaneous reaction mechanisms in the formation of BT mesocrystal under the hydrothermal conditions. One is a dominative *in situ* topochemical conversion reaction in the crystal bulk of the protonated layered titanate, the other is a subordinate dissolution-deposition reaction on the surface of the matrix particles. This is the first time to report the preparation of the titanate mesocrystals with the hydrothermal soft chemical process and the *in situ* topochemical conversion reaction. The platelike BT mesocrystals have been applied to fabricate the [110]-oriented BT ceramic material that shows a very large piezoelectric constant d_{33} value of 788 pC/N.[96]

For the preparation of the BT mesocrystals with spherical morphology, firstly, the layered titanate HTO crystals were used to occur in the intercalation reaction with the *n*-hexadecyl trimethyl ammonium hydroxide (HTMA-OH) or *n*-hexadecyl trimethyl ammonium bromide (HTMA-Br). And then, the layered titanates with increasing interlayer spacing with $HTMA^+$ were treated in the $Ba(OH)_2$ water solution under the hydrothermal soft chemical conditions to form BT particles with book-like morphology via the *in situ* topochemical conversion reaction. Then the book-like BT particles were stirred to shatter the book-like shape and transformed into the BT nanoparticles. Finally, the ordered self-assemble of the BT nanoparticles to the BT agglomerations were carried out under stirring condition. In this case, the BT mesocrystals with spherical morphology were formed. The morphology of the product

particles can be changed dramatically by adding the cationic surfactant in the reaction system. These investigations reveal that the hydrothermal soft chemical process and the *in situ* topochemical conversion reaction are useful for the preparation of mesocrystals.

In addition, the confetti-like, sphere-like, and hollow-sphere BT mesocrystals were prepared by an ultrasonic irradiation approach.[97] In this synthesis process, the $BaCl_2$ and $TiCl_4$ as the starting materials were mixed to form a Ti-based suspended sol. NaOH aqueous solution as a peptizing agent was added into the Ti-based suspended sol. The BT mesocrystals preferred to grow along the [100] axis can be obtained after the ultrasonic of the mixture suspension. The morphology and the size of the BT mesocrystals were affected by the concentration and primary units. The formed BT mesocrystals compose by oriented nanocrystals which aggregate by the self-attachment between (110) planes, and show a single crystal like diffraction pattern.

1.3.4 $Ba_{1-x}Ca_xTiO_3$ mesocrystals

Although BT exhibits large piezoelectricity, its Curie temperature (*Tc*= 130 ^oC) is low, and a phase transition from tetragonal phase to orthorhombic phase around 0 ^oC. Thus, the working temperature of BT as the piezoelectric material is limited in a range of 0–130 ^oC, which is too narrow for practical piezoelectric applications. Doping BT with alkaline earth metal (Ca, Sr) or alkaline metal (K, Na) is an effective method to improve the temperature performance of the piezoelectric materials. Therefore, recently, a large number of studies focus on the $Ba_{1-x}Ca_xTiO_3$, $Ba_{1-x}(Bi_{0.5}K_{0.5})_xTiO_3$, and $Ba_{1-x}(Bi_{0.5}Na_{0.5})_xTiO_3$ materials.[98—101] The platelike $Ba_{0.9}Ca_{0.1}TiO_3$ ((BCT)) mesocrystals with [110]-orientation were developed by our previous work using a novel two-step process.[98] In the first step, the platelike layered titanate HTO crystals are solvothermally treated in a $Ba(OH)_2$–$Ca(OH)_2$ mixed solution. In the second step,

the solvothermally treated samples were heated to form the platelike BCT mesocrystals. The obtained BCT mesocrystal is constructed from well-aligned BCT nanocrystals with a size of about 10–20 nm, and show a single-crystal-like electron diffraction pattern. The BCT mesocrystals were utilized to fabricate an [110]-oriented BCT ceramic, and the ceramic shows a high preferred orientation (76%) and small grain size of about 1–2 μm. Such BCT oriented ceramic has potential application to the high performance piezoelectric materials.

1.3.5 $Ba_{1-x}(Bi_{0.5}K_{0.5})_xTiO_3$ mesocrystals

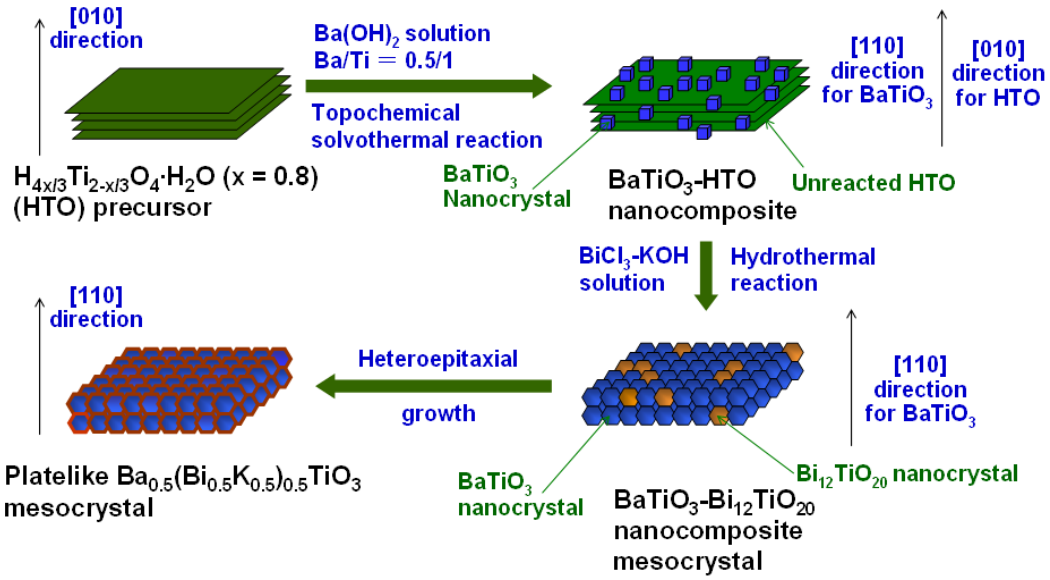

Figure 1.10 Schematic illustrations of formation mechanism of the platelike $Ba_{0.5}(Bi_{0.5}K_{0.5})_{0.5}TiO_3$ (BBKT) mesocrystals from HTO via an in situ topochemical structural conversion reaction.

The $Ba_{0.5}(Bi_{0.5}K_{0.5})_{0.5}TiO_3$ (BBKT) mesocrystals have been developed also by our group recently.[99] Such complex perovskite mesocrystals are very difficult to be prepared via the conventional methods due to their complex chemical compositions. Platelike BBKT mesocrystals were prepared via a novel two-step solvothermal soft chemical process. Incipiently, the platelike layered titanate HTO crystals were

solvothermally treated in a $Ba(OH)_2$ solution to form $BaTiO_3$/HTO (BT-HTO) mesocrystalline nanocomposites. Then the BT-HTO mesocrystalline nanocomposites are hydrothermally treated in $BiCl_3$-KOH solution to form BBNT mesocrystals. In the formation process of the BBKT mesocrystals, firstly, Ba^{2+} ions intercalate into the bulk of HTO crystal through the interlayer pathway by a H^+/Ba^{2+} exchange reaction, and then the Ba^{2+} ions react with the TiO_6 octahedral layers of HTO crystal in the crystal bulk to form the BT nanocrystals with [110]-orientation on the HTO framework via an *in situ* topochemical conversion reaction. Secondly, Bi^{3+} reacted with the residual HTO to produce the $Bi_{12}TiO_{20}$ nanocrystals on the surface of BT nanocrystals by a heteroepitaxial growth mechanism in the nanocomposite. Finally, the BBKT mesocrystals with [110]-orientation is obtained by the reaction of BT and $Bi_{12}TiO_{20}$ in KOH solution via the hydrothermal reaction. The visual formation mechanism of the BBKT mesocrystals is illustrated in Figure 1.10.

1.3.6 (K, Na)NbO_3-based mesocrystals

Among all the candidates of lead-free piezoelectric materials, alkali niobate materials based on (K, Na)NbO_3 have drawn much attention since Saito et al. reported that the piezoelectric constant of (K, Na)NbO_3 oriented ceramics reach amazingly up to 416 pC/N.[102] Furthermore, a significant feature of (K, Na)NbO_3 ceramics lies in the inherent compatibility with nickel electrode, which is absent in the PZT materials but very important for industry due to the significant reduction in processing cost.[103] One of the effective approaches for enhancing piezoelectricity is the reducing of the grain size of the ceramic. The ceramics with small grain size can be fabricated using mesocrystals. Not long ago, in the fabrication processes of $K_{0.5}Na_{0.5}NbO_3$ (KNN) and $(Li_{0.04}K_{0.44}Na_{0.52})(Nb_{0.85}Ta_{0.15})O_3$ (LKNNT) piezoelectric ceramics, a unique core–shell structure was found out.[104] The core region is composed of highly parallel

nanosized subgrains, whereas the shell region consists of larger-sized but similar self-assembled subgrains. The coarse core–shell grains show a single-crystal-like selected area electron diffraction pattern, suggesting the mesocrystallization has occurred in the formation process of the core–shell grains. In the formation process, the nanosized subgrains aggregate by the self-assemble approach to form a typical core–shell grain structure. The KNN based ceramics with the core–shell grains present the highest dielectric constants and the lowest dielectric losses due to their highest densities. However, the piezoelectric constant d_{33} values tended to decline in these fabrication processes.

Another rare instance, in the formation of the single-crystalline orthorhombic $KNbO_3$ nanorods process, an intermediate $KNbO_3$ mesocrystal was observed.[105] The $KNbO_3$ nanorods were prepared from Nb_2O_5 by hydrothermal synthesis at 180 ^oC in a KOH solution using sodium dodecyl sulfate surfactant. The morphology of the $KNbO_3$ product was strongly influenced by the addition of the surfactant and the concentration of the reactants. The nanorod growth mechanism is based on self-assembly of cube-shaped or facetted $KNbO_3$ nanocrystals along [001] growth direction into mesocrystals, which further grown into the nanorods with a [010] zone axis. The orthorhombic to tetragonal and tetragonal to cubic phase transitions of $KNbO_3$ nanorods occurred at significantly lower temperatures, which may be due to the formation of intermediate $KNbO_3$ nanocrystal in the phase transition process.

1.4 Topochemical synthesis

Topochemical synthesis is a very classical and useful approach for the preparation of the targeted particles with the desired morphologies.[106,107] In contrast to the other reactions, the topochemical conversion reaction can be described as special phase

transformations of the parents crystals into the daughter crystals, and are driven by the crystal structures rather than by the chemical nature of the reactants. Therefore, the crystallographic directions of parent and daughter crystals have some certain topological correspondences. Some mesocrystals can be prepared by the topochemical syntheses method as described above.

1.4.1 Approach of topochemical synthesis

The conventional synthesis approaches including solid state reaction process, molten salt process, and hydrothermal/solvothermal process can be utilized for the topochemical synthesis. For the normal solid-solid reaction process, the ball-milled precursor powders with desired compositions should be annealed at high temperatures. This reaction occurs simply via solid-state diffusion at a high temperature. The obtained produces usually have the characteristics of isometric morphology such as cubic or spherical, large particle size, and compositional inhomogeneity.[108,109] Hence, as a general rule, the solid state process is seldom utilized for the topochemical synthesis.

The molten salt process is usually carried out in a low molten salt as a reaction medium, and itself can also act as a reagent. The crystal growth occurs easily in the molten salt medium, the product particles usually have its original crystal morphology, uniform and large particle size. The precursor host particles can react easily with the guest ion or molecule species in the molten-salt via host-guest mechanism to achieve desired composition and morphology of the products.[110-112] Therefore, the molten salt process can usually be used for the topochemical synthesis.

The hydrothermal/solvothermal process is a liquid chemical reaction process under high pressure of above 1 atm and high temperature of above boiling point of the solvent used. When an aqueous solution is used as the solvent, it is called

hydrothermal process. When an organic solvent or organic and aqueous mixed solvent is used, it is called solvothermal process. These processes are widely applied to prepare the ceramics powders. The basic mechanism of crystal nucleation and growth under the hydrothermal and solvothermal conditions is the dissolution-deposition reactions. The particle size is controlled by the crystal growth rate, reaction time, and reaction temperature. The particle morphology is dependent on the crystal growth direction or the non-classical self-assemble direction that is not easy to be controlled in the normal cases. The advantages of the hydrothermal/solvothermal process are preparations of the products with a controllable morphology, a controllable crystal facet, a uniform size distribution, a small crystal size at a relatively low temperature. The hydrothermal/solvothermal process is a potential method for the topochemical synthesis.

1.4.2 Solvothermal soft chemical process for topochemical synthesis

The solvothermal soft chemical process is a useful and unique method for the preparation and design of functional inorganic materials.[93,113,114] The advantages of the hydrothermal/solvothermal process are suitable for the soft chemical synthesis, especially in effectively maintaining the precursor morphologies in the synthesis process. The solvothermal soft chemical process typically comprises two steps: the first step is the preparation of a framework precursor with layered structure and insertion of structural directing-agents (template ions or molecules) into its interlayer space by a soft chemical reaction; the second step is the structural transformation of the structural directing-agent-inserted precursor into a desired structure by a solvothermal reaction. The crystal structure of the product can be controlled by the structural directing-agent used, and the product particle morphology is dependent on the precursor morphology used. This process has been utilized for the synthesis and

design of metal oxides and organic-inorganic nanocomposites with controlled structure, morphology, and chemical composition.[115,116] As described above, the 2D platelike perovskite mesocrystals, such as $BaTiO_3$,[93,94,117] $Ba_{1-x}Ca_xTiO_3$,[98] and $Ba_{1-x}(Bi_{0.5}K_{0.5})_xTiO_3$[99] mesocrystals can be topochemically synthesized from 2D platelike protonated titanate single crystals using the solvothermal soft chemical process.

1.4.3 Layered protonated titanate HTO as precursor for topochemical synthesis

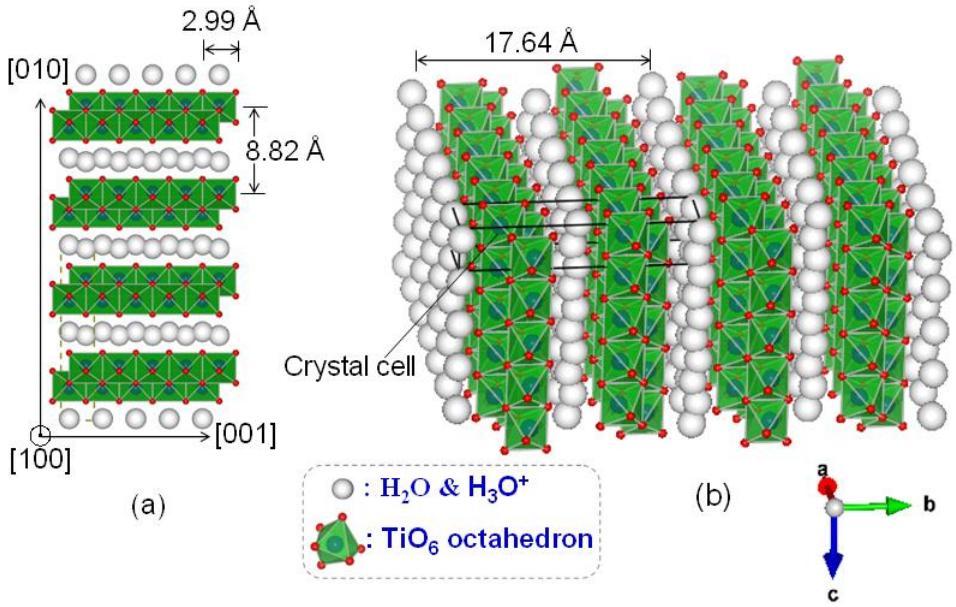

Figure 1.11 Schematic diagrams of HTO ($H_{4x/3}Ti_{2-x/3}O_4 \cdot H_2O$ (x = 0.8)) crystal with (a) [100] zone axis structure and (b) three-dimensional (3D) structure.

Increasing interest has recently been paid to layered titanates with variety 2D structures due to their interesting interlayer chemistry.[118] One of the most studied layered titanate is lepidocrocite (γ–FeOOH)-type protonated titanate, which has a composition of $H_{4x/3}Ti_{2-x/3}O_4 \cdot H_2O$ (x = 0.8) ($H_{1.07}Ti_{1.73}O_4 \cdot H_2O$, abbreviated to HTO) and shows excellent ion-exchange/intercalation reactivities, and can be readily exfoliated/delaminated into its molecular single sheets with a distinctive 2D morphology and a small thickness.[118,119] In the HTO crystal structure, the TiO_6

octahedrons are combined with each other via angle and edge-sharing to form a 2D TiO_6 octahedral sheet, as illustrated in Figure 1.11. The host sheets are stacked with a interlayer spacing of about 8.82 Å in a body-centered orthorhombic relationship (a = 3.7831 Å, b = 17.6413 Å, c = 2.9941 Å), accommodation H_2O and H_3O^+ between them (Figure 1.11). Approximately 52% of the interlayer sites are occupied by H_3O^+ and remaining by H_2O. The positive charge of H_3O^+ is balanced with minus one of the host TiO_6 octahedral sheets arising from the Ti site vacancies.[120,121]

In our previous works, we have used the HTO crystal as a precursor to prepare the various perovskite titanate mesocrystals as described above, and anatase and rutile platelike particles, and furthermore as a template to fabricate oriented ceramics by a reactive template grain growth method. Very recently, the phase transition mechanism of the HTO crystal to anatase under supercritical water has been reported.[122] These results suggest that the HTO crystal is an excellent precursor for the preparations of the titanate mesocrystals and titanium oxides mesocrystals by the topochemical conversion reaction mechanisms.

1.5 Fabrication of oriented ferroelectric ceramic materials

Through the description above, it has learned that the mesocrystal materials have a high orientation, and are constructed from the submicro/nanocrystals with uniform size and mutual coordination. Obviously, such mesocrystalline materials are suitable for developing the oriented ceramics with the high preferred orientation, uniform small grain size, and high density. But based on the investigation of almost all the literatures involving mesocrystals, there are only two literatures (References [98] and [104]) mentioned about the fabrications of oriented ceramics using the mesocrystals. Besides, for improving the piezoelectric and dielectric performances of the oriented

ferroelectric ceramics, the oriented engineering and domain (wall) engineering are very valid approaches. Therefore, the development of the functional mesocrystals for the application to the oriented ferroelectric ceramics materials combining with the oriented engineering and domain (wall) engineering will have a potential application foreground.

1.5.1 Application of oriented engineering to oriented ceramics

The ceramics with the grains intentionally aligned in same crystal-axis direction are called "grain-oriented", "oriented", "textured", "crystallographically textured", or "crystallographically oriented" ceramics.[123] Oriented engineering is a convenient and effective technology of applying crystal-axis-orientation for enhancing the physical and mechanical properties of the functional ceramics with the anisotropic properties. The application of oriented engineering to piezoelectric ceramics was firstly proposed in the late 1960s.[124] The development of lead-free piezoelectric ceramics had been greatly proceeded in 1990s.[102] Afterwards, the discovered lead-free materials are not sufficient to replace lead-containing materials due to their relatively low piezoelectric coefficients. One method of enhancing the piezoelectric coefficients is to develop the oriented piezoelectric ceramics because the piezoelectric materials exhibit crystal-axis anisotropic behavior in their piezoelectric coefficients. The templated grain growth (TGG) or reactive-templated grain growth (RTGG) is a useful technique for producing dense and textured ceramics by using a certain number of anisometric shaped (platelike or needlelike) template particles aligned in a matrix as nucleation sites for the development of the orientation engineering.[125]

In the TGG process, a precursor with an anisometric morphology of an oriented target compound is used as a template, and a complementary equiaxed target compound are mixed together as the starting materials. The oriented ceramic is

developed mainly by the growth of the precursor of the oriented target compound at the expense of equiaxed target compound.[126] The RTGG process with a significant specialty is also an *in situ* topochemical reaction between the precursor template particles with anisotropy morphology and the other equiaxed matrix starting materials. Usually, the particles with platelike or fibrous anisotropy morphology can be selected as the reactive template material. In this process, a green compact made from aligned template particles with the same crystal-axis direction and matrix grains with random direction is calcined or sintered to form the oriented object material. The oriented ceramic is developed mainly by the growth of oriented template particles at the expense of matrix grains.[101] The procedure for preparing oriented ceramics is almost the same as that of the TGG process. The only difference is a calcination step for the green compacts. In the RTGG process, the aligned reactive template particles without a composition of the target compound, and the randomly oriented complementary reactant particles are processed to form the green compacts. The calcination is necessary to cause the *in situ* topochemical reaction that results the formation of particles of the target compound with the desired orientation. The crystal axis of the target compound is determined by the relation between the crystal structures of the reactive template and the target compound. Sometimes the compounds belonging to the perovskite structured and bismuth layer-structured ferroelectrics can cause the expansion of compacts during the formation process.[127]

Several methods are available to evaluate the degree of the preferred orientation quantitatively,[128] but the Lotgering method using XRD data is widely used because of its simplicity.[129] The detailed expression is shown as the following:

$$F = \frac{P - P_0}{1 - P_0}, \quad P = \frac{\Sigma I(h00)}{\Sigma I(hkl)}, \quad P_0 = \frac{\Sigma I_0(h00)}{\Sigma I_0(hkl)}$$

where I and I_0 are the intensities of the (hkl) peaks for the oriented and the non-oriented samples, respectively. The F value ranges from 0 to 1, where F = 0 and 1 correspond to the completely random and the perfectly oriented, respectively.

1.5.2 Application of domain (wall) engineering to oriented ceramics

A ferroelectric crystal has a spontaneous polarization in the crystal bulk even without an applied electric field, and its spontaneous polarization direction can be reversed under an appropriate applied electric field, which is the reason why the ferroelectric crystal can exhibit a large dielectricity. [130,131] Furthermore, the reversal of polarization direction accompanies a deformation in the crystal, which corresponds to the piezoelectric mechanism. The polarization reversal derives from the domain reversal. The domain is a micro-region with the same spontaneous polarization direction in the ferroelectric crystal.[132] A boundary between the domains is named a domain wall. Usually, the ferroelectric crystal has polydomain structure separated by the domain walls, and the spontaneous polarization directions of the different domains exist in some simple corresponding relationships. For instance, for the tetragonal BT single crystal, the angles between the spontaneous polarization directions of the neighboring domains may be only 90 and 180 ^{o}, respectively, as shown in Figure 1.12. For the rhombohedral BT single crystal, the angles include 71, 109, and 180 ^{o}. For the orthorhombic BT single crystal, the angles include 60, 120, and 180 ^{o}. But in the polycrystal structure, the spontaneous polarization direction is not any specific rule because the component crystalline grains are unoriented for the polycrystalline bulk. If the polycrystal is constructed from the oriented building units, such as a mesocrystal, the spontaneous polarization direction will be similar to the single crystal.

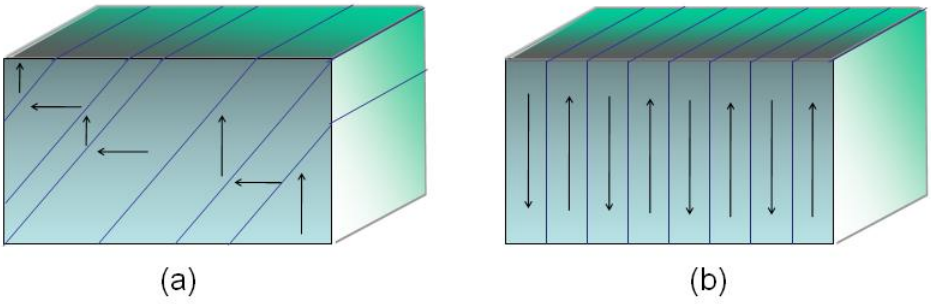

Figure 1.12 Schematic diagram of the simplest type of (a) 90 ^{o} and (b) 180 ^{o} arranged domains (walls) of tetragonal $BaTiO_3$ single crystal. The arrows show the spontaneous polarization direction. The domain extends from one face to a parallel one and the directions of the tetragonal axes are as shown.[133]

The spontaneous polarization direction around the domain walls is unstable, which can be easily reversed under a weak applied electric field. This property can be applied to enhance the dielectricity and piezoelectricity. Therefore, the controlling of the size, structure, and polarization reversal of the domain, and the fabrication and design of the domain are important systematic engineering for the development of the application the ferroelectric materials.[134,135,136,137,138] To achieve much higher piezoelectric properties than those of $Pb(Zr/Ti)O_3$ (PZT) ceramics, the domain engineering as an important technique for obtaining enhanced piezoelectric properties in single crystals have been applied to lead-free ferroelectric materials.[134,139—143] In general, the increase of the domain size and the design of the polarization improvement by enhancing remanent polarization can be carried out by domain engineering, which are not indispensable for the enhancement of the piezoelectric properties.[134-145] The domain size can be decreased by reducing the grain size of the ceramic, which can enhance the dielectricity and piezoelectricity.[146,147]

The above discussions suggest that the spontaneous polarization around the domain walls can contribute significantly to the piezoelectric and dielectric performances. An artificial domain wall can be fabricated using some heteroepitaxy interfaces of different substances with lattice mismatch or/and the different directions

of the spontaneous polarization, as shown in Figure 1.13. The spontaneous polarization direction around the artificial domain walls can be changed to the other direction due to the lattice distortion at the heteroepitaxy interfaces. Therefore, a sloping spontaneous polarization structure can be imported into the interfaces of the different substances, which results in producing the polarization reversal sustaining.[148] The artificial interfaces such as in artificial superlattices can produce an obviously significant enhancement of piezoelectric and dielectric constants.[149–151]

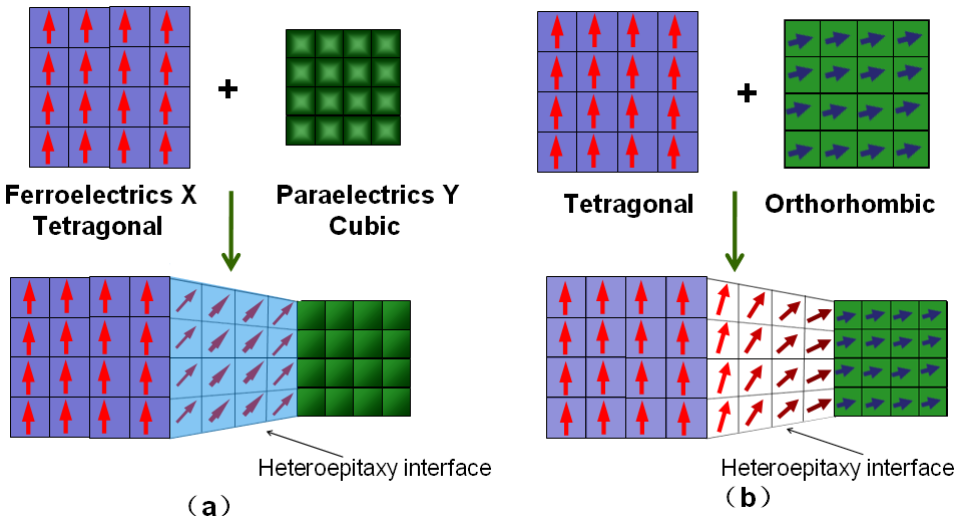

Figure 1.13 Schematic diagrams of imported heteroepitaxy interfaces from (a) composite paraelectricses and (b) composite non-paraelectricses.

At present, the most studies on the superlattices of ferroelectric materials are in regard to 2D $BaTiO_3/SrTiO_3$ superlattice structure prepared by the molecular-beam epitaxy (MBE) process.[152] But the MBE process is inefficient and high cost, and the industrialization production is difficult to achieve by MBE process.[153-155] Furthermore, 3D superlattice structures which can achieve a high density interface is difficult to be fabricated via the MBE process. Hence, the exploration of a new approach to develop the superior superlattice composite materials is expected. The development of the ferroelectric mesocrystalline nanocomposites with the 3D superlattice structure by a

facile low cost process is a significant subject and will attach much attention in the ferroelectric materials field.

1.6 Purposes of present study

As described above, up to now, some studies on the mesocrystals have been reported mainly on the syntheses and formation mechanisms; however, the understandings on mesocrystal properties, formation mechanisms, and especially the potential application possibilities are not enough. Further development of the functional mesocrystals, investigations of the mesocrystal performances and the formation mechanisms are necessary in current nanomaterial research fields. The mesocrystals of ferroelectric materials may be applied to fabricate the high performance ferroelectric ceramics with a high preferential orientation, high relative density, and small grain size. The functional mesocrystalline nanocomposite materials can apply to a novel 3D superlattice ferroelectric material and 3D superlattice photocatalyst with the high efficient electron hole separation effect. Therefore, in this study, the functional ferroelectric mesocrystals, and mesocrystalline nanocomposites of ferroelectric and photocatalytic materials were developed by a solvothermal soft chemical process and a solid state soft chemical process via the *in situ* topochemical conversion mechanism.

The present study aims at (1) the expedition of mesocrystals chemistry and the offer of some good opportunity to understand the formation mechanism of mesocrystalline superstructures, (2) the development of the solvothermal soft chemical process and the solid state soft chemical process via the *in situ* topochemical conversion to synthesize the functional titanate and titanium oxide mesocrystals and their mesocrystalline nanocomposites, (3) the characterizations of the mesocrystal of

$Na_{0.5}Bi_{0.5}TiO_3$ (BNT) and mesocrystalline nanocomposites of $BaTiO_3/SrTiO_3$ (BT/ST), and anatase/rutile, (4) the description of the formation reaction mechanisms and nanostructures of the mesocrystals and mesocrystalline nanocomposites, and (5) the applications of these mesocrystals and mesocrystalline nanocomposites to the ferroelectric and photocatalytic materials.

In Chapter II, the formation and characterization of $Na_{0.5}Bi_{0.5}TiO_3$ (BNT) ferroelectric mesocrystals prepared from a layered titanate $H_{1.07}T_{2.73}O_4 \cdot H_2O$ (HTO) with a lepidocrocite-like structure are described. The BNT mesocrystals were synthesized via solid state reactions in HTO-Bi_2O_3-Na_2CO_3 and HTO-TiO_2-Bi_2O_3-Na_2CO_3 solid-state reaction systems. The BNT mesocrystals are constructed from [100]-oriented BNT nanocrystals. The BNT mesocrystals were formed by an *in situ* topotactic structural transformation mechanism and a combination mechanism of the topotactic structural transformation and an epitaxial crystal growth.

In Chapter III, a reactive-templated grain growth (RTGG) process for the fabrication of the crystal-axis-oriented $Bi_{0.5}Na_{0.5}TiO_3$ (BNT) ceramics using platelike HTO crystals as a template is described. The [100]-oriented BNT ceramics with the high degree of orientation, high density, and small grain size were achieved simultaneously by using a HTO-TiO_2-Bi_2O_3-Na_2CO_3 reaction system. The oriented BNT ceramic is formed by a topochemical conversion reaction of platelike HTO template crystals to platelike BNT mesocrystal particles, and then epitaxial crystal growth of BNT on the BNT mesocrystals. The fabricated oriented BNT ceramic shows a higher piezoelectric constant value of d_{33}* than the non-oriented BNT ceramic.

In Chapter IV, the synthesis, characterization and formation mechanism of the platelike $BaTiO_3/SrTiO_3$ (BT/ST) mesocrystalline nanocomposites are described. The platelike BT/ST mesocrystalline nanocomposites were synthesized by a two-step

solvothermal soft chemical process. In the first step, the platelike HTO crystal was partially reacted with $Ba(OH)_2$ under hydrothermal condition in water solution to prepare a platelike $BaTiO_3$/HTO (BT/HTO) mesocrystalline nanocomposite. In the second step, the BT/HTO mesocrystalline nanocomposite was solvothermally treated in $Sr(OH)_2$ water-alcohol solution, to obtain the platelike BT/ST mesocrystalline nanocomposite.

In Chapter V, the synthesis, characterization, and formation mechanism of platelike TiO_2 polymorphs mesocrystalline nanocomposites synthesized based on topochemical mesocrystal conversion process are described. In this conversion process, the orthorhombic HTO single crystal with [010] direction orientation was successively transformed into monoclinic HTO single crystal, polycrystalline monoclinic {010}-faceted TiO_2 (B) twining, polycrystalline [010]-oriented anatase, and polycrystalline [110]-oriented rutile, respectively. All the nanocrystals formed via the topochemical conversion have specific corresponding relations of crystal orientations. An [010]-oriented anatase/[110]-oriented rutile mesocrystalline nanocomposite can be obtained also using this reaction process. This polymorphs mesocrystalline nanocomposite exhibits a high surface activity for the photocatalytic reaction.

In Chapter VI, the main points concluded in each chapter are summarized. In addition, on the basis of the results of the present study the future prospects for the applications of these results are shown.

1.7 References

(1) Trindade, T.; O'Brien, P.; Pickett, N. L. *Chem. Mater.* **2001**, 13, 3843–3858.

(2) Zhou, L.; O'Brien, P. *Small* **2008**, 4, 1566–1574.

(3) Harfenist, S. A.; Wang, Z. L.; Alvarez, M. M.; Vezmar, I.; Whetten, R. L. *J. Phys. Chem. B* **1996**, 100, 13904–13910.

(4) Cölfen, H.; Antonietti, M. *Angew. Chem. Int. Ed.* **2005**, 44, 5576–5591.

(5) Antonietti, M.; Ozin, G. *Chem. Eur. J.* **2004**, 10, 28–41.

(6) Talapin, D. V.; Lee, J–S.; Kovalenko, M. V.; Shevchenko, E. V. *Chem. Rev.* **2010**, 110, 389–458.

(7) Nie, Z.; Petukhova, A.; Kumacheva, E. *Nat. Nanotech.* **2010**, 5, 15–25.

(8) Collier, C. P.; Vossmeyer, T.; Heath, J. R. *Ann. Rev. Phys. Chem.* **1998**, 49, 371–404.

(9) Cölfen, H.; Antoniett, M. *Mesocrystals and nonclassical crystallization*, John Wiley & Sons Ltd, The Atrium, Southern Gate, Chichester, West Sussex PO19 8SQ, England **2008**.

(10) Cölfen, H.; Mann, S. *Angew. Chem. Int. Ed.* **2003**, 42, 2350–2365.

(11) Song, R. Q.;Cölfen, H. *Adv. Mater.* **2010**, 22, 1301–1330.

(12) Liu, Y. Q.; Zhang, Y.; Wang, J. *CrystEngComm*, **2014**, 26, 5948–5967.

(13) Inumaru, K.; Nakajima, H.; Ito, T.; Misono M. *Chem. Lett.* **1996**, 25, 559–560.

(14) Distaso, M.; Segets, D.; Wernet, R.; Taylor, RK.; Peukert, W. *Nanoscale* **2012**, 4, 864–873.

(15) Ma, Y.; Cölfen, H.; Antonietti, M. *Phys, J. Chem. B.* **2006**, 110, 10822–10828.

(16) Gong, H. F.; Pluntke, M.; Marti, O.; Walther, P.; Gower, L.; Colfen, H.; Volkmer, D. *Colloids Surf. A Physicochem. Eng. Asp.* **2010**, 354, 279–283.

(17) Gebauer, D.; Cölfen, H.; Verch, A.; Antonietti, M. *Adv. Mater.* **2009**, 21, 435–439.

(18) Neira–Carrillo, A.; Acevedo, D. F.; Miras, M. C.; Barbero, C. A.; Gebauer, D.; Colfen, H.; Arias, J. L. *Langmuir* **2008**, 24, 12496–12507.

(19) Xu, A. W.; Antonietti, M.; Cölfen, H.; Fang, Y. P. *Adv. Funct. Mater.* **2006**, 16, 903–908.

(20) Page, M. G; Cölfen, H. *Cryst. Growth Des.* **2006**, 6, 1915–1920.

(21) Gao, Y. X.; Yu, S. H.; Cong, H.; Jiang, J.; Xu, A. W.; Dong, W. F.; Cölfen, H., *J. Phys. Chem. B* **2006**, 110, 6432–6436.

(22) Xu, A. W.; Yu, Q.; Dong, W. F.; Antonietti, M.; Cölfen, H. *Adv. Mater. (Weinheim, Germany)* **2005**, 17, 2217–2221.

(23) Wang, T.; Cölfen, H.; Antonietti, M. *J. Am. Chem. Soc.* **2005**, 127, 3246–3247.

(24) Bolze, J.; Pontoni, D.; Ballauff, M.; Narayanan, T.; Cölfen, H. *J.Colloid Interf. Sci.* **2004**, 277, 84–94.

(25) Rudloff, J.; Antonietti, M.; Cölfen, H.; Pretula, J.; Kaluzynski, K.; Penczek, S. *Macromol. Chem. Phys.* **2002**, 203, 627–635.

(26) Cölfen, H.; Qi, L. *Prog. Coll. Pol. Sci.* **2001**, 117, (Adsorption and Nanostructures), 200–203.

(27) Wang, T. X.; Mitchell, J.; Borner, H.; Colfen, H.; Antonietti, M. *Phys. Chem. Chem. Phys.* **2010**, 12, 11984–11992.

(28) Zhu, J. H.; Yu, S. H.; Xu, A. W.; Cölfen, H. *Chem. Commu.* **2009**, 9, 1106–1108.

(29) Yu, S. H.; Cölfen, H.; Tauer, K.; Antonietti, M. *Nat. Mater.* **2005**, 4, 51–55.

(30) Yu, S. H.; Cölfen, H.; Xu, A. W.; Dong, W., *Cryst. Growth Des.***2004**, 4, 33–37.

(31) Cölfen, H.; Mann, S. *Angew. Chem.* **2003**, 115, 2452–2468.

(32) Petres, J. J.; Dezelic, G,; Tezak, B. *Croat. Chem. Acta* **1969**, 41, 183–186.

(33) Dominguez Bella, S.;Garcia–Ruiz, J. M.; *Cryst. J. Growth* **1986**,79, 236–240.

(34) Ye, J. F.; Liu, W.; Cai, J. G.; Chen, S.; Zhao, X. W.; Zhou, H. H.; Qi, L. M. *J. Am. Chem. Soc.***2011**, 133, 933–940.

(35) Heap, A. D.; Dickens, G. R.; Stewart, L. K. *Mar. Geol.* **2001**,176, 39–54.

(36) Weiner, S.; Addadi, L. J. *Mater. Chem.* **1997**, 7, 689–702.

(37) Flaten, E. M.; Seiersten, M.; Andreassen, J. P. *J. Cryst. Growth* **2009**, 311, 3533–3538.

(38) Geng, X.; Liu, L.; Jiang, J.; Yu, S. H. *Cryst. Growth Des.***2010**, 10, 3448–3453.

(39) Chen, S. F.; Zhu, J. H.; Jiang, J.; Cai, G. B.; Yu, S. H. *Adv. Mater.* **2010**, 22, 540–545.

(40) Grassmann, O.; Neder, R. B.; Putnis, A.; Löbmann, P. *Am. Mineral.* **2003**, 88, 647–652.

(41) Peng, H. B.; Li, K.; Wang, T.; Wang, J.; Wang, J.; Zhu, R. G.; Sun, D. M.; Wang, S. L.

Nanoscale Res. Lett. **2013**, 8, 321.

(42) Burleson, D. G.; Penn, R. L. *Langmuir* **2006**, 22, 402–409.

(43) Gao, P. X.; Wang, Z. L. *Small* **2005**, 1, 945–949.

(44) Farhadi, S.; Siadatnasab, F.; Jahanara, K. *Journal of nanostructures* **2013**, 3, 227–235.

(45) He, F. Q.; Zhao, Y. P. *Appl. Phys. Lett.* **2006**, 88, 193113.

(46) Zhang, Q.; Liu, S. J.; Yu, S. H. *J. Mater. Chem.* **2009**, 19, 191–207.

(47) Chae, K. W.; Zhang, Q. F.; Kim, J. S.; Jeong, Y. H.; Cao, G. Z. *Beilstein J. Nanotechnol.* **2010**, 1, 128–134.

(48) Tang, H.; Chang, J. C.; Shan, Y. Y.; Lee, S. T. *J. Phys. Chem. B* **2008**, 112, 4016–4021.

(49) Mo, M. S.; Um, S. H.; Mai, Y. W.; Zheng, R. K.; Ringer, S. P. *Adv. Mater.* **2008**,20,339–342.

(50) Dong, J. Y.; Lin, W. H.; Hsu, Y. J.; Wong, Shan–Hill. D.; Lu, S. Y. *CrystEngComm* **2011**,13, 6218–6222.

(51) Wang, S. S; Xu, A. W. *CrystEngComm* **2013**, 15, 376–381.

(52) Liu, S.; Zhang, J.; Tu, W.; Bao, J.; Dai Z. *Nanoscale.* **2014**, 2, 2419–2425.

(53) Chen, X.; Mao, S. S. *Chem. Rev.* **2007**, 107, 2891.

(54) Fujishima, A.; Zhang, X.; Tryk, D. A. *Surf. Sci. Rep.* **2008**, 63, 515.

(55) Grätzel, M. *Nature* **2001**, 414, 338.

(56) Deng, D.; Kim, M. G.; Lee, J. Y.; Cho, J. *Energy Environ. Sci.* **2009**, 2, 818.

(57) Banfield, J. F.; Veblen, D. R.; Smith, D. J. *Am. Mineral.* **1991**,76, 343–353.

(58) Marchand, R.; Brohan, L.; Tournoux, M. *Mater. Res. Bull.* **1980**, 15, 1129–1133.

(59) Kröger, N.; Dickerson, M. B.; Ahmad, G.; Cai, Y.; Haluska, M. S.; Sandhage, K. H.; Poulsen, N.; Sheppaard, V. C. *Angew. Chem. Int. Ed.* **2006**, 45, 7239–7243.

(60) Kamat, P. V. *J. Phys. Chem. C* **2007**, 111, 2834–2860.

(61) Karch, J.; Birringer, R.; Gleiter, H. *Nature* **1987**, 330, 556–558.

(62) Hong, Z.; Wei, M.; Lan, T.; Jiang, L.; Cao, G. *Energy Environ. Sci.* **2012**, 5: 5408–5413.

(63) Hong, Z. S.; Xu, Y. X.; Liu, Y. B.; Wei, M. D. *Chem. Eur. J.* **2012**, 18, 10753–10760

(64) Cai, J.; Ye, J.; Chen, S.; Zhao, X.; Zhang, D.; Chen, S.; Ma, Y.; Jin, S.; Qi, L. *Energy Environ. Sci*. **2012**, 5, 7575–7581.

(65) Liu, B.; Zeng, H C. *Chem. Mater.* **2008**, 20, 2711–2718.

(66) Liu, S. J.; Gong, J. Y.; Hu, B.; Yu, S. H. *Cryst. Growth Des.* **2008**, 9, 203–209.

(67) Zhang, D.; Li, G.; Wang, F.; Yu, J. C. *CrystEngComm* **2010**, 12, 1759–1763.

(68) Chen, Q. F.; Ma, W. H.; Chen, C. C.; Ji, H. W.; Zhao, J. C. *Chem. Eur. J.* **2012**, 18, 12584–12589.

(69) Da Silva R. O.; Gonçalves, R. H.; Stroppa, D. G.; Ramirez, A. J.; Leite, E. R. *Nanoscale*, **2011**, 4, 1910–1916.

(70) Tartaj, P.; Amarilla, J.M. *Adv. Mater.* **2011**, 23, 4904–4907.

(71) Tartaj, P. *Chem. Commun*. **2011**, 47, 256–258.

(72) Aoyama, Y.; Oaki, Y.; Ise, R.; Imai, H. *CrystEngComm* **2012**, 14, 1405–1411.

(73) Liao, J.Y.; Lei, B. X.; Chen, H. Y.; Kuang, D. B.; Su, C. Y. *Energy Environ. Sci*. **2012**, 5, 5750–5757.

(74) Fang, J. X.; Ding, B. J.; Gleiter, H. *Chem. Soc. Rev*. **2011**,40, 5347–5360.

(75) Cai, J. G.; Qi, L. M. *Sci. China Chem*. **2012** ,55, 11, 2318–2326.

(76) Hong, Z. S.; Wei, M. D.; Lan, T. B.; Cao, G. Z. *Nano Energ.* **2012**, 1, 466–471.

(77) Zhou, L.; Smyth–Boyle, D.; O'Brien, P. *Chem. Commun*. **2007**,144–146.

(78) Zhou, L.; Smyth–Boyle, D.; O'Brien, P. *J. Am. Chem. Soc.* **2008**, 130, 1309–1320.

(79) Feng, J.; Yin, M.; Wang, Z.; Yan, S.; Wan, L.; Li, Z.; Zou, Z. *CrystEngComm*, **2010**, 12, 3425–3429.

(80) Fang, Z.; Long, L. Y.; Hao, S. H.; Song, Y. X.; Qiang, T. T.; Geng, B. T. *CrystEngComm*. **2014**,16, 2061–2069.

(81) Tachikawa, T.; Zhang, P.; Bian, Z. F.; Majima, T. *J. Mater. Chem. A* **2014**,2, 3381–3388.

(82) Shimakawa, Y.; Saito, T. *Phys. Status. Solidi. B* **2012**, 249, 3, 423–434.

(83) Chandler, C. D.; Roger, C.; Hampden–Smith, M. J. *Chem. Rev*. **1993**, 93, 1205–1241.

(84) Bhalla, A. S.; Guo, R.; Roy, R. *Mater. Res. Innov*. **2000**, 4, 3–26.

(85) Pena, M. A.; Fierro, J. L. G. *Chem. Rev.* **2001**, 101, 1981–2017.

(86) Wang, G. Z.; Ragnhild, S.; Per Martin, R.; Antonius, V. H.; Randi, H.; Tor, G.; Mari–Ann, E. *J. Nanosci. Nanotechno.*, **2007**, 7, 2538–2541.

(87) Rorvik, P. M.; Almli, A.; van Helvoort, A. T.; Holmestad, R.; Tybell, T.; Grande, T.; Einarsrud, M. A. *Nanotechno.* **2008**, 19, 225605.

(88) Demirörs, A. F.; Imhof, A. *Chem. Mater.* **2009**, 21, 3002–3007.

(89) Calderone, V. R.; Testino, A.; Buseaglia, M. T.; Bassoli, M.; Bottino, C.; Viviani, M.; Buseaglia, V.; Nanni, P. *Chem. Mater.* **2006**, 18, 1627.

(90) Kalyani, V.; Vasile, B. S.; Ianculescu, A.; Buscaglia, M. T.; Buscaglia, V.; NanniCryst, P. *Cryst. Growth Des.* **2012**, 12, 4450–4456.

(91) Park, N. H.; Wang, Y. F.; Seo, W.S.; Dang, F.; Wan, C.L.; Koumoto, K. *CrystEngComm* **2013**, 15, 679–685

(92) Ishihara, T.; Kometani, K.; Mizuhara, Y.; Takita, Y. *J. Am.Ceram. Soc.* **1992**, 75, 613.

(93) Feng, Q.; Hirasawa, M.; Yanagisawa, K. *Chem. Mater.* **2001**, 13, 290−296.

(94) Feng, Q.; Hirasawa, M.; Kajiyoshi, K.; Yanagisawa, K. *J. Am. Ceram. Soc.* **2005**, 88, 1415−1420.

(95) Qi, J. Q.; Sun, L.; Du, P.; Li, L. T. *J. Am. Ceram. Soc.* **2010**, 93, 1044−1048.

(96) Wada, S.; Takeda, K.; Muraishi, T.; Kakemoto, H.; Tsurumi, T.; Kimura, T. *Jpn. J. Appl. Phys.* **2007**, 46, 7039–7043.

(97) Dang, F,; Kato, K.; Imai, H.; Wada, S.; Hanedad, H.; Kuwabarae, M. *CrystEngComm* **2010**,12, 3441–3444.

(98) Kong, X. G.; Ishikawa, Y.; Shinagawa, K.; Feng, Q. *J. Am. Ceram. Soc.* **2011**, 94, 3716−3721.

(99) Kong, X. G.; Hu, D. W.; Ishikawa, Y.; Tanaka, Y.; Feng, Q. *Chem. Mater.* **2011**, 23, 3978−3986.

(100) Maurya, D.; Murayama, M.; Pramanick, A.; Reynolds, WT.; An, K.; Priya, S. *J. Appl. Phys.*

2013, 113, 114101–114109.

(101) Maurya, D.; Zhou, Y.; Yan, Y. K.; Priya, S. *J. Mater. Chem. C* **2013**,1,2102–2111.

(102) Saito, Y.; Takao, H.; Tani, T.; Nonoyama, T.; Takatori, K.; Homma, T.; Nagaya, T.;. Nakamura, M. *Nature* **2004**, 432, 84–87.

(103) Li, J. F.; Wang, K.; Zhu, F. Y.; Cheng, L. Q.; Yao, F. Z. *J. Am. Ceram. Soc.* **2013**, 1–20.

(104) Zhen, Y. H.; Li, J. F. *J. Am. Chem. Soc.* **2007**, 90, 3496–3502.

(105) Wang, G. Z.; Selbach, S. M.; Yu, Y. D.; Zhang, X. T.; Grande, T.; Einarsrud, M. A. *CrystEngComm* **2009**, 11, 1958–1963.

(106) Ma, R. Z.; Takada, K.; Fukuda, K.; Iyi, N.; Bando, Y.; Sasaki, T. *Angew. Chem. Int. Ed.* **2008**, 47, 86–89.

(107) Li, C. C.; Li, Q. H.; Chen, L. B.; Wang, T. H. *J. Mater. Chem.* **2011**,21, 11867–11872.

(108) Fu, D.; Itoh, M.; Koshihara, S. Y.; Kosugi, T.; Tsuneyuki, S. *Phys. Rev. Lett.* **2008**, 100.

(109) Panigrahi, M. R.; Panigrahi, S. *Phys. B: Condens. Matter* **2009**, 404, 4267–4272.

(110) Teshima, K.; Niina, Y.; Yubuta, K.; Suzuki, T.; Ishizawa, N.; Shishido, T.; Oishi, S. *Eur. J. Inorg. Chem.* **2007**, 4687–4692.

(111) Zhao, W.; Zhou, H. P.; Yan, Y. K.; Liu, D. *J. Am. Ceram. Soc.***2008**, 91, 1322–1325.

(112) Madaro, F.; Sæterli, R.; Tolchard, J. R.; Einarsrud, M. A.; Holmestad, R.; Grande, T. *CrystEngComm* **2011**, 13, 1304–1313.

(113) Feng, Q.; Honbu, C.; Yanagisawa, K.; Yamasaki, N. Chem. Lett. **1998**, 757–758.

(114) Feng, Q.; Honbu, C.; Yanagisawa, K.; Yamasaki, N. Chem. Mater. **1999**, 11, 2444–2450.

(115) Sasaki, T.; Watanabe, M.; Fujiki, Y.; Kitami, Y. Chem. Mater. **1994**, 6, 1749–1756.

(116) Komori, Y.; Sugahara, Y.; Kuroda, K. Chem. Mater. **1999**, 11, 3–6.

(117) Feng, Q.; Ishikawa, Y.; Makita, Y.; Yamamoto, Y. *J. Ceram. Soc. Jpn.* **2010**, 118, 141–146.

(118) Gao, T.; Fjellvåg, H.; Norby, P. *J. Mater. Chem.* **2009**, 19, 787–794.

(119) Wei, M.; Konishi, Y.; Zhou, H.; Sugihara, H.; Arakawa, H. *Solid State Commun.* **2005**, 133,

493–497.

(120) Reid, A. F.; Mumme, W. G.; Wadsley, A. D. *Acta Cryst.* **1968**, B24, 1228–1233.

(121) Sasaki, T.; Nakano, S.; Yamauchi, S.; Watanabe, M. *Chem. Mater.* **1997**, 9, 602–608.

(122) Liu, C. Q.; Hu, G. X. *RSC Adv.* **2013**, 3, 20877–20882.

(123) Kimura, T. *J. Ceram. Soc. Jpn.* **2006**, 114, 15–25.

(124) Okazaki, K., Narushima, S. *J. Ceram. Soc. Jpn.* **1968**, 76, 19–25.

(125) Yan, Y. K.; Liu, D.; Zhao, W.; Zhou, H. P.; Fang, H. *J. Am. Ceram. Soc.* 2007, 90 (8), 2399–2403.

(126) Kimura, T.; Takahashi, T.; Tani, T.; et al. *J. Am. Ceram. Soc.* **2004**, 87, 1424–1429.

(127) Blum, J. B.; Cannon, W. R. *Am. Ceram. Soc.* **1987**, 19, 131–135.

(128) Seabaugh, M. M.; Vaudin, M. D.; Cline, J. P.; Messing, G. L. *J. Am. Ceram. Soc.* **2000**, 83, 2049–2054.

(129) Lotgering, F. K. *J. Inorg. Nucl. Chem.* **1959**, 9, 113–124.

(130) Lines, M. E.; Glass, A. M. Principles and applications of ferroelectrics and related materials. Clarendon Press, Oxford, **1979.**

(131) Wang, C. L.; Li, J.; Zhao, M. L. Piezoelectric ferroelectric physics, Science Press, Beijing, **2009**.(Chinese)

(132) Doktor–Ingenieur; MPhys, K. S. *Lead–Free Piezoelectric Ceramics* E–Publishing–Service der TU Darmstadt., Darmstadt, **2010**.

(133) Carol Zwick Rosen，Basavaraj V. Hiremath，Robert Everest Newnham. Ferroelectric **1992**, 118–119. American Institute of Physics, New York.

(134) Wang, K.; Li, J. F. *Adv. Funct. Mater.* **2010**, 20, 1924–1929.

(135) Wada, S.; Yako, K.; Kakemoto, H.; Tsurumi, T.; Kiguchi, T. *J. Appl. Phys.* **2005**, 98, 1–7.

(136) Wang, J.; Shi, S. Q.; Chen, L. Q.; Li, Y. L.; Zhang, T. Y. *Acta. Mater.* **2004**, 52, 749–764.

(137) Wada, S.; Muraoka, K.; Kakemoto, H.; Tsurumi, T.; Kumagai, H. *Jpn. J. Appl. Phy.* **2004**, 43,

9B, 6692–6700.

(138) Kuznetsov, D.K.; Shur, V.Ya.; Baturin, I.S.; Menou, N.; Muller, C.H.; Schneller, T.; Sternberg, A. *Ferroelectrics*, **2006**, 340, 1, 161–167.

(139) Jang, H. W.; Ortiz, D.; Baek, S. H.; Folkman, C. M.; Das, R. R.; Shafer, P.; Chen, Y. B.; Nelson, C. T.; Pan, X.Q.; Ramesh, R.; Eom, C. B. *Adv. Mater.* **2009**, 21, 817–823.

(140) Wada, S.; Kakemoto, H.; Tsurumi, T. *Mater. Trans.* **2004**, 45, 178–187.

(141) Wada, S.; Yako, K.; Muraishi, T.; Yokoh, K.; Nam, S. M.; Kakemoto, H.; Tsurumi, T. *Ferroelectrics* **2006**, 340, 17–24.

(142) Wada, S.; Muraishi, T.; Yokoh, K.; Yako, k.; Kamemoto, H.; Tsurumi, T. *Ferroelectrics* **2007** 355, 37–49.

(143) Yako, K.; Kakemoto, H.; Tsurumi, T.; Wada, S. *Mater. Sci. Eng. B* **2005**, 120, 181–185.

(144) Wada, S.; Takeda, K.; Muraishi, T.; Kakemoto, H.; Tsurumi, T.; Kimura, T. *Ferroelectricity* **2008**, 373, 11–21.

(145) Hoshina, T.; Takizawa, K.; Li, J. Y.; Kasama, T.; Kakemoto, H.; Tsurumi, T. *Jpn. J. Appl. Phys.* **2008**, 47, 7607–7611.

(146) Cao, W. W.; Randall, C. A. *J. Phys. Chem. Solids* **1996**, 57, 1499–1505.

(147) Zheng, P.; Zhang, J. L.; Tan, Y. Q.; Wang, C. L. *Acta. Mater.* **2012**, 60, 5022–5030.

(148) Kim, L.; Kim, J.; Waghmare, U. V.; Jung, D.; Lee, J. *Phys. Rev. B* **2005**, 72, 214121.

(149) O'Neill, D.; Bowman, R. M.; Gregg, J. M. *Appl. Phys. Lett.* **2000**, 77, 1520–1522.

(150) Bousquet, E.; Dawber, M.; Stucki, N.; Lichtensteiger, C. Hermet, P.; Gariglio,Jean–Marc Triscone, S.; Ghosez, P. *Nature* **2008**, 452, 732–736.

(151) Ravichandran, J.; Yadav, A. K.; Cheaito, R.; Rossen, P. B.; Soukiassian, A.; Suresha, S. J.; Duda, J. C.; Foley, B. M.; Lee, C. H.; Zhu, Y.; Lichtenberger, A. W.; Moore, J.E.; Muller, D. A.; Schlom, D. G.; Hopkins, P. E.; Majumdar, A.; Ramesh, R.; Zurbuchen, M. A. *Nat. Mater.***2014**, 13, 168–172.

(152) Schlom, D. G.; Chen, L. Q.; Eom, C. B.; Rabe, K. M.; Streiffer, S. K.; Triscone, J. M. *Annu. Rev. Mater. Sci.* **2007**, 37,589–626.

(153) Tenne, D. A.; Bruchhausen, A.; Lanzillotti–Kimura, N. D.; Fainstein, A.; Katiyar, R. S.; Cantarero, A.; Soukiassian, A.; Vaithyanathan, V.; Haeni, J. H.; Tian, W.; Schlom, D. G.; Choi, K. J.; Kim, D. M.; Eom, C. B.; Sun, H. P.; Pan, X. Q.; Li, Y. L.; Chen, L. Q.; Jia, Q. X.; Nakhmanson, S. M.; Rabe, K. M.; Xi, X. X. *Science* **2006**, 313, 1614–1616.

(154) Dawber, M.; Stucki, N.; Lichtensteiger, C.; Gariglio, S.; Ghosez, P.; Triscone, J. M. *Adv. Mater.* **2007**, 19, 4153–4159.

(155) Bousquet, E.; Dawber, M.; Stucki, N.; Lichtensteiger, C.; Hermet, P.; Gariglio, S.; Triscone, J. M.; Ghosez, P. *Nature (London)* **2008**, 452, 732–736.

Chapter II

Topotactic Transformation Reaction from Layered Titanate to Platelike [100]-oriented $Bi_{0.5}Na_{0.5}TiO_3$ Mesocrystals[†]

2.1 Introduction

Perovskite oxide piezoelectric materials due to their unique ability to couple electrical energy and mechanical energy transformations can be applied to several electronic devices such as sensor, actuator and transducer technologies, and so on.[1] Pb-free piezoelectric materials have attracted considerable attention due to the consideration of environmental protection in recent years.[2—4] Bismuth sodium titanate ($Bi_{0.5}Na_{0.5}TiO_3$, BNT) is one of well-known basis ferroelectric materials.[5,6] It has a perovskite structure with rhombohedral *R3c* space system (a = 38.91 nm, α=89.6 °)[7] at room temperature. In the perovskite structure with ABO_3 formula, where the half of A-site is filled with Bi(III), and the other half with Na(I), and the B-site is filled by Ti(IV).[8,9] The BNT has been considered to be one of the most promising candidate materials for the development of Pb-free piezoelectric materials due to its relatively large remnant polarization (P_r = 38 μC/cm^2) and high Curie temperature (T_c =320 ^{o}C).[10,11] The highest temperature phase is a paraelectric cubic phase, and it transforms to the tetragonal phase around 520 ^{o}C and to rhombohedral phase around 260 ^{o}C.[12—15] Similar to the most of other Pb-free piezoelectric materials, the piezoelectricity of BNT is lower than lead-based piezoelectric materials.[16-18] So that many attempts to improve the physical properties of BNT have been carried out by various methods.

There are two kinds of effective techniques to enhance the piezoelectricity. One is domain engineering for the control of the domain size, and another is texture engineering for the control of orientation direction of the piezoelectric materials.

Enhancement of piezoelectricity and reduction of piezoelectric hysteresis for piezoelectric materials can be realized well by decreasing the domain size,[19,20] and the domain size can be decreased by reducing the grain size of the material.[21] Since ferroelectric materials show crystal-axis anisotropic, their piezoelectricity and permittivity are tensor quantities and relate to both the direction of the applied stress and electric field.[22] Therefore, the high piezoelectricity can be achieved by using the crystal-axis-oriented materials as well.[23] It has been reported that the [110]-oriented $BaTiO_3$ ceramic material shows a piezoelectric constant d_{33} value of 788 pC/N,[24] which is much larger than that of the 190 pC/N for the normal $BaTiO_3$ ceramic materials.[25] Consequently, the small grain size and high-degree of orientation ceramics with high density are expected for high performance piezoelectric materials.

Templated grain growth (TGG) method and reaction-templated grain growth (RTGG) method have been developed for the fabrication of the oriented ceramic materials.[26,27] In these methods, the template particles with platelike or fiber-like morphology are necessary, because they can be oriented easily via mechanical methods. The [100]-oriented,[28,29] [001]-oriented,[30,31] [110]-oriented,[23,24] and [111]-oriented[32,33] perovskite ferroelectric ceramic materials, such as $Na_{0.5}Bi_{0.5}TiO_3$ (BNT), $BaTiO_3$, $Bi_{0.5}Na_{0.5}TiO_3$-$BaTiO_3$, $Ba_{0.6}Sr_{0.4}TiO_3$, $Ba_{1-x}Ca_xTiO_3$, have been developed by using the TGG or RTGG methods. Two kinds of platelike particles, $Bi_4Ti_3O_{12}$[27,34] and $Na_{0.5}Bi_{4.5}Ti_4O_{15}$ [12] have been reported to be used as template for the fabrication of oriented BNT ceramic materials by the TGG or RTGG method.[27,34,35] These platelike particles were prepared using the solid state reaction or melt salt methods, which gives large size particles.[36-38] The oriented ceramic materials with small grain size and high density are difficult to be achieved by using these large platelike particles as the templates.[27,34,35]

Up to now, BNT particles have been synthesized using molten salt method,[12,38–41] solid state method,[42] hydrothermal method,[15,43–46] sol–gel method,[47,48] vibro-milling method,[13] and slurry synthesis method.[49] However the obtained BNT particles show a cubic or spherical isotropic morphology except when an anisotropic morphology

precursor is used. BNT platelike particles have been prepared by using molten salt method with $Bi_4Ti_3O_{12}$,[38] $Na_{0.5}Bi_{4.5}Ti_4O_{15}$,[12,40] and $Bi_2Ti_4O_{11}$[41] platelike particles as the precursors. The obtained BNT platelike particles have been used as the template to fabricate oriented BNT ceramic materials by TGG method. [12] However, the high degree of orientation, high density, and small grain size ceramic materials have not been achieved due to the large size and low aspect ratio of BNT platelike template.

A layered titanate $H_{1.07}Ti_{1.73}O_4 \cdot nH_2O$ (HTO) with a lepidocrocite-like structure and small platelike particle size of 200 nm in thickness and 3 μm in width can be synthesized by hydrothermal reaction.[50−52] The HTO platelike particles have been used as the precursors for the syntheses of the perovskites $BaTiO_3$, $Ba_{1-x}Ca_xTiO_3$, and $Ba_{1-x}(Bi_{0.5}K_{0.5})_xTiO_3$ platelike particles by solvothermal reactions.[23,51−53] The platelike particles of the perovskite titanates prepared by this method are constructed from the spherical nanoparticles, and all the spherical nanoparticles of the perovskite titanates in the platelike particles align and show the same [110]-direction orientation, forming the [110]-oriented platelike particles.[23,51,53] The formation mechanisms of the oriented platelike particles are the *in situ* topotactic transformation reaction, where the metal ions are intercalated into the HTO crystal bulk through the interlayer pathway by an exchange reaction, and then react with the layered titanate.

These oriented platelike perovskite polycrystals are a new class of mesocrystal. The mesocrystal is defined as an orientational superstructure with nanometers to micrometers size, which is made from well-aligned oriented crystalline nanoparticles.[54,55] The concept of mesocrystal has just recently been brought forward and developed in 2003,[55] in order to explain that the crystal growth may be a crystalline aggregation-base process via a mesoscale transformation. The mesocrystals, which are assemblies of crystallographically oriented nanocrystals, have potential applications to catalysis, sensing, and energy storage and conversion.[54,56,57] The platelike perovskite mesocrystals are a promising material to fabricate the high degree of orientation, high density, and small grain size ceramic materials for the high performance piezoelectric materials. To the best of our knowledge, the studies on the

syntheses of BNT mesocrystal and other perovskite titanate mesocrystals by heat treatment method using HTO as a precursor have not been reported, and also on fabrication of oriented ceramic materials using HTO template.

In this Chapter, a new challenge on the synthesis of the platelike BNT ferroelectric mesocrystals from the platelike HTO particle precursor by using the heat treatment method, the studies on the formation reaction mechanism and nanostructure, and application of the heat treatment process to the fabrication of the crystal-axis-oriented BNT ceramic materials are described. The platelike BNT particle prepared via this method is constructed from the aligned nanoparticles, and each nanoparticle shows the same [100]-orientation, namely [100]-oriented BNT mesocrystal.

2.2 Experimental section

2.2.1 Preparation of layered titanate $H_{1.07}Ti_{1.73}O_4 \cdot nH_2O$ (HTO) precursor

$H_{1.07}Ti_{1.73}O_4 \cdot nH_2O$ (HTO) powder sample was prepared by acid-treatment of $K_{0.8}Ti_{1.73}Li_{0.27}O_4$ (KTLO) that was synthesized by hydrothermal method reported in literature.[117] 6.9 g of anatase TiO_2 nanoparticles, 5.1 g of KOH, 0.6 g of $LiOH \cdot H_2O$, and 25 mL of distilled water were sealed into a Hastelloy-C-lined vessel with internal volume of 45 mL, and then heated at 250 ^oC for 24 h under stirring conditions. After the hydrothermal treatment, the obtained sample was washed with distilled water and dried at room temperature to obtain $K_{0.80}Ti_{1.73}Li_{0.27}O_4$ (KTLO) crystals. The KTLO crystals (4.0 g) was treated with a 0.2 mol $\cdot L^{-1}$ HNO_3 solution (200 mL) for 24 h under stirring conditions to exchange K^+ and Li^+ in the layered structure with H^+, and then the sample was washed with distilled water. After the acid treatments were done twice, the layered protonated titanate $H_{1.07}Ti_{1.73}O_4 \cdot H_2O$ single crystals were obtained. The as-obtained crystals were collected and washed with distilled water and alcohol, before air-drying at 60 ^oC for 12 h, and then the HTO (3.2 g) single crystals were obtained.

2.2.2 Synthesis of BNT powder samples

Three kinds of Ti-sources, namely platelike HTO particles, anatase TiO_2 nanoparticles, and HTO-TiO_2 mixture, were used in the solid state reaction for synthesis of $Bi_{0.5}Na_{0.5}TiO_3$ (BNT) particles. In the synthesis of the BNT powder from HTO Ti-source, HTO (0.005 mol Ti) and stoichiometric ratio of Bi_2O_3 and Na_2CO_3 (Bi/Na/Ti mole ratio = 0.5:0.5:1) in the solvent of ethanol were mixed by ball milling with 5 mm diameter zirconia balls for 24 h at a rotational speed of 60 r/min. The mixture was dried at 60 ^oC for 6 h, and then heated at a desired temperature for 3 h in air with a heating rate of 10 ^oC/min. Similarly, BNT powder samples were prepared using anatase TiO_2 nanoparticles or mixture of HTO and anatase TiO_2 nanoparticles as the Ti-source instead of the HTO Ti-source. The mole ratio of Ti in the HTO-TiO_2 mixture was 4:6.

2.2.3 Physical Characterization

The structures of powder and ceramic samples were investigated using a powder X-ray diffractometer (Shimadzu, XRD-6100) with Cu Kα (λ = 0.15418 nm) radiation. The size and morphology of the samples were observed using scanning electron microscopy (SEM) (JEOL, JSM-5500S) or field emission scanning electron microscopy (FE-SEM) (Hitachi, S-900). Transmission electron microscopy (TEM) observation and selected-area electron diffraction (SAED) were performed on a JEOL Model JEM-3010 system at 300 kV, and the powder sample was supported on a microgrid. Energy dispersive spectroscopy (EDS) (JEOL, JED-2300T) was measured on the TEM system.

2.3 Results and discussion

2.3.1 Formation of BNT mesocrystal in HTO-Bi_2O_3-Na_2CO_3 reaction system

Figure 2.1 shows the XRD patterns of the powder samples obtained by the heat treatment of HTO-Bi_2O_3-Na_2CO_3 mixture with the stoichiometric ratio of $Bi_{0.5}Na_{0.5}TiO_3$ (BNT). The diffraction peaks of HTO, Na_2CO_3, and Bi_2O_3 phases were

observed before the heat treatment (Figure 2.1a). After heat treatment at 500 ^{o}C, in addition to the small amounts of the unreacted HTO, Na_2CO_3, and Bi_2O_3 phases, new phases of $Bi_{12}TiO_{20}$ (JCPDS File No.34-0097) and BNT (JCPDS File No. 89-3109) were formed (Figure 2.1b), suggesting the partial reaction of the HTO-Bi_2O_3-Na_2CO_3 mixture. The basal spacing of HTO decreased from 0.870 nm to 0.732 nm, due to the dehydration of its interlayer water. At 600 ^{o}C, all the starting HTO, Bi_2O_3, Na_2CO_3 phases were reacted, and the product containing BNT main phase and a very small amount of $Bi_{12}TiO_{20}$ phase was formed. Although the crystal structure of BNT is rhombohedral, the diffraction lines are indexed based on the pseudocubic unit cell because of small rhombohedral distortion, and can be identified by JCPDS powder file card No. 89-3109 (cubic symmetry).[3,12,27,38,58,59] Only BNT phase was obtained above 700 ^{o}C. The formation of the TiO_2 phase was not observed in all the reaction temperature ranges studied here, suggesting the HTO phase was transformed directly into the $Bi_{12}TiO_{20}$ or BNT phases in the reaction system. The formation of BNT phase occurred at much lower temperature in the HTO-Bi_2O_3-Na_2CO_3 reaction system than that in the normal TiO_2-Bi_2O_3-Na_2CO_3 reaction system (see next section) due to the high reactivity of HTO.

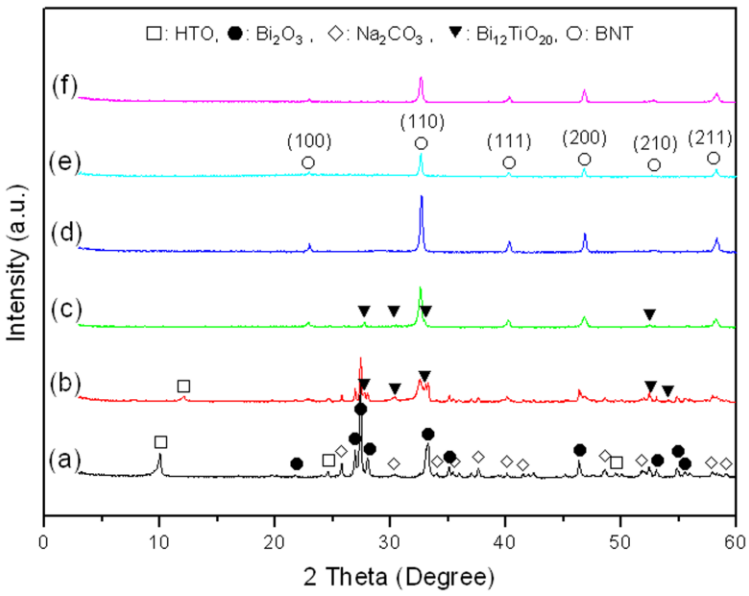

Figure 2.1 XRD patterns of the HTO-Na_2CO_3-Bi_2O_3 mixture (a) before and after heat treatment at (b) 500, (c) 600, (d) 700, (e) 800, and (f) 900 ^{o}C for 3 h, respectively.

The above results indicate that in the HTO-Bi_2O_3-Na_2CO_3 reaction system, firstly the intermediate $Bi_{12}TiO_{20}$ phase is formed by reacting HTO with Bi_2O_3 (reaction (1)), and then the intermediate product reacts with Na_2CO_3 and HTO (reaction (2)), resulting in the formation of BNT phase.

$$6Bi_2O_3 + (1/1.73)\ H_{1.07}T_{1.73}O_4 \cdot nH_2O \rightarrow Bi_{12}TiO_{20} + xH_2O \quad (1)$$

$$Bi_{12}TiO_{20} + 6Na_2CO_3 + (23/1.73)\ H_{1.07}T_{1.73}O_4 \cdot nH_2O \rightarrow$$

$$24Na_{0.5}Bi_{0.5}TiO_3\ (BNT) + 6CO_2 + yH_2O \quad (2)$$

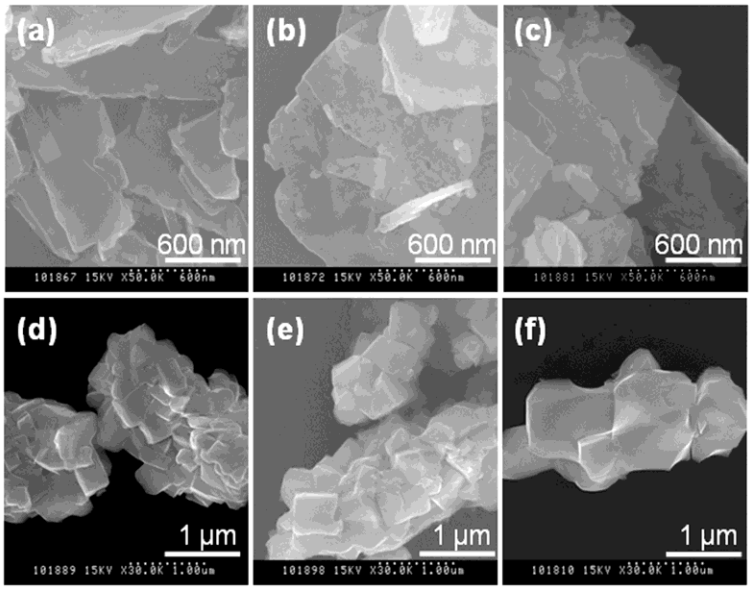

Figure 2.2 FE-SEM images of the HTO-Na_2CO_3-Bi_2O_3 mixture before (a) and after heat treatment at (b) 500, (c) 600, (d) 700, (e) 800, and (f) 900 ^oC for 3 h, respectively.

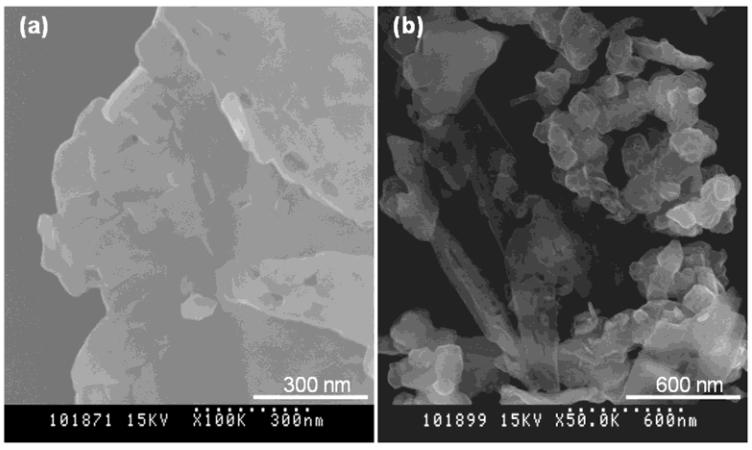

Figure 2.3 FE-SEM images of the (a) HTO-Na_2CO_3-Bi_2O_3 and (b) HTO-TiO_2-Na_2CO_3-Bi_2O_3 mixture after heat treatments at 500 ^oC for 3 h.

Figure 2.2 presents FE-SEM images of the HTO-Bi_2O_3-Na_2CO_3 mixtures before and after the heat treatment. The platelike particle morphology of HTO with about 200 nm in thickness and about 2 µm in width can be observed in the HTO-Bi_2O_3-Na_2CO_3 mixture before the heat treatment. This result indicates that HTO particle morphology has not been damaged during the ball milling treatment. The platelike particles remained its morphology after the heat treatment at 500 ^oC (Figure 2.2b). It is interested to observe some smaller holes with the diameter of about 60 nm and cracks in plate (Figure 2.3).

After the heat treatment at 600 ^oC, the platelike particle morphology was also remained, but the holes and cracks disappeared in platelike particles (Figure 2.2c). The platelike particle is constructed from nanoparticles with a size of about 100 nm. This result suggests that the polycrystalline platelike BNT particles are formed by an *in situ* topotactic reaction mechanism. The platelike particles collapsed, and block-like particles with a size of about 200 nm were formed at 700 ^oC (Figure 2.2d). With increasing the heat treatment temperature to 800 ^oC and 900 ^oC, the sizes of the block-like particles grow up to about 400 nm and 800 nm, respectively (Figure 2.2 e and f).

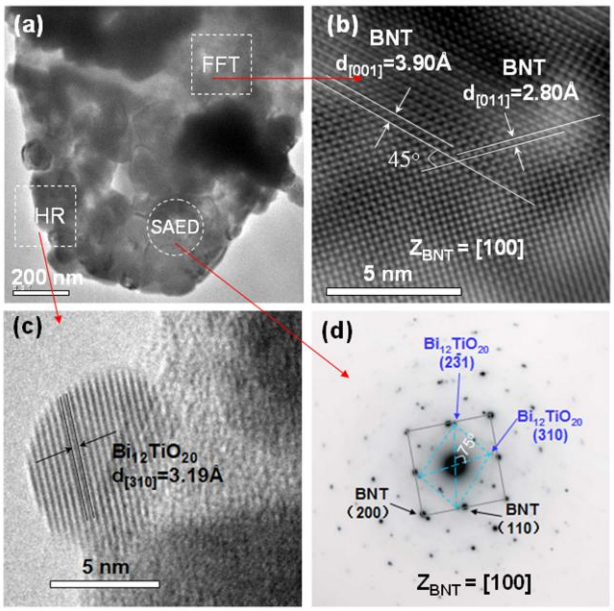

Figure 2.4 (a) TEM image, (b) Fast-Fourier-transform-filtered TEM image, (c) HRTEM image, and (d) SAED patter of the sample obtained after heat treatment of HTO-Na_2CO_3-Bi_2O_3 mixture at

600 ^{o}C for 3 h.

The formation reaction of BNT in the HTO-Bi_2O_3-Na_2CO_3 system was also investigated using TEM, HRTEM and SAED, and the results for the sample obtained at 600 ^{o}C are shown in Figure 2.4. The platelike particle is constructed from nanoparticles with a size of about 100 nm (Figure 2.4a), which is consistent with the FE-SEM result (Figure 2.2c). The Fast-Fourier-transform (FFT) filtered TEM image indicates that the nanoparticles with a size of about 100 nm correspond to the BNT cubic phase, where the fringe spacings of 3.90 Å and 2.80 Å correspond to (001) and (011) facets, respectively, and the angle between the (001) and (011) facets is 45^{o}. Except the BNT nanoparticles of 100 nm, some small spherical nanoparticles with a size of about 5 nm were also observed on the surface of the platelike particle (Figure 2.4c). These small nanoparticles correspond to $Bi_{12}TiO_{20}$ phase which shows a fringe spacing of 3.19 Å matching with the (310) facet.

It is notable that two sets of SAED spots corresponding to the BNT perovskite phase and the $Bi_{12}TiO_{20}$ phase respectively are observed simultaneously in one platelike particle (Figure 2.4d), suggesting that BNT and $Bi_{12}TiO_{20}$ phases coexist in one platelike particle. This result is consistent with the XRD result in Figure 2.2c. The SAED result reveals that all the BNT nanoparticles and all the $Bi_{12}TiO_{20}$ nanoparticles in one platelike particle show the same crystal-axis orientation directions, respectively, because they show the diffraction spot patterns similar to their single crystal diffraction spot patterns, respectively. Furthermore, the polycrystalline platelike BNT particle shows a [100]-axis orientation, and the basal plane of platelike particle corresponds to the (100) facet that is vertical to the [100] orientation. These results reveal that the Reactions (1) and (2) in the formation process of BNT from HTO are the *in situ* topotactic reactions, which result in the formation of the [100]-oriented platelike BNT mesocrystals. The [100]-direction orientation of the BNT platelike mesocrystal is different from the [110]-direction orientation of the platelike $BaTiO_3$[52], $Ba_{0.9}Ca_{0.1}TiO_3$[23], and $Ba_{0.5}Bi_{0.5}K_{0.5}TiO_3$[53] mesocrystals prepared from the HTO precursor by solvothermal reactions.

It has been reported that platelike BNT single crystals with [100]-direction orientation can be prepared by molten-salt reactions using $Bi_4Ti_3O_{12}$[38,40] and $Na_{0.5}Bi_{4.5}Ti_4O_{15}$[3,12] layered compounds as the precursor over 900 °C. The reaction temperature is higher than that formation of the platelike BNT mesocrystals using HTO precursor due to the lower reactivities of $Bi_4Ti_3O_{12}$ and $Na_{0.5}Bi_{4.5}Ti_4O_{15}$ precursors. In the molten-salt processes, first the Bi_2O_2(Ⅱ) layer-structured $Bi_4Ti_3O_{12}$ and $Na_{0.5}Bi_{4.5}Ti_4O_{15}$ platelike particles were synthesized as the precursor by molten salt reactions, and then the platelike particles were reacted with Na_2CO_3 and TiO_2 to transform to the perovskite structure through topochemical conversion.[38,40] Although the possible transformation mechanism from the layered structure to the perovskite structure has been proposed, it is not very clear yet.[12,38]

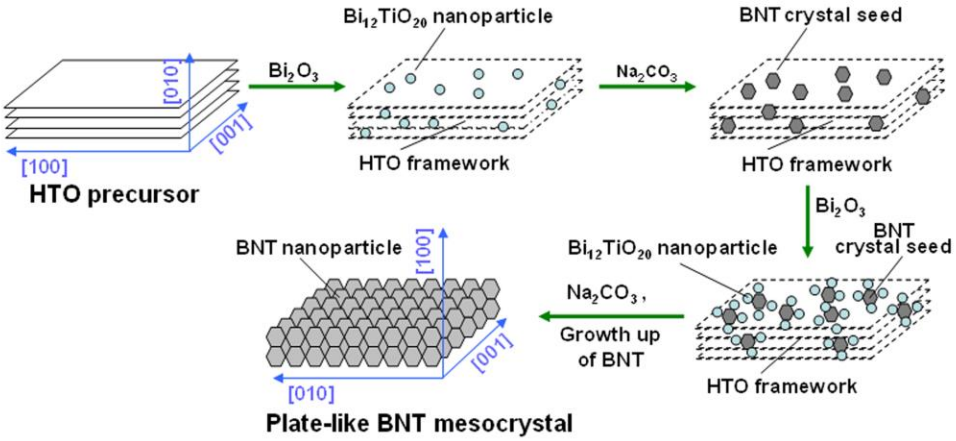

Figure 2.5 Reaction mechanism of the formation of platelike BNT mesocrystal in HTO-Bi_2O_3-Na_2CO_3 solid-state reaction system.

On the base of results described above, we can give a schematic representation for the formation reaction mechanism of the [100]-oriented platelike BNT mesocrystal in the HTO-Bi_2O_3-Na_2CO_3 solid state reaction system as shown in Figure 2.5. In this reaction process, Bi(III) species immigrate into the HTO bulk crystal through its interlayer pathway firstly, and partially react with the TiO_6 octahedral layers of HTO framework to form $Bi_{12}TiO_{20}$ nanoparticles in the HTO bulk crystal by the *in situ* structural transformation reaction. And then $Bi_{12}TiO_{20}$ nanoparticles react with the

TiO_6 octahedral layers and Na(I) species in the bulk crystal to form BNT crystal seeds (nanoparticles). This reaction is also the *in situ* topotactic structural transformation reaction, and formed BNT crystal seeds show [100]-orientation. At the next step, Bi(III) species sequentially reacts with the TiO_6 octahedral layers, which causes the formation of $Bi_{12}TiO_{20}$ nanoparticles on BNT nanoparticles surface by a heteroepitaxial growth mechanism. And then $Bi_{12}TiO_{20}$ nanoparticles on BNT nanoparticles surface react with the TiO_6 octahedral layers and Na(I) species to grow up BNT nanoparticles by an epitaxial growth mechanism.[60] Finally [100]-oriented platelike BNT mesocrystal is obtained by consuming HTO framework completely.

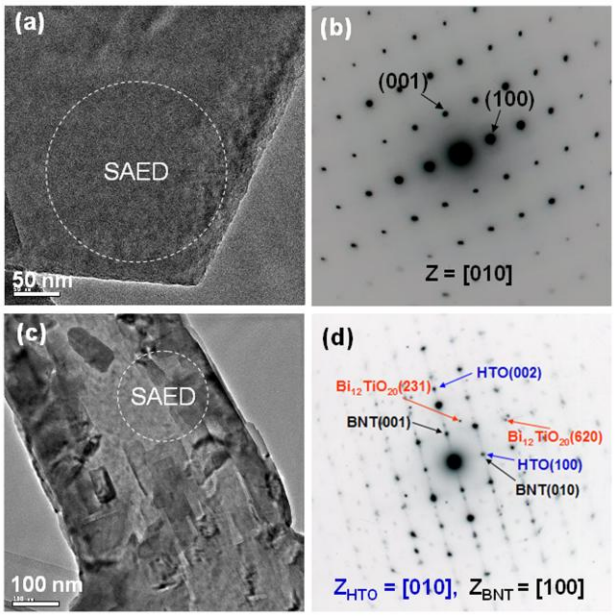

Figure 2.6 (a, c) TEM images and (b, d) SAED patterns of (a, b) HTO and (c, d) platelike particle obtained by heat treatment of HTO-Na_2CO_3-Bi_2O_3 mixture at 500 ^oC for 3h.

To give an exact relationship between the structures of the HTO precursor and the BNT product, TEM and SAED studies were carried out on the HTO and partially reacted sample obtained at 500 ^oC (Figure 2.6). The platelike HTO particle is a single crystal with a smooth particle surface, and the basal plane of the platelike particle corresponds to the (010) facet. After the heat treatment at 500 ^oC, the smooth particle surface changed to rough surface. Three sets of SAED spots for the HTO layered phase, the perovskite BNT phase, and the $Bi_{12}TiO_{20}$ intermediate phase are observed

simultaneously in one platelike particle, indicating that HTO, BNT, and $Bi_{12}TiO_{20}$ phases coexist in one platelike particle. In one platelike particle, the HTO axis-directions of [010], [002], and [100] correspond to the BNT axis-directions of [100], [001], and [010], respectively, suggesting that a three-dimensional topotactic reaction occurs in structural transformation process. That is, there is a specific relationship between the structures of the HTO precursor and the BNT product in the *in situ* topotactic structure transformation process, where (010), (001), and (100) facets of the layered HTO structure are converted to (100), (001), (010) facets of the BNT perovskite structure, respectively (Figure 2.7).

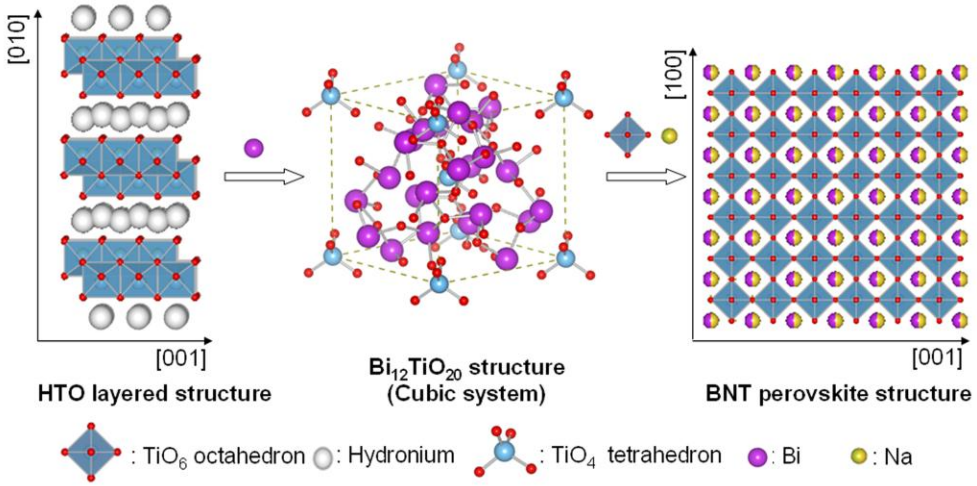

Figure 2.7 Schematic illustration of crystal structural evolution from HTO to BNT in an *in situ* topotactic transformation for HTO-Na_2CO_3-Bi_2O_3 reaction system.

2.3.2 Formation of BNT in TiO_2-Bi_2O_3-Na_2CO_3 reaction system

Normal TiO_2-Bi_2O_3-Na_2CO_3 solid state reaction system was also investigated in order to compare with the HTO-Bi_2O_3-Na_2CO_3 reaction system. Figure 2.8 shows the XRD patterns of the samples obtained by the heat treatment of the TiO_2-Bi_2O_3-Na_2CO_3 mixture with the stoichiometric ratio of BNT. The diffraction peaks of the TiO_2, Na_2CO_3, and Bi_2O_3 phases were observed before the heat treatment (Figure 2.8a). At 700 ^oC, all the starting TiO_2, Bi_2O_3, Na_2CO_3 phases were transformed into the intermediates of tetragonal $Bi_4Ti_3O_{12}$ (JCPDS File No. 47-0398) and cubic

$Bi_{12}TiO_{20}$ (JCPDS File No. 34-0097).[61] Most of the intermediates $Bi_4Ti_3O_{12}$ and $Bi_{12}TiO_{20}$ were transformed to the BNT phase at 800 °C, and only BNT phase was obtained above 900 °C. These results indicate that a higher heat treatment temperature is necessary for the formation of BNT in the normal TiO_2-Bi_2O_3-Na_2CO_3 reaction system than that in the HTO-Bi_2O_3-Na_2CO_3 topotactic reaction system (Figure 2.1). Although HTO has a much larger particles size, it shows a higher reactivity in the BNT formation reaction than anatase TiO_2 nanoparticles.

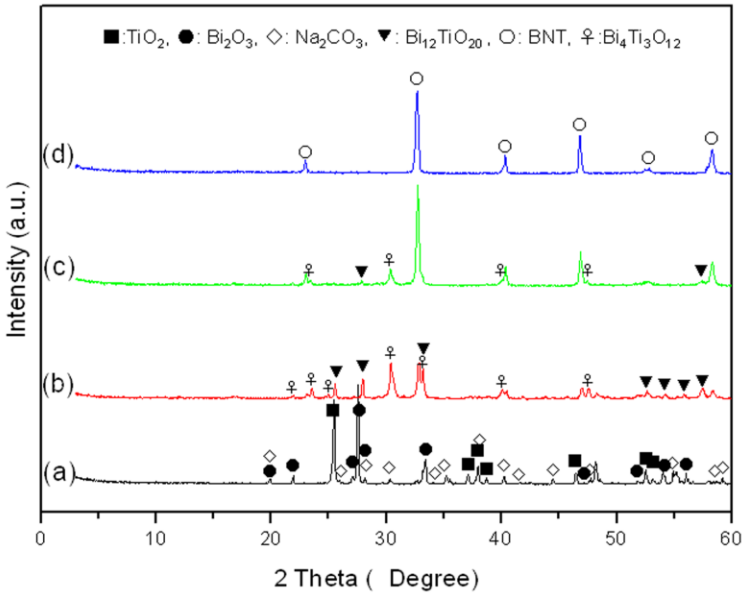

Figure 2.8 XRD patterns of the TiO_2-Na_2CO_3-Bi_2O_3 mixture (a) before and after heat treatment at (b) 700, (c) 800, and (d) 900 °C for 3 h, respectively.

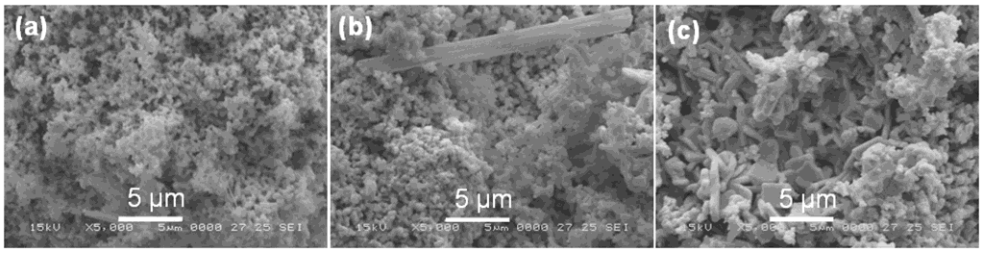

Figure 2.9 SEM images of the samples obtained by heat treatments of TiO_2-Na_2CO_3-Bi_2O_3 mixture at (a) 700, (b) 800, and (c) 900 °C for 3 h, respectively.

The SEM study indicates that the products obtained at 700 °C and 800 °C show

mainly spherical particle morphologies with the small amount of rod-like particles (see Figure 2.9). The rod-like particles maybe correspond to $Bi_4Ti_3O_{12}$ phase.[62,63] The BNT product obtained at 900 ^oC shows a square block morphology with a size of about 5 μm. The particle size of the product increases with increasing the heat treatment temperature.

The formation of the intermediates $Bi_4Ti_3O_{12}$ and $Bi_{12}TiO_{20}$ in the normal TiO_2-Bi_2O_3-Na_2CO_3 solid state reaction system for the synthesis of the BNT phase has been also reported.[64,65] In this reaction system, firstly $Bi_{12}TiO_{20}$ is formed by reaction (3), then $Bi_{12}TiO_{20}$ is transformed to $Bi_4Ti_3O_{12}$ by reaction (4),[65] and finally $Bi_4Ti_3O_{12}$ is transformed to BNT by reaction (5),[27,34] as follows:

$$6Bi_2O_3 + TiO_2 \rightarrow Bi_{12}TiO_{20} \quad (3)$$

$$Bi_{12}TiO_{20} + 8TiO_2 \rightarrow 3Bi_4Ti_3O_{12} \quad (4)$$

$$Bi_4Ti_3O_{12} + 2Na_2CO_3 + 5TiO_2 \rightarrow 8Na_{0.5}Bi_{0.5}TiO_3\ (BNT) + 2CO_2 \quad (5)$$

This is different to the reactions (1) and (2) where without formation of the intermediate $Bi_4Ti_3O_{12}$ in the HTO-Bi_2O_3-Na_2CO_3 topotactic reaction system. This fact can be explained by differences in the intermediate $Bi_{12}TiO_{20}$ formation mechanism in these two reaction system. In the HTO-Bi_2O_3-Na_2CO_3 reaction system, the formation of the intermediate $Bi_{12}TiO_{20}$ nanoparticles occurs on the BNT crystal seeds surface in the HTO crystal bulk where has enough Ti(IV)-source for the formation of BNT. Therefore, the $Bi_{12}TiO_{20}$ nanoparticles show a high reactivity and can be transformed directly to the BNT by the epitaxial growth mechanism as shown in Figure 2.5. On the other hand, in the TiO_2-Bi_2O_3-Na_2CO_3 solid state reaction system, the formation of the intermediate $Bi_{12}TiO_{20}$ occurs on the interface between TiO_2 and Bi_2O_3 particles surface. The intermediate $Bi_{12}TiO_{20}$ cannot be transformed directly to BNT, due to where has not enough Ti(IV)-source. Two-steps reaction is necessary to provide the enough Ti(IV)-source. Firstly the intermediate $Bi_{12}TiO_{20}$ reacts with TiO_2 to form another intermediate $Bi_4Ti_3O_{12}$ by the reaction (4), and then the intermediate $Bi_4Ti_3O_{12}$ reacts with TiO_2 and Na_2CO_3 to form the final product

BNT.

2.3.3 Formation of BNT mesocrystal in HTO-TiO_2-Bi_2O_3-Na_2CO_3 reaction system.

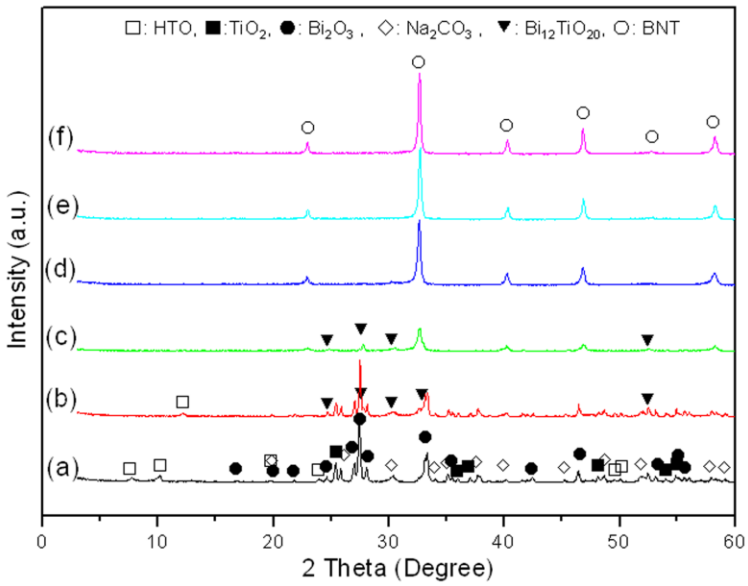

Figure 2.10 XRD patterns of the HTO-TiO_2-Bi_2O_3-Na_2CO_3 mixture (a) before and after heat treatment at (b) 500, (c) 600, (d) 700, (e) 800, and (f) 900 ^oC, respectively. The Ti mole ratio of HTO/TiO_2 = 4:6.

We also studied the formation of BNT in HTO-TiO_2-Bi_2O_3-Na_2CO_3 reaction system where both of HTO and TiO_2 nanoparticle were used as Ti-sources, because high oriented and high density BNT ceramic materials can be prepared using this reaction system (see the next section). We chose the mole ratio of HTO/TiO_2 = 4:6 in HTO-TiO_2-Bi_2O_3-Na_2CO_3 reaction system because such condition is suitable for the fabrication of high oriented ceramic materials.[27,34] Before the heat treatment, the diffraction peaks of HTO, TiO_2, Na_2CO_3, and Bi_2O_3 phases were observed (Figure 2.10 a). After the heat treatment at 500 ^oC, in addition to the dehydrated HTO, TiO_2, Na_2CO_3, and Bi_2O_3 phases, the intermediate $Bi_{12}TiO_{20}$ and BNT phases were also observed (Figure 2.10b), suggesting the partial reaction of the HTO-TiO_2-Bi_2O_3-Na_2CO_3 mixture. Since the peak intensity of TiO_2 did not change, it can be concluded

that the TiO_2 did not take part in the reaction at this reaction temperature. The basal spacing of HTO also decreased from 0.870 nm to 0.732 nm, due to the dehydration of the interlayer water.

At 600 ^{o}C, all starting Bi_2O_3, Na_2CO_3, HTO, TiO_2 phases were reacted, and the product containing BNT main phase and a small amount of $Bi_{12}TiO_{20}$ phase was formed (Figure 2.10c). Only BNT phase was obtained above 700 ^{o}C (Figures 2.10d to f). These results are similar to the HTO-Bi_2O_3-Na_2CO_3 reaction system (Figure 2.1), which is different to TiO_2-Bi_2O_3-Na_2CO_3 system (Figure 2.8). The BNT phase can be formed at low temperature (700 ^{o}C) without forming the intermediate $Bi_4Ti_3O_{12}$ in the HTO-TiO_2-Bi_2O_3-Na_2CO_3 reaction system. The full width at half of maximum (FWHM) of the BNT phase obtained from the HTO-TiO_2-Bi_2O_3-Na_2CO_3 reaction system (0.448 ^{o}) was larger than that from the HTO-Bi_2O_3-Na_2CO_3 reaction system (0.292 ^{o}) at 600 ^{o}C. This result reveals that the HTO-Bi_2O_3-Na_2CO_3 reaction system has higher reactivity and gives a higher crystallinity of the BNT phase than the HTO-TiO_2-Bi_2O_3-Na_2CO_3 reaction system.

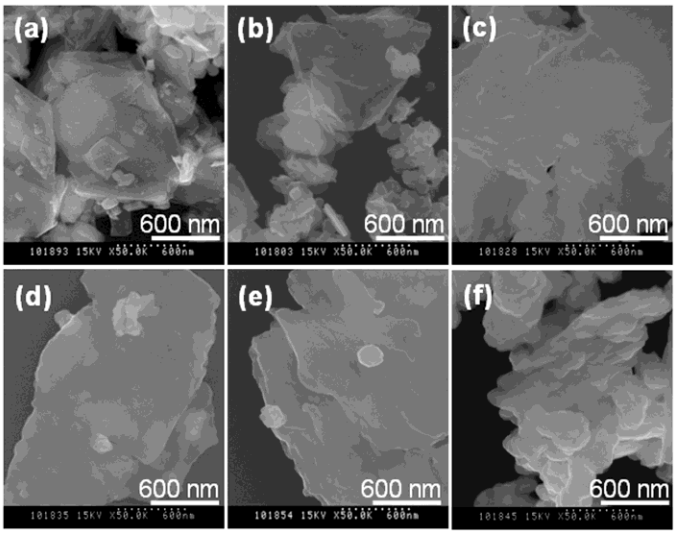

Figure 2.11 FE-SEM images of the HTO-TiO_2-Bi_2O_3-Na_2CO_3 mixture (a) before and after heat treatment at (b) 500, (c) 600, (d) 700, (e) 800, and (f) 900 ^{o}C, respectively. The Ti mole ratio of HTO/TiO_2 = 4:6.

The FE-SEM results reveal that HTO shows platelike morphology before the heat

treatment in the HTO-TiO_2-Bi_2O_3-Na_2CO_3 mixture (Figure 2.11). The platelike particles and small nanoparticles were observed in sample after the heat treatment at 500 ^oC, and some fissures were formed on the platelike particles (Figure 2.3b). The nanoparticles correspond to the unreacted TiO_2, Bi_2O_3, and Na_2CO_3. After the heat treatment in a temperature range of 600 to 800 ^oC, the unreacted TiO_2, Bi_2O_3, and Na_2CO_3 nanoparticles disappeared and were fused into the platelike particles, while the platelike particles grow up to the larger platelike particles. The larger platelike particle is constructed from nanoparticles with a size of about 150 nm that is larger than the nanoparticles (100 nm) in the platelike BNT particle prepared in the HTO-Bi_2O_3-Na_2CO_3 reaction system. This result suggests that a mass-transport process from the TiO_2 nanoparticles to the platelike particles occurs, resulting in the crystal growth on the platelike BNT particle in this temperature range. When the heat treatment temperature was reached to 900 ^oC, the platelike particle collapsed into small particles with a size of 300 nm, which is similar to the HTO-Bi_2O_3-Na_2CO_3 reaction system.

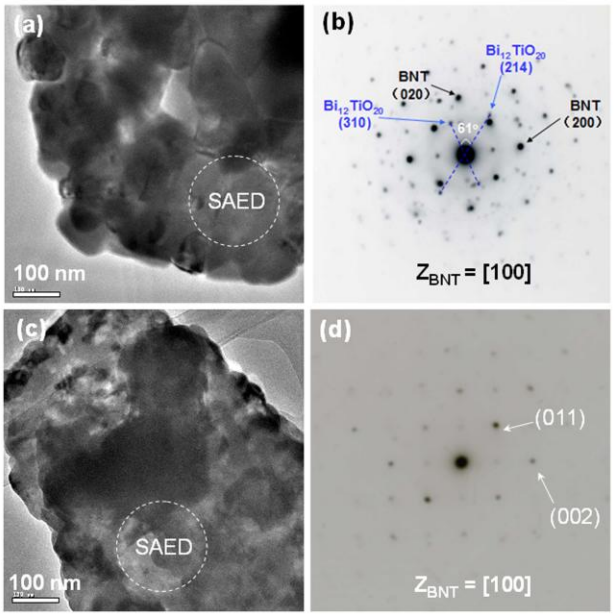

Figure 2.12 (a, c) TEM images and (b, d) SAED patters of the samples obtained by heat treatment of HTO-TiO_2-Na_2CO_3-Bi_2O_3 mixture at (a, b) 600 ^oC and (c, d) 700 ^oC for 3 h, respectively.

In order to understand the formation reaction of the BNT phase in the HTO-TiO_2-

Bi_2O_3-Na_2CO_3 reaction system, the obtained samples were also investigated using TEM and SAED (Figure 2.12). The platelike particle prepared at 600 ^oC shows two-sects of diffraction spot patterns which are similar to the single crystals. One corresponds to the BNT phase and another corresponds to $Bi_{12}TiO_{20}$ phase. The BNT nanoparticles in a platelike particle show the same orientation to the [100]-direction, due to formation of the [100]-oriented BNT mesocrystal. This result is also similar to the HTO-Bi_2O_3-Na_2CO_3 reaction system at 600 ^oC (Figure 2.4d). The TEM image of the sample prepared at 700 ^oC also presents a platelike morphology, but it is thicker than the platelike BNT mesocrystal prepared in the HTO-Bi_2O_3-Na_2CO_3 reaction system, where the nanoparticles constructing the platelike mesocrystal are not observed clearly (Figure 2.12c). This is because the platelike mesocrystal is too thick to be transmitted by the electron beam of the TEM system. The platelike BNT mesocrystal retained the [100]-orientation and shows the single crystal SAED pattern after the heat treatment at 700 ^oC, although it grow up. An EDS analysis on the platelike BNT mesocrystal indicated that the platelike mesocrystal shows a homogeneous chemical composite distribution with an average mole ratio of Bi/Na/Ti=0.48:0.48:1.0 (see Figure 2.13), which is in good accordance with designed composition of BNT. This result reveals that the crystal growth of the [100]-oriented platelike BNT mesocrystal via a mass-transport process occurs by the epitaxial growth mechanism.

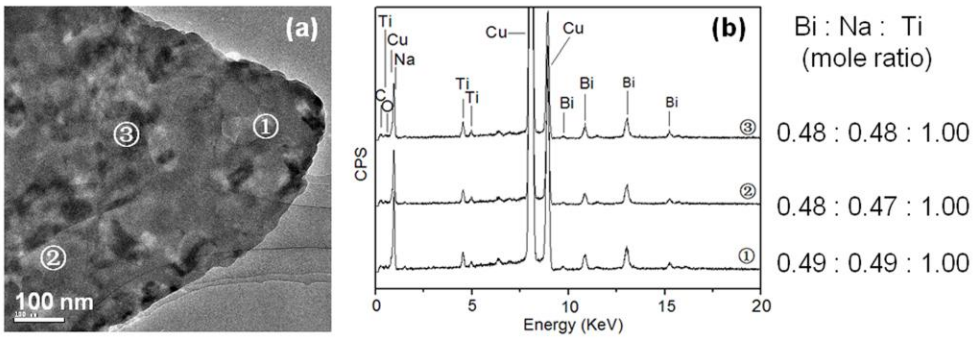

Figure 2.13 (a) TEM image and (b) EDS spectra of the sample obtained by heat treatment of HTO-TiO_2-Na_2CO_3-Bi_2O_3 mixture at 700 ^oC for 3 h. EDS spectra ①, ② and ③ correspond to those at the positions marked ①, ②, and ③ in TEM image.

On the base of results described above, a reaction mechanism of the formation of the [100]-oriented platelike BNT mesocrystal in HTO-TiO_2-Bi_2O_3-Na_2CO_3 solid state reaction is given in Figure 2.14. In the first step of the reaction, the platelike HTO particles react with Na_2CO_3 and Bi_2O_3 to form the platelike BNT mesocrystal by the *in situ* topotactic reaction similar to the case in the HTO-Bi_2O_3-Na_2CO_3 reaction system as shown in Figure 2.5, because HTO shows the higher reactivity in the formation reaction of the BNT phase than that of TiO_2 nanoparticles. This reaction is almost completed at 600 ^oC, and the platelike BNT mesocrystal constructed from [100]-direction oriented-nanoparticles are formed. In the second step of the reaction, TiO_2 nanoparticles react with Na_2CO_3, Bi_2O_3 to form the BNT phase on the platelike BNT mesocrystal surface by an epitaxial crystal growth mechanism. The epitaxial growth can lower the reaction temperature for the formation of the BNT phase from the TiO_2-Bi_2O_3-Na_2CO_3 reaction system. This is the reason why the formation of the BNT phase can be completed in the HTO-TiO_2-Bi_2O_3-Na_2CO_3 reaction system at lower temperature (700 ^oC) than that in the TiO_2-Bi_2O_3-Na_2CO_3 reaction system (900 ^oC). The epitaxial growth of the BNT phase on the platelike mesocrystal surface accompanies the consumption of unreacted TiO_2, Na_2CO_3, and Bi_2O_3 in the reaction system and fusion of these particles into the platelike mesocrystals by the mass-transport process. In the epitaxial growth process, the [100]-oriented BNT nanoparticles in the platelike mesocrystal act as crystal seeds, namely the oriented nanoparticles grew up and keep their [100] orientation. This is the reason why the larger [100]-oriented platelike BNT mesocrystal can be formed in the HTO-TiO_2-Bi_2O_3-Na_2CO_3 reaction system.

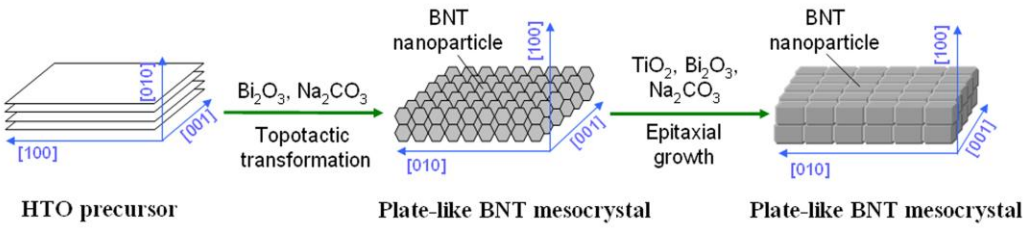

Figure 2.14 Reaction mechanism of the formation of platelike BNT mesocrystal in HTO-TiO_2-

Bi_2O_3-Na_2CO_3 solid-state reaction.

2.4 Conclusions

The [100]-oriented platelike BNT mesocrystals can be prepared using HTO-Bi_2O_3-Na_2CO_3 and HTO-TiO_2-Bi_2O_3-Na_2CO_3 reaction systems. The platelike BNT mesocrystals prepared by these methods are constructed from [100]-oriented BNT nanocrystals. The platelike BNT mesocrystals are formed by topotactic structural transformation mechanism in the HTO-Bi_2O_3-Na_2CO_3 reaction system and by the combination mechanism of the topotactic structural transformation and the epitaxial crystal growth in the HTO-TiO_2-Bi_2O_3-Na_2CO_3 reaction system, respectively. The HTO precursor shows high reactivity in the formation reaction of BNT, resulting formation of BNT at lower temperature than those with TiO_2 nanoparticles and layered compounds of $Bi_4Ti_3O_{12}$ and $Na_{0.5}Bi_{4.5}Ti_4O_{15}$ platelike particles as the precursors.

2.5 References

(1) Aksel, E.; Jones, J. L. *Sensors* **2010**, 10, 1935–1954.

(2) Saito, Y.; Takao, H.; Tani, T.; Nonoyama, T.; Takatori, K.; Homma, T.; Nagaya, T.; Nakamura, M. *Nature* **2004,** 432, 84–87.

(3) Zeng, J. T.; Kwok, K. W.; Tam, W. K.; Tian, H. Y.; Jiang, X. P.; Chan, H. L. W. *J. Am. Ceram. Soc.* **2006**, 89, 3850–3853.

(4) Safari, A.; Abazari, M. *IEEE Trans. Ultrason. Ferroelectr. Freq. Control* **2010**, 57, 2165–2176.

(5) Smolenskii, G. A.; Isupov, V. A.; Agranovskaya, A. I.; Krainik, N. N. *Sov. Phys. Solid State (Engl. Transl.)* **1961**, 2, 2651–2654.

(6) Jaffe, B.; Cook, W. R.; Jaffe, H. *Piezoelectric Ceramics*; Academic Press: London, **1971**, 1.

(7) Elkechai, O.; Manier, M.; Mercurio, J. P. *Phys. Status Solidi A* **1996**, 157, 499–560.

(8) Dorcet, V.; Trolliard, G. A T. *Acta. Mater.* **2008**, 56, 1753–1761.

(9) Trolliard, G.; Dorcet, V. *Chem. Mater.* **2008**, 20, 5074–5082.

(10) Barick, B. K.; Choudhary, R. N. P.; Pradhan, D. K. *Mater. Chem. Phys.* **2012**, 132, 1007–1014.

(11) Suchanicz, J. *J. Phys. Chem. Solids* **2001**, 62, 1271–1276.

(12) Setasuwon, P.; Kijamnajsuk, S. *Sci. Technol. Adv. Mater.* **2006**, 7, 780–784.

(13) Khamman, O.; Watcharapasorn, A.; Pengpat, K.; Tunkasiri, T. *J. Mater. Sci.* **2006**, 41, 5391–5394.

(14) Yamamoto, K.; Suzuki, M.; Noguchi, Y.; Miyayama, M. *Jpn. J. Appl. Phys.* **2008**, 47, 7623–7629.

(15) Liu, Y. F.; Lu Y. N.; Dai, S. H. *J. Alloys Compd.* **2009**, 484, 801–805.

(16) Zuo, R. Z.; Su, S.; Wu, Y.; Fu, J.; Wang, M.; Li, L. T. *Mater. Chem. Phys.* **2008**, 110, 311–315.

(17) Liao, Y. W.; Xiao, D. Q. *J. Mater. Sci. Technol.* **2009**, 25, 777–780.

(18) Yang, J. N.; Liu, P.; Bian, X. B.; Jing, H. X.; Wang, Y. J.; Zhang, Y.; Wu, Y.; Song, W. H. Dielectric, *Mater. Sci. Eng. B* **2011**, 176, 260–265.

(19) Wada, S.; Takeda, K.; Muraishi, T.; Kakemoto, H.; Tsurumi, T.; Kimura, T. *Ferroelectr.* **2008**, 373, 11–21.

(20) Sabolsky, E. M.; Trolier–McKinstry, S.; Messing, G. L. *J. Appl. Phys.* **2003**, 93, 4072–4080.

(21) Cao, W.; Randall, C. A. *J. Phys. Chem. Solids* **1996**, 57, 1499–1505.

(22) Waanders, J. W. *Piezoelectric Ceramics: Properties and applications*. Philips Components: Eindhoven, Netherlands, **1991**, 41–64.

(23) Kong, X. G.; Ishikawa, Y.; Shinagawa, K.; Feng Q. *J. Am. Ceram. Soc.* **2011**, 94, 3716–3721.

(24) Wada, S.; Takeda, K.; Muraishi, T.; Kakemoto, H.; Tsurumi T.; Kimura T. *Jpn. J. Appl. Phys.* **2007**, 46, 7039–7043.

(25) Takahashi, H.; Numamoto, Y.; Tani, J.; Tsurekawa, S. *Jpn. J. Appl. Phys.* **2006**, 45, 7405–7408.

(26) Kimura, T. *J. Ceram. Soc. Jpn.* **2006**, 114, 15–25.

(27) Kimura, T.; Takahashi, T.; Tani, T.; Saito, Y. *J. Am. Ceram. Soc.* **2004**, 87, 1424–1429.

(28) Kimura, T.; Takahashi, T.; Tani, T.; Saito, Y. *Ceram. Int.* **2004**, 30, 1161–1167.

(29) Wu, M. J.; Li, Y. X.; Wang, D.; Yin, Q. R. *Ceram. Int*. **2008**, 34, 753–756.

(30) Xue, H.; Xiong, Z. X. *J. Alloys Compd.* **2009**, 467, 338–341.

(31) Su, S.; Zuo, R. H.; Lv, D. Y.; Fu, J. *Powder Technol*. **2012**, 217, 11–15.

(32) Soto, T.; Kimura, T. *Ceram. Int*. **2008**, 34, 757–760.

(33) Sugawara, T.; Shimizu, M.; Kimura, T.; Takatori, K; Tani, T. *Ceram. Trans.* 2**003**, 136, 389–406.

(34) Motohashi, T.; Kimura, T. *J. Eur. Ceram. Soc.* **2007**, 27, 3633–3636.

(35) Kimura, T.; Motohashi T. *Key Eng. Mater.* **2009**, 388, 209–212.

(36) Roy, M.; Indu Bala; Barbar, S. K.; Jangid, S.; Dave P. *J. Phys. Chem. Solids* **2011**, 72, 1347–1353.

(37) Jovalekić, C.; Zdujić, M. *Ceram. Int.* **2010**, 36, 789–792.

(38) Wu, M.; Li, Y. *Mater. Lett.* **2010**, 64, 1157–1159.

(39) Setasuwon, P.; Kijamnajsuk S. *Cryst. Eng. Comm.* **2009**, 11, 1947–1950.

(40) Zhao, W.; Zhou, H. P.; Yan, Y. K.; Liu, D. *J. Am. Ceram. Soc.* **2008**, 91, 1322–1325.

(41) Setasuwon, P.; Vaneesorn, N.; Kijamnajsuk, S.; Thanaboonsombut, A. *Sci. Technol. Adv. Mat.* **2005**, 6, 278–281.

(42) Radha Velchuri; Vijaya kumar, B.; Rama Devi, V.; Prasad, G.; Vithal, M. *Ceram. Int*. **2010**, 36, 1485–1489.

(43) Lencka, M. M.; Oledzka, M.; Riman, R. E. *Chem. Mater.* **2000**, 12, 1323–1330.

(44) Pookmanee, P.; Rujijanagul, G.; Ananta, S.; Heimann, R. B.; Phanichphant, S. *J. Eur. Ceram. Soc.* **2004**, 24, 517–520.

(45) Jing, X. Z.; Li, Y. X.; Yin, Q. G. *Mater. Sci. Eng.B* **2003**, 99, 506–510.

(46) Wang, Y. G.; Xu, G.; Yang, L. L.; Ren, Z. H.; Wei, X.; Weng, W. J.; Du, P. Y.; Shen, G.; Han, G. R. *Ceram. Int*. **2009**, 35, 1657–1659.

(47) Kim, C. Y.; Sekino, T.; Niihara, K. *J. Am. Ceram. Soc*. **2003**, 86, 1464–1467.

(48) Kanie, K.; Sakai, H.; Tani, J.; Takahashi, H.; Muramatsu A. *Mater. Trans.* **2007**, 48, 2174–2178.

(49) Qi, J. Q.; Sun, L.; Du, P.; Li, L. T. *J. Am. Ceram. Soc.* **2010**, 93, 1044–1048.

(50) Feng, Q.; Hirasawa, M.; Kajiyoshi, K.; Yanagisawa, K. *J. Am. Ceram. Soc.* **2005**, 88, 1415–1420.

(51) Feng, Q.; Hirasawa, M.; Yanagisawa, K. *Chem. Mater.* **2001**, 13, 290–296.

(52) Feng, Q.; Ishikawa, Y.; Makita, Y.; Yamamoto, Y. *J. Ceram. Soc. Jpn.* **2010**, 118, 141–146.

(53) Kong, X. G.; Hu, D. W.; Ishikawa, Y.; Tanaka, Y.; Feng, Q. *Chem. Mater.* **2011**, 23, 3978–3986.

(54) Zhou, L.; O'Brien, P. *Small* **2008**, 4, 1566–1574.

(55) Cölfen, H; Mann, S. *Angew. Chem. Int. Ed.* **2003**, 42, 2350–2356.

(56) Ye, J. F.; Liu, W.; Cai, J. G.; Chen, S.; Zhao, X. W.; Zhou, H. H.; Qi, L. M. *J. Am. Chem. Soc.* **2011**, 133, 933–940.

(57) Song, R. Q.; Cölfen, H. *Adv. Mater.* **2010**, 22, 1301–1330.

(58) Fukuchi, E.; Kilnura, T. *J. Am. Ceram. Soc.* **2002**, 85, 1461–1466.

(59) Chou, C. S.; Yang, R. Y.; Chen, J. H.; Chou, S.W. *Powder Technol.* **2010**, 199, 264–271.

(60) Trolliard, G.; Benmechta, R.; Mercurio, D. *Acta Mater.* **2007**, 55, 6011–6018.

(61) Zhou, J. K.; Zou, Z. G.; Ray, A. K.; Zhao, X. S. *Ind. Eng. Chem. Res.* **2007**, *46*, 745–749.

(62) Molla, A. R.; Tarafder, A.; Karmakar, B. *J. Mate.r Sci.* **2011**, 46, 2967–2976.

(63) Pei, L.; Li, M.; Liu, J.; Yu, B.; Wang, J.; Zhao, X. *Mater. Lett.* **2010**, 64, 364–366.

(64) Aksel, E.; Jones, J. L. *J. Am. Ceram. Soc.* **2010**, 93, 3012–3016.

(65) Navarro-Rojero, M. G.; Romero, J. J.; Rubio-Marcos, F.; Fernandez, J. F. *Ceram. Int.* **2010**, 36, 1319–1325.

† Chapter II (Topotactic Transformation Reaction from Layered Titanate to Platelike [100]-oriented $Bi_{0.5}Na_{0.5}TiO_3$ Mesocrystals) was **Reprinted (adapted) with permission from** (DENGWEI HU, XINGANG KONG, KOTARO MORI, YASUHIRO TANAKA, KAZUNARI SHINAGAWA, QI FENG, FERROELECTRIC MESOCRYSTALS OF BISMUTH SODIUM TITANATE: FORMATION MECHANISM, NANOSTRUCTURE, AND APPLICATION TO PIEZOELECTRIC MATERIALS, *INORGANIC CHEMISTRY*, **2013**, 52, 10542–10551.).

Chapter III

Fabrication of [100]-oriented $Bi_{0.5}Na_{0.5}TiO_3$ Ceramics with Small Grain Size and High Density Based on $Bi_{0.5}Na_{0.5}TiO_3$ Mesocrystal Formation Mechanism†

3.1 Introduction

Pb-free piezoelectric materials have been recently demanded from the viewpoint of environmental protection.[1,2] One of the well-known Pb-free ferroelectrics is barium titanate ($BaTiO_3$, or BT), which exhibits a tetragonal symmetry of perovskite structure at room temperature having large piezoelectricity.[3] But its Curie temperature (T_c=130 ^oC) is low, and a phase transition from tetragonal phase to orthorhombic phase around 0 ℃.[4] Therefore, the working temperature of BT is limited in a range of 0 to 130 ^oC, which is too narrow for actual piezoelectric applications. It is very necessary to develop or/and improve the other Pb-free ferroelectrics.

In chapter II, $Bi_{0.5}Na_{0.5}TiO_3$ (BNT), a well-known ferroelectric material,[5;6] has been introduced. It has a perovskite structure with rhombohedral *R3c* space system at room temperature.[7] The BNT is considered as one of the most promising candidate materials for the replacement of Pb-based piezoelectric materials because of its high Curie temperature (T_c =320 ^oC) and interesting ferroelectric properties.[5,8-10] Therefore it has a wider application temperature range than BT. However, similar to the most of other Pb-free piezoelectric materials, the piezoelectricity of BNT is lower than Pb-based piezoelectric materials.[6,11,12]

For enhancing the piezoelectricity, domain engineering for the control of the domain size and texture engineering for the control of direction orientation of the piezoelectric ceramics are effective methods. The increase of piezoelectricity and the

decrease of ferroelectric hysteresis for piezoelectric ceramics can be realized well by decreasing the domain size,[13–15] and the domain size can be decreased by reducing the grain size of the ceramic.[16,17] Since piezoelectric ceramics show crystal-axis anisotropic, their piezoelectricity and permittivity are tensor quantities and relate to both the directions of the applied stress and electric field, and also to the directions perpendicular to these.[18] Therefore, the high piezoelectricity can be achieved also by using the crystal-axis-oriented ceramics.[19] So that, if an oriented piezoelectric ceramic with small grain size can be fabricated, both of the domain engineering and texture engineering techniques can be applied to the piezoelectric ceramic simultaneously, and a new class of high performance piezoelectric material is expected. However, it has not been achieved yet.

Reactive-templated grain growth (RTGG) method is widely applied to the fabrication of the oriented ceramics. A significant specialty of the RTGG method is an *in situ* topotactic reaction between the precursor template particles with anisotropy morphology and other equiaxed matrix starting materials. In this method, a green compact made from aligned template particles with the same crystal-axis direction and matrix grains with random direction is calcined or sintered to form the oriented object material.[20] The oriented ceramic is developed mainly by the growth of oriented template particles at the expense of matrix grains.[21,22] Usually, the particles with platelike or fibrous anisotropy morphology can be selected as the template material. Three kinds of the platelike particles, $Bi_4Ti_3O_{12}$,[126,23] $Na_{0.5}Bi_{0.5}TiO_3$,[22] and $Na_{0.5}Bi_{4.5}Ti_4O_{15}$[24] have been reported to be used as the templates for the fabrication of oriented BNT or BNT-based ceramics by RTGG method. These platelike particles were prepared using the solid state reaction or molten salt methods, which gives template particles with large size and non-uniform morphology.[23,25–28] The oriented ceramics with small grain size and high density are difficult to be achieved by using such large and non-uniform template particles.[126,23,29]

Small and uniform platelike particles of layered titanate $H_{1.07}Ti_{1.73}O_4 \cdot nH_2O$ (HTO) crystals with a lepidocrocite-like structure can be prepared by hydrothermal

reaction.[30–32] The HTO platelike particles have been used as the precursors for the syntheses of the perovskite $BaTiO_3$, $Ba_{1-x}Ca_xTiO_3$, and $Ba_{1-x}(Bi_{0.5}Na_{0.5})xTiO_3$ platelike particles by solvothermal reactions.[19,33,34] The platelike perovskite titanate particles prepared by this method are constructed from the spherical nanoparticles. All the spherical nanoparticles in the platelike particle align and show the same [110]-direction orientation, resulting in the formation of the oriented-platelike polycrystalline particles.[19,33,34] Such oriented-platelike polycrystalline particles can be defined as a new category of mesocrystals.[35, 36] The $Ba_{1-x}Ca_xTiO_3$ platelike mesocrystal has been used as the template for the fabrication of the [110]-oriented $Ba_{1-x}Ca_xTiO_3$ ceramic with the fine grain size of 1 μm by a templated grain growth (TGG) process.[19] The HTO platelike particles can be used also as the precursors for the preparation of the platelike $Bi_{0.5}Na_{0.5}TiO_3$ mesocrystals with [100]-orientation by the solid state reaction as described in chapter II. It is expected that an oriented BNT ceramic with small grain size could be obtained by using the HTO platelike particles as the template in the RTGG method. However, to the best of our knowledge, the study on the fabrication of oriented ceramics using HTO as the template has not been reported at all.

In this Chapter, an RTGG process for the fabrication of the crystal-axis-oriented BNT ceramics using the platelike HTO particles as the template was described. The effects of the starting compositions and sintering conditions on the orientation, grain size, and density of the ceramics were studied. The [100]-oriented BNT ceramics with the high degree of orientation, high density, and small grain size were achieved simultaneously for the first time by using the RTGG process, and the apparent piezoelectric constant d_{33}^* values of the oriented BNT ceramics also were given for the first time. The success in the fabrication of such BNT ferroelectric ceramic materials is a significant milestone to challenge the high performance Pb-free piezoelectric materials by applying the both of the domain engineering and the texture engineering to the piezoelectric ceramics simultaneously.

3.2 Experimental procedure

3.2.1 Preparation of oriented BNT ceramics

Platelike $H_{1.07}Ti_{1.73}O_4 \cdot nH_2O$ (HTO) powder sample was prepared by acid-treatment of platelike $K_{0.8}Ti_{1.73}Li_{0.27}O_4$ (KTLO) powder that was synthesized by hydrothermal method reported in literature.[31] The starting materials of Bi_2O_3 (0.0125 mol), Na_2CO_3, HTO and TiO_2 powders were mixed thoroughly according to the BNT stoichiometric ratio, where the Ti mole ratio of TiO_2/HTO was selected as 0:10, 5:5, 6:4, 7:3, and 8:2, respectively. This well mixed starting materials powders (0.57 g) with solvent (3 g, 60 vol% toluene–40 vol% ethanol), binder (0.08 g, poly(vinyl butyral) (PVB)), and plasticizer (74 μL, di-n-butyl phthalate (DBP)) were milled by ball milling with 5 mm diameter zirconia balls at a rotational speed of 60 r/min for 48 h. The resultant slurry was cast on a polyethylene terephthalate (PET) film tape to form a green sheet using an auto film applicator (Tester Sangyo, PI-1210 Filmcoater) by a doctor blade technique.[37] After drying at room temperature, the green sheet was stacked into 64 layers with a size of 12 mm × 12 mm, and then pressed at 20 MPa for 3 min at room temperature to form a green compact with a thickness of about 2 mm. The green compact was calcined with a desired temperature program in air. Finally the calcined samples were naturally cooled down to room temperature.

3.2.2 Physical characterization

The structures of powder and ceramic samples were investigated using a powder X-ray diffractometer (XRD-6100, Shimadzu, Japan) with Cu Kα (λ = 0.15418 nm) radiation. The degree of orientation (Lotgering factor, *F*) of the ceramics samples in [100]-direction were evaluated from diffraction peak density of XRD in the range of 3° to 60° using the Lotgering's formula,[38]

$$F = \frac{P - P_0}{1 - P_0}, \quad P = \frac{\Sigma I(h00)}{\Sigma I(hkl)}, \quad P_0 = \frac{\Sigma I_0(h00)}{\Sigma I_0(hkl)}$$

where I and I_0 are the intensities of the (hkl) peaks for the oriented and the non-oriented samples, respectively. The F value ranges from 0 to 1, where F = 0 and 1

correspond to completely random and perfectly oriented, respectively. The BNT powder sample prepared using TiO_2 as Ti-source was used as the non-oriented standard for evaluating the P_0 value.

The size and morphology of the samples were characterized using scanning electron microscopy (SEM, JSM-5500S, JEOL, Japan). In the cross-section observation of the ceramic sample, firstly the ceramic sample was polished using a buffing machine (S5629, Marumoto Struers K.K., Japan) and a vibratory polisher (VibroMet 2, Buehler, USA), and then the polished sample was thermally etched for 30 min at a temperature lower than 100 ^{o}C sintering temperature. The density of the sintered compact was determined by a specific gravity measurement kit (SMK-401, Shimadzu, Japan) with Archimedes' principle. The theoretical density of 5.997 $g \cdot cm^{-3}$ of BNT was used to calculate the relative density.[23,39]

For the measurement of the piezoelectricity using a 31 resonator, the BNT ceramic was sized into $2.0 \times 2.0 \times 0.5$ mm^3 (0.5 mm // [100]) by cutting with a crystal cutter and polishing with a diamond slurry. Gold electrodes were prepared on the top and bottom surfaces with an area of 2.0×2.0 mm^2 by sputtering method. Both polarization-electric field (P-E) and strain-electric field (S-E) behaviors were measured at room temperature and 0.1 Hz using a ferroelectric character evaluation system. A slope of the S-E curve from 0 to 80 kV/cm was regarded as an apparent d_{33}^* value.[40–42]

3.3 Results and discussions

3.3.1 Fabrication of oriented BNT ceramic using HTO-Bi_2O_3-Na_2CO_3 reaction system

Firstly the oriented BNT ceramics were fabricated by the RTGG method using the HTO-Bi_2O_3-Na_2CO_3 reaction system. The XRD patters of HTO-Bi_2O_3-Na_2CO_3 mixture powders (random sample) and its green sheet (oriented sample) prepared by tape casting are presented in Figs. 1(a) and (b), respectively. The green sheet shows stronger relative intensity of (020) peak of HTO than the power sample, which illustrates the platelike HTO particles are oriented to [010]-direction in the green sheet.

The green compacts of HTO-Bi_2O_3-Na_2CO_3 were calcined at 500 ^oC to remove the organic matters in the green compacts, and then sintered at a temperature in the range of 900 to 1100 ^oC for 3 h. At 500 ^oC, (020) peak of HTO disappeared, and a new phase of $Bi_{12}TiO_{20}$ appeared (Figure 3.2(c)). These results suggest that reaction (1) occurs in the reaction system.

$$6Bi_2O_3 + (4/1.73)H_{1.07}T_{1.73}O_4 \cdot nH_2O \rightarrow Bi_{12}TiO_{20} + xH_2O \qquad (1)$$

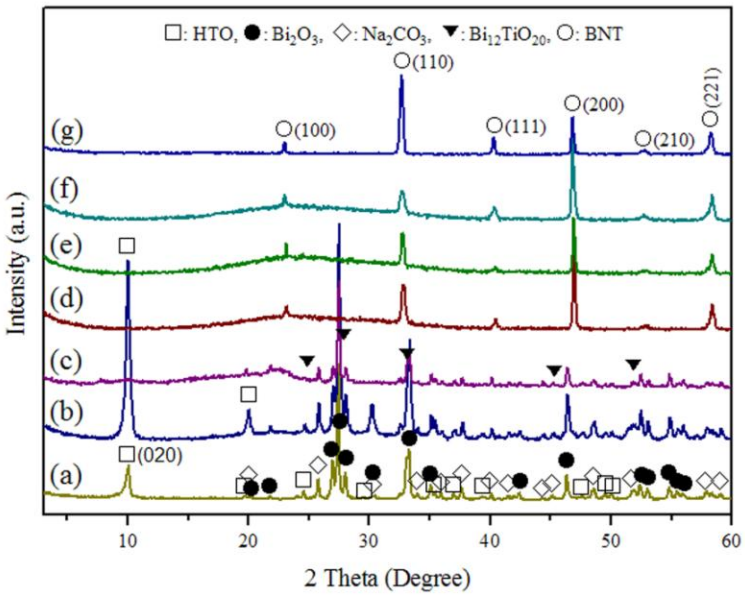

Figure 3.1 XRD patterns of (a) powder sample and (b) green sheet of HTO-Bi_2O_3-Na_2CO_3, and samples obtained after calcinations of HTO-Bi_2O_3-Na_2CO_3 green compacts at (c) 500, (d) 900, (e) 1000, and (f) 1100 ^oC for 3 h, respectively, and (g) non-oriented BNT powder sample.

A small amount of BNT phase was also observed, which reveals that the BNT phase can be formed at 500 ^oC. After sintering above 900 ^oC, single BNT phase was formed (Figs. 2(d)–(f)). The results of the formations of $Bi_{12}TiO_{20}$ intermediate and BNT product phases are consistent with the result obtained by calcination of HTO-Bi_2O_3-Na_2CO_3 mixture powder at the same temperature. Compared with the non-oriented BNT powder sample prepared by calcination of TiO_2-Bi_2O_3-Na_2CO_3 mixture (Figure 3.1(g)), the sintered ceramic samples show the strongest peak of (200) instead of (110) peak of the non-oriented sample. The result reveals that the obtained ceramic samples are oriented to [100]-direction. With an increase of the calcinations

temperature, the degree of orientation increases from $F_{(100)}$ = 39% at 900 °C to $F_{(100)}$ = 68% at 1100 °C.

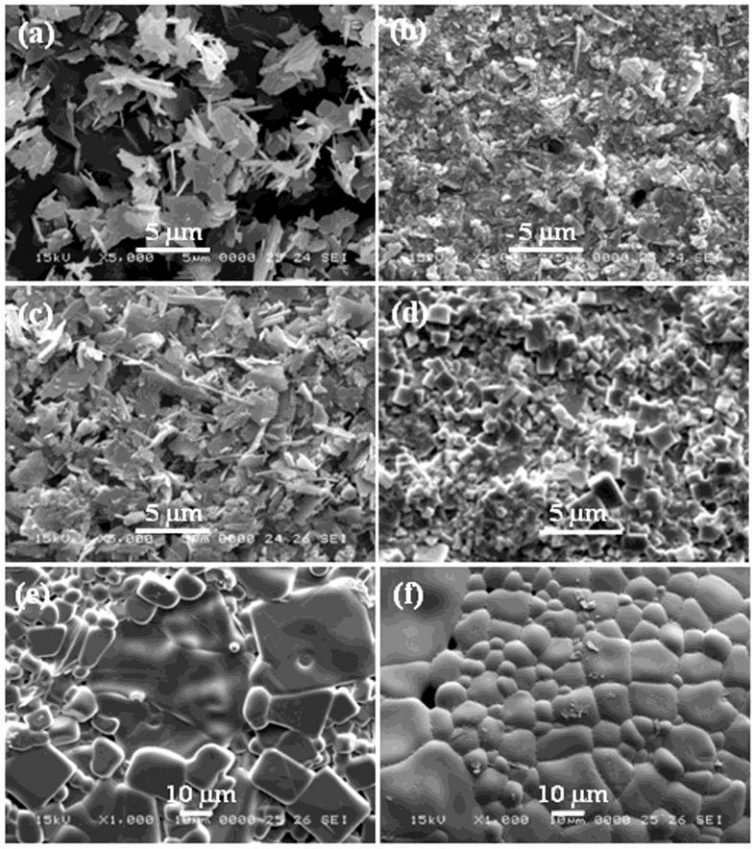

Figure 3.2 SEM images of (a) HTO template crystals, (b) HTO-Bi_2O_3-Na_2CO_3 green sheet, and samples obtained after calcinations of HTO-Bi_2O_3-Na_2CO_3 green compacts at (c) 500, (d) 900, (e) 1000, and (f) 1100 °C for 3 h, respectively.

The SEM results indicate that the HTO particles used as the template have platelike particle morphology with a size of about 3 μm in width and 0.2 μm in thickness (Figure 3.2(a)). The HTO particles in the green sheet are oriented, where the basal plane of platelike particles is parallel to the green sheet surface, and the particles are adhesive together by the binder and plasticizer (Figure 3.2(b)). Thermogravimetric and differential thermal analysis (TG-DTA) curves of fabricated HTO-Bi_2O_3-Na_2CO_3 green compact are given in Figure 3.3. The HTO-Bi_2O_3-Na_2CO_3 green compact shows an endothermic peak about 170 °C with a weight loss, which indicates a dehydration reaction of the crystal water and interlayer water of HTO, and exothermic peaks about

300 °C to 400 °C with a large weight loss, which correspond to the decomposition of the organic matters in the green compact is completed at 500 °C. The platelike particles were observed clearly after calcination at 500 °C due to losing the organic binder and plasticizer, where the platelike particles still maintained the intrinsic morphology and orientation (Figure 3.2(c)), although HTO lost its layered structure. This result implies that a topotactic structural transformation reaction takes place during this calcination process. When the green compact was sintered at 900 °C, the platelike particles disappeared and the uniform cubic particles with a size of about 1.5 μm were observed (Figure 3.2(d)). This result indicates that the platelike morphology breaks and transformed into the smaller cubic BNT particles. At 1000 and 1100 °C, the BNT grain size grew up with the increase of the sintering temperature (Figure 3.2(e) and (f)). These samples have a wide grain size distribution in a range of 5 to 50 μm.

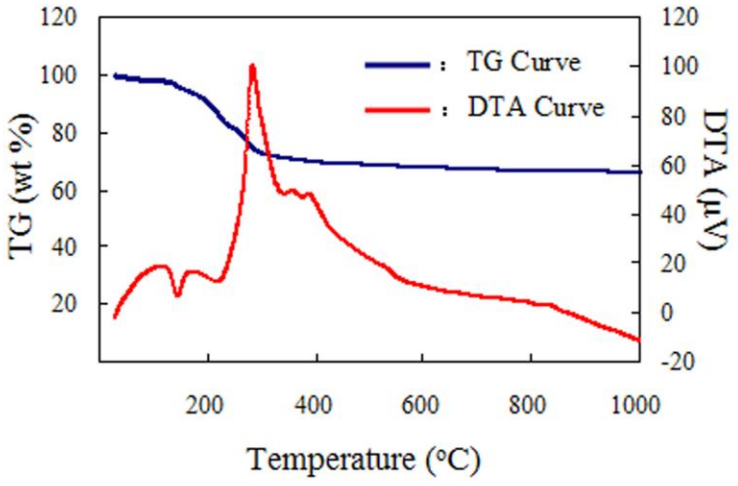

Figure 3.3 TG-DTA curves of HTO-Bi_2O_3-Na_2CO_3 green compact. The TG-DTA analysis was conducted on a DTG-60H thermogravimetric analyzer (SHIMADZU) in static air with a heating speed of 10 °C/min.

3.3.2 Fabrication of oriented BNT ceramic using HTO-TiO_2-Bi_2O_3-Na_2CO_3 reaction system

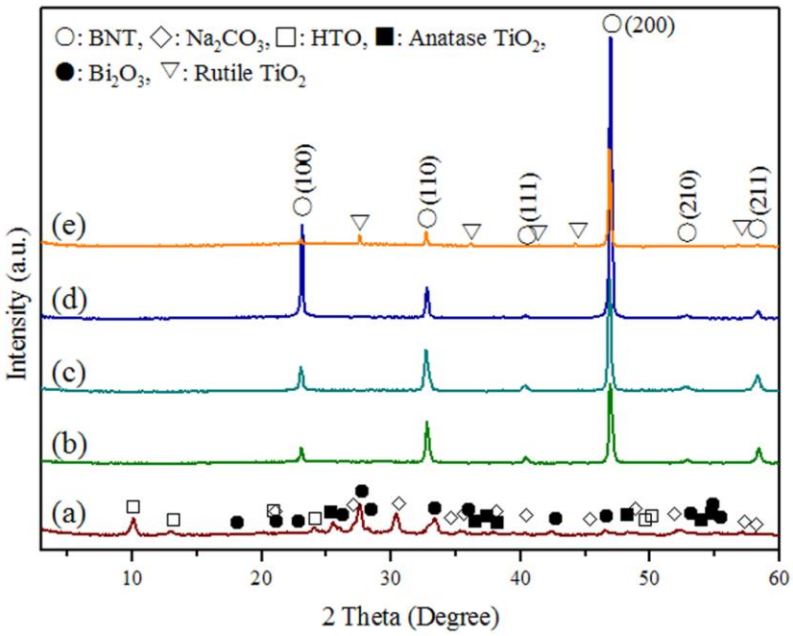

Figure 3.4 XRD patterns of (a) HTO-TiO_2-Bi_2O_3-Na_2CO_3 green sheet and samples obtained after calcinations of HTO-TiO_2-Bi_2O_3-Na_2CO_3 green compacts at (b) 900, (c) 1000, (d)1100, and (e) 1200 ^oC for 3 h, respectively. TiO_2/HTO Ti-mole ratio is 6: 4.

It has been reported that the addition of matrix is effect to enhance the degree of orientation and mass density of the ceramic, and the ratio of the matrix to the template strongly affects the degree of orientation of the ceramics in the RTGG process.[126,43] To obtain the BNT ceramic with higher degree of orientation than that of obtained using HTO-Bi_2O_3-Na_2CO_3 reaction system, we fabricated BNT ceramics using HTO-TiO_2-Bi_2O_3-Na_2CO_3 reaction system, where anatase TiO_2 nanoparticles were used as the matrix, and studied the effect of TiO_2 nanoparticle matrix on the degree of orientation. Figure 3.4 shows the XRD patterns of the ceramic samples fabricated using the HTO-TiO_2-Bi_2O_3-Na_2CO_3 reaction system with TiO_2/HTO Ti-mole ratio of 6:4. BNT ceramic with [100]-orientation was formed at 900 ^oC. The degree of orientation of the BNT ceramics fabricated using HTO-TiO_2-Bi_2O_3-Na_2CO_3 reaction system enhances with the increase of the sintering temperature up to 1100 ^oC. Impurity of rutile TiO_2 phase was observed at 1200 ^oC, which accompanies the decrease of the degree of orientation. The formation of rutile phase is due to the evaporations of Na and Bi components at the high temperature conditions. This result is different from the case using $Bi_4Ti_3O_{12}$ as the template for the oriented BNT ceramic where a single phase

can be obtained at 1200 °C.[126]

The degree of orientation of the BNT ceramics fabricated using HTO-TiO_2-Bi_2O_3-Na_2CO_3 reaction system is dependent on the TiO_2/HTO mole ratio and sintering temperature, as shown in Figure 3.5. The degree of orientation of the BNT ceramics enhances with increasing TiO_2/HTO Ti-mole ratio, and reaches the maximum value at 6:4, and then decreases for the samples fabricated at 900, 1000, and 1100 °C, respectively. At the same TiO_2/HTO Ti-mole ratio, the degree of orientation of the BNT ceramics enhances with the increase of the sintering temperature up to 1100 °C.[126] The highest degree of orientation of 81% can be achieved at TiO_2/HTO Ti-mole ratio of 6:4 and 1100 °C.

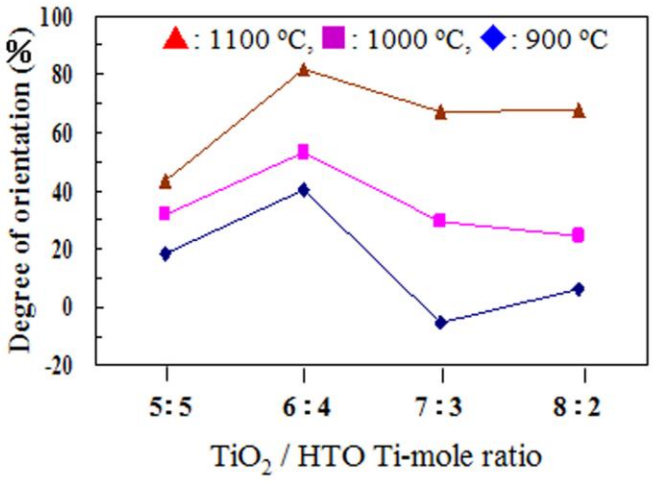

Figure 3.5 Relationships between degree of orientation and TiO_2/HTO Ti-mole ratio at different calcination temperatures in HTO-TiO_2-Bi_2O_3-Na_2CO_3 reaction system.

The microstructural analysis of ceramic samples obtained using HTO-TiO_2-Bi_2O_3-Na_2CO_3 reaction system was carried out, and the SEM images are illustrated in Figure 3.6. For the samples with TiO_2/HTO Ti-mole ratio of 6:4, the ceramic fabricated at 900 °C is constructed from cubic grains of about 1 μm. The grains grow up to about 5 μm, accompanying formation of a dense sintered body, with the increase of the temperature to 1100 °C (Figure 3.6(a)–(c)). A similar grain growth behavior was also observed for the samples with other TiO_2/HTO Ti-mole ratios. By comparing the ceramics fabricated at 1100 °C, the sample with TiO_2/HTO Ti-mole ratio of 5:5 has

almost the same grain size as the sample of 6:4, while grain sizes of 7:3 and 8:2 samples are much larger than the sample of 6:4 (Figs. 5(d)–(f)). The grain size grows up with increasing matrix TiO_2 fraction in the starting mixture in the TiO_2/HTO Ti-mole ratio range of 6:4 to 8:2.

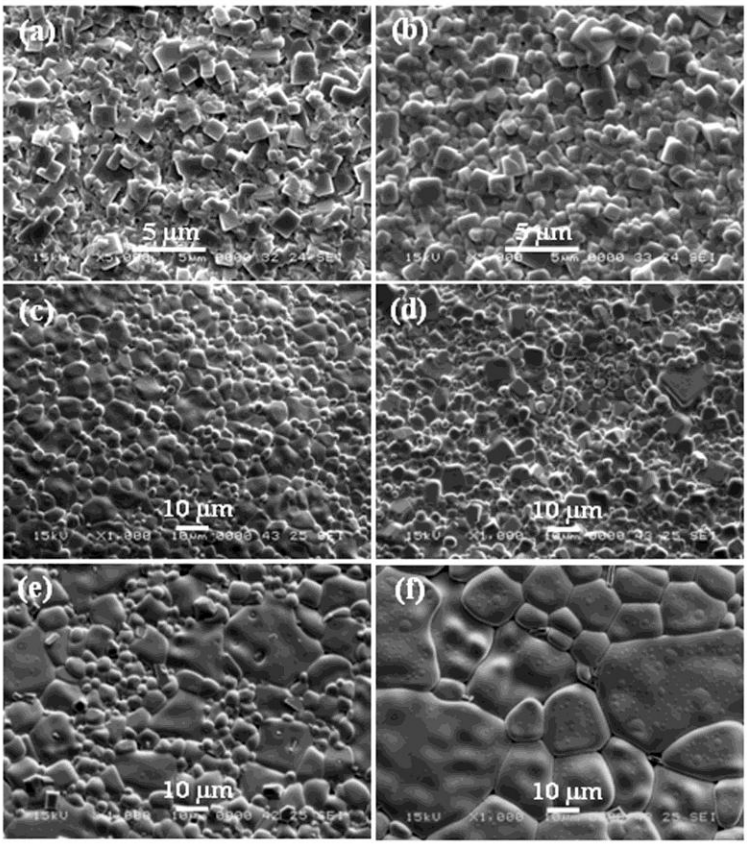

Figure 3.6 SEM images of ceramic surfaces of the samples obtained by calcinations of HTO-TiO_2-Bi_2O_3-Na_2CO_3 green compacts at (a) 900, (b) 1000, and (c–f) 1100 ^oC for 3 h. TiO_2/HTO Ti-mole ratios are (a, b, and c) 6 : 4, (d) 5 : 5, (e) 7 : 3, and (f) 8 : 2, respectively.

3.3.3 Influence of chemical composition on oriented BNT ceramics

It has been reported that addition of stoichiometric excess Bi [44] or Na [23,44] components in the starting mixture can improve the relative density and the orientation of the oriented BNT ceramics by the RTGG method with $Bi_4Ti_3O_{12}$ as the template because the excess Bi and Na can form liquid phases during the sintering, which causes liquid phase crystal growth.[23,44] The liquid phase can promote grain growth by reducing crystal growth activation energy. Here the influence of chemical

composition of the starting on the orientation of BNT ceramics was discussed using the HTO-TiO_2-Bi_2O_3-Na_2CO_3 reaction system with TiO_2/HTO=6:4. Seven kinds of starting mixtures with 5 mol% metal element excess or/and lacking, as shown in Table 3.1, were used in ceramic fabrication at 1100 ^oC, and compared with the stoichiometric sample. The XRD results reveal that the main phases are BNT in all these ceramic samples (Figure 3.7). When the excess Bi was added in the reaction system, the $Bi_{12}TiO_{20}$ phase is observed as impurity phase (Figure 3.7(b)), and rutile type of TiO_2 phase is observed in the Ti excess reaction system (Figure 3.7(d)). However, almost no impurity phase was observed in the Na excess reaction system (Figure 3.7(a) and (c)).

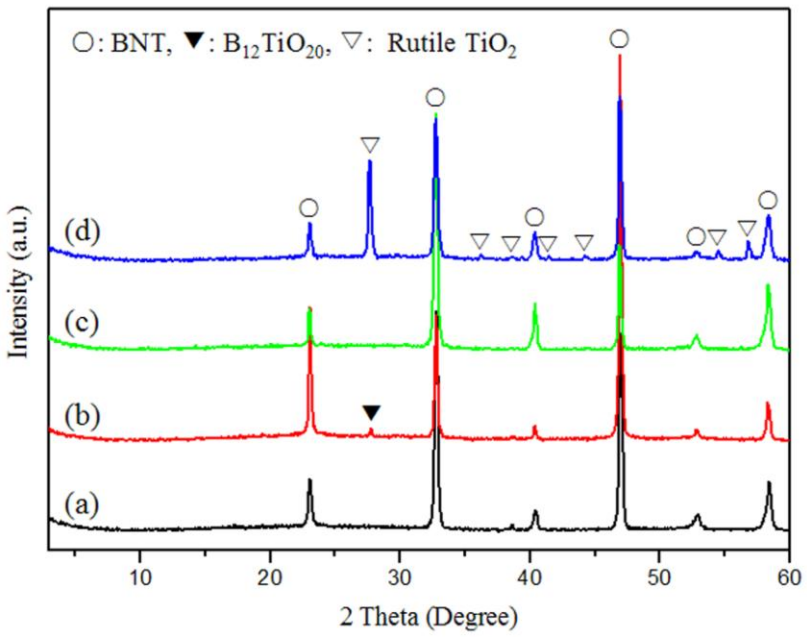

Figure 3.7 XRD patterns of ceramic samples obtained by calcinations of HTO-TiO_2-Bi_2O_3-Na_2CO_3 green compacts with (a) Bi and Na of excess 5 mol%, (b) Bi of excess 5 mol%, (c) Na of excess 5 mol%, and (d) Ti of excess 5 mol% at 1100 ^oC for 3 h, respectively. TiO_2/HTO Ti-mole ratio = 6 : 4.

All these samples show the same [100]-orientation, while stoichiometric sample shows the highest degree of orientation (Table 3.1). The Bi excess samples show a smaller decrease in degree of orientation, while the Na excess samples show a larger decrease in degree of orientation. These results suggest that element excess and

lacking decrease the degree of orientation for the fabrication of BNT oriented ceramics by using HTO as the template, which is different from the $Bi_4Ti_3O_{12}$ template.

Table 3.1 Degree of orientation in [100]-direction for BNT ceramics fabricated using HTO-TiO_2-Bi_2O_3-Na_2CO_3 reaction system with different chemical compositions.

Sample No.	Mole ratio of element in BNT ceramics system			Degree of orientation (%)
	Bi	Na	Ti	
S1	0.5	0.5	1	81
S2	0.525	0.5	1	27
S3	0.5	0.5	1.05	62
S4	0.5	0.525	1	2
S5	0.525	0.525	1	24
S6	0.475	0.525	1	3
S7	0.525	0.475	1	63
S8	0.475	0.475	1	27

TiO_2/HTO Ti-mole ratio = 6 : 4, sintering at 1100 ^oC for 3 h.

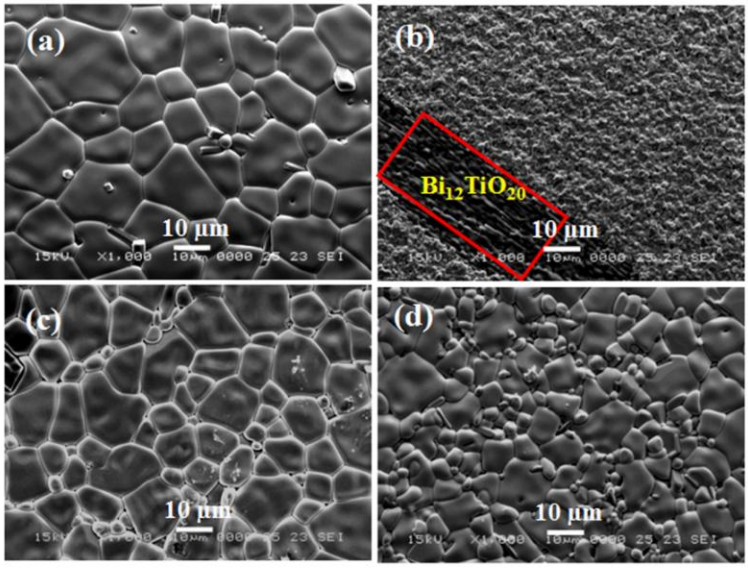

Figure 3.8 SEM images of ceramic surfaces of the samples obtained by calcinations of HTO-TiO_2-Bi_2O_3-Na_2CO_3 green compacts with (a) Bi and Na of excess 5 mol%, (b) Bi of excess 5 mol%, (c) Na of excess 5 mol% and (d) Ti of excess 5 mol% at 1100 ^oC for 3 h, respectively. TiO_2/HTO Ti-mole ratio = 6 : 4.

Figure 3.8 presents SEM images of the ceramic samples fabricated using the excess composition reaction systems at 1100 ^{o}C. The samples with excess Na have large grain size and high density (Figure 3.8(a) and (c)), suggesting the excess Na component promotes the grain growth due to the liquid phase sintering.[23] The grain growth for the ceramic sample was observed also in the Ti excess reaction system (Fig.7(d)), suggesting that the excess Ti component also promotes the ceramic sintering by liquid phase sintering mechanism. The Bi excess sample shows small grain size except small amount of large fibrous particles (Figure 3.8(b)). The large fibrous particles can be assigned to the $Bi_{12}TiO_{20}$ phase (Figure 3.7(b)),[27,45] and the small grains can be assigned to BNT phase. This result suggests that the excess Bi inhibits the BNT grain growth in the sintering process. Although excess Na and Ti components promote the ceramic sintering by the liquid phase sintering mechanism, the enhancement of the orientation was not observed. This result is different from the case using the $Bi_4Ti_3O_{12}$ as the template, where the liquid phase sintering enhances the orientation.

3.3.4 Influence of sintering conditions on oriented BNT ceramics

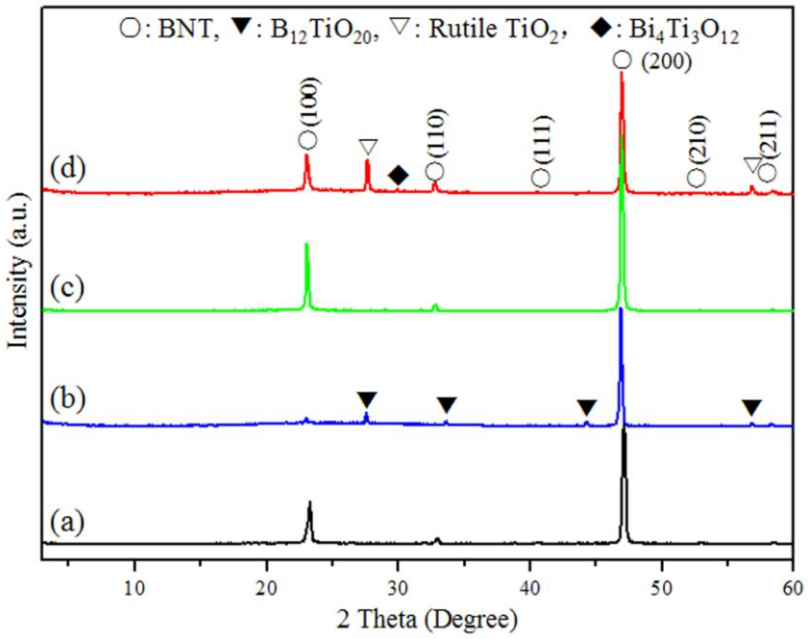

Figure 3.9 XRD patterns of the ceramic samples fabricated by calcinations of HTO-TiO_2-Bi_2O_3-Na_2CO_3 green compacts using different calcination temperature programs. (a) TP-500-900, (b) TP-900-1100, (c) TP-500-900-1100, and (d) TP-500-900-1200. TiO_2/HTO Ti-mole ratio = 6 : 4.

In order to clarify the influence of the sintering process on the oriented BNT ceramics, five kinds of sintering temperature programs, as shown in Table 3.2, were designed and carried out on the HTO-TiO_2-Bi_2O_3-Na_2CO_3 reaction system with TiO_2/HTO Ti-mole ratio of 6:4. The XRD patterns of the fabricated ceramic samples are shown in Figure 3.9, and their degrees of orientation, the relative densities, and the grain sizes are listed in Table 3.2.

Table 3.2 Degree of orientation in [100]-direction, relative density, and average grain size of BNT ceramics fabricated using different calcination temperature programs.

Sample No.	Calcination temperature program	Degree of orientation (%)	Relative density (%)	Average grain size (μm)
TP-500-900	500 °C (3h) - 900 °C (3h)	82	85	1
TP-500-900-1100	500 °C (3h) - 900 °C (3h) -1100 °C (3h)	95	98	2
TP-500-900-1200	500 °C (3h) - 900 °C (3h) -1200 °C (3h)	87	81	25
TP-900-1100	900 °C (3h) - 1100 °C (3h)	79	89	2.8
TP-500-1100	500 °C (3h) - 1100 °C (3h)	81	96	5

TiO_2/HTO Ti-mole ratio = 6 : 4 in HTO-TiO_2-Bi_2O_3-Na_2CO_3 reaction system.

The degree of orientation and relative density of TP-500-900 sample is 82% and 85%, respectively. The low relative density reveals that the sintering does not progress at 900 ^oC. At this temperature, the formation reaction of BNT phase is completed, and it gives a fairly high degree of orientation. TP-500-900-1100 sample shows the highest degree of orientation and relative density. The result suggests that the sintering progresses at 1100 ^oC, and the sintering causes the enhancement of the orientation. The XRD result indicates that impurity phases of rutile TiO_2 and $Bi_4Ti_3O_{12}$ are formed in TP-500-900-1200 sample (Figure 3.9(d)). This maybe due to volatilization of Na or/and Bi component at the high temperature of 1200 ^oC. The Na or/and Bi volatilization also causes low density and low orientation of the ceramic (Table 3.2). The impurity phase of $Bi_{12}TiO_{20}$ was also observed in TP-900-1100 sample (Figure 3.9(b)). In this case, the organic matters were decomposed at the high temperature of

900 ^{o}C, and Na component may be volatilized during the decomposition of the organic matters at this temperature. This sample shows the lowest degree of orientation, which maybe due to that Na lacking in the reaction system. The above results indicate that the 3-step calcination program of TP-500-900-1100 is effective for the fabrication of the high orientation and high density ceramic. This 3-step temperature program includes decomposition of the organic matters at 500 ^{o}C, completion of BNT formation reaction at 900 ^{o}C, and then sintering of BNT particles at 1100 ^{o}C.

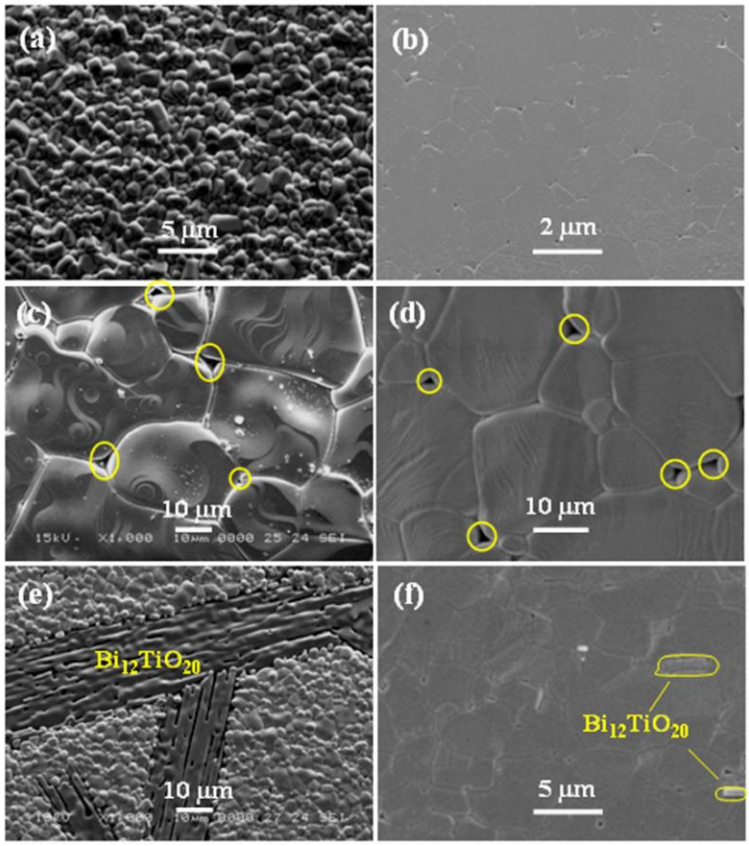

Figure 3.10 SEM images of (a, c, and e) surfaces and (b, d, and f) cross-sections of the ceramic samples obtained by calcinations of HTO-TiO_2-Bi_2O_3-Na_2CO_3 green compacts using different calcination temperature programs. (a) TP-500-900-1100, (b) TP-500-900-1200, and (c) TP-900-1100. TiO_2/HTO Ti-mole ratio = 6 : 4.

The SEM images of the surfaces and the cross-sections of the ceramic samples obtained by calcinations of green compacts using different temperature programs are

shown in Figure 3.10, and their average grain sizes are given in Table 3.2. The grain sizes and morphologies observed on the ceramic surfaces are almost same as which in the cross-sections for all these samples. The morphology of platelike template particle was not observed in the cross-sections of all the samples. This is different from the cases using $Bi_4Ti_3O_{12}$ and $Na_{0.5}Bi_{0.5}TiO_3$ as the templates for the BNT or BNT based oriented ceramics, where the platelike morphology of the templates is retained after the sintering, due to the large particle size and low reactivity of the templates.[126,22,46] The retention of template morphology causes the formation of BNT ceramics with low density. In the present case, the HTO template has small particle size and shows high reactivity. The platelike morphology of the HTO template is destroyed and transformed to small particles in the sintering process. This is the reason why the BNT ceramic with high density and small grain size can be obtained by using the HTO template.

The TP-500-900-1100 sample has a narrow grain size distribution, and its grain size of 2 μm (Figs. 9(a, b)) is much smaller than 5 μm of MS-500-1100 sample (Figure 3.6(c)). The result reveals that completion of BNT phase formation at 900 ^oC and then sintering at 1100 ^oC are effective to fabricate a high orientation, small grain size, and high density ceramic.

The TP-500-900-1200 sample has a large grain size of about 25 μm and some pores at the grain boundaries (Figs. 9(c, d)). The sintering at 1200 ^oC not only causes great grain growth but also Na and Bi component volatilization. In the TP-900-1100 sample, in addition to the small grains, some large fibrous grains were observed also on the ceramic surface (Figure 3.10(e)). The small grains correspond to the BNT phase and the large fibrous grains to the $Bi_{12}TiO_{20}$ phase (Figure 3.9(b)). Small fibrous $Bi_{12}TiO_{20}$ grains were observed in the cross-section (Figure 3.10(f)), suggesting less Na volatilization from ceramic inside.

The above results reveal that the 3-step calcination temperature program can give the oriented BNT ceramic with high density of 98%, high degree of orientation of 95%, and small grain size of 2 μm. It has been reported that the highest degree of orientation for the oriented BNT ceramics fabricated with $Bi_4Ti_3O_{12}$[23] and

$Na_{0.5}Bi_{4.5}Ti_4O_{15}$[24] as the template are 79%, and 60%, respectively, and the highest density of oriented BNT ceramics fabricated with $Bi_4Ti_3O_{12}$ as the template was 86%.[23,43] Therefore, the density of 98% and degree of orientation of 95% of the TP-500-900-1100 sample are the highest values up to now.

3.3.5 Formation mechanism of oriented BNT ceramics in the RTGG process

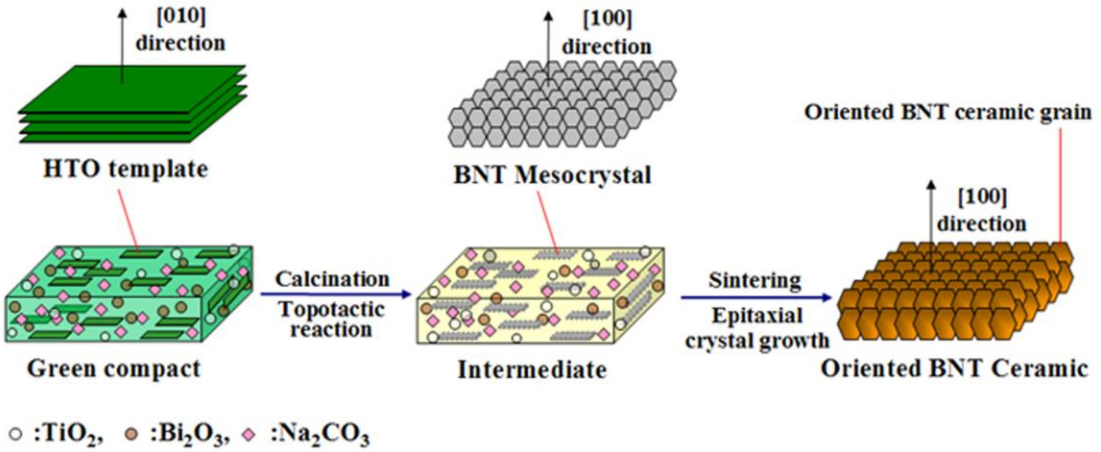

Figure 3.11 Formation mechanism of [100]-oriented BNT ceramic in the HTO-TiO_2-Bi_2O_3-Na_2CO_3 reaction system.

On the basis of the results described above and our recent study, the formation mechanism of [100]-direction oriented BNT ceramic in the HTO-TiO_2-Bi_2O_3-Na_2CO_3 reaction system is given in Figure 3.11. In the first step, the platelike oriented HTO particles react with Na_2CO_3 and Bi_2O_3 in the green compact to form BNT mesocrystals by an in situ topotactic structural transformation reaction mechanism, because HTO shows the higher reactivity in the formation reaction of the BNT phase than that of TiO_2 nanoparticles. The platelike BNT mesocrystal is constructed from [100]-direction oriented-nanoparticles. This topotactic reaction is completed at around 700 ^oC. In the second step of the reaction, TiO_2 nanoparticle matrixes react with Na_2CO_3 and Bi_2O_3 to form the BNT phase on the platelike BNT mesocrystal surface by an epitaxial crystal growth mechanism.[22] The epitaxial growth of the BNT phase on the platelike mesocrystal surface results the consumption of unreacted TiO_2,

Na_2CO_3, and Bi_2O_3 in the reaction system by the mass-transport process and the growth up of the BNT nanoparticles in the platelike mesocrystal. In the epitaxial growth process, the [100]-oriented BNT nanoparticles in the platelike mesocrystal act as crystal seeds, namely the oriented nanoparticles grow up and keep their [100] orientation. This reaction is completed at around 900 ^oC, which give an oriented BNT ceramic with low density. The BNT mesocrystals lost their platelike morphology and are transformed into small grains at this temperature. Finally the low density ceramic is sintered to high density ceramic at the high temperature over 1100 ^oC, where grain size grows up and degree of orientation enhances.

The formation of the BNT mesocrystals contributes to not only the high orientation but also the uniform grain size of the ceramic, where less abnormal grain growth occurs. This is the main reason why the highly oriented BNT ceramics with small grain size can be fabricated by using the HTO-TiO_2-Bi_2O_3-Na_2CO_3 reaction system. The formation of the BNT mesocrystals in the HTO template reaction system is different from the other template reaction systems, such as $Bi_4Ti_3O_{12}$ and $Na_{0.5}Bi_{4.5}Ti_4O_{15}$ template reaction systems. In the $Bi_4Ti_3O_{12}$[23] and $Na_{0.5}Bi_{4.5}Ti_4O_{15}$[25,28] template reaction systems, the platelike template particles are transformed to platelike BNT single crystals by an *in situ* topotactic microcrystal conversion reaction instead of the platelike BNT mesocrystals.[25,47] Since the platelike BNT single crystals formed by the *in situ* topotactic microcrystal conversion reaction have large particle sizes, the sintering of the large particles into high density ceramic with small grain size is difficult.

3.3.6 Piezoelectricity of oriented BNT ceramics

A preliminary piezoelectric study on the oriented BNT ceramic sample TP-500-900-1100 fabricated using the HTO-TiO_2-Bi_2O_3-Na_2CO_3 reaction system was carried out. Figure 3.12 shows at room temperature bipolar polarization-electric field (P-E) loop and strain-electric field (S-E) curve, and unipolar S-E curve of the oriented ceramic sample. This is the first time to give the P-E loop and S-E curve for the oriented BNT ceramics, due to the oriented BNT ceramic with enough high density

for the piezoelectric measurement is obtained for the first time by the present study. The P-E loop was ferroelectric. The remanent polarization (P_r) and coercive field (E_c) were about 18 μC/cm^2 and 59 kV/cm, respectively. These P_r and E_c values are smaller than 38 μC/cm^2 and 73 kV/cm of the non-oriented BNT ceramic, respectively. [48]

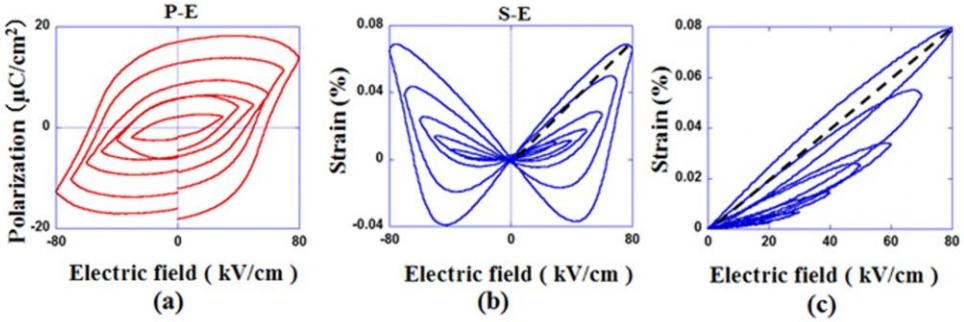

Figure 3.12 (a) Bipolar polarization-electric field (P-E) loops, (b) bipolar strain-electric field (S-E) curves, and (c) unipolar strain-electric field (S-E) curves for BNT ceramic sample of TP-500-900-1100.

The bipolar and unipolar S-E curves were ferroelectric also, and bipolar S-E curve is well butterfly shaped. The apparent piezoelectric constant d_{33}^* values of 90 pC/N and 100 pC/N are estimated from the slopes of the bipolar and unipolar S-E curves, respectively. These d_{33}^* values are larger than that of not exceeding 74 pC/N reported for the non-oriented BNT ceramics.[49,50] This is also the first report of the piezoelectric constant d_{33} for oriented BNT ceramic. The d_{33}^* value may be further enhanced after optimizing the measurement conditions.

3.4 Conclusions

The HTO-TiO_2-Bi_2O_3-Na_2CO_3 reaction system can be used to fabricate the oriented BNT ceramic with high density, high degree of the orientation along [100]-direction, and small grain size by the RTGG method. The oriented BNT ceramic is formed by topotactic transformation reaction of platelike HTO template particles to platelike BNT mesocrystal particles, and then epitaxial crystal growth of BNT on the BNT mesocrystal particles. The epitaxial crystal growth reaction is affected by TiO_2/HTO

mole ratio, chemical component of the starting material, and calcination conditions, which affect the degree of orientation, density, and grain size of the BNT ceramic. The fabricated oriented BNT ceramic shows a higher d_{33}^* value than the non-oriented BNT ceramic, suggesting the promising application to high performance Pb-free piezoelectric materials.

3.5 References

(1) Hiruma, Y.; Aoyagi, R.; Nagata, H.; Takenaka K. *Jpn. J. Appl. Phys.* **2004**, 43, 7556–7559.

(2) Tang, X. G; Chew, K. H.; Chan, H. L. W. *Acta. Mater.* **2004**, 52, 5177–5183.

(3)Wada, S.; Takeda, K.; Muraishi, T.; Kakemoto, H.; Tsurumi, T.; Kimura, T. *Jpn. J. Appl. Phys.* **2007**, 46, 7039–7043.

(4) Fu, D.; Itoh, M.; Koshihara, S. Y.; Kosugi, T.; Tsuneyuki, S. *Phys. Rev. Lett.* **2008**, 100, 227601.

(5) Lencka, M. M.; Oledzka, M.; Riman, R. E. *Chem. Mater.* **2000**, 12, 1323–1330.

(6)Zuo, R.; Su, S.; Wu, Y.; Fu, J.; Wang, M.; Li, L. *Mater. Chem. Phys.* **2008**, 110, 311–315.

(7) Maurya, D.; Murayama, M.; Pramanick, A.; Reynolds, W. T.; An, K.; Priya, S. *J. Appl. Phys.* **2013**, 113, 114101-114101-9.

(8) Dorcet, V.; Trolliard, G.; Boullay, P. *Chem. Mater.* **2008**, 20, 5061–5073.

(9) Trolliard, G.; Dorcet, V. *Chem. Mater.* **2008**, 20, 5074–5082.

(10) Bai, W. F.; Hao, J. G.; Fu, F.; Li, W.; Shen, B.; Zhai, J.W. *Mater. Lett.* **2013**, 97, 137–140.

(11) Liao, Y.W.; Xiao, D.Q. *J. Mater. Sci. Technol.* **2009**, 25, 777–780.

(12)Yang, J. N.; Liu, P.; Bian, X. B.; Jing, H. X.; Wang, Y. J.; Zhang, Y.; Wu, Y.; Song, W. H. Dielectric, *Mater. Sci. Eng. B* **2011**, 176, 260–265.

(13) Wada, S.; Takeda, K.; Muraishi, T.; Kakemoto, H.; Tsurumi, T.; Kimura, T. *Ferroelectrics* **2008**, 373, 11–21.

(14) Hoshina, T.; Takizawa, K.; Li, J. Y.; Kasama, T.; Kakemoto, H.; Tsurumi, T. *Jpn. J. Appl. Phys.* **2008**, 47, 7607–7611.

(15) Sabolsky, E. M.; Trolier–McKinstry, S.; Messing, G. L. *J. Appl. Phys.* **2003**, 93, 4072–4080.

(16) Cao, W. W.; Randall, C. A. *J. Phys. Chem. Solids* **1996**, 57, 1499–1505.

(17) Zheng, P.; Zhang, J. L.; Tan, Y. Q.; Wang, C. L. *Acta. Mater.* **2012**, 60, 5022–5030.

(18) Waanders, J. W. *Piezoelectric Ceramics, Properties and applications*. Eindhoven, Philips Components;**1991**.

(19) Kong, X. G.; Ishikawa, Y.; Shinagawa, K.; Feng Q. *J. Am. Ceram. Soc.* **2011**, 94, 3716–3721.

(20) Kimura, T.; Takahashi, T.; Tani, T.; Saito, Y. *Ceram. Int.* **2004**, 30, 1161–1167.

(21) Kimura, T.; Takahashi, T.; Tani, T.; Saito, Y. *J. Am. Ceram. Soc.* 2**004**, 87, 1424–1429.

(22) Maurya, D.; Zhou, Y.; Yan, Y. K.; Priya, S. *J. Mater. Chem. C* **2013**, 1, 2102–2111.

(23) Motohashi, T.; Kimura, T. *J. Eur. Ceram. Soc.* **2007**, 27, 3633–3636.

(24) Kim, I. W.; Ahn, C.W.; Choi, G.H.; et al. *ICAE 2011, proceedings of the International Conference on Advanced Electromaterials.* November 7-10, **2011** in Jeju, Korea.

(25) Wu, M.; Li, Y. *Mater. Lett.* **2010**, 64, 1157–1159.

(26) Yilmaz, H.; Messing, G. L.; Trolier-mckinstry, S. *J. Electroceram.* **2003**, 11, 207–215

(27) Jovalekić, Č.; Zdujić, M. *Ceram. Int.***2010**, 36, 789–792.

(28) Setasuwon, P.; Kijamnajsuk, S. *Sci. Technol. Adv. Mater.* **2006**, 7, 780–784.

(29) Kimura, T.; Motohashi, T. *Key Eng. Mater.* **2009**, 388, 209–212.

(30) Wen, P. H.; Itoh, H.; Tang W. P.; Feng, Q. *Langmuir* 2**007**, 23, 11782–11790.

(31) Feng, Q.; Ishikawa, Y.; Makita, Y.; Yamamoto, Y. *J. Ceram. Soc. Jpn.* **2010**, 118, 141–146.

(32) Wen, P. H.; Xue, M.; Ishikawa, Y.; Itoh, H.; Feng, Q. *ACS Appl. Mater. Interfaces* **2012**, 4, 1928−1934.

(33) Feng, Q.; Hirasawa, M.; Yanagisawa, K. *Chem. Mater.* **2001**, 13, 290–296.

(34) Kong, X. G.; Hu, D. W.; Ishikawa, Y.; Tanaka, Y.; Feng, Q. *Chem. Mater.* **2011**, 23, 3978−3986.

(35) Zhou, L.; O'Brien, P. *Small* **2008**, 4, 1566–1574.

(36) Cölfen, H; Mann, S. *Angew. Chem. Int. Ed.* **2003**, 42, 2350–2356.

(37) Mistler, R.E.; Twiname, E. R. *Tape Casting, Theory and Practice* American Ceramic Society, Westerville, Ohio, **2000**, 83–186.

(38) Lotgering, F. K. *J. Inorg. Nucl. Chem.* **1959,** 9, 113–123.

(39) Qi, J. Q.; Sun, L.; Du, P.; Li, L. T. *J. Am. Ceram. Soc.* **2010**, 93, 1044−1048.

(40) Yako, K.; Kakemoto, H.; Tsurumi, T.; Wada, S. *Mater. Sci. Eng. B* **2005**, 120, 181–185.

(41)Wada, S.; Yako, K.; Muraishi, T.; Yokoh, K.; Nam, S. M.; Kakemoto, H.; Tsurumi, T. *Ferroelectrics* **2006**, 340, 17–24.

(42)Wada, S.; Shimizu, S.; Pulpan, P.; Kumada, N.; Tanaka, D.; Furukawa, M.; Moriyoshi, C.; Kuroiwa, Y. *J. Ceram. Soc. Jpn.* **2010**, 118, 691–695.

(43) Fukuchi, E.; Kimura, T.; Tani, T.; Takeuchi, T.; Saito, Y. *J. Am. Ceram. Soc.* **2002**, 85, 1461–1466.

(44) Kimura, T.; Fukuchi, E.; Tani, T. *Jpn. J. App. Phys.* **2005**, 44, 8055–8061.

(45) Motohashi, T.; Kimura, T. *J. Am. Ceram. Soc.* **2008**, 91, 3889–3895.

(46) Su, S.; Zuo, R. Z.; Lv, D. Y. *J. Alloys Compd.* **2012**, 519, 25–28.

(47) Zhao, W.; Zhou, H. P.; Yan, Y. K.; Liu, D. *J. Am. Ceram. Soc.* **2008**, 91, 1322–1325.

(48) Takenaka, T.; Nagata, H. *Key Eng. Mate.* **1999**, 157–158, 57–64.

(49) Elkechai, O.; Manier, M.; Mercurio, J. P. *Phys. Status. Solidi. A* **1996**, 157, 499–506.

(50) Sakata, K.; Takenaka, T.; Naitou, Y. *Ferroelectrics* **1992**, 131, 219–226.

† Chapter III (Fabrication of [100]-oriented $Bi_{0.5}Na0.5TiO_3$ Ceramics with Small Grain Size and High Density Based on $Bi_{0.5}Na_{0.5}TiO_3$ Mesocrystal Formation Mechanism) was **Reprinted (adapted) with permission from** (DENGWEI HU, KOTARO MORIA, XINGANG KONG,KAZUNARI SHINAGAWA, SATOSHI WADA, QI FENG. FABRICATION OF [100]-ORIENTED BISMUTH SODIUM TITANATE CERAMICS WITH SMALLGRAIN SIZE AND HIGH DENSITY FOR PIEZOELECTRIC MATERIALS, *JOURNAL OF THE EUROPEAN CERAMIC SOCIETY*. **2014**, 34, 1169–1180.). **Copyright @ 2013 Journal of the European Ceramic Society.**

Chapter IV

Solvothermal Topochemical Synthesis of Mesocrystalline $Ba_{0.5}Sr_{0.5}TiO_3$ and $BaTiO_3/SrTiO_3$ Nanocomposite via Topochemical Mesocrystal Conversion

4.1 Introduction

The study on metal oxides perovskites with an ABO_3 formula is of great scientific and technological interest for their outstanding ferroelectric, piezoelectric, dielectric, pyroelectric, and catalytic responses.[1—3] One of a well-known and the most investigated perovskite materials is barium titanate ($BaTiO_3$, BT). It has a considerably high dielectric constant,[4,5] large piezoelectricity,[6] and ferroelectric properties[7] which are essential for electronic components and electro-optical materials.[8,9] BT exists in various crystallographic modifications, of which the tetragonal and cubic polymorphs are the most studied.[10,11] Its ferroelectric tetragonal polymorph is the thermodynamically stable form in the temperature range from 0 to 130 ℃. And its paraelectric cubic polymorph is the thermodynamically stable above the Curie temperature of 130 ℃. Another well-known perovskite oxide with a very close lattice dimension to $BaTiO_3$ is strontium titanate ($SrTiO_3$, ST). ST is an incipient ferroelectric, which remains thermodynamically stable and paraelectric cubic structure at room temperature in its unstressed form.[12] ST is considered to be a promising material for tunable microwave applications due to its high dielectric constant and low loss.[13] However, these simple titanate materials are not still satisfied

with the needs of the extensive applications.

Crystallographic structures determine their applied properties, and for perovskite titanates, one efficient approach of changing the structure is making mixed perovskite titanates.[10, 14] Oxide heterostructures with atomically abrupt interfaces, defined by atomically flat surface terraces and single-unit-cell steps, can be grown on well-prepared single-stepped substrates.[15,16] In this research field, $BaTiO_3/SrTiO_3$ (BT/ST) composites with strained-layer superlattices have been developed and attracted considerable attentions.[17–20] They are reported occurring in significant enhancements of dielectric constants and remanent polarization due to horizontal strain within layered heterostructure.[21,22] This horizontal strain can effectively produce high-strain energy derived from the lattice strain sustained in BT due to its ～2.2% lattice mismatch with ST.[21,23–26] At present, a significantly reactive molecular beam epitaxy (MBE) approach has been achieved for the fabrication of the BT/ST composites.[18,27,28] However, MBE approach is complicated and depends on the very sensitive substrate and expensive stacking configuration.[12,29-31] In the strain engineering field, the high strain energy from the heteroepitaxy interfaces with the high density strain is very beneficial for a large enhancement in the Curie temperature and remanent polarization of various ferroelectrics.[23,24] Although the present BT/ST composites obtained by the MBE process show more excellent dielectric and piezoelectric performances than conventional BT/ST composites, their formed heteroepitaxy interfaces are lack, and only issue from some horizontal strained planes between the above and below layers of the thin films. For practical applications, a facile process that can introduce high strains into materials is highly desirable for enhancing the material performance and reducing the production costs and reaction times.[12] Hence, it is very expectative for the development of a new process to replace the complicated and expensive MBE approach.

The development of mesocrystals is a recent research topic which is attracting the attention of scientists working in different fields of physics, chemistry, and materials science. [32] Mesocrystal is constructed from well-aligned oriented crystalline nanocrystals, [33,34] can offer unique new opportunities for materials design, and be applied to catalysis, sensing, and energy storage and conversion. [35-37] Some titanate mesocrystals are developed by our previous works. [38——41] Some BT and ST mesocrystals have been prepared very recently. [13,32,42,43] It is worth noting that a highly strained mesostructured BT/ST composite film has been fabricated by a surfactant-templated sol–gel method. [12] The fabricated film shows robust ferroelectricity derived from the abundant compressive stress which was created by the lattice mismatch between the BT and ST crystals.

In this Chapter, the ingenious design of two-step solvothermal soft chemistry process for the development a novel kind of platelike BT/ST mesocrystalline nanocomposites and $Ba_{0.5}Sr_{0.5}TiO_3$ mesocrystals is described. The platelike mesocrystalline nanocomposites are very difficult to be prepared via the conventional approaches duo to their high orientation and multicomponent chemical composition. In our design process, a layered $H_{4x/3}Ti_{2-x/3}O_4 \cdot H_2O$ (x = 0.8) (HTO) single crystal with lepidocrocite (γ–FeOOH)-type two-dimension structure was prepared and significantly employed as precursor. Keeping appropriate reactivity in reaction system is important to obtain the BT/ST nanocomposite mesocrystal and avoid forming $Ba_xSr_{1-x}TiO_3$ solid solution. Under high reactive conditions, the formed BT/ST nanocomposite will be transformed into $Ba_xSr_{1-x}TiO_3$ solid solution. These conditions can be achieved by controlling the polarity of the reaction solvent and reaction temperature. These conditions can be achieved by controlling the polarity of the reaction solvent and reaction temperature. The obtained BT/ST mesocrystalline nanocomposites constructed from crystal-axis-oriented individual BT and ST

nanocrystals have to withstand temperatures around 900 ^{o}C, and likely lead to the enhancement of the applicable temperature range. It should be noted that the high stain with high density probably occurs in the BT/ST mesocrystalline nanocomposite due to the high dense ferroelectric heterointerface with lattice mismatch, suggesting very promising for the more drastic enhancement of piezoelectric and dielectric performances.

4.2 Experimental Section

4.2.1 Materials and preparation of $H_{4x/3}Ti_{2-x/3}O_4 \cdot H_2O$ (x = 0.8) (HTO) precursor

All reagents used in this study were of analytical grade and without further purification. $H_{4x/3}Ti_{2-x/3}O_4 \cdot H_2O$ (x = 0.8) (HTO) crystals were prepared as reported by us previously.[44] 6.9 g of anatase TiO_2 nanoparticles, 5.1 g of KOH, 0.6 g of $LiOH \cdot H_2O$, and 25 mL of distilled water were sealed into a Hastelloy-C-lined vessel with internal volume of 45 mL, and then heated at 250 ^{o}C for 24 h under stirring conditions. After the solvothermal treatment, the obtained sample was washed with distilled water and dried at room temperature to obtain $K_{0.80}Ti_{1.73}Li_{0.27}O_4$ (KTLO) crystals. The KTLO crystals (4.0 g) was treated with a 0.2 mol·L^{-1} HNO_3 solution (500 mL) for 24 h under stirring conditions to exchange K^+ and Li^+ in the layered structure with H^+, and then the sample was washed with distilled water. After the acid treatments were done twice, the layered protonated titanate $H_{1.07}Ti_{1.73}O_4 \cdot H_2O$ single crystals were obtained. The as-obtained crystals were collected and washed with distilled water and ethanol, before air-drying at 60 ^{o}C for 12 h, and then the HTO (3.2 g) single crystals were obtained.

4.2.2 Solvothermal syntheses of $Ba_xSr_{1-x}TiO_3$ solid solution and BT/ST

nanocomposite

The platelike $Ba_xSr_{1-x}TiO_3$ solid solution and BT/ST mesocrystalline nanocomposites were synthesized by a two-step solvothermal soft chemical process. In the first step, the platelike HTO crystals (0.096 g) were partially reacted with $Ba(OH)_2$ (molar ratio of Ti/Ba = 2) in 30 mL water-ethanol mixed solutions with different volume ratios under solvothermal and stirring conditions at 150 and 200 ^oC for 12 h, respectively. After washing the first-step products by 0.1 mol· L^{-1} acetic acid and distilled water in sequence, $BaTiO_3$/HTO (BT/HTO) nanocomposite were obtained.[40,41] The samples are designated as BH-T-x/y, where T is reaction temperature and x/y is volume ratio of water/ethanol. In the second step, the BH-T-x/y sample (0.094 g) was solvothermally treated with $Sr(OH)_2$ (0. 114g $Sr(OH)_2$ $8H_2O$, Sr of excess 50%) in 30 mL water-ethanol mixed solutions with different volume ratios under stirring condition at 200 ^oC for 12 h. After the second-step solvothermal treatment, the product was filtered firstly, and then washed by 0.1 mol· L^{-1} acetic acid and distilled water in sequence, finally dried at room temperature. For the investigation of the thermodynamically stable, the obtained produce was annealed at a desired temperature for 3 h then naturally cooled down to room temperature.

4.2.3 Characterization

The structures of crystalline samples were investigated using a powder X-ray diffractometer (Shimadzu, XRD-6100) with Cu Kα (λ = 0.15418 nm) radiation. The size and morphology of the crystalline samples were observed using scanning electron microscopy (SEM) (JEOL, JSM-5500S) or field emission scanning electron microscopy (FE-SEM) (Hitachi, S-900). Transmission electron microscopy (TEM)/(high-resolution TEM (HR-TEM)) observation and selected-area electron

diffraction (SAED) were performed on a JEOL Model JEM-3010 system at 300 kV, and the crystal samples were supported on a Cu microgrid. Energy-dispersive spectroscopy (EDS; JEOL JED-2300T) was measured on the TEM system. Energy dispersive spectroscopy mapping (EDS-mapping) was observed using a combined HRTEM-EDS system (JEOL Model JEM-2100F HRTEM / EX-24063JGT EDX) as a function of the local relative concentration of the elements present. High Angle Angular Dark Field-Scanning Transmission Electron Microscopy (HAADF-STEM) was carried out on the HRTEM system.

4.3 Results and Discussion

4.3.1 Synthesis of $BaTiO_3$/HTO nanocomposites

For the synthesis of the platelike BT/ST mesocrystalline nanocomposite, we have designed an ingenious two-step solvothermal soft chemistry process to inhibit the platelike morphology destruction and prevent generating $Ba_xSr_{1-x}TiO_3$ solid solution. In the first step, the HTO precursor is reacted partially with $Ba(OH)_2$ to obtain a $BaTiO_3$/HTO (BT/HTO) nanocomposite. In the second step, the BT/HTO nanocomposite is reacted with $Sr(OH)_2$ to transform HTO in the nanocomposite to ST to obtain the platelike BT/ST mesocrystalline nanocomposite.

Firstly we have to synthesize a BT/HTO nanocomposite suitable for the synthesis of BT/ST mesocrystalline nanocomposite in the next step. Figure 4.1 presents the XRD partners of the HTO crystals before and after treatments in $Ba(OH)_2$ solutions at 150 and 200 ^oC for 12 h, respectively. Before the treatments, the basal spacing of 0.882 nm corresponds to the (020) crystal plane of HTO crystal with the layered lepidocrocite (γ–FeOOH)-type structure.[45] The unreacted HTO and generated BT phases can be easily observed after the treatments under the different conditions,

indicating that the HTO precursor is partially transformed to BT phase. The basal spacing of the HTO crystal decreased to 0.863 nm because of H^+/Ba^{2+} ion-exchange in the layered structure. The BT phase can be well identified by JCPDS File No. 71-1964 (cubic symmetry). The crystal structure of BT polymorph is tetragonal symmetry at room temperature usually. The formed BT phase can be indexed to a pseudocubic unit cell because of small tetragonal distortion. These results indicate that the mixed phases of BT and HTO can be obtained under the solvothermal conditions in the temperature range of 150 to 200 °C.

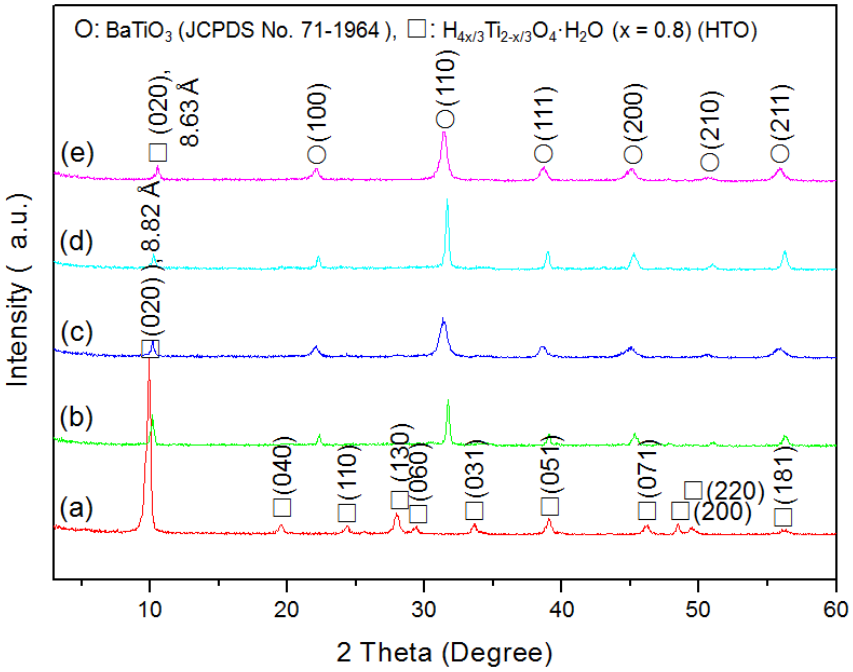

Figure 4.1 XRD patterns of (a) $H_{4x/3}Ti_{2-x/3}O_4 \cdot H_2O$ (x = 0.8) (HTO) crystals and samples obtained by solvothermal treatments of HTO-$Ba(OH)_2$ mixtures in (b, d) water solution and (c, e) water-ethanol mixed solvent (volume ratio = 5:25) at (b, c)150 °C and (d, e) 200 °C for 12 h, respectively.

Figure 4.2 shows the FE-SEM images of the HTO crystals before and after solvothermal treatments in $Ba(OH)_2$ solutions at 150 and 200 °C for 12 h, respectively. HTO crystals have platelike morphology with smooth surface and particle size of about 200 nm thicknesses and about 2 μm widths (Figure 4.2a). After the

solvothermal treatments in $Ba(OH)_2$ solutions, all the obtained samples show the platelike morphology also. In the samples of BH-150-30/0 and BH-200-30/0 obtained in water solvent, small particles with an average size about 20 nm are sparsely distributed on the surface of the platelike particles (Figure 4.2b, d). In the samples of BH-150-5/25 and BH-200-5/25 obtained in water-ethanol mixed solvent, the platelike particle surface is densely covered by small particles with an average size about 50 nm (Figure 4.2c, e). These results suggest that the platelike morphology of HTO crystal can be maintained after solvothermal treatments at 150 to 200 ^{o}C.

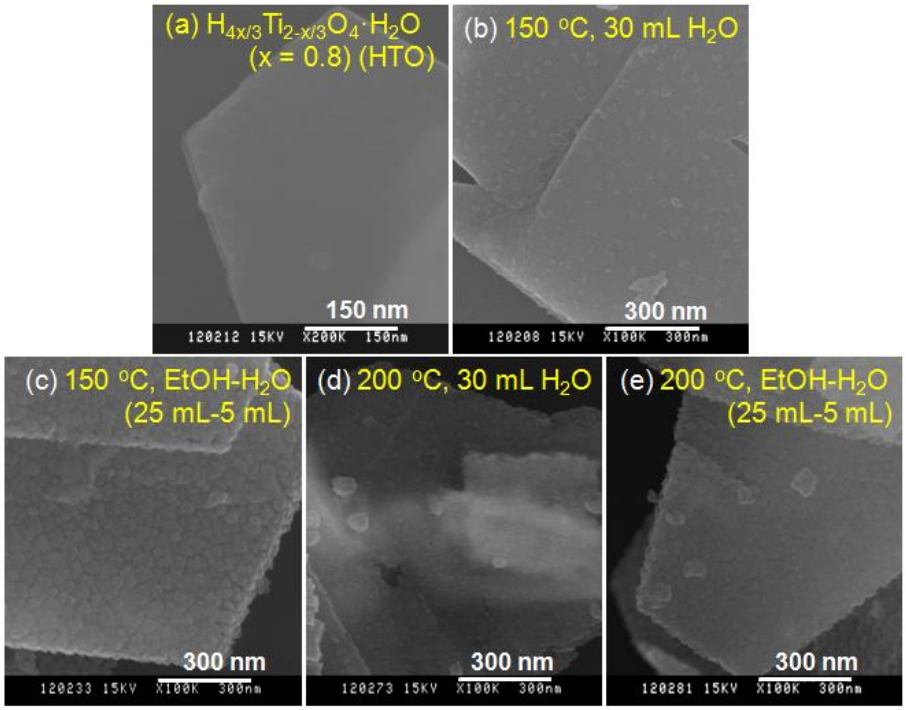

Figure 4.2 FE-SEM images of (a) HTO crystals and samples obtained by solvothermal treatments of HTO-$Ba(OH)_2$ mixtures in (b, d) water solution and (c, e) water-ethanol mixed solvent (volume ratio = 5:25) at (b, c) 150 ^{o}C and (d, e) 200 ^{o}C for 12 h, respectively.

In order to understand the formation of the mixed phases of BT and HTO from HTO single crystal in detail, TEM/HRTEM observations and SAED investigations of the HTO crystals before and after thermal treatment were performed. TEM image and SAED pattern of HTO single crystal are shown in Figure 4.3. The crystal with smooth

surface and platelike morphology is consistent with the FESEM image (Figure 4.2a). In the SAED pattern of HTO, the clear and ordered diffraction spots can be easily assigned to the HTO phase with orthorhombic system located along the [010] zone axis (Figure 4.3a, b). The [010] direction (*b*-axis direction) is perpendicular to the basal plane of the platelike HTO crystal. Figure 4.4 presents TEM images, HRTEM images, and SAED patterns of the samples of BH-150-30/0 and BH-200-30/0. TEM images reveal that the platelike crystals still maintain smooth surface and almost intact except some nanoparticles on the surface. The nanocrystals with the sizes of 5 and 10 nm arrange at the edge of the platelike samples of BH-150-30/0 and BH-200-30/0 giving rise to a hierarchical comb-like form, respectively (Figure 4.4a, g).

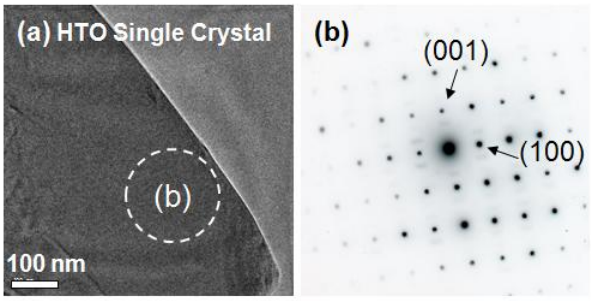

Figure 4.3 (a) TEM image and (b) SAED pattern of HTO single crystal.

In the SAED pattern of Figure 4.4b, three sets of SAED spots for the layered HTO lepidocrocite phase, the BT perovskite phase, and anatase phase are simultaneously observed in one platelike crystal, revealing that BT, HTO, and anatase phases coexist in one platelike crystal of the sample of BH-150-30/0. The [100] and [001] directions of the HTO phase correspond to the [001] and [1-10] directions of the BT phase, to the [100] and [001] directions of the anatase phase, respectively. The anatase phase can be formed because of dehydration of HTO crystal under thermal treatment conditions. The anatase phase cannot be observed in the XRD pattern (Figure 4.1b)

due to its very low crystallinity. But the SAED pattern of Figure 4.4h implies that only BT and HTO phases coexist in one platelike crystal of the BH-200-30/0 sample. This result suggests that the anatase may be not formed or the formed anatase reacted with Ba^{2+} to generate BT phase at higher temperature than 150 ^{o}C. The corresponding relationships of the crystal directions between the BT and HTO phases in the sample of BH-200-30/0 are same as that in the sample of BH-150-30/0. The [010] zone axis of precursor HTO crystal agrees with the [110] zone axis of the generated BT crystal after solvothermal treatment. The inserted FFT pattern in (d) HRTEM image show the same reciprocal lattice spots in Figure 4.4f. This result suggests that the nanoparticles on the surface of the platelike crystal have the same composite and crystalline structure to the platelike matrix crystal. These nanoparticles have the same orientation in one platelike particle. These sparse distributed nanoparticles (see Figure 4.2b, d) were formed by the dissolution-deposition reaction probably. These results suggest that the platelike BT/HTO nanocomposite can be obtained by solvothermal treatment of HTO and $Ba(OH)_2$ solution at 150 to 200 ^{o}C, and the formation of BT phase mainly occurred in the platelike particle bulk.

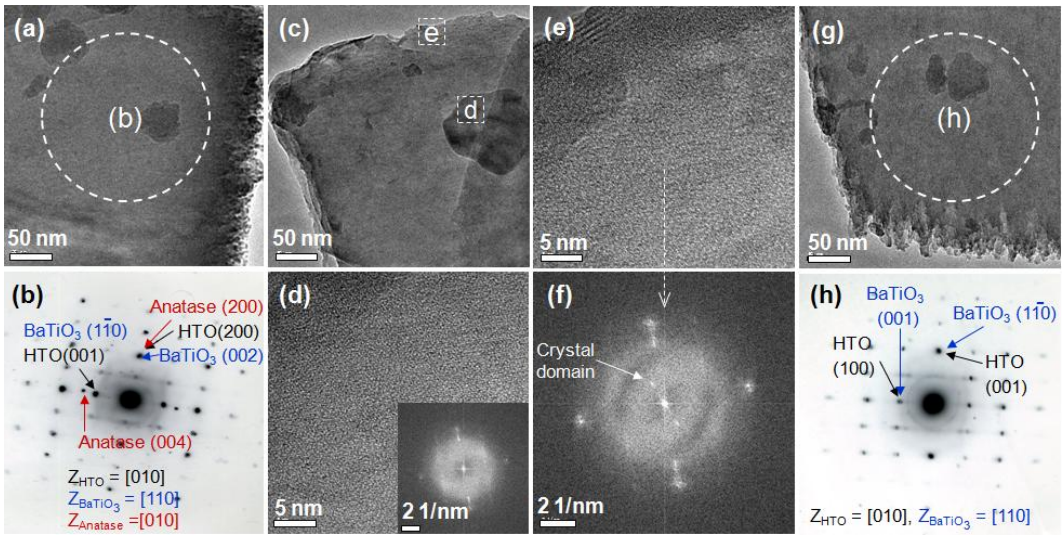

Figure 4.4 (a, c, g) TEM images, (b, h) SAED patterns, and FFT (fast Fourier transform) pattern

of samples obtained by solvothermal treatments of HTO single crystals and $Ba(OH)_2$ (molar ratio of Ti/Ba = 2) in water solution at (a–f) 150 °C and (g, h) 200 °C for 12 h, respectively. (d, e) HRTEM images are from the (d, e) white panes in (c) TEM image. The inserted FFT pattern in (d) HRTEM image is from the whole region of (d) HRTEM image.

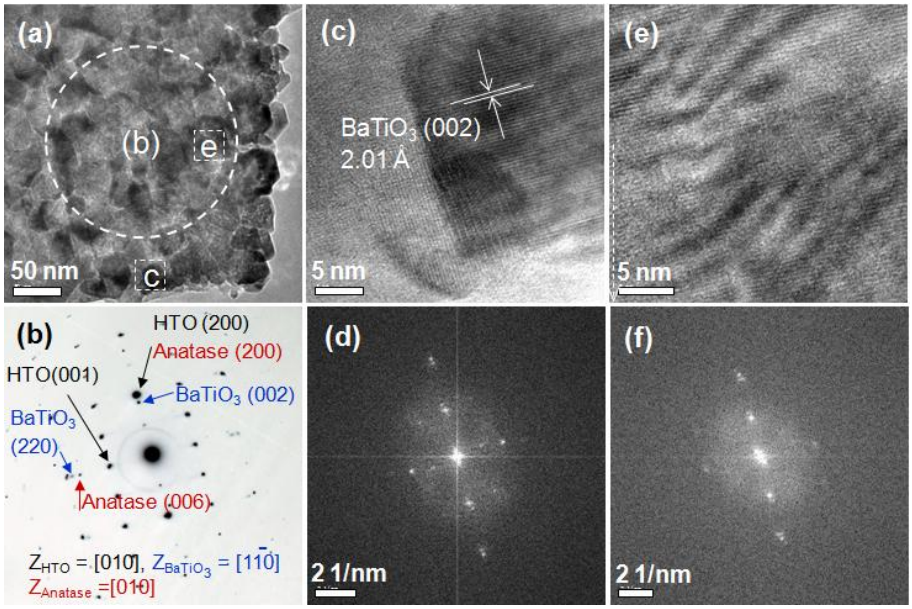

Figure 4.5 (a) TEM image and (b) SAED pattern of sample obtained by solvothermal treatment of HTO single crystals and $Ba(OH)_2$ (molar ratio of Ti/Ba = 2) in water-ethanol (volume ratio = 5:25) mixed solvent at 150 °C for 12 h. (c, e) HRTEM images are from the (c, e) white panes in (a) TEM image, respectively. (d, f) FFT patterns are from whole region of (c, e) HRTEM images, respectively.

The nanostructural investigation results of the BH-150-5/25 sample are illustrated in Figure 4.5. TEM image presents that the platelike polycrystal is constructed from nanocrystals with an average 50 nm size (Figure 4.5a), which agree with the FESEM image (Figure 4.2c). Similar to the BH-150-30/0 sample, the HTO, BT perovskite, and anatase phases can be also simultaneously observed in the SAED pattern (Figure 4.5b), and the relationships of crystal orientations between these nanocrystals agree with which of BH-150-30/0 sample. The clear lattice fringe of 0.201 nm in HRTEM image can be well in accord with the (002) plane of the BT phase (Figure 4.5c). The FFT patterns are well consistent with the SAED pattern and show the two phases

including HTO and BT. These results imply that the BT phase preferentially generate from the platelike particle surface, and BT/HTO nanocomposite can be obtained under solvothermal treatment of HTO and $Ba(OH)_2$ in water-ethanol mixed solvent. This result is relatively consistent with a BT/HTO nanocomposite reported by our previous work.[41]

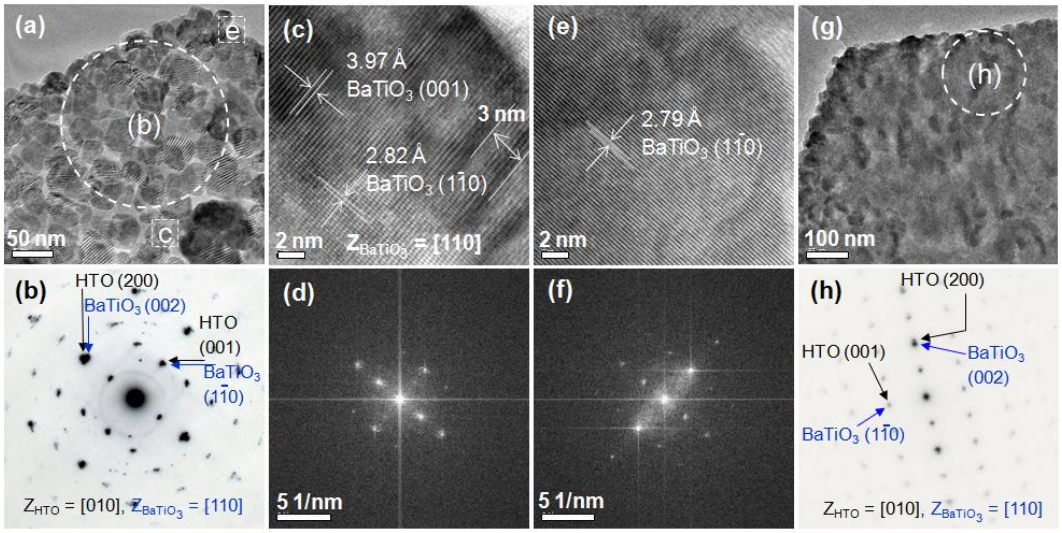

Figure 4.6 (a, g) TEM images and (b, h) SAED patterns of samples obtained by solvothermal treatments of HTO single crystals and $Ba(OH)_2$ (molar ratio of Ti/Ba = 2) in water-ethanol (volume ratios = (a, b) 5:25, (g, h) 10:20) mixed solvents at 200 ^{o}C for 12 h. (c, e) HRTEM images are from the (c, e) white panes in (a) TEM image, respectively. (d, f) FFT patterns are from the whole region of (c, e) HRTEM images, respectively.

TEM image, SAED pattern, HRTEM images, and FFT patterns of the BH-200-5/25 sample are shown in Figure 4.6a–f. Platelike polycrystal constructed from nanocrystals with an average 50 nm size can be observed. It is very interesting that some larger fringes (about 3 nm) than lattice fringes on the nanocrystals can be observed, and the larger fringes show different orientations on different nanoparticles. We consider that they may be polarization domains of BT ferroelectricity phase. Such crystal domains with very small size at the 'optimum' size range of ~10 nm are

easily controlled and altered for the development of the advanced functional materials.[46] It is the first time to find the crystal domains with a very small size by the solvothermal process. In the SAED pattern of the platelike polycrystal, two sets of clear and ordered diffraction spots can be easily assigned to the HTO phase and BT phase are simultaneously observed. The generated BT nanocrystals present [110] zone axis located on the basal plane of HTO crystal corresponding to the [010] zone axis of HTO crystal. The corresponding relationships of the crystal orientations between the HTO phase and BT phase are same as the other BT/HTO nanocomposites. The clear lattice fringes of 0.397 and 0.279–0.282 nm in HRTEM images can be well assigned to for the (001) and (1-10) planes of the BT phase, respectively (Figure 4.6c, e). The FFT patterns presenting reciprocal lattice spots of two-dimensional BT crystal are consistent with the SAED result. These results further suggest that the nanocrystals on the surface of the polycrystal are BT nanocrystals. The platelike BT/HTO nanocomposite can also be obtained by the solvothermal reactions at 150 to 200 ^{o}C.

For the investigation of the effect on the introduction of ethanol in the thermal reaction for the preparation of the BT/HTO nanocomposite, the solvothermal treatment of HTO and $Ba(OH)_2$ in water-ethanol (volume ratio = 10:20) mixed solution solvent at 200 ^{o}C for 12 h was also carried out. The TEM image and SAED pattern of the obtained sample are shown in Figure 4.6g and h, respectively. A handful of nanocrystals can be observed on the surface of the platelike crystal. Its roughness on the surface is in between the samples of BH-200-30/0 and BH-200-5/25. Also two sets of SAED spots for the HTO lepidocrocite and BT perovskite phases can be simultaneously observed in one platelike polycrystal, suggesting that the sample is BT/HTO nanocomposite. This result implies that the generated BT nanocrystals on the surface of the obtained platelike BT/HTO nanocomposite increase with the increase the ethanol volume in thermal reaction system.

The above results suggest that in the platelike BT/HTO nanocomposite prepared in the water solvent, the formed BT nanoparticles are distributed uniformly in the platelike particle bulk, while in that prepared in water-ethanol mixed solvent, the formed BT nanoparticles are preferentially distributed near the platelike particle surface. This difference can be explained by different solubilities of $Ba(OH)_2$ and HTO in the solvents with different polarity. Their solubilities enhance with increasing the solvent polarity, namely, water/ethanol ratio. In the water solvent with high polarity, Ba^{2+} ions can early migrate into the HTO bulk crystal from the interlayer space, and reaction with HTO in the bulk crystal, resulting formation of the uniform BT/HTO nanocomposite. On the other hand, in the ethanol solvent with low polarity, it is difficult to migrate Ba^{2+} ions into the HTO bulk crystal, and the formation reaction of BT preferentially occurs around the HTO platelike particle surface, resulting formation of BT around the surface of the platelike particle. Therefore, the solvent polarity can affect the nanostructure of BT/HTO nanocomposite. Furthermore, the crystal size of BT in the BT/HTO nanocomposite increases with increasing reaction temperature.

4.3.2 Solvothermal treatments of BT/HTO nanocomposites in $Sr(OH)_2$ water solution

In order to obtain the BT/ST nanocomposite, the BT/HTO nanocomposites were solvothermally treated in $Sr(OH)_2$ solution. Figure 4.7 presents the XRD patterns of the samples obtained by solvothermal treatments of different kinds of platelike BT/HTO nanocomposites in $Sr(OH)_2$ solution at 200 ^oC for 12 h. In addition to the slight unreacted HTO phase, the other diffraction lines can be well identified by JCPDS File No. 39-1395 (cubic symmetry) for $Ba_{0.5}Sr_{0.5}TiO_3$ solid solution. The results suggest that the mixture of BT and ST phases cannot be obtained by the

solvothermal treatment the BT/HTO nanocomposites and $Sr(OH)_2$ in the water solvent, but the $Ba_{0.5}Sr_{0.5}TiO_3$ solid solution.

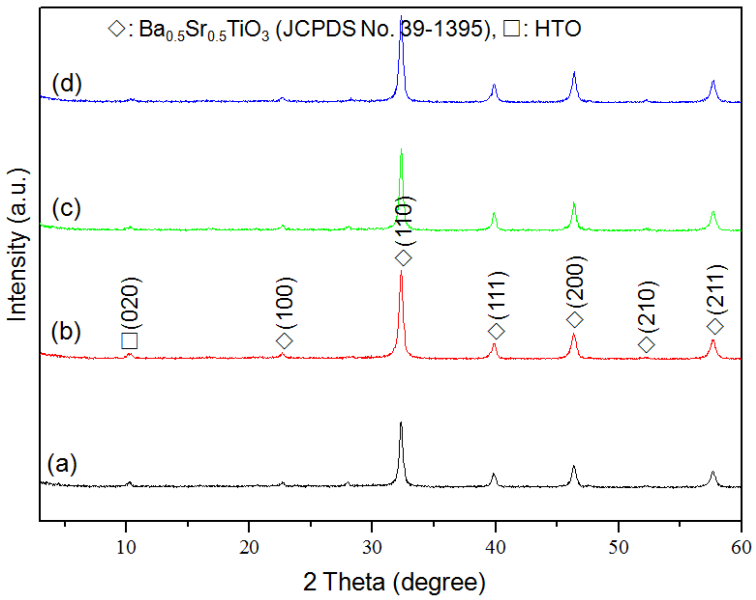

Figure 4.7 XRD patterns of samples obtained by solvothermal treatments of $Sr(OH)_2$ (Sr of excess 50%) in water solution with $BaTiO_3$(BT)/HTO nanocomposites at 200 ^oC for 12 h. BT/HTO nanocomposites prepared by thermal treatments of HTO and $Ba(OH)_2$ mixtures in (a, c) water solution and (b, d) water-ethanol mixed solvent (volume ratio = 5:25) at (a, b)150 ^oC and (c, d) 200 ^oC for 12 h, respectively.

Figure 4.8 shows the FE-SEM images samples obtained by solvothermal treatments of these platelike BT/HTO nanocomposites and $Sr(OH)_2$ in water solvent at 200 ^oC for 12 h. All the products present polycrystalline platelike particle morphology, indicating that the platelike morphology of the HTO crystal has not been damaged during the second step solvothermal treatment. When the samples of BH-150-30/0 and BH-200-30/0 were employed as the precursors, the platelike $Ba_{0.5}Sr_{0.5}TiO_3$ particle is constructed from nanocrystals with an average size approximately 200 nm (Figure 4.8a, c). The nanocrystal size is bigger than that (average size approximately 80 nm) prepared by solvothermal treatments of BH-150-5/25 and BH-200-5/25 samples.

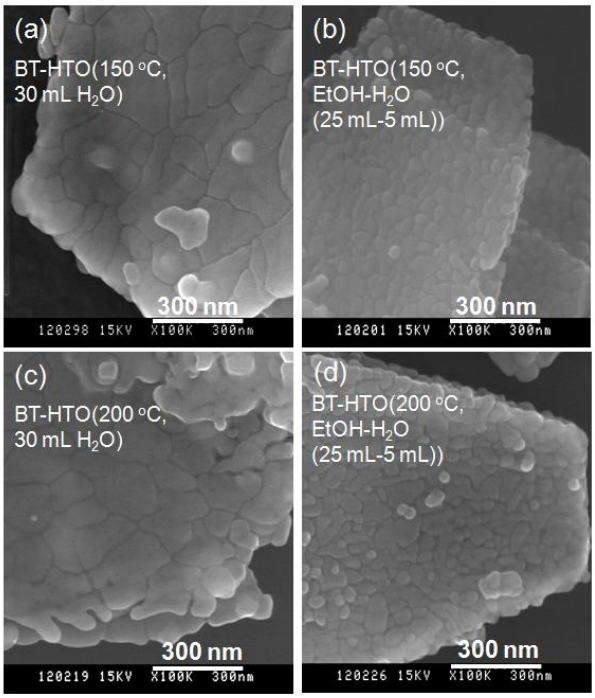

Figure 4.8 FE-SEM images of samples obtained by solvothermal treatments of $Sr(OH)_2$ (Sr of excess 50%) and BT/HTO nanocomposites in water solution at 200 ^{o}C for 12 h. BT/HTO nanocomposites prepared by thermal treatments of HTO and $Ba(OH)_2$ mixtures in (a, c) water solution and (b, d) water-ethanol mixed solvent (volume ratio = 5:25) at (a, b)150 ^{o}C and (c, d) 200 ^{o}C for 12 h, respectively.

Figure 4.9 present corresponding TEM images and SAED patterns. The platelike polycrystals are constructed from the nanocrystals with uniform nanoparticle distribution, and the sizes of the nanocrystal are consistent with the FESEM results (Figure 4.8). When the solvothermal treatments of the Sr $(OH)_2$ and the samples of BH-200-30/0 and BH-200-5/25 at 200 ^{o}C were carried out, some domain areas can be observed in the platelike polycrystals (Figure 4.9e, g). All the SAED patterns show the single-crystal-like SAED spots which can be well assigned to the $Ba_{0.5}Sr_{0.5}TiO_3$ phase with [110] zone axis located on the basal plane, suggesting that all the obtained platelike polycrystals are mesocrystals. Based on the results described above, the platelike $Ba_{0.5}Sr_{0.5}TiO_3$ mesocrystals can be prepared by the two-step solvothermal

reaction process.

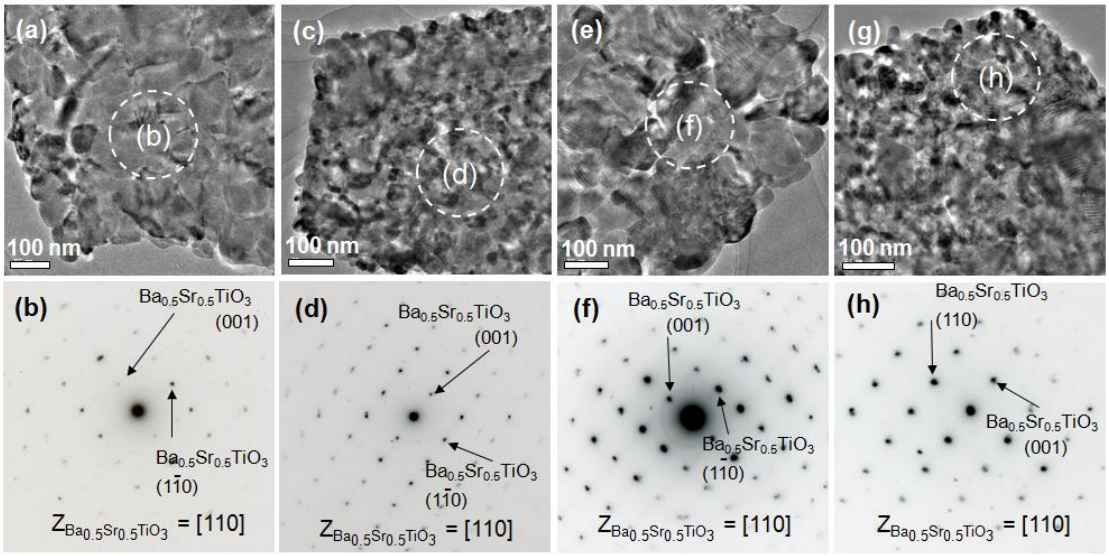

Figure 4.9 (a, c, e, g) TEM images and (b, d, f, h) SAED patterns of samples obtained by solvothermal treatments of $Sr(OH)_2$ (Sr of excess 50%) and BT/HTO nanocomposites in water solution at 200 ^oC for 12 h. BT/HTO nanocomposites prepared by thermal treatments of HTO and $Ba(OH)_2$ mixtures in (a, e) water solution and (c, g) water-ethanol mixed solvent (volume ratio = 5:25) at (a–d)150 ^oC and (e–h) 200^oC for 12 h, respectively.

4.3.3 Influence of different nanostructures of BT/HTO nanocomposites on nanostructure of $Ba_{0.5}Sr_{0.5}TiO_3$ mesocrystals

The results described above indicate that the nanoparticles in the $Ba_{0.5}Sr_{0.5}TiO_3$ mesocrystals are larger when BH-150-30/0 and BH-200-30/0 nanocomposite samples were used as precursor than which used BH-150-5/25 and BH-200-5/25 nanocomposite samples as precursor. This result implies that BH-150-5/25 and BH-200-5/25 samples prepared in water-ethanol mixed solvent exhibit lower reactivity in the formation reaction of $Ba_{0.5}Sr_{0.5}TiO_3$ than BH-150-30/0 and BH-200-30/0 samples prepared in water solvent. The difference is due to different nanostructures of BT/HTO nanocomposites prepared in different solvents. In the BT/HTO nanocomposites prepared in water-ethanol mixed solvent, the BT nanoparticles

mainly distribute around the surface of the platelike particles. To react with HTO in the bulk platelike particle, Sr^{2+} ions have to pass through BT layer on the surface platelike particle, or firstly react with BT on the surface. But migration of Sr^{2+} ions into the platelike particle is no easy because most of HTO on the surface has been transformed to BT. Furthermore the reactivity of BT is lower than HTO in the formation $SrTiO_3$ (ST). On the other hand, in the BT/HTO nanocomposites prepared in water solvent, the BT nanoparticles distribute uniformly in the platelike particles. Sr^{2+} ions can migrate easily into the bulk platelike particle through the interlayer of unreacted HTO, and react with HTO at the whole place in the platelike particle to form ST nanoparticles. And then BT and ST nanoparticles react to form $Ba_{0.5}Sr_{0.5}TiO_3$ mesocrystals.

Although the $Ba_{0.5}Sr_{0.5}TiO_3$ mesocrystals with the different nanostructures can be obtained, the dominative solvothermal reactions are *in situ* topochemical conversion reaction, giving rise to maintaining the platelike morphology. The corresponding relations of the crystal orientations of the obtained $Ba_{0.5}Sr_{0.5}TiO_3$ mesocrystals are same. These results suggest that the platelike $Ba_{0.5}Sr_{0.5}TiO_3$ mesocrystals with different nanostructures can be obtained and controlled via adjusting nanostructure of BT/HTO nanocomposite precursors by the solvothermal reactions.

4.3.4 Solvothermal reaction of BT/HTO nanocomposite with $Sr(OH)_2$ in water-ethanol mixed solvent

For the preparation of the BT/ST nanocomposite, water-ethanol mixed solvents instead of the water solvent were used for the solvothermal reactions of the BT/HTO nanocomposites and $Sr(OH)_2$. Figure 4.10 shows the XRD patterns of samples obtained by solvothermal treatments of the four kinds of BT/HTO nanocomposites and $Sr(OH)_2$ in water-ethanol mixed solvent (volume ratio = 10:20) at 200 ^oC for 12 h.

In these solvothermal reactions, the employed platelike BT/HTO nanocomposites as precursors are the samples of BH-150-30/0, BH-150-5/25, BH-200-30/0, and BH-200-5/25, respectively. It is very interesting when the BH-200-30/0 sample was employed as precursor, two sets of XRD patterns with a typical perovskite oxide structure can be simultaneously observed in Figure 4.10c. One of XRD pattern corresponding to larger lattice constant can be readily indexed to the BT phase (JCPDS File No. 39-1395, cubic symmetry) and other one to ST phase (JCPDS File No. 74-1296, cubic symmetry), respectively. This observation reveals that a mixture of BT and ST phases was formed. But for the other products, in addition to the slight unreacted HTO phase, only the $Ba_{0.5}Sr_{0.5}TiO_3$ solid solution phase can be well identified by JCPDS File No. 39-1395 (cubic symmetry) when the samples of BH-150-30/0, BH-150-5/25, and BH-200-5/25 acted as precursors. These results suggest that the sample of BH-200-30/0 is a probably suitable precursor for the preparation of the BT/ST nanocomposite.

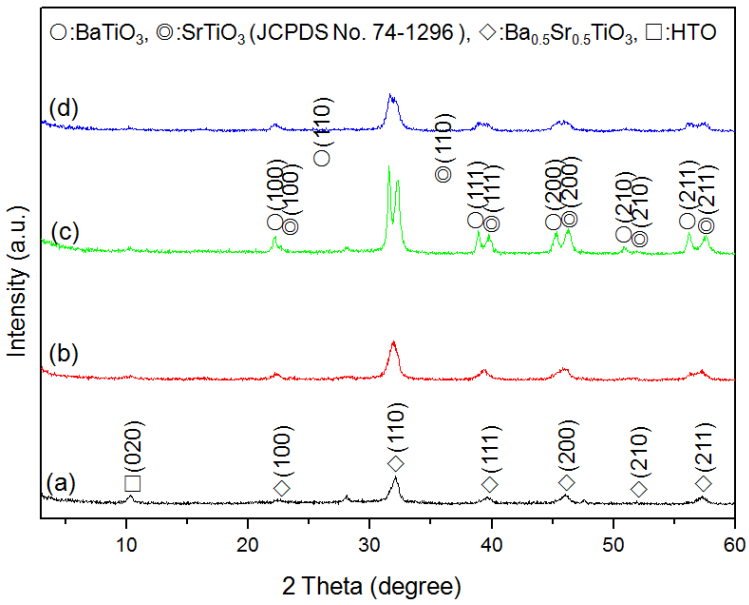

Figure 4.10 XRD patterns of samples obtained by solvothermal treatments of $Sr(OH)_2$ (Sr of excess 50%) and BT/HTO nanocomposites in water-ethanol mixed solvent (volume ratio = 10:20) at 200 ^{o}C for 12 h. BT/HTO nanocomposites prepared by solvothermal treatments of HTO and

$Ba(OH)_2$ mixtures in (a, c) water solution and (b, d) water-ethanol mixed solvent (volume ratio = 10:20) at (a, b)150 ^oC and (c, d) 200 ^oC for 12 h, respectively.

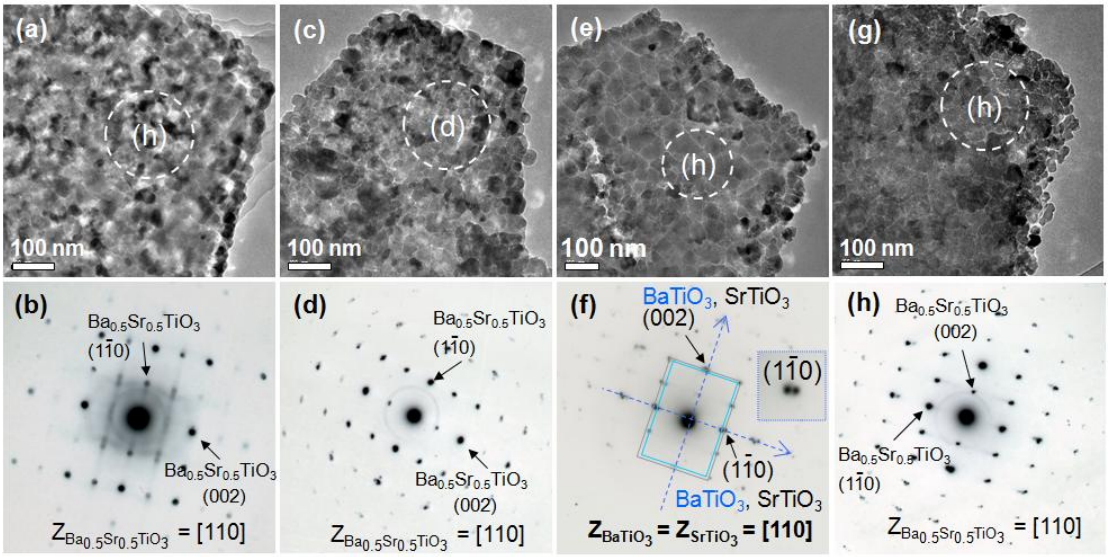

Figure 4.11 (a, c, e, g) TEM images and (b, d, f, h) SAED patterns of samples obtained by solvothermal treatments of $Sr(OH)_2$ (Sr of excess 50%) and BT/HTO nanocomposites in water-ethanol mixed solvent (volume ratio = 10:20) at 200 ^oC for 12 h. BT/HTO nanocomposites prepared by thermal treatments of HTO and $Ba(OH)_2$ mixtures in (a, b, e, f) water solution and (c, d, g, h) water-ethanol mixed solvent (volume ratio = 10:20) at (a, b, c, d)150 ^oC and (e, f, g, h) 200 ^oC for 12 h, respectively.

Figure 4.11 shows the TEM images and SAED patterns of the samples obtained by the solvothermal treatments of the BT/HTO nanocomposites and $Sr(OH)_2$ in water-ethanol mixed solvent (volume ratio = 10:20) at 200 ^oC for 12 h. All the obtained samples present the platelike morphology and polycrystal structure constructed from nanocrystals. The constituent nanocrystals in the platelike polycrystals obtained from the precursors of BH-150-30/0 and BH-200-30/0 have larger average sizes of about 60 nm and 80 nm, respectively, than which of about 50 nm obtained from the precursors of BH-150-5/25 and BH-200-5/25 samples. When the sample of BH-200-30/0 was employed as precursor, it is very interesting that two sets of perovskite SAED spot patterns corresponding single-crystal-like BT and ST phases are

simultaneously observed in one platelike polycrystal (Figure 4.11f), revealing that BT and ST phases coexist in one platelike polycrystal and agreeing with the XRD result (Figure 4.10c). This result suggests that the mixture of BT and ST phase is BT/ST nanocomposite, and the platelike polycrystal is mesocrystal. These results reveal that the platelike BT/ST mesocrystalline nanocomposite can be obtained by the solvothermal treatment of $Sr(OH)_2$ and the samples of BH-200-30/0 as a suitable precursor in water-ethanol mixed solvent. It is worth pointing out that the crystal orientation of [110] zone axis of ST phase is entirely consistent with BT phase. The result suggests that Sr^{2+} ions react with HTO in the HTO/BT nanocomposite and the reaction transforms topotactically HTO to ST nanoparticles.

The other SAED patterns show the single-crystal-like SAED spots which can be assigned to the $Ba_{0.5}Sr_{0.5}TiO_3$ phase with [110] zone axis located on the basal plane (Figure 4.11b, d, h), which agree with XRD patterns (Figure 4.10a, b, d), respectively. In the case of BH-150-30/0 precursor, firstly Sr^{2+} ions react with HTO in the HTO/BT nanocomposite and the reaction transforms topotactically HTO to ST nanoparticles, and then the $Ba_{0.5}Sr_{0.5}TiO_3$ phase is formed by reaction of ST nanoparticles and BT nanoparticles because BT nanoparticles is very small which exhibit high reactivity with ST nanoparticles. Namely prevention of the reaction between BT nanoparticles and formed ST nanoparticles is a key point to obtain BT/ST nanocomposite. In the cases of BH-150-5/25 and BH-200-5/25 precursors, although the particle size of BT is enough large, BT particles locate nearly at HTO/BT platelike particle surface. To react with HTO in the bulk platelike particles, firstly Sr^{2+} ions have to react with BT nanoparticles on the surface, and then react with HTO in the bulk particle, which causes easily the $Ba_{0.5}Sr_{0.5}TiO_3$ phase but not BT/ST nanocomposite. Therefore, uniform distribution of BT nanoparticles in the HTO/BT precursor is another key point to obtain BT/ST nanocomposite.

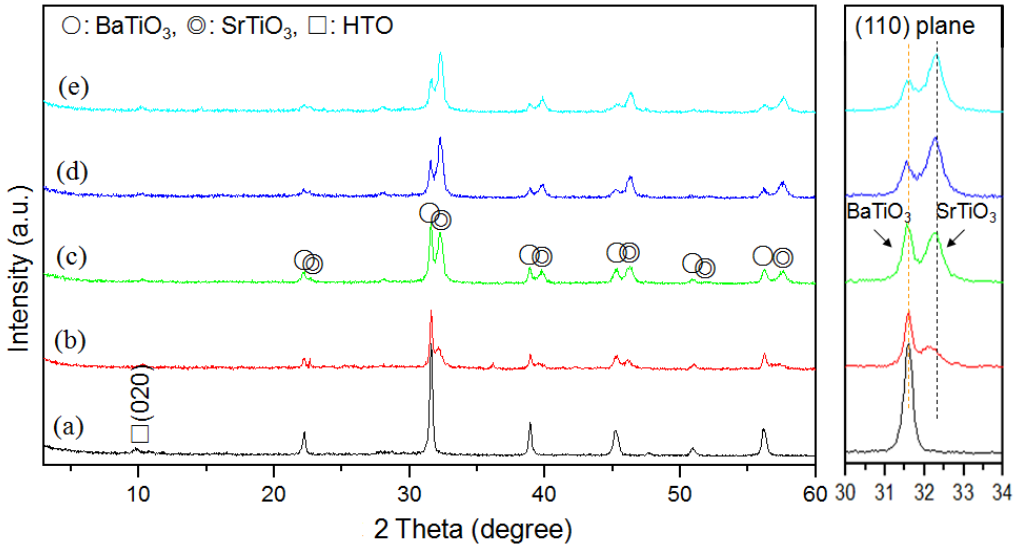

Figure 4.12 XRD patterns of samples obtained by solvothermal treatments of $Sr(OH)_2$ and BT/HTO nanocomposites in water-ethanol mixed solvents with volume ratios of (a) 0:30, (b) 5:25, (c) 10:20, (d)15:15, (e) 20:10 at 200 ^{o}C for 12 h, respectively. BT/HTO nanocomposites prepared by solvothermal treatments of HTO and $Ba(OH)_2$ mixtures in 30 mL water solution at 200 ^{o}C for 12 h. Right XRD patterns correspond to the peaks in the two theta of 30–34^{o}.

To investigate the influence of solvent polarity on the formation of BT/ST nanocomposite, BH-200-30/0 precursor is solvothermally treated with Sr(OH)2 in water-ethanol mixed solvents with different water/ethanol ratios. Figure 4.12 presents the XRD patterns of the samples obtained by the solvothermal reactions at 200 ^{o}C for 12 h. Only the peaks of BT phase but without peaks of ST phase were observed in the sample prepared in the pure ethanol solvent (Figure 4.12a), owing to the low reactivity in the ethanol solvent. The peaks intensities of ST phase increase with increasing water content in the solvent, owing to increase of the reactivity. The enhancement of the reactivity is due to enhancing the polarity of the solvent that increases the solubilities of $Sr(OH)_2$ and Ti species. The peak intensity of ST phase become almost same as that of BT phase, and then the peak intensity of BT phase decreased with increasing water content in the solvent, and finally disappeared in the

pure water solvent (Figure 4.7c). These results imply that in the high water content solvent, the formed ST nanoparticles can react with BT nanoparticles causing formation of $Ba_{0.5-x}Sr_{0.5+x}TiO_3$ solid solution phase in the solvothermal reaction in the high reactivity solvent. Namely, the BT/ST nanocomposite will disappears under high reactivity conditions.

4.3.5 Nanostructural and compositional studies on BT/ST nanocomposite

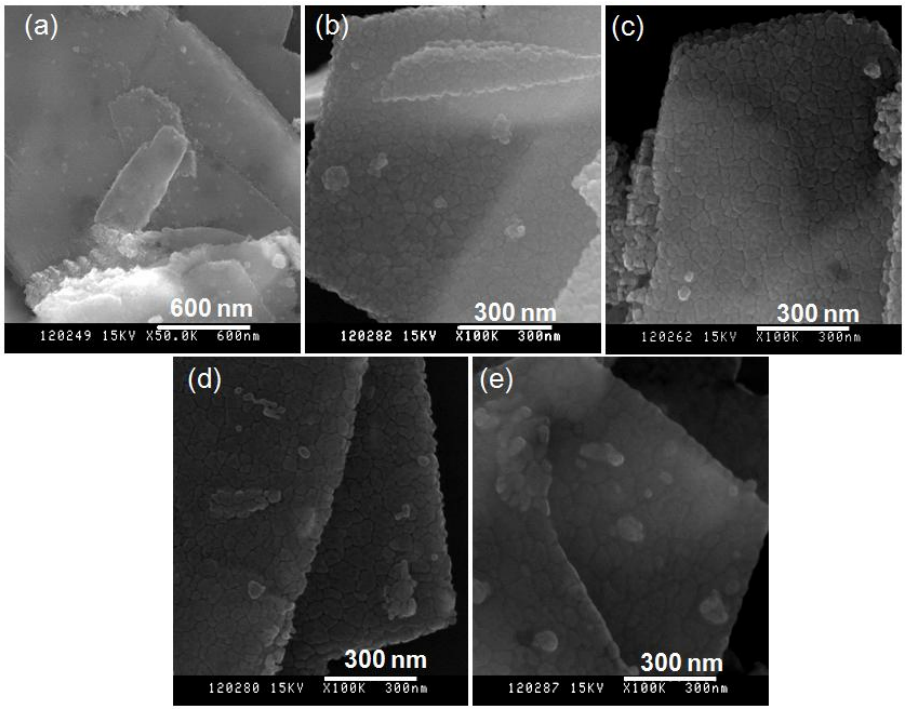

Figure 4.13 FE-SEM of samples obtained by solvothermal treatments of $Sr(OH)_2$ and BT/HTO nanocomposite in water-ethanol mixed solvents with volume ratios of (a) 0:30, (b) 5:25, (c) 10:20, (d)15:15, (e) 20:10 at 200 ^oC for 12 h, respectively. BT/HTO nanocomposites prepared by solvothermal treatments of HTO and $Ba(OH)_2$ mixtures in 30 mL water at 200 ^oC for 12 h.

The investigations of the nanostructure and composition of the BT/ST nanocomposites were performed. Figure 4.13 presents the FE-SEM of the samples obtained by solvothermal treatments of the BH-200-30/0 precursor and $Sr(OH)_2$ in water-ethanol mixed solvents with different water contents at 200 ^oC for 12 h. All the obtained products show the typical platelike polycrystalline morphology, and are

constructed from nanocrystals with an average size of about 50 nm. Figure 4.14 shows the corresponding TEM images, SAED patterns, and EDS spectra. The TEM images agree with the FE-SEM images. Two sets of single-crystal-like SAED spot patterns for each sample can be assigned to the BT and ST phases, revealing all the polycrystals are BT/ST mesocrystalline nanocomposites also. The above results reveal that the platelike BT/ST mesocrystalline nanocomposites can be obtained by the solvothermal treatment of $Sr(OH)_2$ and the BH-200-30/0 precursor in water-ethanol mixed solvents with water/ethanol volume ratios in a range of 5:25 to 20:10.

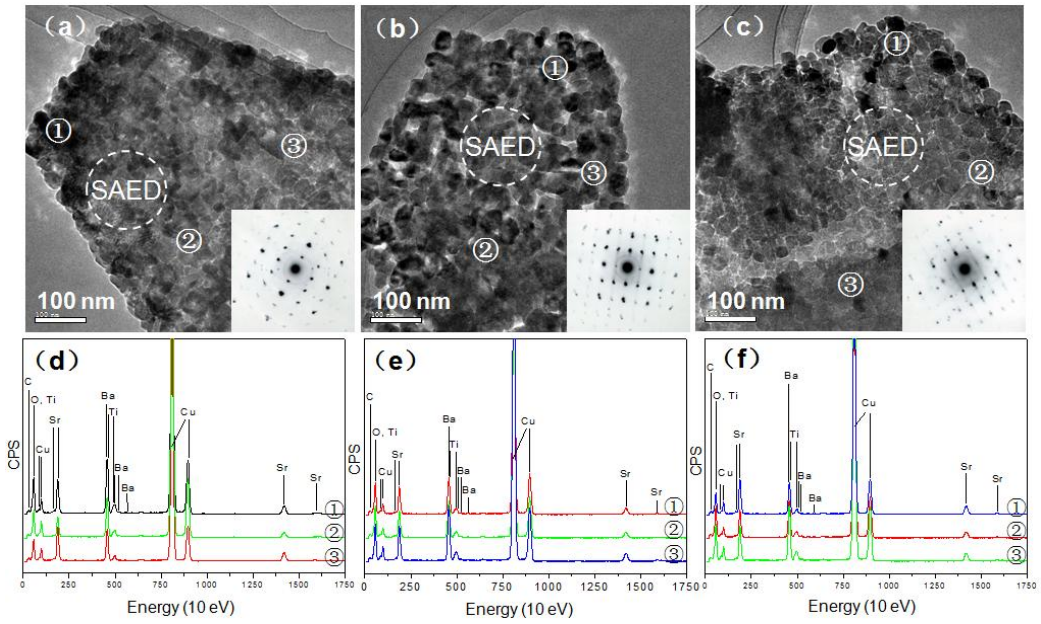

Figure 4.14 (a, b, c) TEM images of samples obtained by solvothermal treatments of BT/HTO nanocomposites and $Sr(OH)_2$ in water-ethanol mixed solvents with volume ratios of (a) 5:25, (b) 10:20 and (c) 15:15 at 200 ^{o}C for 12 h, respectively. (d, e, f) EDS spectra of samples correspond to the (a, b, c) samples, respectively. EDS spectra of the regions labeled "①", "②", and "③ " correspond to the positions marked ①, ②, and ③ in TEM images, respectively. The inset of SAED patterns are from the corresponding platelike polycrystals, respectively, and the electron beam is perpendicular to the basic plane of the platelike polycrystals.

The chemical composition distributions in these platelike crystals are investigated

using EDS analysis. Three positions in each platelike polycrystal present almost the same EDS spectra (Figure 4.14a, b, c), suggesting uniform chemical composition distribution of Ba and Sr in the electron beam size of about 200 nm in the each platelike BT/ST mesocrystalline nanocomposite. The molar ratios of Ti:Ba:Sr from EDS analysis results in BT/ST nanocomposites are listed in Table 4.1. The average molar ratio results indicate that the Sr content increases, while Ba content decreases with the increase of the water content in the reaction solvent. This result reveals that the reactivity of HTO/BT nanocomposite with $Sr(OH)_2$ enhances with increasing the polarity of the reaction solvent, which is also well consistent with the peak intensity change of XRD (Figure 4.12b, c, d). The result also implies that the Ba^{2+} ions are partially replaced by the Sr^{2+} ions in the formation process of the BT/ST mesocrystalline nanocomposite. It is noteworthy that the Ba/Sr molar ratio is close to one when the water/ethanol volume ratio is 10:20, namely the equal amounts of BT and ST in the BT/ST nanocomposite composition are formed under this reaction condition. These results suggest that the BT/ST ratio can be adjusted by controlling the water content in the reaction solvent.

Table 4.1 Atom quantity ratio of Ti:Ba:Sr from EDS spectra of regions in BT/ST nanocomposite composition.

	(a) (Water-ethanol, 5:25)			(b) (Water-ethanol,10:20)			(c) (Water-ethanol,15:15)		
	Ti	Ba	Sr	Ti	Ba	Sr	Ti	Ba	Sr
①	1.00	0.52	0.44	1.00	0.55	0.47	1.00	0.42	0.61
②	1.00	0.49	0.33	1.00	0.44	0.55	1.00	0.38	0.63
③	1.00	0.52	0.40	1.00	0.48	0.48	1.00	0.42	0.82
Average ratio	1.00	0.51	0.39	1.00	0.48	0.51	1.00	0.40	0.67

Figure 4.15 shows the EDS-mapping TEM images of the platelike BT/ST mesocrystalline nanocomposite obtained by solvothermal treatment of the BT/HTO

nanocomposite and $Sr(OH)_2$ in water-ethanol mixed solvent with volume ratio of 10:20 at 200 ^oC for 12 h. The uniform distributions of Ba and Sr on one platelike polycrystal can be clearly observed, suggesting that homogeneous chemical composition distributions of Ba and Sr in the platelike mesocrystalline nanocomposite. The BT and ST nanocrystals were not detected individually EDS-mapping TEM images, which may be due to the stacking structure of the BT and ST nanocrystals or BT-ST core-shell nanoparticle structure in the platelike BT/ST mesocrystalline nanocomposite.

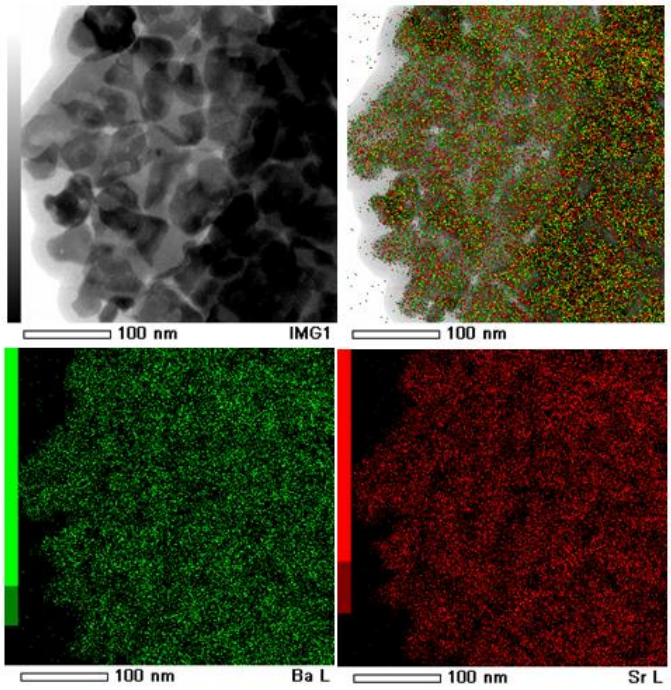

Figure 4.15 EDS-mapping TEM images of platelike BT/ST mesocrystalline nanocomposite. The mesocrystal was obtained by solvothermal treatment of BT/HTO nanocomposites and $Sr(OH)_2$ in water-ethanol mixed solvent with volume ratio of 10:20 at 200 ^oC for 12 h.

For the detailed investigation of the distribution of the BT and ST nanocrystals inside the block of platelike BT/ST mesocrystalline nanocomposite, the TEM and HRTEM observations were carried out on the BT/ST mesocrystalline nanocomposite after grind and ultrasound dispersion treatment (Figure 4.16). The TEM image

presents some individual and agglomerated nanocrystals (Figure 4.16a), suggesting that some of the platelike mesocrystal broken after grind and ultrasound dispersion treatment. All the HRTEM images dominantly reveal the lattice fringes of 0.272–0.285 nm which can be indexed to the (110) planes of BT and ST phases. This result is a consistent with the strongest diffraction lines of (110) planes in XRD patterns (Figure 4.10c). The directions of the (110) planes in the agglomerated nanocrystals are uniform (Figure 4.16b, c), while the individual dispersed nanocrystals are different (Figure 4.16e, f). FFT pattern form HRTEM image of an individual nanoparticle shows one set of clear reciprocal lattice spots which can be attributed to the single ST phase (Figure 4.16g, h). These results suggest that the platelike BT/ST mesocrystalline nanocomposite is constructed by stacking individual BT and ST nanocrystals instead of the BT-ST core–shell nanoparticles.

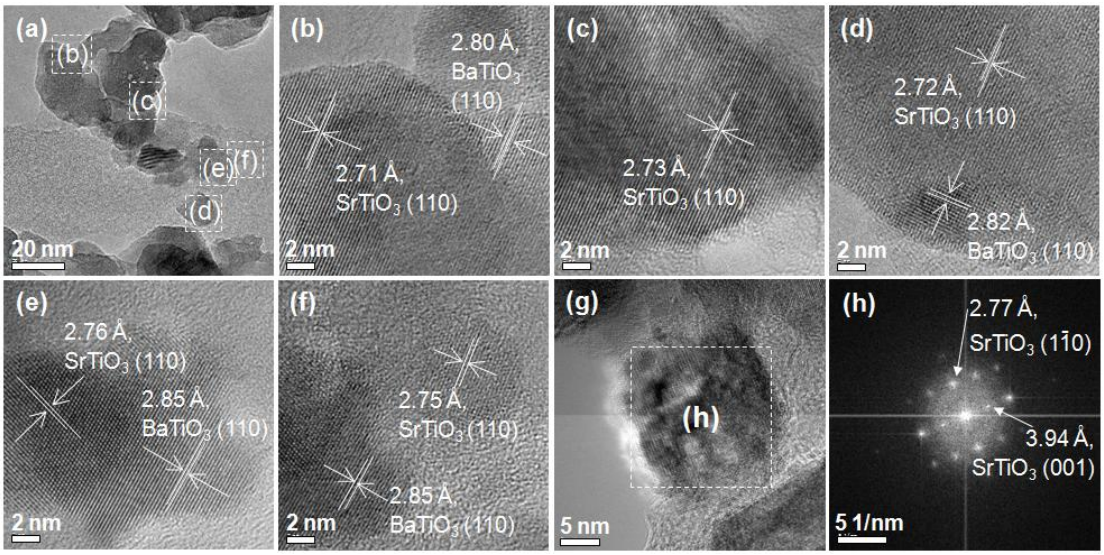

Figure 4.16 (a) TEM image of platelike BT/ST mesocrystalline nanocomposite after grind and ultrasound dispersion treatment. (b, c, d, e, f) HRTEM images are from the (b, c, d, e, f) white panes in (a) TEM image, respectively. (g) HRTEM image and (h) FFT pattern from the (h) white pane in (g) HRTEM image of another partial platelike BT/ST mesocrystalline nanocomposite after and ultrasound dispersion treatment.

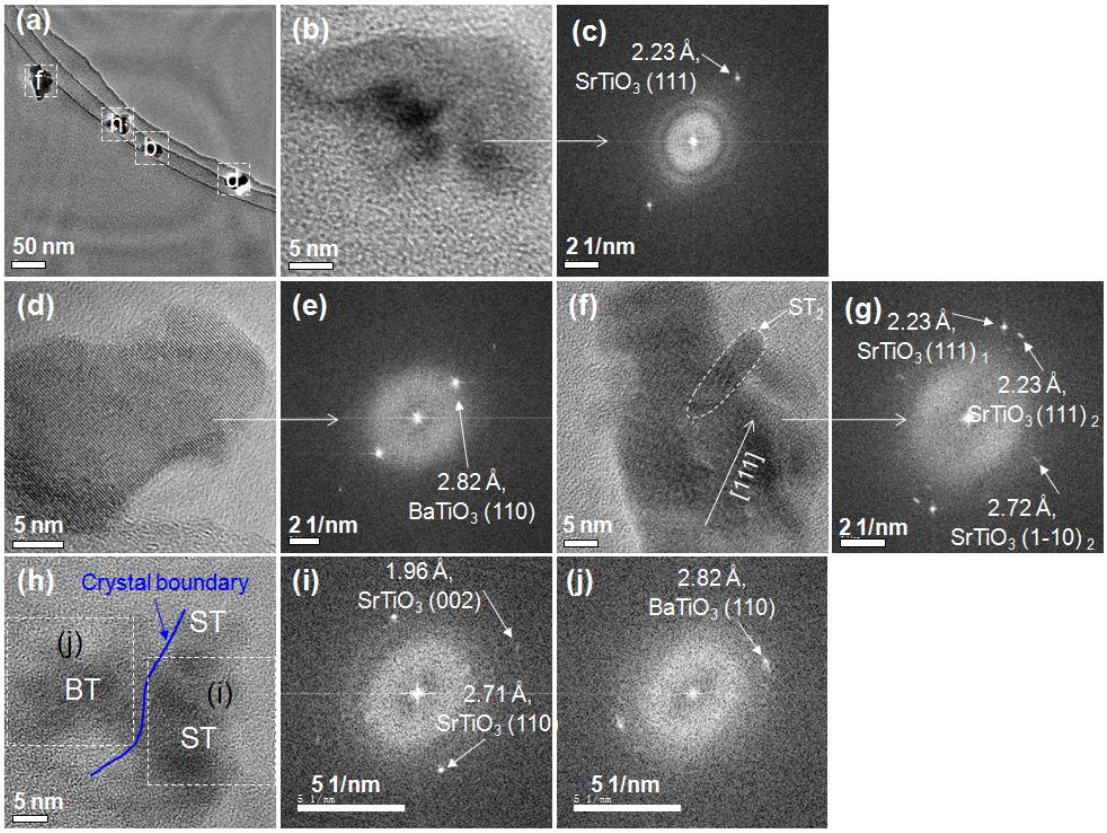

Figure 4.17 (a) TEM and (b, d, f, h) HRTEM images of platelike BT/ST mesocrystalline nanocomposite after grind and ultrasound dispersion treatment. (b, d, f, h) HRTEM images are from the (b, d, f, h) white panes in (a) TEM image, respectively. (c, e, g, i and j) FFT patterns are from (b, d, f, h) HRTEM images, respectively.

To qualitatively analyze individual BT and ST nanocrystals derived from the platelike BT/ST mesocrystalline nanocomposite further, some representative individual BT and ST nanocrystals obtained by the grind and ultrasound dispersion treatment of the platelike BT/ST mesocrystalline nanocomposite were investigated also. Figure 4.17 shows TEM image, HRTEM images and FFT patterns of the individual BT and ST nanoparticles. All the nanoparticles with ～50 nm size present some lattice fringes on the surface, and their corresponding selected area FFT patterns with some reciprocal lattice spots which can be indexed to the BT (Figure 4.17d and e, h and j) and ST (Figure 4.17b and c, f and g, h and i) phases. Although both the BT

and ST phases coexist in the nanoparticles (see Figure 4.17h, i, j), the existing crystal boundary implies that this nanoparticle constructed from smaller individual nanoparticles is a nanocomposite. Figure 4.18 presents the corresponding EDS spectra investigated in the areas with the size of about 50 nm from the (b, d, f, h) white panes of (a) TEM image in Figure 4.17, respectively. The results suggest the uniform chemical composition distribution of Ba or/and Sr in the each nanoparticle, which agree the corresponding results of HRTEM images and FFT patterns. These results further reveal that the platelike BT/ST mesocrystalline nanocomposite is constructed by stacking individual BT and ST nanocrystals.

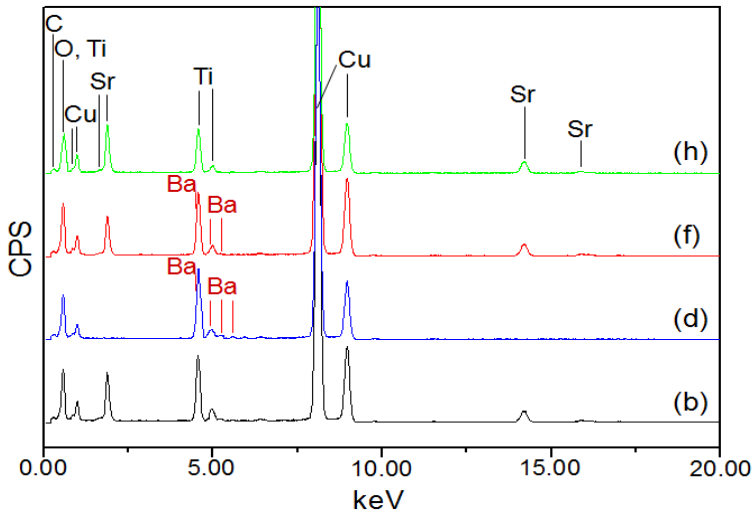

Figure 4.18 EDS spectra of samples derived from (b, d, f, h) white panes of (a) TEM image in Figure 4.17, respectively. The electron beam size is approximately 50 nm.

4.3.6 Topochemical conversion mechanisms of platelike mesocrystalline $Ba_{0.5}Sr_{0.5}TiO_3$ and BT/ST nanocomposites

The mesocrystalline conversion process from the HTO single crystal precursor to mesocrystalline BT/ST nanocomposite and their topological correspondences can be described as a schematic diagram in Figure 4.19a. The mesocrystalline BT/ST nanocomposite is formed by the two-step topochemical process. In the first step, Ba^{2+}

ions are intercalated into the HTO bulk crystal through the its interlayer pathway by a H^+/Ba^{2+} exchange reaction, and then the Ba^{2+} ions react with the TiO_6 octahedral layers of HTO in the crystal bulk to form the BT phase.[47] In the solvothermal topochemical reaction, half of the HTO crystal is transformed to the BT nanocrystals because the Ti/Ba mole ratio in the reaction system is 1/0.5. The dissolution-deposition reaction is also possible on the platelike particle surface. In the present case, the topochemical conversion reaction is dominative, owing to the low concentration of $Ba(OH)_2$. The HTO/BT nanocomposite platelike particles formed by this reaction have uniform distribution of BT nanoparticle and the BT particle size increases with increasing the reaction temperature, when the reaction is carried in water solvent. However, when the reaction is carried in water-ethanol solvent, the formation reaction of BT nanoparticles is preferentially occurs near the surface of the platelike particle owing to the low polarity of the solvent and low solubility of $Ba(OH)_2$, in which Ba^{2+} ions are difficult to migrate in the HTO bulk crystal. There is a definitely corresponding relationship between the crystal-axis directions of HTO and BT structures (Figures 4.4b and h, 4.5b, 4.6b and h), namely all the BT nanocrystals in one platelike crystal of the BT/HTO nanocomposite present the same crystal-axis orientation in the [110]-direction agreeing with the [010]-direction of the HTO matrix crystal.

In the second step reaction of solvothermal treatment of the BT/HTO nanocomposite in the $Sr(OH)_2$ solution is also a topochemical conversion reaction similar to the first step. When the HTO/BT nanocomposite with uniform distribution of BT nanoparticles is used as precursor, incipiently, the Sr^{2+} ions are intercalated into the residual HTO bulk crystal through the interlayer pathway by the H^+/Sr^{2+} exchange reaction, and then the Sr^{2+} ions react with the unreacted HTO matrix crystal to form the ST nanoparticles until consuming all the HTO phase. The BT/ST mesocrystalline

nanocomposite is formed at this stage. However, BT and ST nanoparticles can react together further by the topochemical reaction, and then the platelike mesocrystal of $Ba_{0.5}Sr_{0.5}TiO_3$ solid solution is formed under the high reactive conditions, such as in water solvent at 200°C. When the HTO/BT nanocomposite prepared in the water-ethanol mixed solvent is used as the precursor, the situation is different owing to the platelike particle surface of the HTO/BT precursor is covered by BT. In this case, firstly Sr^{2+} ions react with BT nanoparticles locating on the platelike particle surface before migrating into the bulk crystal, which causes formation of $Ba_{0.5}Sr_{0.5}TiO_3$ solid solution nanoparticles from the platelike particle surface. Therefore, the BT/ST mesocrystalline nanocomposite is difficult to be obtained by using such precursor.

In the second step reaction, the dissolution-deposition reaction is also possible on the platelike particle surface, but the topochemical conversion reaction is dominative, which results the formation of the platelike mesocrystals of BT/ST nanocomposite and $Ba_{0.5}Sr_{0.5}TiO_3$ solid solution. Therefore, there are the corresponding relations between the crystal orientations of the HTO precursor and the generated mesocrystals. The directions of [100], [001], and [010] directions of HTO single crystals correspond to the [001], [1-10], and [110] directions of BT, ST, and $Ba_{0.5}Sr_{0.5}TiO_3$ nanocrystals, respectively. Therefore, in the BT/ST mesocrystalline nanocomposite, there is epitaxial interface (grain boundary) between BT and ST nanoparticles. Since the lattice dimensions between BT and ST are slightly different, the lattice mismatch can result lattice distortions in BT and ST structures on the interface, such nanocrystal is promising for the high performance piezoelectric materials and dielectric materials.

Figure 4.19b illustrates the variation from layered lepidocrocite(γ–FeOOH)-type structure of HTO single crystal to the perovskite structure of BT/ST mesocrystalline nanocomposite via an *in situ* topochemical mesocrystalline conversion reaction. In the HTO layered structure, the TiO_6 octahedra are combined with each other via angle

and edge-sharing to form a two-dimension TiO_6 octahedral sheet. In the conversion reaction to the BT structure, the TiO_6 octahedra in the layered structure are partially shifted to the positions of the perovskite structure with edge-sharing TiO_6 octahedra, and this process has to satisfy the principle of minimum energy and space requirements to make the stable perovskite BT structure. In the conversion reaction to the ST structure, similar reaction occurs also. At the BT/ST interface, the formation of $Ba_xSr_{1-x}TiO_3$ solid solution layer is possible. Thus, the obtained product is likely to a perovskite nanocomposite with a BT/$Ba_xSr_{1-x}TiO_3$/ST nanostructure.

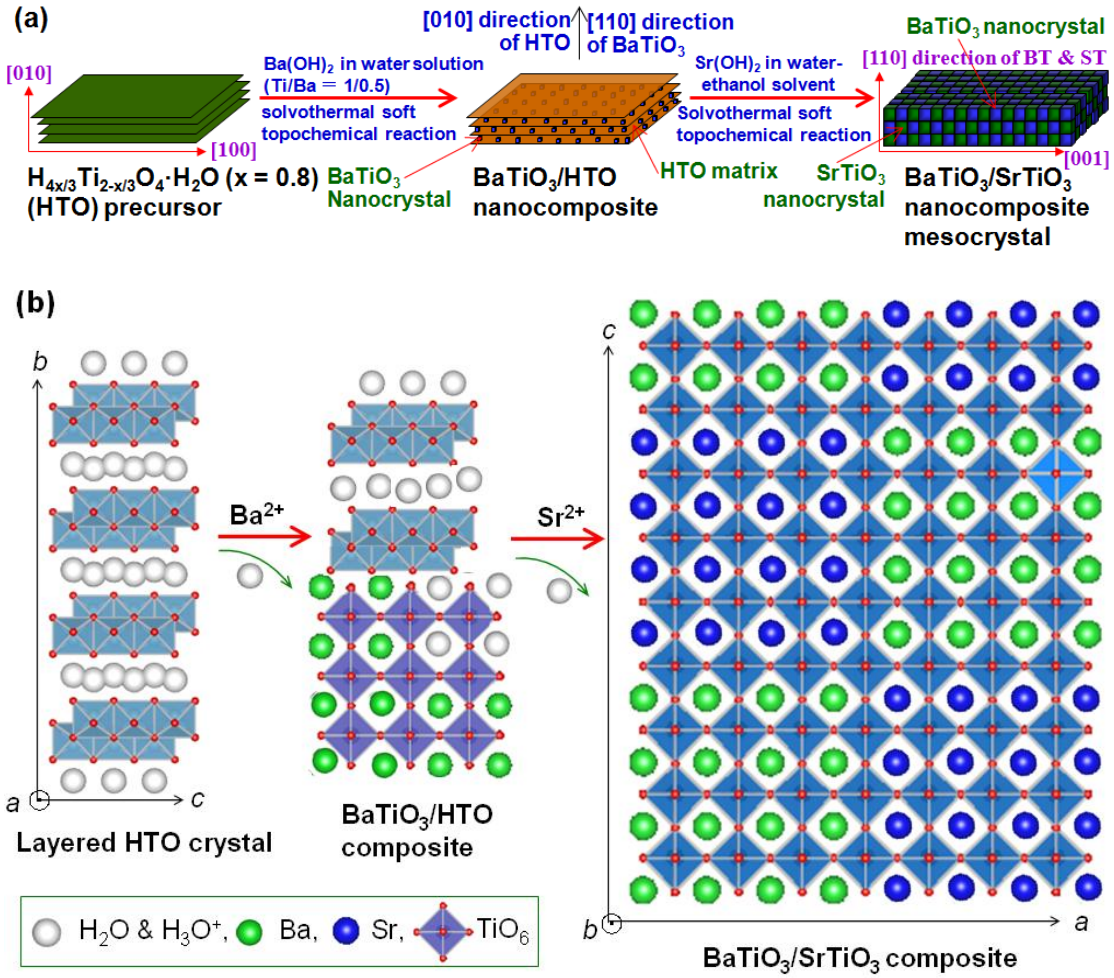

Figure 4.19 (a) Schematic representation of formation mechanism of platelike BT/ST mesocrystalline nanocomposite via two-step topochemical soft solvothermal processes from layered protonated titanate single crystal. (b) Variation of crystal structure from layered lepidocrocite (γ–FeOOH)-type single crystal to possible composite perovskite mesocrystal via an

in situ topochemical mesocrystal conversion reaction with a rotated behavior of TiO_6 octahedra.

On the basis of the mechanism described above, firstly the HTO/BT nanocomposite with uniform distribution and enough large crystal size of BT nanoparticles is necessary. In the second step reaction of conversion HTO/BT to BT/ST nanocomposite, keeping appropriate reactivity in reaction system is important. Under high reactive conditions, the formed BT/ST nanocomposite will be transformed into $Ba_xSr_{1-x}TiO_3$ solid solution. These conditions can be achieved by controlling the polarity of the reaction solvent and reaction temperature.

4.3.7 Anneal treatments of platelike BT/ST mesocrystalline nanocomposites

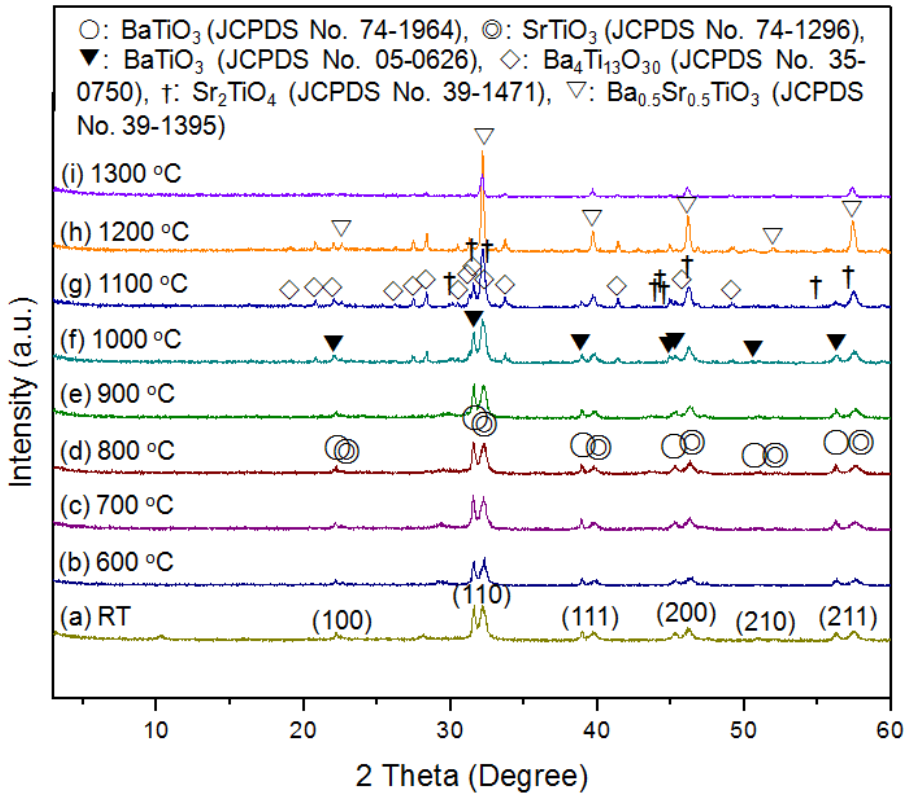

Figure 4.20 XRD patterns of BT/ST mesocrystalline nanocomposites before (a) and after anneal treatments at different temperatures for 3 h. The BT/ST mesocrystalline nanocomposites were prepared by the solvothermal soft process in water-ethanol mixed solvent with volume ratio of 10:20 at 200 ^{o}C for 12 h.

The BT/ST mesocrystalline nanocomposite prepared by the solvothermal treatment of $Sr(OH)_2$ and the BH-200-30/0 precursor in water-ethanol mixed solvent with volume ratio of 10:20 is employed for the anneal investigation. Figure 4.20 shows the XRD patterns of BT/ST mesocrystalline nanocomposites before and after anneal treatments at different temperatures for 3 h. The nanostructure of BT/ST nanocomposite does not change below 900 ^{o}C of the anneal temperature (Figure 4.20b–e). Over 900 ^{o}C, the balance of two equivalent compositions between the BT and ST phases was broken. In anneal temperature range between 1000 and 1200 ^{o}C, the tetragonal BT polymorph phase (JCPDS No. 05-0626) was formed, suggesting that the pseudo-cubic symmetry of the BT phase transformed into the tetragonal symmetry. In addition to the BT and ST phases, the $Ba_4Ti_{13}O_{30}$ (indexed by JCPDS File No. 35-0750: orthorhombic symmetry, cell = 1.406 × 1.707 × 0.987 nm), Sr_2TiO_4 (indexed by JCPDS File No. 39-1471: tetragonal symmetry, cell = 0.3886 × 1.259 nm, I*4mmm*), and $Ba_xSr_{1-x}TiO_3$ solid solution phase can be observed in this temperature range, where x is the dependence on the contents of the $Ba_4Ti_{13}O_{30}$ and Sr_2TiO_4 phases. A main phase of the $Ba_{0.5}Sr_{0.5}TiO_3$ solid solution (indexed by the by the JCPDS File No. 39-1395) was formed when the anneal temperature was elevated to 1300 ^{o}C. These results imply that the BT/ST composite phase can be stable up to a quite high temperature of 900 ^{o}C. A complex quinary system with BT/ST/$Ba_4Ti_{13}O_{30}$/Sr_2TiO_4/$Ba_xSr_{1-x}TiO_3$ composition can be obtained at the anneal temperatures between 1000 to 1200 ^{o}C. Figure 4.21 shows the SEM images of the samples obtained by the anneal treatments of the platelike BT/ST mesocrystalline nanocomposites at different temperatures. The platelike morphology of the nanocomposite can withstand up to 1100 ^{o}C, and started to destroy by the high temperature anneal at 1200 ^{o}C. The quinary system with

BT/ST/$Ba_4Ti_{13}O_{30}$/Sr_2TiO_4/$Ba_xSr_{1-x}TiO_3$ composition can maintain a platelike morphology up to 1100 ^oC. Such composite with a complex chemical composition is promising to be used in the strain engineering due to existing with different crystal symmetries.

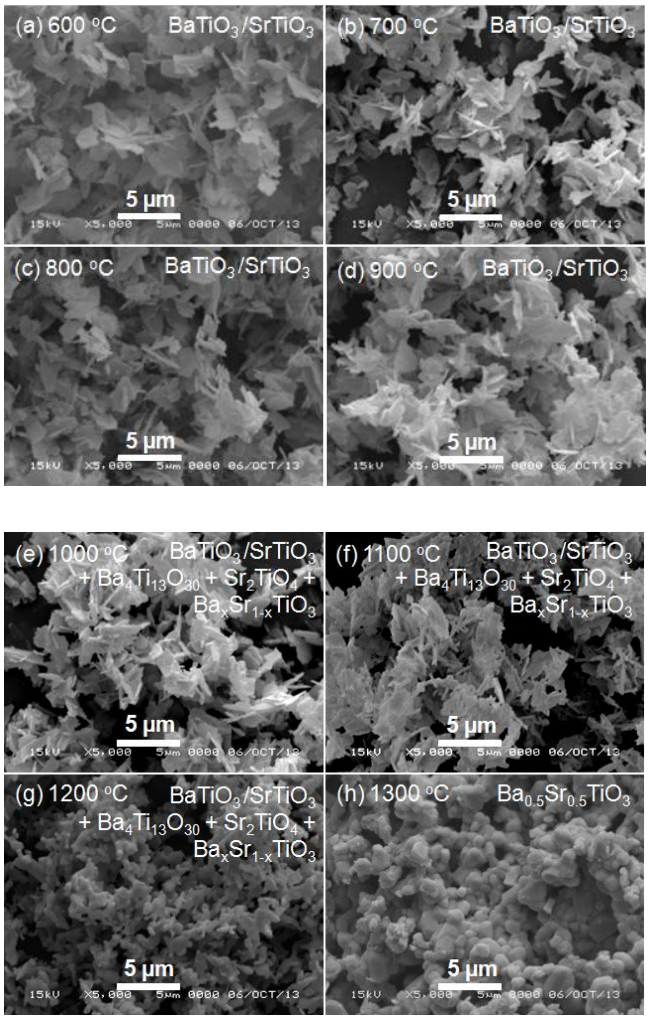

Figure 4.21 SEM images of samples obtained by anneal treatments of platelike BT/ST mesocrystalline nanocomposite s at (a) 600, (b) 700, (c) 800, (d) 900, (e) 1000, (f) 1100, (g) 1200, (h) 1300 ^oC for 3 h, respectively.

Figure 4.22 presents the TEM images and SAED patters of samples obtained by anneal treatments of the platelike BT/ST mesocrystalline nanocomposites at 600 and 900 ^oC for 3 h, respectively. At 600 ^oC of the anneal temperature, the obtained mesocrystal constructed from the nanocrystals shows the platelike morphology

(Figure 4.22a). The nanocrystal size is not obvious change after the anneal treatment (Figures 4.11e, 4.14b). Its SAED pattern still exhibits the structure of mesocrystalline BT/ST nanocomposite (Figure 4.22b), which agrees with the XRD result shown in Figure 4.21b. At the elevated anneal temperature of 900 ^{o}C, a sintered platelike particle was formed, in which the nanoparticle boundary became unclear (Figure 4.22c). Two sets of clear SAED spot patterns can be easily identified and assigned to BT and ST with the same [110] zone axis, respectively (Figure 4.22d). These results suggest that the sintered platelike BT/ST nanocomposite constructed from uniform crystal-axis-oriented BT and ST nano-unites can be obtained after the anneal treatment at 900 ^{o}C.

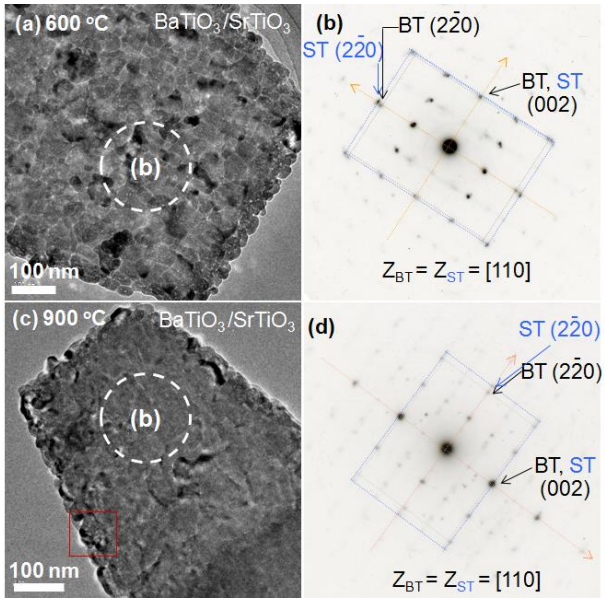

Figure 4.22 (a, c) TEM images and (b, d) SAED patters of samples obtained by anneal treatments of platelike BT/ST mesocrystalline nanocomposite at (a, b) 600 ^{o}C and (c, d) 900 ^{o}C for 3h, respectively.

4.3.8 Nanostructural comparison with conventional two-dimensional BT/ST superlattice

Figure 4.23 illustrates the two-dimensional nanostructures of the BT/ST superlattice

obtained by the conventional MBE approach and the three-dimensional nanostructure of the mesocrystalline BT/ST nanocomposite prepared in this study. The conventional BT/ST superlattice is constructed from the periodically epitaxially grew BT and ST layers, which provides a two-dimensional heterointerface between BT and ST layers. However, in the mesocrystalline BT/ST nanocomposite prepared in this study, the mesocrystalline BT and ST nanocrystals can provide a three-dimensional heterointerface between the crystal-axis-oriented BT and ST nanoparticles. Therefore, the heterointerface density is three times higher than the conventional BT/ST superlattice. Such high dense ferroelectric heterointerface with lattice mismatch is promising for the strain engineering to achieve the sharp enhancement of the piezoelectric and dielectric performances.

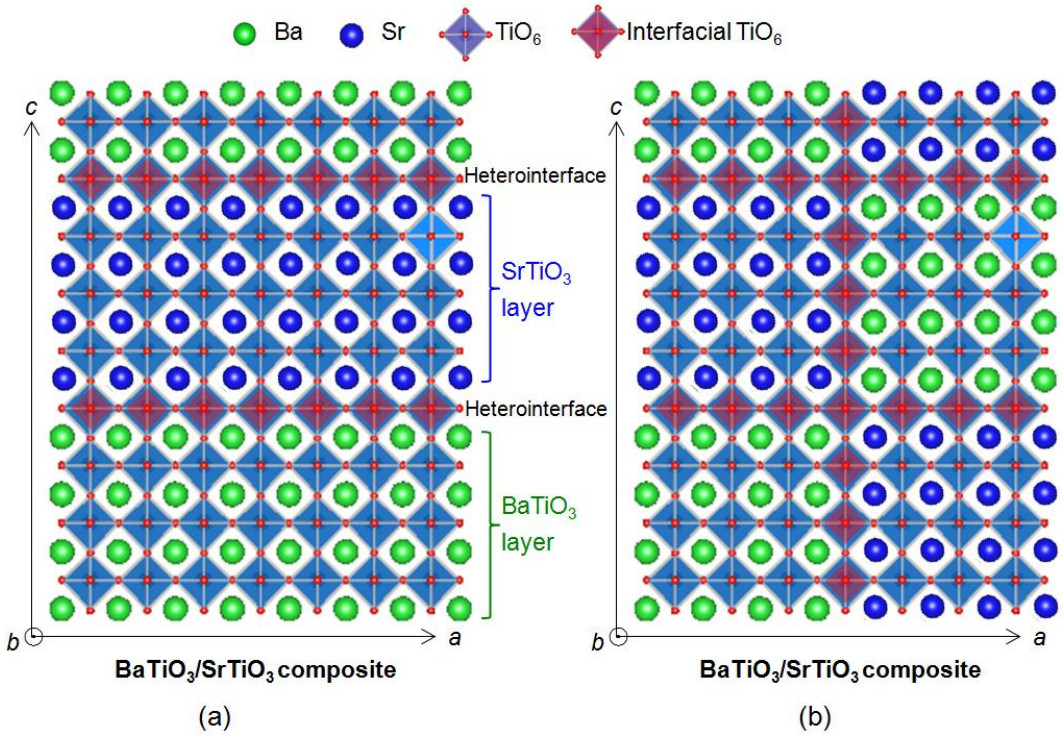

Figure 4.23 (a) Planar illustrations of local environments possible for conventional BT/ST composite with superlattice and abrupt heterointerfaces obtained by MBE approach, and (b) novel platelike BT/ST mesocrystalline nanocomposite with multiplied abrupt heterointerfaces obtained by novel two-step solvothermal soft chemistry process. In (a) illustration, a two-dimensional heterointerface between BT and ST layers can be provided. In (b) illustration, each BT or ST

structure unit has an utmost of six heterointerfaces contacted its six faces containing the above and below, right and left, and front and back, which providing a three-dimensional heterointerface.

4.4 Conclusions

The two-step solvothermal topochemical process is an effective approach for the preparation of the platelike BT/ST mesocrystalline nanocomposite and $Ba_{0.5}Sr_{0.5}TiO_3$ mesocrystal. In the first step reaction, the BT/HTO nanocomposite is formed by the partial transformation of HTO to BT. The nanostructure and BT nanoparticle size in the BT/HTO nanocomposite are dependent on reaction temperature and polarity of reaction solvent. The BT/HTO nanocomposite with uniform BT nanoparticle distribution and enough large BT particle size obtained at 200 ^{o}C in water solvent is an optimal candidate as a precursor for the preparation of the BT/ST nanocomposite. In the second step reaction, the BT/ST mesocrystalline nanocomposite and $Ba_{0.5}Sr_{0.5}TiO_3$ mesocrystal are formed by reacting the BT/HTO nanocomposite with $Sr(OH)_2$. Keeping appropriate reactivity in reaction system is important to obtain the BT/ST mesocrystalline nanocomposite. Under high reactive conditions, the formed BT/ST nanocomposite will be transformed into $Ba_xSr_{1-x}TiO_3$ solid solution. These conditions can be achieved by controlling the polarity of the reaction solvent and reaction temperature. These conditions can be achieved by controlling the polarity of the reaction solvent and reaction temperature. The BT nanocrystals and ST nanocrystals epitaxially connect together in the mesocrystalline BT/ST nanocomposite, which can provide a three-dimensional heterointerface between the crystal-axis-oriented BT and ST nanoparticles. Such high dense ferroelectric heterointerface with lattice mismatch is promising for the strain engineering to achieve the sharp enhancement of the piezoelectric and dielectric performances.

4.5 References

(1) Chandler, C. D.; Roger, C.; Hampden-Smith, M. *J. Chem. Rev.***1993**, 93, 1205–1241.

(2) Pena, M. A.; Fierro, J. L. G. *Chem. Rev.* **2001**, 101, 1981–2017.

(3) Huang, L.; Chen, Z.; Wilson, J. D.; Banerjee, S.; Robinson, R. D.; Herman, I. P.; Laibowitz, R.; O'Brien, S. *J. Appl. Phys.* **2006**, 100, 034316/1–034316/10.

(4) Dutta, P. K.; Asiaie, R.; Akbar, S. A.; Zhu, W. D. *Chem. Mater.* **1994**, 6, 1542–1548.

(5) Nickolay Golego; Studenikin, S. A.; Michael Cocivera *Chem. Mater.* **1998,** *10*, 2000–2005.

(6) Wada, S.; Takeda, K.; Muraishi, T.; Kakemoto, H.; Tsurumi, T.; Kimura, T. *Jpn. J. Appl. Phys.* **2007**, 46, 7039–7043.

(7) Lee, T.; Aksay, I. A. *Cryst. Growth Des.* **2001**, 1, 401–419.

(8) Setter, N.; Waser, R. *Acta Mater.* **2000**, 48, 151–178.

(9) Lee, J.-Y.; Lee, J.-H.; Hong, S.-H.; Lee, Y. K.; Choi, J.-Y. *Adv. Mater.* **2003**, 15, 1655–1658.

(10) Demirörs, A. F.; Imhof, A. *Chem. Mater.* **2009**, 21, 3002–3007.

(11) Niederberger, M.; Garnweitner, G.; Pinna, N.; Antonietti. M. *J. Am. Chem. Soc.* **2004**, 126, 9120–9126.

(12) Suzuki, N.; Zakaria, Mohamed B.; Torad, Nagy L.; Wu, Kevin C.-W.; Nemoto, Y.; Imura, M.; Osada, M.; Yamauchi, Y. *Chem. Eur. J.* **2013**, 19, 4446–4450.

(13) Calderone, V. R.; Testino, A.; Buseaglia, M. T.; Bassoli, M.; Bottino, C.; Viviani, M.; Buseaglia, V.; Nanni, P. *Chem. Mater.* **2006**, 18, 1627–1633.

(14) Kyomen, T; Sakamoto, R.; Sakamoto, N.; Kunugi, S.; Itoh, M. *Chem. Mater.* **2005**, 17, 3200–3204.

(15) Kawasaki, M.; Takahashi, K.; Maeda, T.; Tsuchiya, R.; Shinohara, M.; Ishiyama, O.; Yonezawa, T.; Yoshimoto, M.; Koinuma, H. *Science,***1994**,266, 1540–1542.

(16)Yamada, H.; Ogawa, Y.; Ishii, Y.; Sato, H.; Kawasaki, M.; Akoh, H.; Tokura, Y. *Science*. **2004**, 305, 646–648.

(17) Hiltunen, J.; Lappalainen, J.; Puustinen, J.; Lantto, V.; Tuller, H. L. *Opt. Express,* **2008**, 16,

8219–8228.

(18) Soukiassian, A.; Tian, W.; Vaithyanathan, V.; Haeni, J. H.; Chen, L. Q.; Xi, X. X.; Schlom, D. G.; Tenne, D. A.; Sun, H. P.; Pan, X. Q.; Choi, K. J.; Eom, C. B.; Li, Y. L.; Jia, Q. X.; Constantin, C.; Feenstra, R. M.; Bernhagen, M.; Reiche, P.; Uecker, R. *J. Mater. Res.* 2008, 23, 1417−1432.

(19) Hosokura, T.; Iwaji, N.; Nakagawa, T.; Ando, A.; Takagi, H.; Sakabe, Y.; Hirao, K. *Cryst. Growth Des.* **2011**, 11, 4253–4256

(20) Levanyuk, A. P.; Misirlioglu, I. B. *Appl. Phys.Lett.* **2013**,103, 192906/1–192906/5.

(21) Shimuta, T.; Nakagawara, O.; Makino, T.; Arai, S.; Tabata, H.; Kawai, T. *J. Appl. Phys.* **2002**, 91, 2290–2294.

(22) Kim, L.; Jung, D.; Kim, J.; Kim, Y. S.; Lee, J. *Appl. Phys. Lett.* **2003**, 82, 2118–2120.

(23) Haeni, J. H.; Irvin, P.; Chang, W.; Uecker, R.; Reiche, P.; Li, Y. L.; Choudhury, S.; Tian, W. Hawley, M. E.; Craigo, B.; Tagantsev, A. K.; Pan, X. Q.; Streiffer, S. K.; Chen, L. Q.; Kirchoefer, S. W.; Levy, J.; Schlom, D. G. *Nature* **2004**, 430, 758–761.

(24) Choi, K. J.; Biegalski, M.; Li, Y. L.; Sharan, A.; Schubert, J.; Uecker, R.; Reiche, P.; Chen, Y. B.; Pan, X. Q.; Gopalan, V.; Chen, L. Q.; Schlom, D. G.; Eom, C. B. *Science* **2004**, 306, 1005–1009.

(25) MacManus-Driscoll, J. L.; Zerrer, P.; Wang, H.; Yang, H.; Yoon, J.; Fouchet, A.; Yu, R.; Blamire, M. G.; Jia, Q. *Nat. Mater.* **2008**, 7, 314–320.

(26) Harrington, S. A.; Zhai, J.; Denev, S.; Gopalan, V.; Wang, H.; Bi, Z.; Redfern, S. A. T.; Beak, S. H.; Bark, C. W.; Eom, C. B.; Jia, Q.; Vickers, M. E.; MacManus-Driscoll, J. L. *Nat. Nanotechnol.* **2011**, 6, 491–495.

(27) Schlom, D. G.; Chen, L. Q.; Pan, X. Q.; Schmehl, A.; Zurbuchen, M. A. *J. Am. Ceram. Soc.* **2008**, 91, 2429−2454.

(28) Xiong, C.; Pernice, Wolfram H. P.; Ngai, Joseph H.; Reiner, James W.; Kumah, D.; Walker, Frederick J.; Ahn, Charles H.; Tang, Hong X. *Nano Lett.* **2014**, 14, 1419−1425.

(29) Bousquet, E.; Dawber, M.; Stucki, N.; Lichtensteiger, C. Hermet, P.; Gariglio, Jean–Marc

Triscone, S.; Ghosez, P. *Nature* **2008**, 452, 732–736.

(30) Dawber, M.; Stucki, N.; Lichtensteiger, C.; Gariglio, S.; Ghosez, P.; Triscone, J. M. *Adv. Mater.* **2007**, 19, 4153–4159.

(31) Tenne, D. A.; Bruchhausen, A.; Lanzillotti-Kimura, N. D.; Fainstein, A.; Katiyar, R. S.; Cantarero, A.; Soukiassian, A.; Vaithyanathan, V.; Haeni, J. H.; Tian, W.; Schlom, D. G.; Choi, K. J.; Kim, D. M.; Eom, C. B.; Sun, H. P.; Pan, X. Q.; Li, Y. L.; Chen, L. Q.; Jia, Q. X.; Nakhmanson, S. M.; Rabe, K. M.; Xi, X. X. *Science* **2006**, 313, 1614–1616.

(32) Kalyani, V.; Vasile, B. S.; Ianculescu, A.; Buscaglia, M. T.; Buscaglia, V.; NanniCryst, P. *Cryst. Growth Des.* **2012**, 12 (9), 4450–4456.

(33) Zhou, L.; O'Brien, P. *Small* **2008**, 4, 1566–1574.

(34)Cölfen, H.; Mann, S. *Angew. Chem. Int. Ed.* **2003**, 42, 2350–2365.

(35) Cölfen, H.; Antonietti, M. Angew. *Chem. Int. Ed.* **2005**, 44, 5576–5591.

(36) Ye, J. F.; Liu, W.; Cai, J. G.; Chen, S.; Zhao, X. W.; Zhou, H. H.; Qi, L. M. *J. Am. Chem. Soc.***2011**, 133, 933–940.

(37) Song, R. Q.; Cölfen, H. *Advanced Materials* 22 (**2010**), 12, 1301–1330.

(38) Feng, Q.; Hirasawa, M.; Yanagisawa, K. *Chem. Mater.* **2001**, 13, 290−296.

(39) Feng, Q.; Hirasawa, M.; Kajiyoshi, K.; Yanagisawa, K. J. *Am. Ceram. Soc.* **2005**, 88, 415−1420.

(40) Kong, X. G.; Ishikawa, Y.; Shinagawa, K.; Feng, Q. J. *Am. Ceram. Soc.* **2011**, 94, 3716−3721.

(41) Kong, X. G.; Hu, D. W.; Ishikawa, Y.; Tanaka, Y.; Feng, Q. *Chem. Mater.* **2011**, 23, 3978−3986.

(42) Park, N. H.; Wang, Y. F.; Seo, W.S.; Dang, F.; Wan, C.L.; Koumoto, K. *CrystEngComm* **2013**, 15, 679–685.

(43) Dang, F,; Kato, K.; Imai, H.; Wada, S.; Hanedad, H.; Kuwabarae, M. *CrystEngComm* **2010**,12, 3441–3444.

(44) Wen, P. H.; Itoh, H.; Tang W. P.; Feng, Q. *Langmuir* **2007**, 23, 11782–11790.

(45) Iid, M.; Sasaki, T.; Watanabe, M. *Chem. Mater.* **1998**, 10, 3780–3782.

(46) Lyons, B. P.; Clarke, N.; Groves, C. *Energy Environ. Sci*. **2012**,5, 7657−7663.

(47) Feng, Q.; Ishikawa, Y.; Makita, Y.; Yamamoto, Y. J. *Ceram. Soc. Jpn.* **2010**, 118, 141–146.

Chapter V

Topochemical Mesocrystal Conversion of Titanate Single Crystals to Mesocrystalline Nanocomposites of TiO_2 Polymorphs with Photocatalytic Response

5.1 Introduction

The study of nanocrystals has become an intense and major interdisciplinary research area in recent decenniums because nanocrystals can serve as building units to construct hierarchically structured materials.[1,2] Crystallization control of polycrystals constructed from nanocrystals, including the design of the morphology, size, dimensionality, composition, etc., has been a focus of recent interest in material science due to the strong correlation between these parameters and their properties.[3,4] In this field, mesocrystals have attracted considerable attention very recently.[5] Mesocrystal is constructed from well-aligned oriented crystalline nanocrystals,[2,6] and has potential applications to catalysis, sensing, and energy storage and conversion.[7,8]

TiO_2 nanomaterials have attracted considerable attention from both academic and industrial communities, owing not only to their wide applications in the fields of dye-sensitized solar cells (DSSCs), photocatalysis, photocatalytic degradation of toxic pollutants, energy storage and conversion, electrochromic, and sensing, etc, but also to their low cost, safety, and environmental benignity. TiO_2 has various polymorphs,[7] including anatase, rutile, TiO_2 (B), brookite, TiO_2 (H), etc. The differences in lattice structures and morphologies cause different electronic band structure and different surface geometric structures, which determine the physical and chemical properties of TiO_2 materials.

Up to now, nanorod-like,[9,10] cable-like,[11] hollow spheres,[12] nanowires,[13] ellipsoid,[7] and bipyramid-like[14,15] TiO_2 mesocrystals have been synthesized by sol-gel method and hydrothermal method. It has been reported that the anatase TiO_2 mesocrystals with the [010] zone axis have potential application in improved lithium insertion behavior for lithium ionic batteries because of the intrinsic single-crystal-like nature as well as high porosity of the nanoporous mesocrystals.[7] The aligned [001]-oriented rutile nanorods present a large reversible charge–discharge capacity and excellent cycling stability.[9] Anatase mesocrystal-like porous nanostructures exhibit a multifunctional response, including the good capabilities for photocatalytic degradation and enzyme immobilization.[16] The TiO_2 mesocrystals can exhibit excellent photocatalytic performance owing to their large surface area, high porosity, and oriented subunit alignment.[11,16-18] The efficient flexible DSSCs have been fabricated by the growth of the aligned anatase TiO_2 nanorods on a Ti-foil substrate for a photo-anode, in which the mesocrystalline TiO_2 nanorod arrays on Ti substrates with excellent antireflective properties which could enhance light harvesting performance.[19]

Topochemical conversion method is a very useful way for the preparation of the crystals with a desired morphology via ion exchange, intercalation/deintercalation, and exfoliation reaction mechanisms. The topochemical reactions can be described as special phase transformations of the parent crystals into the daughter crystals, in which the crystallographic orientations of parent and daughter crystals have some certain topological correspondences. Layered titanates are excellent precursors for the topochemical synthesis, owing to their excellent ion-exchange, intercalation/deintercalation, and exfoliation reactivities.[20] Some TiO_2 nanomaterials have been synthesized by the topochemical reactions using the layered titanate precursors.[21–24]

Increasing interest has recently been paid to a protonated titanate with composition $H_{4x/3}Ti_{2-x/3}O_4 \cdot H_2O$ (x=0.8, abbreviated to HTO) and lepidocrocite (γ–FeOOH)-type 2D structure, which can be readily exfoliated/delaminated into its molecular single sheets

with distinctive 2D morphology and small thickness.[20,25] Its crystal structure consists of 2D corrugated host layers of edge and corner sharing TiO_6 octahedra and interlayer hydronium ions, which compensate for the negative charge that arises from the vacancy of Ti.[20] In our previous works, some topochemical reactions have been designed and carried out using HTO platelike crystal precursor, which have demonstrated that the HTO platelike crystals can be topotactically transformed to the platelike mesocrystals of $BaTiO_3$,[26-28] $Ba_{1-x}Ca_xTiO_3$,[29] $Ba_{1-x}(Bi_{0.5}K_{0.5})_xTiO_3$,[30] and $Bi_{0.5}Na_{0.5}TiO_3$[31] perovskites by solvothermal reactions and solid state reactions. The platelike mesocrystals can be used to develop the oriented perovskite ceramics with high density, high degree of the preferred orientation, and small grain size by reactive templated grain growth method.[32]

In this Chapter, an interesting route to synthesize the platelike mesocrystalline nanocomposites of TiO_2 polymorphs from the HTO platelike single crystals via a topochemical mesocrystal conversion mechanism was described. The [010]-oriented HTO platelike single crystals are successively transformed into {010}-faceted TiO_2 (B) twinning, [010]-oriented anatase, and [110]-oriented rutile polycrystals, but retain the platelike morphology via heat-treatment, which results in the formations of four kinds of platelike mesocrystalline nanocomposites of TiO_2 polymorphs in the topochemical conversion processes. The mesocrystalline nanocomposites of anatase/rutile polymorphs exhibit unexpectedly high surface photocatalytic activity. It can be explained by enhancing electron-hole separation effect in the mesocrystalline nanocomposite structure and high photocatalytic activity of anatase {010} facet exposing on the mesocrystal surface, which provides a promising nanostructure for the photocatalyst.

5.2 Experimental Section

5.2.1 Materials and Synthesis

All reagents used in this study were of analytical grade and without further purification. $H_{4x/3}Ti_{2-x/3}O_4 \cdot H_2O$ (x = 0.8) (HTO) crystals were prepared as reported by

us previously.[24] 6.9 g of anatase TiO_2 nanoparticles, 5.1 g of KOH, 0.6 g of $LiOH \cdot H_2O$, and 25 mL of distilled water were sealed into a Hastelloy-C-lined vessel with internal volume of 45 mL, and then heated at 250 ^oC for 24 h under stirring conditions. After the hydrothermal treatment, the obtained sample was washed with distilled water and dried at room temperature to obtain $K_{0.80}Ti_{1.73}Li_{0.27}O_4$ (KTLO) crystals. The KTLO crystals (10.0 g) was treated with a 0.2 mol $\cdot L^{-1}$ HNO_3 solution (500 mL) for 24 h under stirring conditions to exchange K^+ and Li^+ in the layered structure with H^+, and then the sample was washed with distilled water. After the acid treatments were done twice, the layered protonated titanate $H_{1.07}Ti_{1.73}O_4 \cdot H_2O$ single crystals were obtained. The as-obtained crystals were collected and washed with distilled water and alcohol, before air-drying at 60 ^oC for 12 h, and then the HTO (7.9 g) single crystals were obtained. For the synthesis of TiO_2, the layered HTO crystals were heat-treated at a desired temperature for 3 h in air with a heating rate of 10 ^oC min^{-1}, then natural cooling to room temperature.

5.2.2 Physical analysis

The structures of crystalline samples were investigated using a powder X-ray diffractometer (Shimadzu, XRD-6100) with Cu Kα (λ = 0.15418 nm) radiation. The size and morphology of the crystalline samples were observed using scanning electron microscopy (SEM) (JEOL, JSM-5500S) or field emission scanning electron microscopy (FE-SEM) (Hitachi, S-900). Transmission electron microscopy (TEM)/(high-resolution TEM (HRTEM)) observation and selected-area electron diffraction (SAED) were performed on a JEOL Model JEM-3010 system at 300 kV, and the powder samples were supported on a Cu microgrid. Energy-dispersive spectroscopy (EDS; JEOL JED-2300T) was measured on the TEM system. The thermal behavior of HTO crystals was analyzed using thermogravimetric and differential thermal analyses (TG-DTA) conducted on a DTG-60H thermogravimetric analyzer (Shimadzu) in static air with a heating speed of 10 ^oC min^{-1} from room temperature to 1100 ^oC. The N_2 adsorption-desorption isotherms and Barrett-Joyner-Halenda (BJH) pore size distribution were investigated on a

Quantachrome Autosorb-1-MP apparatus at 77 K. The specific surface area was calculated from the N_2 adsorption isotherm using the Brunauer-Emmett-Teller (BET) method.

5.2.3 Photocatalytic characterization

The TiO_2 crystalline samples (20 mg) were immersed in 20 mg L^{-1} methylene blue (MB) aqueous solution (100 mL) under dark and stirring conditions. The resulted suspension was placed in the dark with stirring for 2 h to reach the adsorption-desorption equilibrium. The irradiation was carried out under stirring with a 100 W ultraviolet light (UVA, Asahi Spectra, LAX-Cute) located at 5.0 cm horizontal lamp-sample distance. The variations in the concentrations of methylene blue in the aqueous suspension with irradiation time were recorded by using a Shimadzu UV-2450 spectrophotometer. For the comparison, the Degussa P25 sample with a particle size of 30 nm and a composition of 80% anatase and 20% rutile, and BET surface area of 63 m^2 g^{-1} [21,33] was used as the standard sample for the photocatalytic measurement.

5.3 Results and Discussion

5.3.1 Transformation of HTO to TiO_2 by heat-treatment

For the synthesis of platelike TiO_2 mesocrystals via topochemical reaction, the platelike HTO crystals with lepidocrocite (γ–FeOOH)-type structure as precursor were anneal-treated. The layered HTO phase has a basal spacing of 0.882 nm that corresponds to the *d*-value of (020) plane (Figure 5.1a).[34] The EDS analysis result reveals that Li^+ and K^+ were exchanged completely with H^+ after the acid-treatment of KTLO (Figure 5.2). For the investigation of the detailed phase transformation from HTO to TiO_2, the HTO crystals were annealed at some periodic temperatures up to 1000 ^oC, and XRD patterns of the products are shown in Figure 5.1. The HTO phase can be transformed into three kinds of TiO_2 polymorphs, including TiO_2(B), anatase, and rutile, after heat-treatment. With the increase of the heat-treatment temperature, the strongest

(020) peak of the lepidocrocite phase shifted to the right because of the deintercalation of the interlayer water resulting in the decrease of the basal spacing, and then disappeared above 300 °C. The TG-DTA curves of HTO crystal show a large endothermic peak at 90 °C with an obviously losing weight, which correspond to the deintercalation of the interlayer water (Figure 5.3). The dehydration of HTO is almost completed at 400 °C, while the layered structure is retained up to 250 °C.

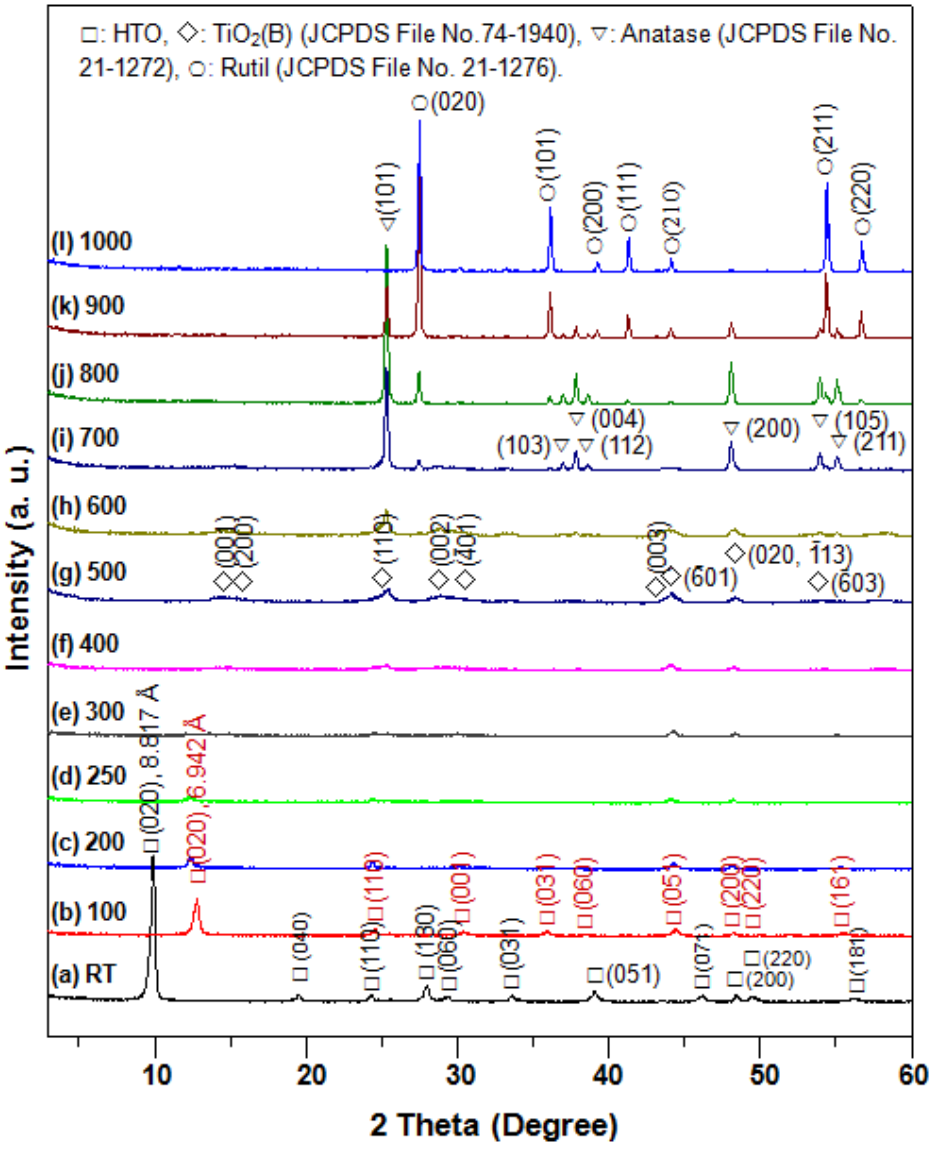

Figure 5.1 XRD patterns of HTO crystals (a) before and (b–l) after heat-treatments at different temperatures for 3 h.

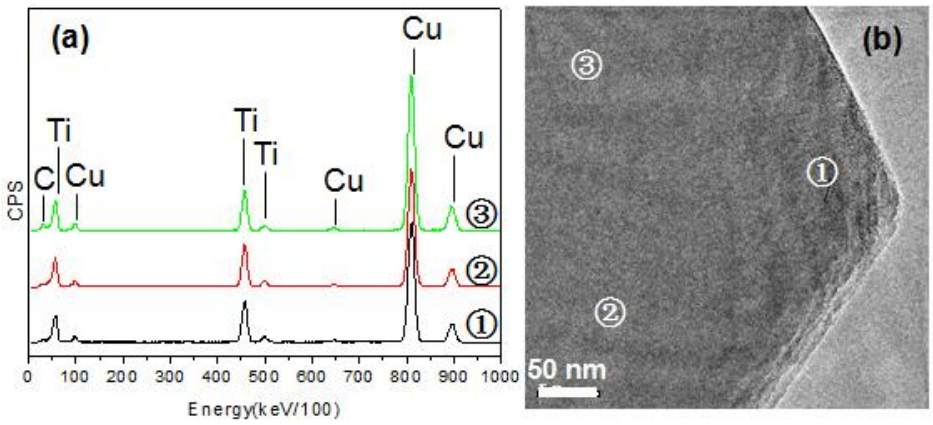

Figure 5.2 (a) EDS spectra and (b) TEM image of $H_{4x/3}Ti_{2-x/3}O_4 \cdot H_2O$ (x=0.8) ($H_{1.07}Ti_{1.73}O_4$, HTO) crystals obtained from $K_{0.80}Ti_{1.73}Li_{0.27}O_4$ (KTLO) crystals by ion-exchange reaction. EDS spectra ①, ② and ③ correspond to those at the positions marked ①, ②, and ③ in TEM image, respectively.

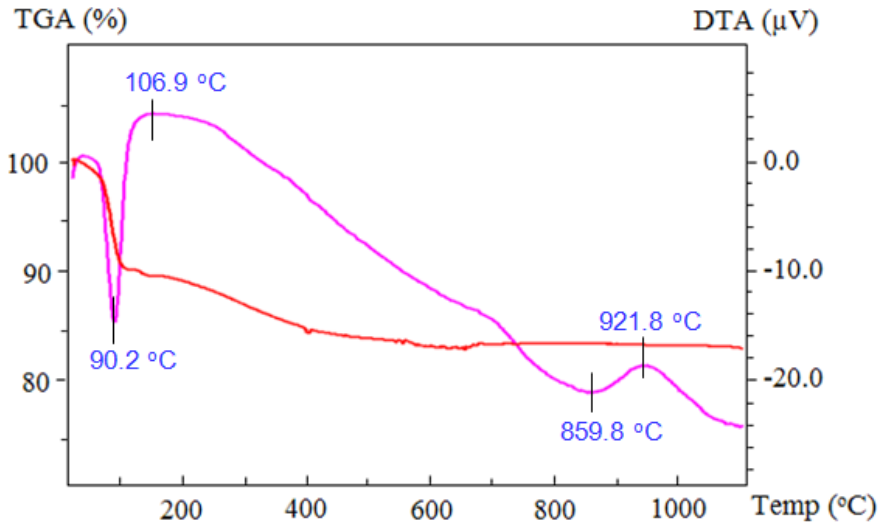

Figure 5.3 TG-DTA curves of HTO crystals from room temperature to 1100 °C with a heating speed of 10 °C min^{-1}.

At 250 °C heat-treatment temperature, the XRD pattern presents the diffraction peaks of the layered phase and a monoclinic TiO_2(B) phase (JCDS File No. 74-1940) (see Figure 5.4). Since the diffraction peaks are very weak, the crystallinities of the formed

TiO_2(B) and HTO are pretty low. As treating in temperatures ranging from 300 to 400 ^oC, a mixture of the TiO_2(B) phase and anatase phase (JCDS File No. 21-1272) appeared. At 500 ^oC the weak peaks of TiO_2(B) and anatase phases were observed because of their poor crystallinities. With elevating temperatures of heat-treatment, the anatase main phase and small amount of rutile phase (JCPDS No. 21-1276) simultaneously appeared at 700 ^oC, the rutile main phase and small amount of anatase phase appeared at 900 ^oC, and then the rutile single phase was obtained at 1000 ^oC. The anatase single phase cannot be obtained by calcination of HTO, which is different from the $H_2Ti_2O_4(OH)_2$ and $H_2Ti_3O_7$ crystals, in which the single anatase phase can be obtained by calcination at 700 ^oC.[35,36] The above XRD results reveal that HTO phase is firstly transformed into TiO_2(B) phase, then into anatase phase, and finally into rutile phase. The TiO_2(B) and anatase phases are metastable TiO_2 phases.

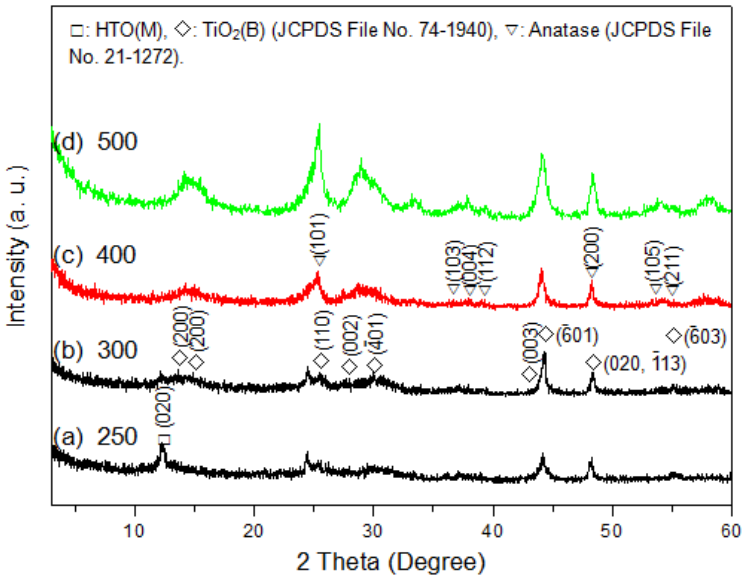

Figure 5.4 XRD patterns of samples with low diffraction peak intensities obtained by heat-treatment of HTO crystals in a temperature range of 250–500 ^oC for 3 h.

Figure 5.5 shows FE-SEM images of the morphology evolution of HTO crystals from room temperature to 900 ^oC. At room temperature, the HTO crystal has a platelike

particle size of 200 nm in thickness and 3 μm in width and smooth crystal surface. Above 700 ^{o}C, the platelike particle was gradually gaped and the cracks were formed. The platelike particle is constructed from nanocrystals, and the size of the nanocrystals increases from 150 to 500 nm with increasing the temperature from 700 to 900 ^{o}C, which accompanies the crack growing up. The platelike crystals still retained the platelike morphology up to 900 ^{o}C, and then broke down and the nanocrystals grew up to be micro-scale crystals at 1000 ^{o}C (see Figure 5.6). This behavior is similar to the topochemical decomposition of platelike $MgCO_3$ crystals to MgO crystals by heat-treatment.[37]

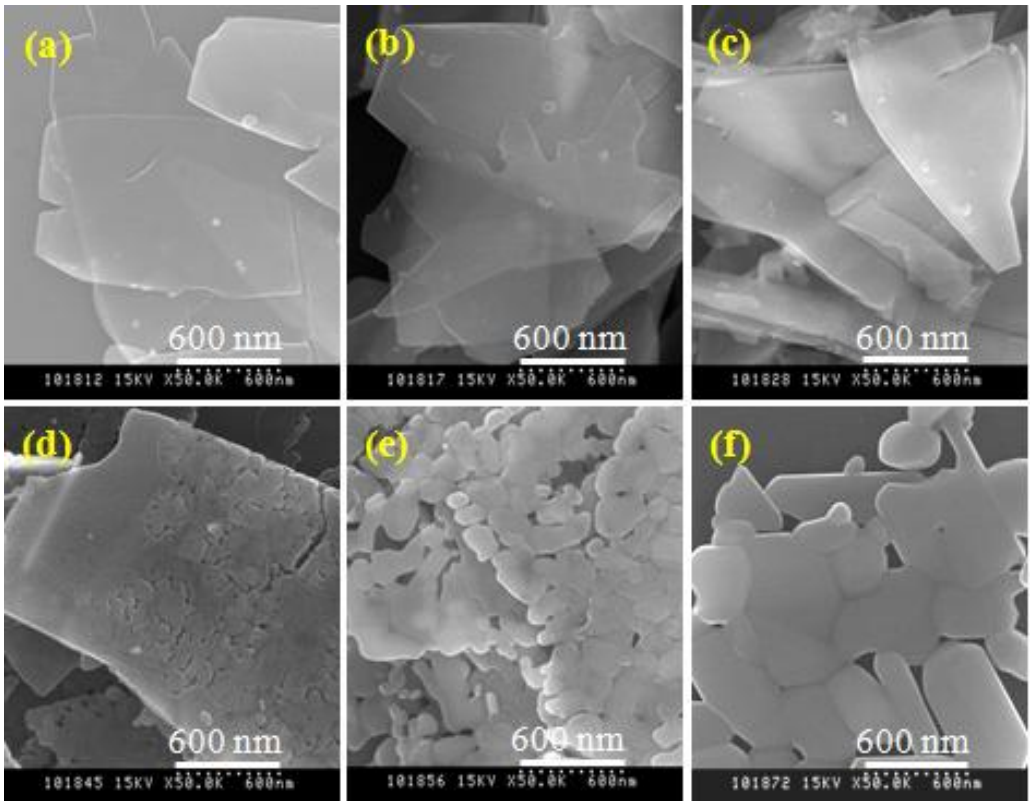

Figure 5.5 FE-SEM images of HTO crystals (a) before and after heat-treatments at (b) 500, (c) 600, (d) 700, (e) 800, and (f) 900 ^{o}C for 3h, respectively.

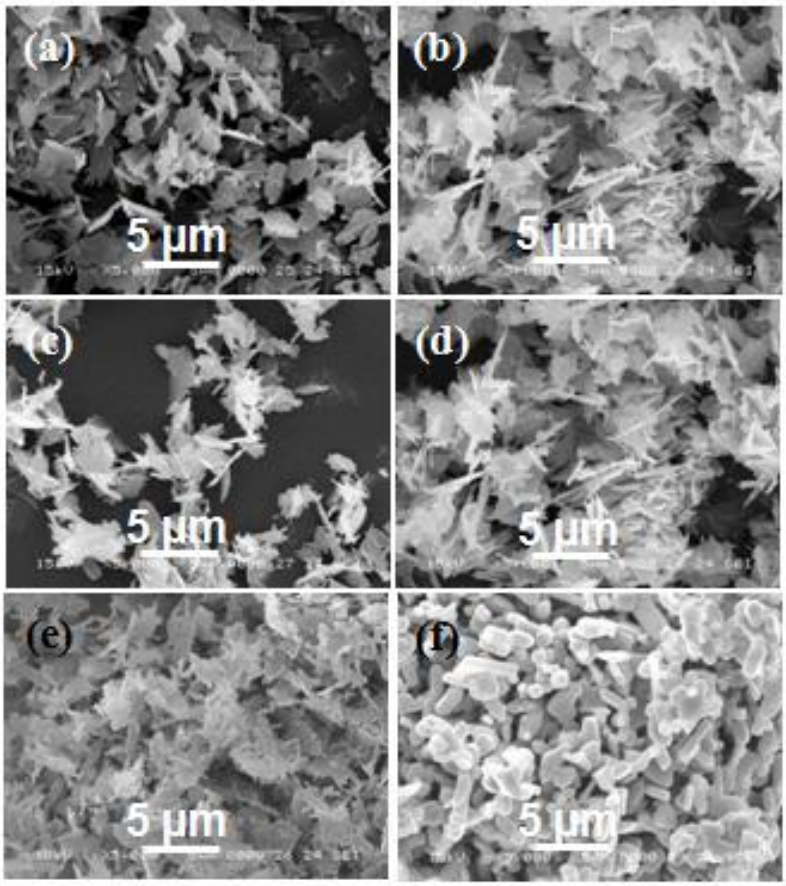

Figure 5.6 SEM images of HTO crystals (a) before and after heat-treatments at (b) 600, (c) 700, (d) 800, (e) 900, and (f) 1000 ^{o}C for 3 h, respectively.

5.3.2 Nanostructural study on topochemical convention reaction from HTO to TiO_2

In order to understand the conversion mechanism from HTO to TiO_2 polymorphs in detail, TEM/HRTEM observations and SAED investigations of the HTO crystals before and after heat-treatment were performed. The TEM images present the crystals with the platelike morphology after heat-treatment up to 900 ^{o}C, which agrees with the SEM image results (Figure 5.6). In the SAED pattern of HTO, the clear and ordered diffraction spots can be easily assigned to the HTO phase with orthorhombic system located along the [010] zone axis (Figure 5.7a, b). The [010] direction (*b*-axis direction) is perpendicular to the basal plane of the platelike HTO crystal. After heat-treatment at 100 ^{o}C, the diffraction spots of the (100) and (001) planes with same interplanar spacing as HTO precursor were observed, but the angle between the (001) and (100) planes

changed from 90° to 92°. The result suggests that HTO phase changes from orthorhombic system to monoclinic system after the dehydration of its interlayer water. We designate the orthorhombic and monoclinic HTO phases as HTO(O) and HTO(M), respectively, for distinguishing their structures in this study.

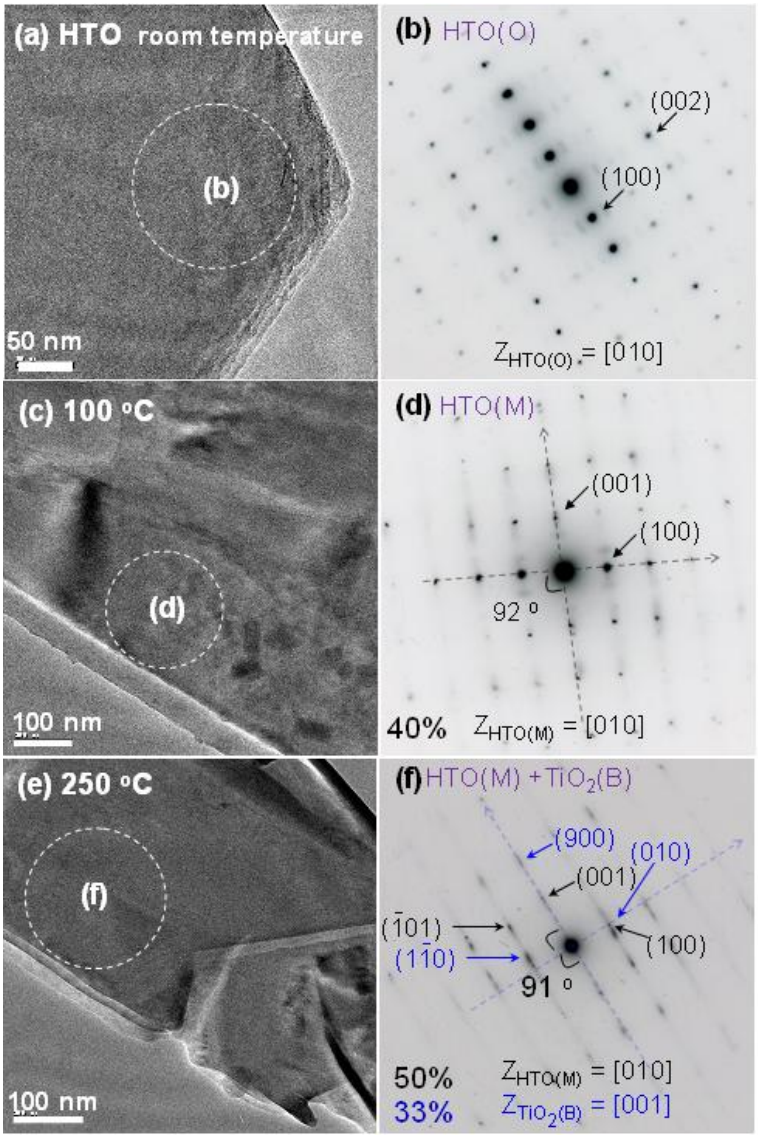

Figure 5.7 (a, c, e) TEM images and (b, d, f) SAED patterns of HTO crystals (a, b) before and after heat-treatments at (c, d) 100 and (e, f) 250 °C for 3 h, respectively.

Two sets of electron diffraction spot patterns can be observed in the SAED pattern of the sample after heat-treatment at 250 °C (Figure 5.7f). One can be readily relegated to

the HTO(M) phase, and the other can be readily relegated to TiO_2(B) phase. The (001), (-101) and (100) diffraction spots of HTO(M) were observed. The angle between the directions vertical to the (001) and (100) planes is 91°. The (900), (1-10) and (010) diffraction spots of TiO_2(B) were observed. The angle between the directions vertical to the (100) and (010) planes is 90 ° that is consistent with the cell parameters of TiO_2(B) (JCPDS No. 74-1940). The result reveals that the direction vertical to the (001) plane and [100] direction of HTO(M) correspond to the directions vertical to the (100) and (010) planes of TiO_2(B), respectively.

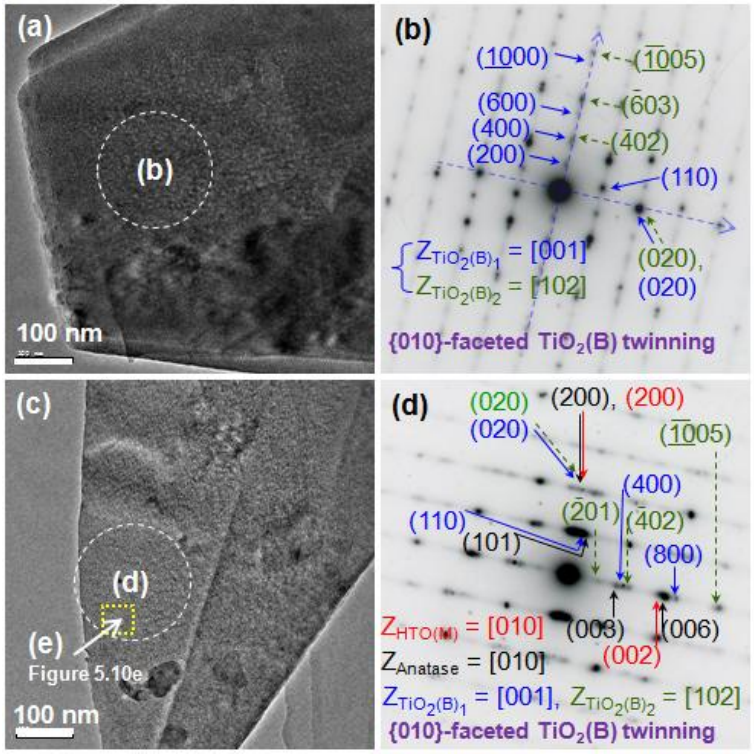

Figure 5.8 (a, c) TEM images and (b, d) SAED patterns of HTO crystals after heat-treatment at 300 °C for 3 h.

It is interesting that two sets of diffraction spots of TiO_2(B) were simultaneously observed in one SAED pattern of the sample after heat-treatment at 300 °C (Figure 5.8), namely two different orientations of TiO_2(B) crystals appear in the one platelike particle. We designate which as $TiO_2(B)_1$ and $TiO_2(B)_2$. The diffractions of (200), (400), (600)

planes of $TiO_2(B)_1$ and the diffractions of (-402), (-603), (-1005) planes of $TiO_2(B)_2$ are lined in same direction (Figure 5.8b), namely, the direction vertical to the (100) plane of $TiO_2(B)_1$ overlaps with the direction vertical to the (-201) plane of $TiO_2(B)_2$. This fact reveals that $TiO_2(B)_1$ crystal and $TiO_2(B)_2$ crystal are twinning. The zone axes of $TiO_2(B)_1$ and $TiO_2(B)_2$ can be decided as the [001] and [102] directions, respectively. The communal (020) plane of the $TiO_2(B)_1$ and $TiO_2(B)_2$, being vertical to the (100) plane of $TiO_2(B)_1$ and the (-201) plane of $TiO_2(B)_2$ respectively, is observed as a strong diffraction spot, which reveals the formation of a {010}-faceted $TiO_2(B)$ twinning.[38,39]

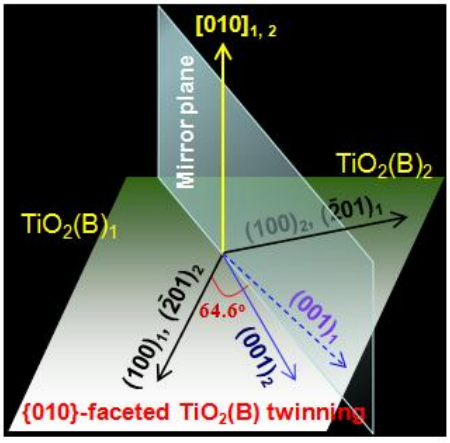

Figure 5.9 Schematic diagram of crystal plane relationships for {010}-faceted $TiO_2(B)$ twinning. The angle between the direction vertical to (100) plane or (-201) plane and the mirror plane is 64.6°. The directions of (h, k, l) correspond to the directions vertical to (h, k, l) planes.

A schematic diagram of crystallographic correspondences between $TiO_2(B)_1$ and $TiO_2(B)_2$ in the {010}-faceted $TiO_2(B)$ twinning is illustrated in Figure 5.9. The directions vertical to the $(100)_1$ pane and the $(-201)_1$ plane of $TiO_2(B)_1$ overlap to the directions vertical to the $(-201)_2$ plane and the $(100)_2$ plane of $TiO_2(B)_2$, respectively, where the angle between the directions vertical to the (100) and (-201) planes for each crystal is 129.2°. The [010] direction is a communal zone axis of $TiO_2(B)_1$ and $TiO_2(B)_2$. Therefore, there is a mirror plane on the [010] zone axis in $TiO_2(B)_1/TiO_2(B)_2$ twinning, and the angle between the direction vertical to the (100) plane or the (-201) plane and

the mirror plane is 64.6°. These analytical results reveal that the obtained TiO_2(B) crystal is a mirror reflection twinning which grow up along the direction vertical to the (100) plane or the (-201) plane on the mirror plane.[38,39] It is the first time to observe the TiO_2(B) twinning obtained by the heat-treatment of layered titanate, as far as we know.

In addition to the $TiO_2(B)_1/TiO_2(B)_2$ twinning phase, the HTO(M) phase and anatase phase located along the same [010] zone axis can be observed simultaneously in one platelike particle (Figure 5.8d). The direction of the [010] zone axis of anatase phase corresponds to the [001] zone axis of $TiO_2(B)_1$ and [102] zone axis of $TiO_2(B)_2$, which also correspond to the [010] zone axis of the HTO(M) phase. Therefore, the [001] direction of the anatase crystal overlaps to the [001] direction of the HTO(M) crystal, and the direction vertical to the (100) plane or the (-201) plane of the $TiO_2(B)_1/TiO_2(B)_2$ twinning.

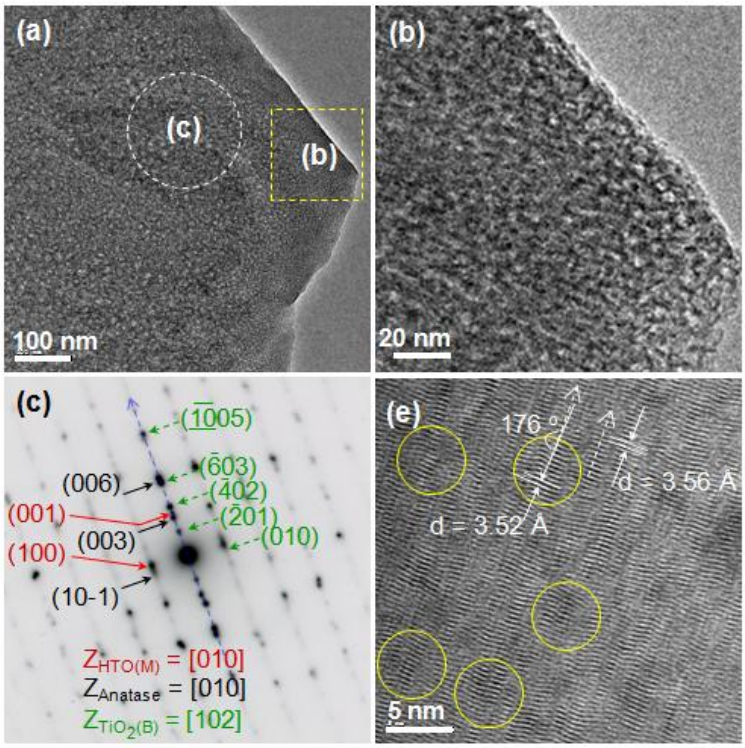

Figure 5.10 (a) TEM, (b) HRTEM images, and (c) SAED pattern of sample obtained by heat-treatment of HTO crystals at 300 °C for 3 h. (e) HRTEM image derived from a position in yellow square of TEM image in Figure 5.8c.

The TEM image result reveals that the platelike particle obtained by heat-treatment at 300 ^{o}C is a polycrystal constructed from nanocrystals with 4 nm size (see Figure 5.10). The SAED pattern of the platelike particle suggests that the nanocrystals in one platelike particle are aligned in same crystal orientation, namely the platelike particle is a mesocrystal. The lattice distortion was observed in the HRTEM image of the platelike particle of the nanocomposite (see Figure 5.10e). It exhibits wavy line lattice fringes with lattice spacings of about 0.352–0.356 nm with distorted crystal lattices angle of about 4^{o}. The lattice spacings are close to the (110) plane (d = 0.354 nm) of HTO(M), the (110) plan (d = 0.356 nm) of TiO_2(B), and the (101) plan (d = 0.352 nm) of anatase crystals. These lattice fringes of the different phases show the almost same orientations but locate at different nanocrystals which are separated by the crystal boundaries. The similar *d* value and almost same orientation of these planes are likely to result in a strong diffraction spot with an ellipse sharp in Figure 5.8d.

TEM images of sample obtained by heat-treatment of HTO crystals at 400 ^{o}C show the platelike particles constructed from nanocrystals (Figure 5.11). The SAED patterns present the formation of a mixture of TiO_2(B) and anatase phases. Although [001]-oriented $TiO_2(B)_1$ and [102]-oriented $TiO_2(B)_2$ were observed in different platelike crystals, respectively, but $TiO_2(B)_1/TiO_2(B)_2$ twinning was not observed in one platelike particle. The SAED pattern results suggest that about 40% platelike crystals contain the [001]-oriented $TiO_2(B)_1$, and other 60% platelike crystals contain the [102]-oriented $TiO_2(B)_2$. The [010], [100], and [001] directions of anatase crystals correspond to the directions of [001], vertical to (010) plane and (100) plane of $TiO_2(B)_1$, and the directions of [102], vertical to (010) plane and (-201) plane of $TiO_2(B)_2$, respectively, which are similar to the relationship between anatase and $TiO_2(B)_1/TiO_2(B)_2$ twinning formed at 300 ^{o}C (Figure 5.8). The crystal boundaries between anatase phase and TiO_2(B) phase can be observed in HR-TEM images (Figure 5.11e, f), which reveals that the platelike particles are constructed form the different crystalline phases. The lattice fringes of (200) (d=0.185 nm) and (004) (d=0.239 nm) for the anatase phase, (020)

(d=0.182 nm) and (-402) (d=0.253 nm) for the TiO_2(B) phase, and (200) (d=0.190 nm) for the HTO(M) phase were observed, respectively. The directions of the (200) plane of HTO(M), (020) plane of TiO_2(B), and (200) plane of anatase agree with each other, and the directions of (-402) plane of TiO_2(B) and (004) plane of anatase agree with each other. This result suggests that the (200) plane of HTO(M) is transformed to (020) plane of TiO_2(B), and then to (200) plane of anatase; while (-402) plane of TiO_2(B) is transformed to (004) plane of anatase in the topochemical reaction.

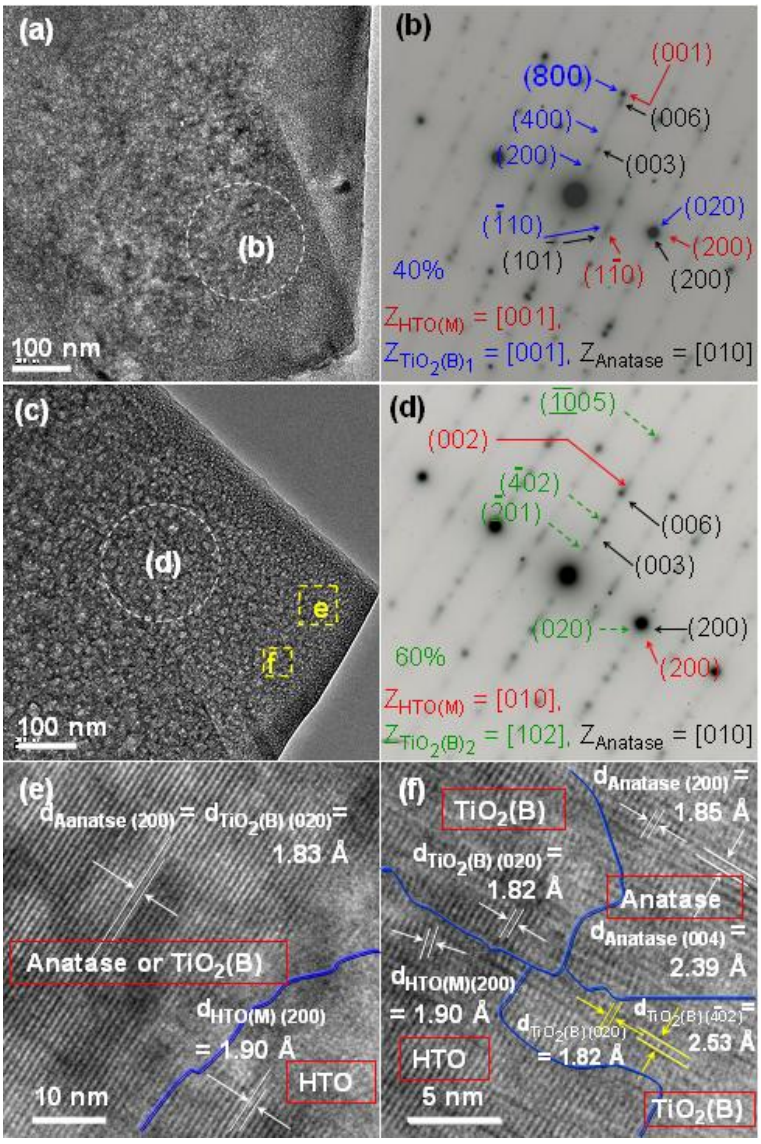

Figure 5.11 (a, c) TEM images, (b, d) SAED patterns, and (e, f) HRTEM images of samples obtained by heat-treatment of HTO crystals at 400 ^{o}C for 3 h. The HRTEM images are from the

yellow (e, f) panes in (c) TEM image, respectively.

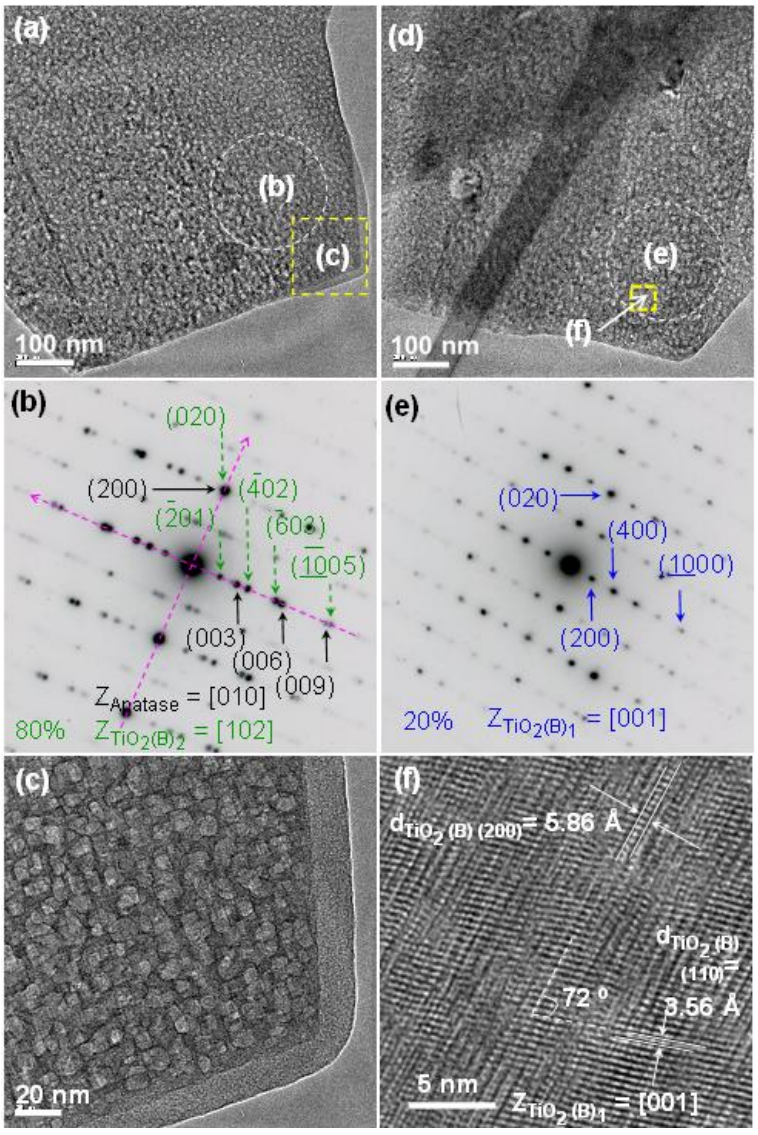

Figure 5.12 (a, d) TEM images, (b, e) SAED patterns, and (c, f) HRTEM images of samples obtained by thermal treatment of HTO crystals at 600 ^{o}C for 3 h.

Figure 5.12 shows TEM imagines and SAED patterns of sample obtained at 600 ^{o}C. The platelike crystals are constructed from nanocrystals similar to that obtained at 400 ^{o}C, while the nanocrystals grew up to about 10 nm (Figure 5.12c). The [010]-oriented anatase phase and [001]- and [102]-oriented TiO_2(B) phases were observed, but without the twinning phase, which is similar also to the case at 400 ^{o}C. However, the fraction of

the [001]-oriented $TiO_2(B)_1$ reduce to 20%, and the [102]-oriented TiO_2 $(B)_2$ increases to 80%, suggesting the $TiO_2(B)_2$ is more stable than $TiO_2(B)_1$ at the high temperature. In HRTEM image of $TiO_2(B)_2$, the lattice fringes of (200) (d=0.586 nm) and (110) (d=0.356 nm) of $TiO_2(B)$ were observed clearly. The angle between the (200) and (110) planes is 72 ^{o}, which is extremely close to the value calculated from the $TiO_2(B)$ cell parameter (72.19 ^{o}, JCPDS No. 74-1940). The result also reveals that the $TiO_2(B)_1$ crystal is [001]-orientation, which agree with the SAED pattern (Figure 5.12e) .

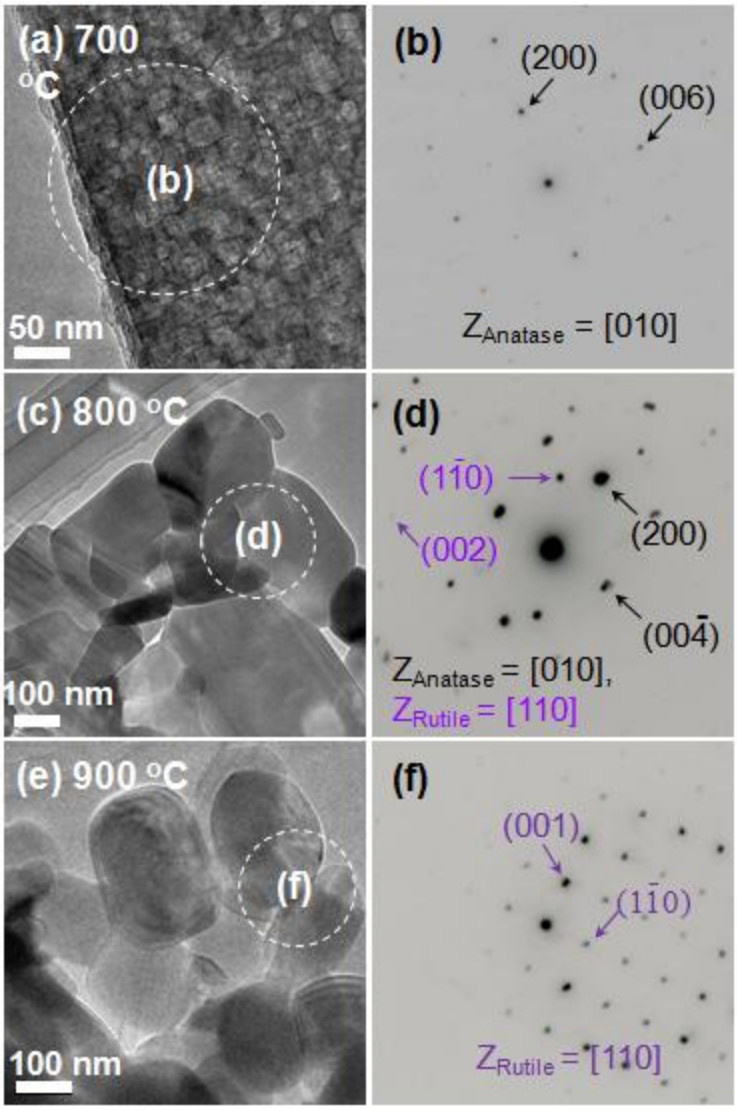

Figure 5.13 (a, c, e) TEM images and (b, d, f) SAED patterns of samples obtained by heat-treatments of HTO crystals at (a, b) 700, (c, d) 800, and (e, f) 900 ^{o}C for 3 h, respectively.

Figure 5.13 shows TEM images and SAED patterns of the samples heat-treated at 700, 800, and 900 ^{o}C, respectively. The platelike polycrystalline particles are constructed from nanocrystals, while each SAED pattern of the polycrystal looks like a single crystal, revealing the formation of mesocrystalline platelike crystals in which the nanocrystals aligned in the same orientation direction. The SAED pattern of anatase and rutile phases can be indexed to the [010] and [110] zone axis diffractions, respectively, namely the nanocrystals of anatase and rutile in the mesocrystalline platelike crystals exhibit [010]-orientation and [110]-orientation, respectively. Only the diffraction spots of the anatase phase were observed at 700 ^{o}C owing to the low content of rutile phase at this temperature (Figure 5.1i). The diffraction spots of [010]-oriented anatase and [110]-oriented rutile phases were simultaneously observed in the sample prepared at 800 ^{o}C (Figure 5.8d). The results suggest that the [010] axis of the anatase structure is transformed to the [110] axis of rutile structure in the topochemical reaction from anatase to rutile. The angle between the [001] direction of anatase and the [001] direction of rutile on the basal plane is 25.0^{o} (Figure 5.14). This result reveals that the [001] and [100] directions of anatase structure correspond to the [001] and [1-10] directions of rutile structure by rotating an angle of 25.0^{o} on the (010) plane of anatase in the topochemical conversion reaction from anatase to rutile.

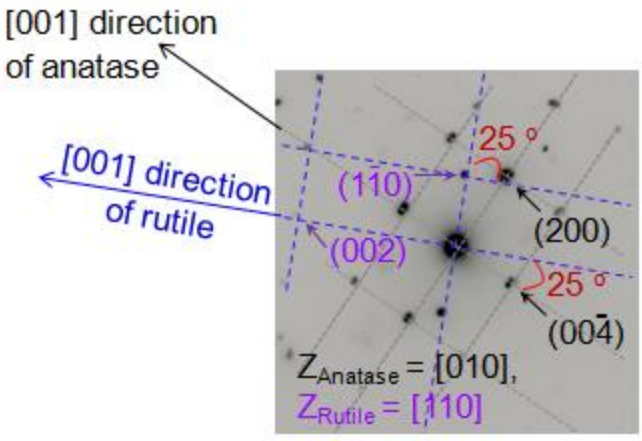

Figure 5.14 SAED pattern of sample heat-treated at 800^{o}C. Two sets of diffraction patterns were

observed. The strong one is anatase phase ((indicated by gray dotted line), and the weak one is rutile phase ((indicated by blue dotted line). The [010]-direction of the anatase crystal structure corresponds to the [110]-direction of rutile crystal structure, and the angle between the directions of the [001]-direction of anatase and the [001]-direction of rutile is 25.0 ^{o}.

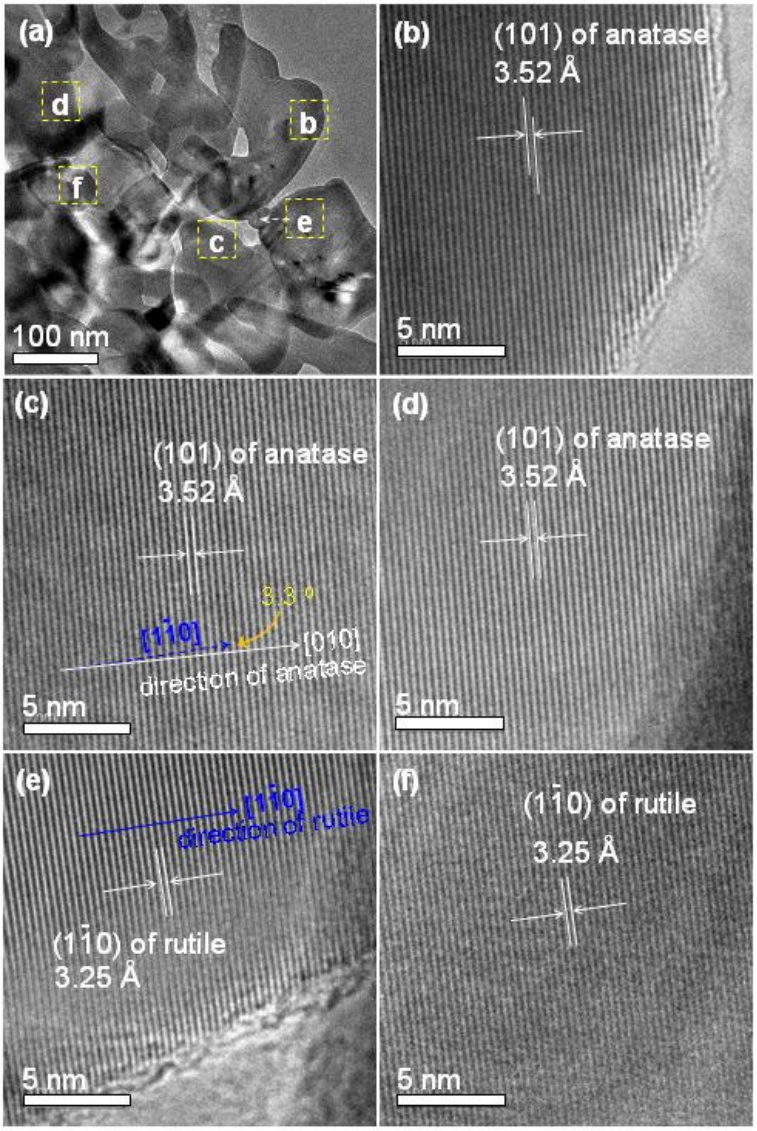

Figure 5.15 (a) TEM image and (b – f) HRTEM images from (b – f) yellow panes in (a), respectively, of HTO crystal after heat-treatment at 800 ^{o}C for 3 h. The angle between between the direction of the (101) plane of the anatase phase and the (1-10) plane of the rutile phase is 3.3 ^{o}.

To prove the crystallographic correspondences between the anatase and rutile structures in detail, the nanostructure of mesocrystalline anatase/rutile nanocomposite platelike particles obtained at 800 ^{o}C was investigated using HRTEM (Figure 5.15). In one platelike particle, all the anatase nanocrystals exhibit lattice fringes of (101) plane in the same orientation and all the rutile nanocrystals also exhibit lattice fringes of (1-10) plane in the same orientation. The angle between the directions of the (101) plane of the anatase and (1-10) plane of the rutile is very small about 3.3^{o}. This result reveals that the (101) plane of the anatase is transformed to the (1-10) plane of the rutile. The nanostructural analysis results described above indicate that there are specific topological crystallographic correspondences between the structures of the precursor and products in the topochemical reactions.

5.3.3 Phase compositions and lattice constants of products

The variations of the phase composition fractions with elevating temperatures in heat-treatment process of HTO crystal are shown in Figure 5.16. The phase composition fractions of the products prepared in the temperature range of 100 to 600 ^{o}C were estimated using the statistic results of over 10 pieces of the SAED patterns, and which prepared in the temperature range of 700 to 1000 ^{o}C were estimated from XRD peak intensity data using the following equation.[40]

$$F_R = (1 + 0.8I_A/I_R)^{-1}$$

where F_R , I_A and I_R represent the rutile fraction, the integrated intensities of (101) diffraction peak of anatase phase and (110) diffraction peak of rutile phase, respectively. There are three kinds of metastable intermediates, HTO(M), TiO_2(B), and anatase, in the structural transformation process from HTO(O) precursor to the final thermodynamic stable rutile phase. The anatase phase is relatively stable in a wide temperature range from 300 to 900 ^{o}C. The thermostability increases in an order of HTO(O) < HTO(M) < TiO_2(B) < anatase < rutile. In the temperature range of 250–400 ^{o}C, three kinds of metastable phases coexist, which may be a main reason of the low crystallinities of

these mesocrystals at this temperature range. It is noted that the TiO_2(B) and anatase phases can be formed from HTO phase at lower temperatures of 250 and 300 °C, respectively, than that of 400 °C for the anatase formation from $H_2Ti_nO_{2n+1}$ ($3 \leqq n \leqq 6$),[41] and 300 and 600 °C for the TiO_2(B) and anatase formations from $H_2Ti_nO_{2n+1} \cdot xH_2O$,[42] and 400 and 700 °C for the TiO_2(B) and anatase formations from $H_2Ti_3O_7$.[36]

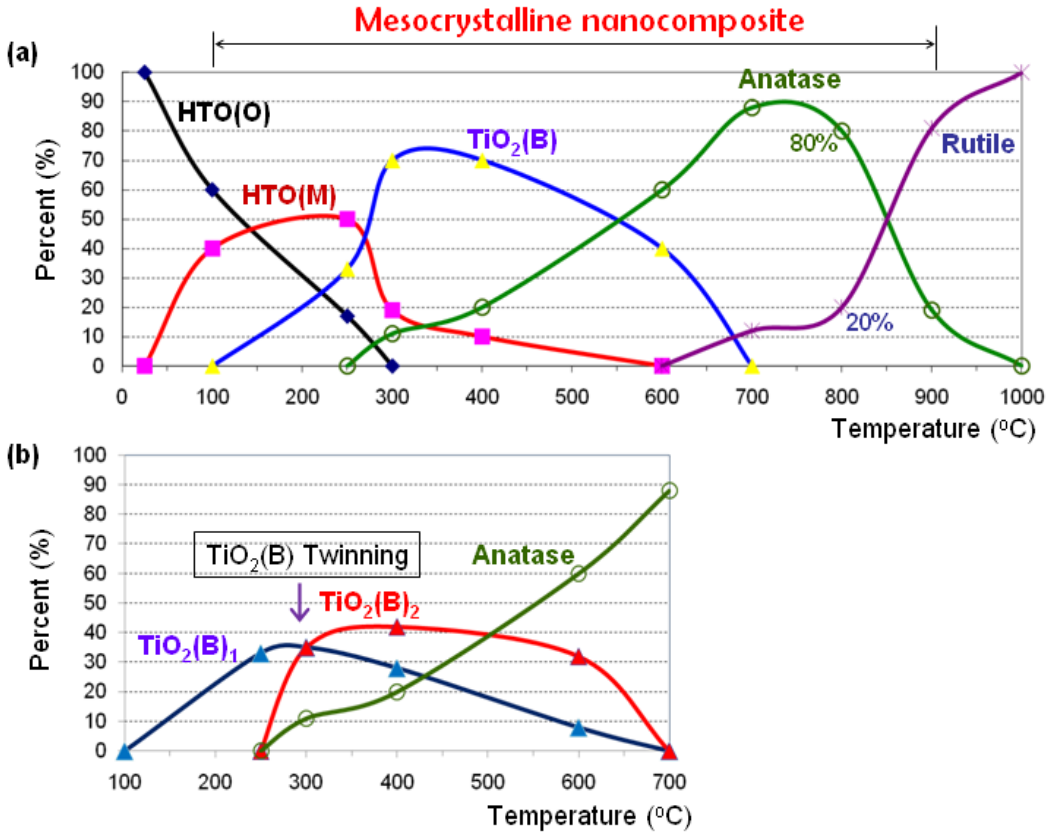

Figure 5.16 (a) Trend curves of formed intermediate crystalline phases in heat-treatment process of HTO crystal with elevating temperature. (b) Trend curves of formation and consumption of $TiO_2(B)_1$, $TiO_2(B)_2$, and anatase phases in the temperature range of 100 to 700 °C.

Figure 5.16b shows the trend curves of the formation and consumption of $TiO_2(B)_1$, $TiO_2(B)_2$, and anatase phases in the temperature range of 100 to 700 °C. $TiO_2(B)_1$ and $TiO_2(B)_2$ phases achieve the maximums at 300 and around 400 °C, respectively. The anatase phase increases with elevating temperature above 250 °C, which accompanied

consumption of $TiO_2(B)_1$ phase. The $TiO_2(B)_2$ phase is more stable than the $TiO_2(B)_1$ phase in the temperature range above 300 °C. These results suggest that the anatase phase is formed mainly by the consumption of the $TiO_2(B)_1$ phase below 600 °C and by the consumption of the $TiO_2(B)_2$ phase above the temperature.

The lattice constants and chemical formulas of HTO, $TiO_2(B)$, anatase, and rutile are summarized in Table 5.1. The lattice constants of HTO(O), anatase, and rutile were calculated using XRD results, and which of HTO(M), $TiO_2(B)$ were evaluated using the SAED results. The chemical formula of HTO was determined using TG-DTA results. The *b*-axis and *c*-axis of HTO(M) increases and decreases, respectively, with the elevating of the heat-treatment temperature from 100 to 400 °C, owing to change of the chemical composition. The lattice parameters of the $TiO_2(B)_1$ and $TiO_2(B)_2$ are very closed, which is a precondition for the formation of twinning.

Table 5.1 Lattice constants and chemical compositions of HTO and crystal phases obtained by heat-treatments of HTO at different temperatures.

No.	Compounds	Symmetry [a]	Chemical formula [b]	*a* (Å)	*b* (Å)	*c* (Å)
1	HTO(O)	Orthorhomb	$H_{1.07}Ti_{1.73}O_4 \cdot 1.03H_2O$	3.783	17.68	2.994
2	HTO(M) (100 °C)	Monoclinic $\beta = 91.9°$	$H_{1.07-x}Ti_{1.73}O_4 \cdot (0.15+x/2)H_2O$ $(0 \leqq x < 0.15)$	3.806	13.93	2.968
3	HTO(M) (250 °C)	Monoclinic $\beta = 90.7°$	$H_{0.92}Ti_{1.77}O_4$	3.770	14.35	2.947
4	HTO(M) (300 °C)	Monoclinic $\beta = 90.6°$	$H_{0.70}Ti_{1.83}O_4$	3.792	14.60	2.901
5	HTO(M) (400 °C)	Monoclinic $\beta = 90.4°$	$H_{0.25}Ti_{1.94}O_4$	3.842	14.68	2.803
6	$TiO_2(B)_1$ ([001]-oriented)	Monoclinic $\beta = 107.1°$	TiO_2	12.08	3.674	6.508
7	$TiO_2(B)_2$ ([102]-oriented)	Monoclinic $\beta = 107.1°$	TiO_2	12.08	3.685	6.493
8	Anatase	Tetragonal	TiO_2	3.784	3.784	9.514
9	Rutile	Tetragonal	TiO_2	4.596	4.596	2.949

[a] Lattice constants of HTO(O), HTO(M) at 100 °C, anatase, and rutile crystals are according to the

data of the XRD patterns. The symmetry and lattice constants of other crystals are according to the statistics from the investigation of over 10 pieces of the SAED patterns of the samples.

[b] Chemical formulas of HTO(O) and HTO(M) are estimated from TG-DTA results.

5.3.4 Conversion reaction mechanism of HTO to TiO_2 mesocrystals

The mesocrystalline conversion process and topological correspondences between the HTO single crystal precursor and mesocrystalline TiO_2 polymorphs can be described as a schematic diagram in Figure 5.17. Firstly, the HTO(O) single crystal precursor with platelike morphology and [010]-orientation is transformed into the HTO(M) crystal in the temperature range of 100–300 ^{o}C by dehydration reaction. The [010] and [001] directions of the HTO(M) crystal correspond to the [010] and [001] directions of HTO(O), respectively, but the angle between the (100) plane and (001) plane changes slightly from 90^{o} to 92^{o}. Secondly, the HTO(M) phase is transformed to the TiO_2 $(B)_1$ phase with the orientation of [001] zone axis at 250 ^{o}C. The [010] direction and [001] direction of the HTO(M) phase correspond to the [001] direction and direction vertical to (100) plane of the $TiO_2(B)_1$ phase, respectively. Another $TiO_2(B)_2$ phase with the orientation of [102] zone axis is formed at 300 ^{o}C, which connects to the $TiO_2(B)_1$ phase and results in the formation of the {010}-faceted $TiO_2(B)_1/TiO_2(B)_2$ twinning. The $TiO_2(B)_1/TiO_2(B)_2$ twinning disappears at 400 ^{o}C, which accompanies the consumption of $TiO_2(B)_1$ phase and the increasing of anatase phase. The $TiO_2(B)$ phases are transformed into anatase completely at 700 ^{o}C. The [010] and [001] directions of anatase phase correspond to the [001] direction and the direction vertical to (100) plane of the $TiO_2(B)_1$ phase, and the [102] direction and the direction vertical to (-201) plane of the $TiO_2(B)_2$ phase, respectively. Finally, the anatase phase is transformed to the [110]-oriented rutile phase above 700 ^{o}C, where the [010] direction of anatase phase corresponds to the [110] direction of rutile, and [001] direction of anatase to the [001] direction of rutile after rotating an angle of 25.0^{o} on the {010} facet of anatase. The platelike particle morphology maintains up to 900 ^{o}C. The platelike $TiO_2(B)_2$, anatase,

and rutile formed in the topochemical conversion process are mesocrystals, and four kinds of the mesocrystalline nanocomposites of HTO/TiO_2(B), HTO/TiO_2(B)/anatase, TiO_2(B)/anatase, and anatase/rutile polymorphs can be formed in the reaction system as shown in Figure 5.16.

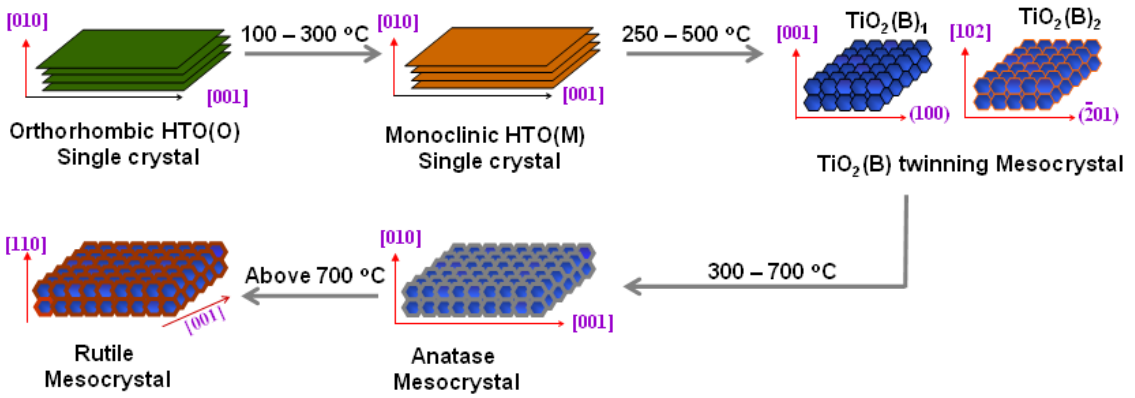

Figure 5.17 Schematic diagram of mesocrystalline conversion process from HTO precursor single crystal to rutile mesocrystal and topological correspondences of precursor and products. The directions of (h, k, l) correspond to the directions vertical to (h, k, l) planes.

On the basis of the above results and discussion, a schematic representation of the crystal structural correspondences in the evolution process from HTO precursor to the TiO_2 (B), anatase, and rutile in sequence is illustrated in Figure 5.18. In the HTO crystal structure, the TiO_6 octahedra are connected with each other via corner-sharing and edge-sharing to form a 2D TiO_6 octahedral host sheet. The host sheets are stacked with a basal spacing of about 0.882 nm in a body-centered orthorhombic system (Table 5.1), accommodation H_2O and H_3O^+ between them. Approximately 52% of the interlayer H_2O molecules are protonated to H_3O^+ which compensates for the negative charge of the host sheet.[43] In the evolution process of the HTO structure to the TiO_2 structures, firstly, the HTO structure loses the interlayer H_2O molecules, resulting in the decrease of the basal spacing from 0.882 nm to 0.694 nm. After the dehydration, the orthorhombic HTO structure is distorted to the monoclinic HTO structure, where the angle between the (100) and (001) planes is changed from 90 to 92°.

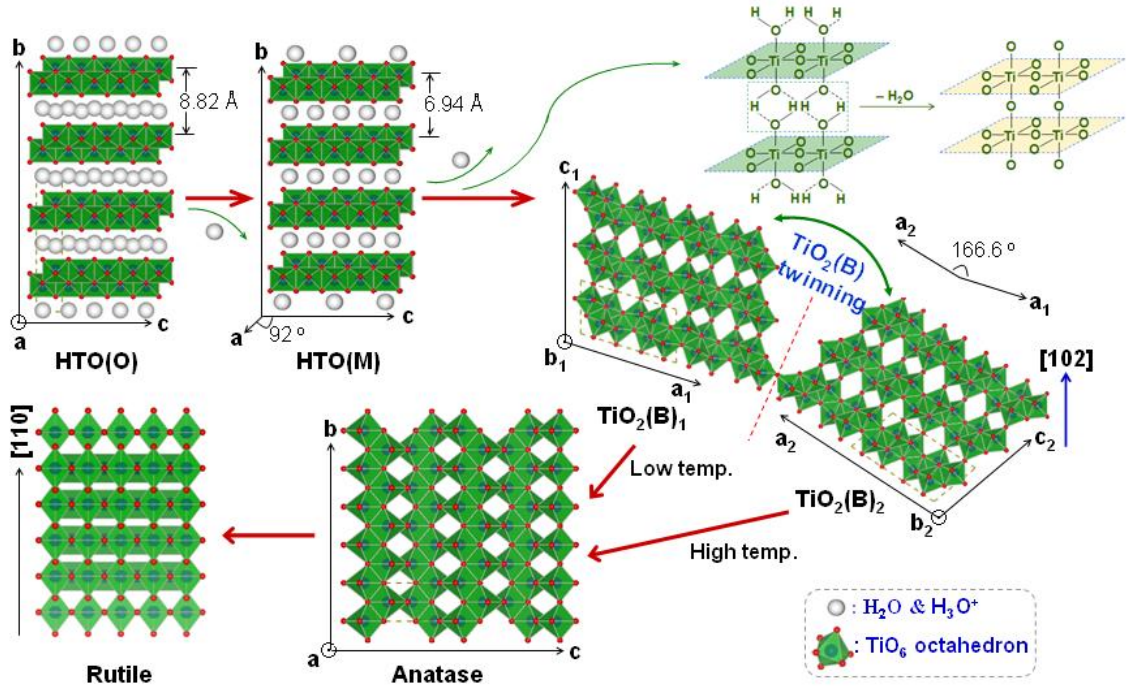

Figure 5.18 Schematic representation of crystal structure and devolution process for layered HTO crystal and its reconstruction to TiO_2(B), anatase, rutile in sequence after thermal treatment.

Secondly, after completely losing the interlayer H_2O molecules derived from the accommodation H_2O, the interlayer H_2O molecules derived from the accommodation H_3O^+ start to be lost successively above 200 ^oC. In this reaction, the hydrogen bonds between the top and bottom [$TiO_6(OH_3^+)$] octahedral layers are dehydrated to the Ti-O-Ti bonds accompanying the release of the crystal water molecules completely, to form a three-dimensional (3D) TiO_6 octahedral sawtooth-like tunnel structure of TiO_2(B), where the [001] zone axis of the $TiO_2(B)_1$ and [102] zone axis of the $TiO_2(B)_2$ correspond to the [010] zone axis of HTO(M). The resulting in the 3D TiO_6 octahedral sawtooth-like structure is self-adjusted to satisfy the principle of minimum energy and space requirements to make the metastable TiO_2(B) structure. The crystal lattice shrinkage occurs in the process of collapsing the layered structure to the sawtooth-like structure. To satisfy the principle of minimum energy and space requirements, the partial area of the sawtooth-like structure is distorted to relieve the stress in the crystal lattice, which causes formation of the {010}-faceted $TiO_2(B)_1/TiO_2(B)_2$ twinning

structure by partial bending the sawtooth-like structure from the [001]-oriented $TiO_2(B)_1$ to [102]-oriented $TiO_2(B)_2$.[38] Without the $TiO_2(B)_1/TiO_2(B)_2$ twinning at the starting stage of $TiO_2(B)$ formation is due to less stress in the lattice. When most of HTO is transformed to $TiO_2(B)$, the large stress in the lattice causes the formation of the $TiO_2(B)_1/TiO_2(B)_2$ twinning.

The $TiO_2(B)$ phase is transformed to the [010]-oriented anatase phase starting at about 300 ^oC. The formation of the anatase phase results to relieve the stress in the crystal lattice by consumption of the $TiO_2(B)$ phase, which may be the reason why the $TiO_2(B)$ twinning structure disappears above 300 ^oC. The [001]-oriented $TiO_2(B)_1$ exhibits a higher reactivity than that of the [102]-oriented $TiO_2(B)_2$ in the conversion to the anatase phase (Figure 5.16b), implying that the active energy of shifting TiO_6 octahedra from the [001]-oriented $TiO_2(B)_1$ structure to the [010]-oriented anatase structure is lower than that from the [102]-oriented $TiO_2(B)_2$ structure to the [010]-oriented anatase structure in the topochemical process. Brohan et al.[44] have given a conversion mechanism for the detailed phase transformation from TiO_2 (B) to anatase. The typical transformation from $TiO_2(B)$ to anatase is explained by the split or shear of (-201) plane of $TiO_2(B)$ to form (10-3) plane of anatase, along with the [-20-3] direction of $TiO_2(B)$ structure. This conversion mechanism has been used to explain the TiO_2 polymorphs conversions from the layered $H_{0.54}Ti_{1.865}\square_{0.135}O_4$ [45] (□, vacancy) and $H_2Ti_nO_{2n+1}\cdot xH_2O$[42] phases obtained by heat-treatment process.

In this study, we found the crystallographic topological correspondences, namely the [010] direction of HTO(M) corresponds to the [001] direction of $TiO_2(B)_1$ or the [102] direction of $TiO_2(B)_2$, and the [010] direction of anatase; the direction vertical to the (100) plane of HTO(M) corresponds to the [010] direction of $TiO_2(B)$ and the [100] direction of anatase; furthermore the [001] direction of HTO(M) corresponds to the direction vertical to (100) plane of $TiO_2(B)_1$ or direction vertical to (-201) plane of $TiO_2(B)_2$, and the [001] direction of anatase. These results also suggest that the (200) plane (0.189 nm) of HTO(M) is transformed to (020) plane (0.187 nm) of $TiO_2(B)$, and

then to (200) plane (0.189 nm) of anatase; while (001) plane (0.297 nm) of HTO(M) is transformed to (400) plane (0.291 nm) of $TiO_2(B)_1$ or to (-402) plane (0.253 nm) of $TiO_2(B)_2$, and then to (003) plane (0.317 nm) of anatase in the topochemical conversion reaction. The larger interplanar distance differences of (-402) plane (0.253 nm) of $TiO_2(B)_2$ with (001) plane (0.297 nm) of HTO(M) and (003) plane (0.317 nm) of anatase than that of (400) plane (0.291 nm) of $TiO_2(B)_1$ may be the reason why higher reaction temperatures are necessary for the transformations from HTO(M) to $TiO_2(B)_2$ and $TiO_2(B)_2$ to anatase than which from HTO(M) to $TiO_2(B)_1$ and $TiO_2(B)_1$ to anatase, namely the larger active energies are necessary for the larger structural change in the formation and conversion reactions of $TiO_2(B)_2$.

Finally, the [010]-oriented anatase mesocrystal is transformed into the [110]-oriented rutile mesocrystal at the high temperature. The crystal structures of anatase and rutile differ by the distortion of each TiO_6 octahedra and by the assembly pattern of the each TiO_6 octahedra chains.[46] In the anatase structure, the octahedra is significantly distorted and each octahedra contacts with eight neighbor octahedra, in which four sharing a corner and four sharing an edge. In the rutile structure, the TiO_6 octahedra is not regular, showing a slight orthorhombic distortion, and each octahedra contacts with ten neighbor octahedra, where two sharing edge oxygen pairs and eight sharing corner oxygen atoms. In the topochemical mesocrystalline conversion process from anatase to rutile, the sharing edge or/and corner of TiO_6 octahedra in the anatase structure are partially broken, accompanying the octahedra rotating and reconnecting to positions of the rutile structure. The formation mechanism of the mesocrystalline polymorphs in the present study is different from the mesocrystal formation mechanisms of the mesoscale oriented self-assembly process of nanocrystals and the classical crystal growth process for the formation of bridged nanocrystals.[23, 26-34] We call the formation mechanism of the TiO_2 mesocrystals from the HTO crystal a topochemical mesocrystal conversion mechanism.

5.3.5 Photocatalytic response of mesocrystalline nanocomposites

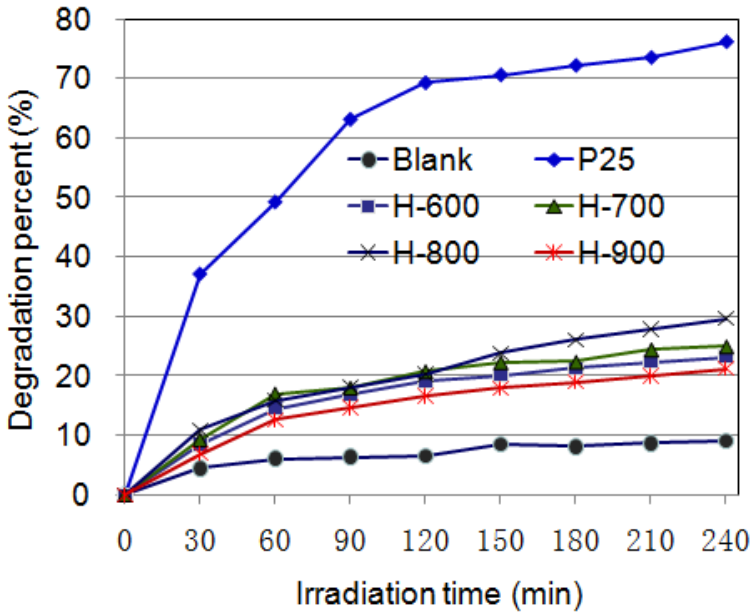

Figure 5.19 Variations of degradation percent of methylene blue with irradiation time under UV light irradiating conditions for TiO_2 samples.

Since the anatase and rutile nanocrystals have potential application as the photocatalyst, we investigated the photocatalytic activity of the TiO_2 mesocrystalline nanocomposites prepared from HTO crystals. The commercial P25 nanocrystal sample was used as the standard sample for the comparison. The samples prepared from HTO are named H-X, where X corresponds to the temperature of heat-treatment. Figure 5.19 shows the variations of degradation percent of methylene blue (MB) with irradiation time under UV light irradiating conditions for the TiO_2 samples.

The commercial P25 exhibits the highest photocatalytic activity in the samples, and the degradation is 75% at 240 min. In the samples prepared from HTO, the degradation at 240 min increases in an order of H-900 < H-600 < H-700 < H-800, namely H-800 shows the highest photocatalytic activity in the TiO_2 mesocrystalline nanocomposites. It has been reported that the photocatalytic activity of TiO_2 is dependent on the crystal structure, specific surface area, and crystallinity.[47–49] Anatase phase shows higher activity than rutile and TiO_2(B) phases, owing to the longer lifetime of the excited

electron in anatase phase than which in rutile and TiO_2(B) phases.[50——53] The photocatalytic activity enhances with increasing specific surface area because the photocatalytic reaction occurs at TiO_2 surface. The crystal defect traps the excited electron and hole, and acts as recombination centers of the electron-hole pairs, therefore the photocatalytic activity decrease with decreasing the crystallinity.[52—55]

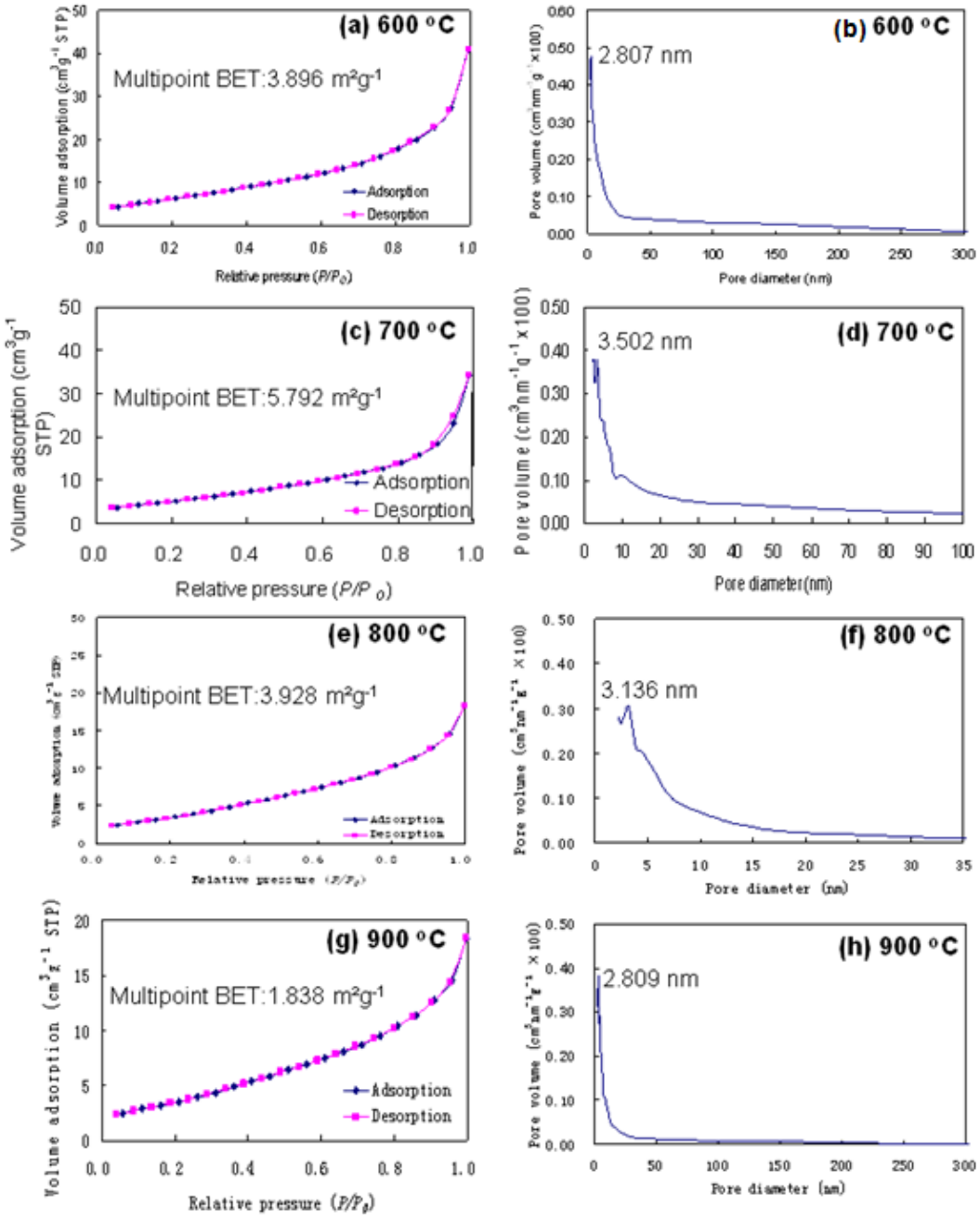

Figure 5.20 (a, c, e, g) Nitrogen adsorption-desorption isotherms and (b, d, f, h) pore size

distributions of HTO crystals after thermal treatments at different temperatures for 3 h.

For the explanation of the photocatalytic activity order of the mesocrystalline nanocomposite samples, we measured specific surface area and pore size of the samples. Nitrogen adsorption-desorption isotherms reveal that all the samples prepared from HTO show the similar type II isotherms without obvious hysteresis hoop (see Figure 5.20), suggesting that it is less porous or nonporous.[56,57] The P25 sample exhibits a large specific surface area of 63 m^2/g, while the mesocrystalline nanocomposite samples have small specific surface areas of 3.9, 5.8, 3.9, and 1.8 m^2/g for H-600, H-700, H-800, and H-900, respectively. This result suggests that the higher photocatalytic activity of P25 is due to its larger specific surface area than the samples prepared from HTO. Although the degradation of MB by P25 is 2.5 times higher than H-800 at 240 min, the specific surface area of P25 is 16 times higher than H-800. This result implies that H-800 exhibits a higher surface photocatalytic activity than that of P25.

Because the photocatalytic activity enhances with increase of the crystallinity and anatase phase exhibits higher photocatalytic activity than which of TiO_2(B) and rutile phase. Therefore, the increase of photocatalytic activity with increasing the heat-treatment temperature up to 800 ^oC in the samples prepared from HTO can be explained by increases of the crystallinity and the composition fraction of anatase in the mesocrystalline nanocomposites. The decrease of the photocatalytic activity with increasing heat-treatment above 800 ^oC can be explained by decreases of the specific surface area and the composition fraction of anatase in the mesocrystalline nanocomposites.

It is interesting that although H-800 has lower anatase content and specific surface area, but it exhibits higher photocatalytic activity than that of H-700. It has been reported that anatase/rutile composite system, such as P25 containing 80 % anatase and 20 % rutile, enhances the high photocatalytic activity.[50] The conduction band of anatase is little higher than that of rutile and valence band of anatase is little lower than that

rutile.[58] When electrons are excited by UV light, the excited electrons in the conduction band of anatase can move to the conduction band of rutile, while the hole in the valence band of rutile can move to anatase valence band, which improves the electron-hole separation, namely increases the lifetime of the exciton, which is important to enhance the photocatalytic activity.[49,59] This is the reason why P25 containing 80 % anatase and 20 % rutile exhibits the high photocatalytic activity.[50,60] Since H-800 mesocrystal also contains 80% anatase and 20 % rutile, we think its high photocatalytic activity can be explained also by the charge separation effect. It has been reported that the TiO_2(B)/anatase composite system also provides the electron-hole separation effect similar to the anatase/rutile composite system, and also exhibits high photocatalytic activity.[61] This suggests that the electron-hole separation effect is also possible in the H-600 mesocrystalline nanocomposite. However, it show lower photocatalytic activity, which may be owing to its low crystallinity.

The result in this study reveals that the mesocrystalline nanocomposites of anatase/rutile polymorphs is an ideal photocatalytic system, because TiO_2 polymorph nanocrystals are orderly aligned and connected by heteroepitaxial interface where the electron and hole can be transferred easily for the electron-hole separation.[49,60,62,63] It should be noted also that the anatase nanocrystals in the mesocrystalline platelike particles expose {010} facet on the surface. It has been reported that {010}-faceted surface of anatase exhibits higher photocatalytic activity than other low index facets, such as {001}, {010} and {101}, owing to its favorable surface atomic structure and surface electronic structure for the photocatalytic reaction.[24,64] Therefore above results imply that if the {010}-faceted mesocrystalline nanocomposite of anatase/rutile polymorphs with high specific surface area can be prepared, the photocatalytic activity would be improved dramatically.

5.4 Conclusions

The four kinds of TiO_2 mesocrystalline nanocomposites of HTO(M)/TiO_2(B),

HTO(M)/ TiO_2(B)/anatase, TiO_2(B)/anatase, anatase/rutile polymorphs with platelike morphology can be developed via the heat-treatment process from the layered titanate single crystals. The mesocrystalline nanocomposites are formed via the topochemical mesocrystal conversion mechanism. There are specific crystallographic topological correspondences between the precursor, intermediates, and the final product in the topochemical mesocrystal conversion reaction. The mesocrystalline nanocomposites are constructed from nanocrystals which show the same orientation direction for the same polymorphs. The {010}-faceted TiO_2(B) twinning is also formed in the topochemical conversion process from HTO to anatase. The [102]-oriented $TiO_2(B)_2$ phase is more stable than the [001]-oriented $TiO_2(B)_1$ phase. The mesocrystalline nanocomposite constructed from 80% anatase and 20% rutile nanocrystals exhibits highest photocatalytic activity in these mesocrystalline nanocomposites, which can be explained by the superior electron-hole separation effect in the mesocrystalline structure. Furthermore, the mesocrystalline nanocomposite with high active {010}-facet surface of anatase on the surface is expected as a promising nanostructure for the high performance photocatalyst.

5.5 References

(1) Trindade, T.; O'Brien, P.; Pickett, N. L. *Chem. Mater.* **2001**, 13, 3843–3858.

(2) Zhou, L.; O'Brien, P. *Small* **2008**, 4, 1566–1574.

(3) Peng, X. G.; Manna, L.; Yang, W. D.; Wichham, J.; Scher, E.; Kadavanich, A.; Alivisatos, A. P. *Nature* **2000**, 404, 59–61.

(4) Zhou, L.; Wang, W. Z.; Xu, H. L. *Cryst. Growth Des.* **2008**, 8, 728–733.

(5) Cölfen, H.; Antonietti, M. *Angew. Chem. Int. Ed.* **2005**, 44, 5576–5591.

(6) Cölfen, H.; Mann, S. *Angew. Chem. Int. Ed.* **2003**, 42, 2350–2365.

(7) Ye, J. F.; Liu, W.; Cai, J. G.; Chen, S.; Zhao, X. W.; Zhou, H. H.; Qi, L. M. *J. Am. Chem. Soc.* **2011**, 133, 933–940.

(8) Song, R. Q.; Cölfen, H. *Adv*. *Mater*. **2010**, 12, 1301–1330.

(9) Hong, Z. S.; Wei, M. D.; Lan, T. N.; Jiang, L. L.; Cao, G. Z. *Energy Environ Sci*. **2012**, 5, 5408–5413.

(10) Cai, J.; Ye, J.; Chen, S.; Zhao, X.; Zhang, D.; Chen, S.; Ma, Y.; Jin, S.; Qi, L. *Energy Environ Sci*. **2012**, 5, 7575–7581.

(11) Liu, B.; Zeng, H. C. *Chem. Mater.* **2008**, 20, 2711–2718.

(12) Liu, S. J.; Gong, J. Y.; Hu, B.; Yu, S. H. *Cryst. Growth Des.* **2008**, 9, 203–209.

(13) Zhang, D.; Li, G.; Wang, F.; Yu, J. C. *CrystEngComm* **2010**, 12, 1759–1763.

(14) Chen, Q. F.; Ma, W. H.; Chen, C. C.; Ji, H. W.; Zhao, J. C. *Chem. Eur. J.* **2012**, 18, 12584–12589.

(15) Rafael O. Da Silva; Ricardo H. Gonçalves; Daniel G. Stroppa; Antonio J. Ramirezb; Edson R. *Nanoscale* **2011, 3,** 1910–1916.

(16) Tartaj, P.; Amarilla, J. M. *Adv*. *Mater*. **2011**, 23, 4904–4907.

(17) Tartaj, P. *Chem. Commun*. **2011**, 47, 256–258.

(18) Aoyama, Y.; Oaki, Y.; Ise, R.; Imai, H. *CrystEngComm*. **2012**, 14, 1405–1411.

(19) Liao, J. Y.; Lei, B. X.; Chen, H. Y.; Kuang, D. B.; Su, C. Y. *Energy Environ. Sci.* **2012**, 5, 5750–5757.

(20) Gao, T.; Fjellvåg, H.; Norby, P. *J. Mater. Chem.* **2009**, 19, 787–794.

(21) Wen, P. H.; Xue, M.; Ishikawa, Y.; Itoh, H.; Feng, Q. *ACS Appl. Mater. Interfaces* **2012**, 4, 1928−1934.

(22) Wen, P. H.; Ishikawa, Y.; Itoh, H.; Feng, Q. *J. Phys. Chem. C* **2009**, 113, 20275–20280.

(23) Wen, P. H.; Itoh, H.; Tang W. P.; Feng, Q. *Microporous Mesoporous Mater.* **2008**, 116, 147–156.

(24) Wen, P. H.; Itoh, H.; Tang W. P.; Feng, Q. *Langmuir* **2007**, 23, 11782–11790.

(25) Wei, M. D.; Konishi, Y.; Zhou, H. S.; Sugihara, H.; Arakawa, H. *Solid State Commun*. **2005**, 133, 493–497.

(26) Feng, Q.; Hirasawa, M.; Yanagisawa, K. *Chem. Mater.* **2001**, 13, 290–296.

(27) Feng, Q.; Hirasawa, M.; Kajiyoshi, K.; Yanagisawa, K. *J. Am. Ceram. Soc.* **2005**, 88, 1415–

1420.

(28) Feng, Q.; Ishikawa, Y.; Makita, Y.; Yamamoto, Y. *J. Ceram. Soc. Jpn*. **2010**, 118, 141–146.

(29) Kong, X. G.; Ishikawa, Y.; Shinagawa, K.; Feng Q. *J. Am. Ceram. Soc.* **2011**, 94, 3716–3721.

(30) Kong, X. G.; Hu, D. W.; Ishikawa, Y.; Tanaka, Y.; Feng, *Q. Chem. Mater.* **2011**, 23, 3978–3986.

(31) Hu, D. W.; Kong, X. G.; Mori, K.; Tanaka, Y.; Shinagawa, K.; Feng, Q. *Inorg. Chem.* **2013**, 52, 10542–10551.

(32) Hu, D. W.; Mori, K.; Kong, X. G.; Shinagawa, K.; Wada, S.; Feng, Q. *J. Eur. Ceram. Soc.* **2014**, 34, 1169–1180.

(33) Carneiro, J. T.; Savenije, T. J.; Moulijn, J. A.; Mul, G. *J. Phys. Chem. C* **2011**, 115, 2211–2217.

(34) Lida, M.; Sasaki, T.; Watanabe, M. *Chem. Mater*. **1998**, 10, 3780–3782.

(35) Zhang, L. Z.; Lin, H.; Wang, N.; Lin, C. F.; Li J. B. *J. Alloys Compd.* **2007**, 431, 230–235.

(36) Pavasupree, S.; Suzuki, Y.; Yoshikawa, S.; Kawahata, R. *J. Solid State Chem.* **2005**, 178, 3110–3116.

(37) The Ceramic Society of Japan, editors. *Ceramics Processing–Powder Preparation and Forming (in Japanese)*; The Ceramic Society of Japan: Tokyo, **1998**, p. 49.

(38) Callister Jr., William D.; Rethwisch, David G. *Materials Science and Engineering: An Introduction*. John Wiley & Sons, Inc.: New York, **2007**, p. 94, 185–188.

(39) Hofmeister, H. In: Nalwa, H. S., editors. *Encyclopedia of Nanoscience and Nanotechnology 3*, American Scientific Publishers: Stevenson Ranch, North Lewis Way, **2004**, p. 431–452.

(40) Spurr, R. A.; Myers, H. *Anal. Chem*. **1957**, 29, 760–762.

(41) Morgado, E.; de Abreu, M.A.S.; Pravia, O.R.C.; Marinkovic, B.A.; Jardim, P.M.; Rizzo, F.C.; Araújo, A.S. *Solid State Sci.* **2006**, 8, 888–900.

(42) Yoshida, R.; Suzuki, Y.; Yoshikawa, S. *J. Solid State Chem.* **2005,** 178, 2179–2185.

(43) Sasaki, T.; Nakano, S.; Yamauchi, S.; Watanabe, M. *Chem. Mater.* **1997**, 9, 602–608.

(44) Brohan, L.; Verbaere, A.; Tournoux, M.; Demazeau, G. *Mater. Res. Bull*. 1982, 17,355–361 (in French).

(45) Sutrisno, H.; Sunarto *Indo. J. Chem*. **2010**, 10(2), 143–148.

(46) Linsebigler, A. L.; Lu, G. Q.; Yates, J. T. *Chem. Rev*. **1995**, 95, 735–758.

(47) Carneiro, J. T.; Savenije, T. J.; Moulijn, J. A.; Mul, G. *J. Phys. Chem. C* **2010**, 114 (1), 327–332.

(48) Luo Y.; Liu, X. Y.; Huang, J. G. *CrystEngComm*. **2013**, 15, 5586–5590.

(49) Scanlon, D. O.; Dunnill, C. W.; Buckeridge, J.; Shevlin, S. A.; Logsdail, A. J.; Woodley, S. M.; Catlow, C. R. A.; Powell, M. J.; Palgrave, R. G.; Parkin, I. P.; Watson, G. W.; Keal, T. W.; Sherwood, P.; Walsh, A.; Sokol, A. A. *Nat. Mater.* **2013**, 12, 798–801.

(50) Hurum, D. C.; Gray, K. A. *J. Phys. Chem. B* **2005**, 109, 977–980.

(51) Xu, M. C.; Gao, Y. K.; Moreno, E. M.; Kunst, M.; Muhler, M.; Wang, Y. M.; Idriss, H.; Wöll, C. *Phys. Rev. Lett.* **2011,** 106, 138302.

(52) Yan, M. C.; Chen, F.; Zhang, J. L.; Anpo, M. *J. Phys. Chem. B* **2005**, 109, 8673–8678.

(53) Emilio, C. A.; Litter, M. I.; Kunst, M.; Bouchard, M.; Colbeau–Justin, C. *Langmuir* **2006**, 22 (8), 3606–3613.

(54) Wu, N. Q.; Wang, J.; Tafen D. N.; Wang, H.; Zheng, J. G.; Lewis, J. P.; Liu, X. G.; Leonard, S. S.; Manivannan, A. *J. Am. Chem. Soc.* **2010**, 132, 6679–6685.

(55) Zhao, C. X; Luo, H. A.; Chen, F.; Zhang, P.; Yi, L. H.; You, K. Y. *Energy Environ. Sci*. **2014**, 7, 1700–1707.

(56) Li, N.; Liu, G.; Zhen, C.; Li, F.; Zhang, L. L.; Cheng, H. M. *Adv. Funct. Mater.* **2011**, 21, 1717–1722.

(57) Gregg, S. J.; Sing, K. S. W. *Adsorption, Surface Area and Porosity*, Academic Press: New York 1991.

(58) Kavan, L.; Gratzel, M.; Gilbert, S. E.; Klemenz, C.; Scheel, H. J. *J. Am. Chem. Soc.* **1996,** 118, 6716–6723.

(59) Miyagi, T.; Kamei, M.; Mitsuhashi, T.; Ishigaki, T.; Yamazaki, A. *Chem. Phys. Lett.* **2004,** 390, 399–402.

(60) Hurum, D. C.; Agrios, A. G.; Gray, K. A.; Rajh, T.; Thurnauer, M. C. *J. Phys. Chem. B* **2003,** *107*, 4545–4549.

(61) Liu, B.; Khare, A.; Aydil, E. S. *ACS Appl. Mater. Interfaces* **2011**, 3, 4444–4450.

(62) Park, J. T.; Patel, R.; Jeon, H.; Kim, D. J.; Shin, J. S.; Kim, J. H. *J. Mater. Chem.* **2012**, 22, 6131–6138.

(63)Liu, Z. Y.; Zhang, X. T.; Nishimoto, S.; Jin, M.; Tryk, D. A.; Murakami, T.; Fujishima, A.

Langmuir **2007**, 23, 10916–10919.

(64) Pan, J.; Liu, G.; Lu, G. Q.; Cheng, H. M. *Angew. Chem. Int. Ed*. **2011**, 50, 2133–2137.

Chapter VI Summary

In the present study, an *in situ* topochemical conversion reaction process was utilized to develop platelike $Bi_{0.5}Na_{0.5}TiO_3$ (BNT) mesocrystals, $BaTiO_3/SrTiO_3$ (BT/ST), and TiO_2 polymorphs mesocrystalline nanocomposites, and fabricate the oriented BNT ceramics. A layered titanate $H_{4x/3}Ti_{2-x/3}O_4 \cdot H_2O$ ($x = 0.8$) ($H_{1.07}Ti_{1.73}O_4 \cdot H_2O$, abbreviated to HTO) single crystal with lepidocrocite (γ–FeOOH)-type two-dimensional structure acts as precursor and Ti-source. The detailed reaction mechanisms and the crystallographic topological correspondences among the precursor, mesocrystalline intermediates, and the final mesocrystalline product were clarified on the basis of the nanostructural analysis results. We call the formation mechanism of these mesocrystals from the HTO crystal an *in situ* topochemical mesocrystal conversion. This new strategy can be utilized to control the crystal structure, crystal orientation, crystal composition, crystal size, and crystal morphology for the development of the advanced functional mesocrystal materials.

The platelike BNT mesocrystals with [100]-orientation and TiO_2 polymorphs mesocrystalline nanocomposites can be prepared by using the solid state reaction processes. The [100]-oriented BNT ceramics with high density and preferred orientation can be fabricated by a reactive-templated grain growth (RTGG) method with the formation mechanism of the BNT mesocrystals. Its piezoelectric constant is higher than conventional unoriented BNT ceramics. The platelike BT/ST mesocrystalline nanocomposites with [110]-orientation and the dense and high strain in its microstructure were prepared by using the two-step hydrothermal/solvothermal soft chemical processes. The success in developing these ferroelectric platelike titanate mesocrystals and mesocrystalline nanocomposites is a significant milestone to challenge the high performance lead-free ferroelectric materials by applying the domain engineering, oriented engineering, and strain engineering to the ferroelectric materials or their nanocomposite materials.

Furthermore, a series of platelike TiO_2 polymorphs mesocrystalline nanocomposites,

including mesocrystalline HTO/TiO_2(B), HTO/TiO_2(B)/anatase, TiO_2(B)/anatase, and anatase/rutile nanocomposites can be generated in sequence from the transformation of the HTO single crystal. There are specific crystallographic topological correspondences among the precursor, intermediates, and the final product in the topochemical mesocrystal conversion reaction. The anatase/rutile mesocrystalline nanocomposite exhibits high surface photocatalytic activity although they have small specific surface areas, which can be explained by the superior electron-hole separation effect in the mesocrystalline structure and high active {010}-facet surface of anatase on the surface. The success in developing these platelike TiO_2 polymorphs mesocrystalline nanocomposites not only expands TiO_2 mesocrystals chemistry and offers a good opportunity to understand the formation process of these unique mesocrystalline superstructures, but also points the way for improving future TiO_2 catalysts.

The main results and points of the present study are summarized as follow:

In Chapter I, some reviews on the synthesis, the formation mechanisms, characterizations, and the applications of conventional mesocrystals were described. The general introduction for the topochemical synthesis, and the layered protonated titanate as a precursor for topochemical synthesis of the mesocrystals were mentioned. The fabrications of the oriented ferroelectric ceramic materials with the oriented engineering and domain (wall) engineering were introduced. Furthermore, the purposes of the present study were clarified.

In Chapter II, the formation and characterization of BNT ferroelectric mesocrystals prepared from a layered titanate HTO with a lepidocrocite-like structure were described. The BNT mesocrystals were synthesized via solid state reactions in HTO-Bi_2O_3-Na_2CO_3 and HTO-TiO_2-Bi_2O_3-Na_2CO_3 solid-state reaction systems. The BNT mesocrystals are constructed from [100]-oriented BNT nanocrystals. The BNT mesocrystals were formed by an *in situ* topotactic structural transformation mechanism and a combination mechanism of the topotactic structural transformation and an epitaxial crystal growth.

In Chapter III, an RTGG process for the fabrication of the crystal-axis-oriented

BNT ceramics using the layered platelike HTO single crystal as a template was described. The [100]-oriented BNT ceramics with the high degree of orientation, high density, and small grain size were achieved simultaneously by using a HTO-TiO_2-Bi_2O_3-Na_2CO_3 reaction system. The oriented BNT ceramic was formed by a topochemical conversion reaction of platelike HTO template crystals to platelike BNT mesocrystal particles, and then epitaxial crystal growth of BNT on the BNT mesocrystals. The fabricated oriented BNT ceramic shows a higher piezoelectric constant value of d_{33}* than the nonoriented BNT ceramic.

In Chapter IV, the development of the platelike BT/ST mesocrystalline nanocomposites using a novel two-step solvothermal soft chemical process and the reaction mechanism were described. The two-step solvothermal soft chemical process is an effective method for the preparation of the platelike BT/ST mesocrystalline nanocomposites. In the first hydrothermal treatment step, the BT/HTO nanocomposite was formed by partial transformation of HTO to $BaTiO_3$. In the second solvothermal treatment step, the platelike BT/HTO nanocomposite crystal was solvothermally treated in $Sr(OH)_2$ solution to obtain the platelike BT/ST mesocrystalline nanocomposite The BT/ST mesocrystalline nanocomposite was formed by two-step topochemical mesocrystal conversion reaction on the HTO-based platelike framework. The platelike BT/ST mesocrystalline nanocomposite prepared by this approach is oriented BT/ST polycrystal constructed from the BT/ST nanocrystals with the same [110] orientation. Such BT/ST mesocrystalline nanocomposite can withstand the temperature up to around 900 ^oC and possibly shows the dense and high strain in its microstructure, which can lead to the sharp enhancement of the piezoelectric and dielectric performance.

In Chapter V, four kinds of platelike mesocrystalline nanocomposites of TiO_2 polymorphs were successfully prepared based on a topochemical mesocrystal conversion mechanism. In this conversion process, a [010]-oriented platelike titanate HTO single crystal with lepidocrocite-like structure was successively transformed into [001]- and [102]-oriented TiO_2(B) phases including a {010}-faceted TiO_2(B) twinning, [010]-oriented anatase phase, and [110]-oriented rutile phase. The platelike

particle morphology is retained in the topochemical conversion process. The platelike particles are constructed from nanocrystals which well-aligned in same orientation for the same phase, resulting in the formations of HTO/TiO_2(B), HTO/TiO_2(B)/anatase, TiO_2(B)/anatase, and anatase/rutile mesocrystalline nanocomposites. The reaction mechanism and the crystallographic topological correspondences among the precursor, intermediates, and the final product were given on the basis of the nanostructural analysis results. The mesocrystalline nanocomposite of anatase/rutile polymorphs exhibits unexpectedly high surface photocatalytic activity, which can be explained by the superior electron-hole separation effect and the high activity of {010}-faceted anatase surface in the mesocrystalline nanocomposite. These mesocrystalline nanocomposites are expected as a potential nanostructure for the high performance photocatalyst.

The results described above conclude that the *in situ* topochemical mesocrystal conversion reaction process is an attractive approach. This approach can be employed not only for the development of the platelike functional titanate ferroelectric mesocrystal and mesocrystalline nanocomposite materials but also for the preparation of the platelike TiO_2 polymorphs mesocrystalline nanocomposite catalysis materials. The mesocrystalline size, morphology, structure, and composition can be controlled by adjusting the reaction conditions in the *in situ* topochemical mesocrystal conversion reaction process.

From the view point of the application of domain (wall) engineering, oriented engineering, and strain engineering to the oriented ferroelectric titanate mesocrystal materials for sharply enhancing the dielectric and/or piezoelectric performance, the solvothermal soft chemical process and solid state process can provide the suitable ceramic powders with anisometric morphology (platelike or fiber), small and uniform grain size, and high degree orientation. From the view point of the application of the facilitation of efficient electron hole separation and the exposure of dominant reactive crystal facet to TiO_2 polymorphs mesocrystalline nanocomposite surface for the improvement of the photocatalytic response, the solid state process with the *in situ* topochemical conversion reaction mechanism can afford possible mesocrystalline

nanocomposites with high photocatalytic performance.

From the view point of fundamental study, this dissertation gives the reaction mechanisms for the formation of functional ferroelectric titanate materials and photocatalytic TiO_2 polymorphs materials in the *in situ* topochemical conversion reaction processes. These mechanisms will serve also as a guide to develop the syntheses of other materials in the solvothermal processes and solid state processes. Therefore, both the solvothermal chemical processes and solid state processes accompanying with the *in situ* topochemical conversion reaction are of notable significance for the fundamental research, and can provide important knowledge for controlling the chemical reaction process to achieve the materials of advanced functions.

In our next challenges, we will try to decrease the grain size with nanoscale of the oriented BNT ceramics, and evaluate its various physical properties, so that the BNT ceramics can be suitable to be applied to the ferroelectric devices. We also plan to fabricate the oriented BT/ST nanocomposite thin films using the formation mechanism of the BT/ST mesocrystalline nanocomposites. In the preparation process, we will design the effective approach for enhancing the orientation degree and density of the nanocomposite thin films, and control the domain size and strain variable of thin films by adjusting the fabrication process and sintering conditions. Moreover, we will appraise various physical properties of the optimal BT/ST nanocomposite thin films, and consider applying them to the high performance lead-free ferroelectric devices. About the applications and improvements of the photocatalytic performance of the TiO_2 polymorphs mesocrystalline nanocomposite materials, we will continue using the layered HTO single crystal as precursor. A new approach for exfoliating layered HTO single crystal into thinner HTO nanosheets and topochemical convention of the thin HTO nanosheets to TiO_2 polymorphs mesocrystalline nanocomposite materials will be developed. The specific surface area enhanced TiO_2 polymorphs mesocrystalline nanocomposite materials will improve their photocatalytic performance dramatically. In addition, we will appraise various physical properties of the optimal TiO_2 polymorphs mesocrystalline nanocomposite

materials, and consider applying them to the novel high performance catalytic materials for environmental remediation and water splitting.

In the present study, we have shown that the *in situ* topochemical conversion reaction mechanism devoting to the solvothermal reaction process and solid state reaction process can also determine the transformation of a single crystal into a mesocrystal and mesocrystalline nanocomposite. We can call this kind of *in situ* topochemical conversion reaction as *in situ* topochemical mesocrystal conversion reaction. As a whole, the results of this study suggest that the *in situ* topochemical mesocrystal conversion of suitable precursors, either single crystals or mesocrystals, can be employed to generate a variety of mesocrystalline nanocomposite functional materials with the desired morphology, conjecturable structure, adjustable composition, and uniformly aligned orientation in control.

Publications

Publication in Journals

[1] **Dengwei Hu**, Xingang Kong, Kotaro Mori, Yasuhiro Tanaka, Kazunari Shinagawa, Qi Feng, Ferroelectric mesocrystals of bismuth sodium titanate: formation mechanism, nanostructure, and application to piezoelectric materials. *Inorganic Chemistry*, **2013**, 52, 10542−10551.

[2] **Dengwei Hu,** Kotaro Moria, Xingang Kong,Kazunari Shinagawa, Satoshi Wada, Qi Feng. Fabrication of [100]-oriented bismuth sodium titanate ceramics with smallgrain size and high density for piezoelectric materials. *Journal of the European Ceramic Society*. 2014, 34, 1169–1180.

[3] Xingang Kong, **Dengwei Hu**, Yoshie Ishikawa, Yasuhiro Tanaka, and Qi Feng. Solvothermal soft chemical synthesis and characterization of nanostructured $Ba_{1-x}(Bi_{0.5}K_{0.5})_xTiO_3$ platelike particles with crystal-axis orientation. *Chemistry of Materials*, **2011**, 23, 3978−3986.

[4] Xingang Kong, **Dengwei Hu**, Puhong Wen, Tomohiko Ishii, Yasuhiro Tanaka, Qi Feng; Transformation of potassium Lindquist hexaniobate to various potassium niobates: solvothermal synthesis and structural evolution mechanism. *Dalton Transactions*, **2013**, 42, 7699−7709.

[5] **Dengwei Hu,** Wenxiong Zhang, Yasuhiro Tanaka, Naoshi Kusunose, Yage Peng, Qi Feng, Mesocrystalline nanocomposites of TiO_2 polymorphs: topochemical mesocrystal conversion, characterization, and photocatalytic response, submitted.

Publication in Conferences

[1] **Dengwei Hu,** Xingang Kong, Qi Feng. Synthesis of plate-like $Ba_{0.5}(Bi_{0.5}Na_{0.5})_{0.5}TiO_3$ particles by solvothermal soft chemical process, 第 18 回ヤングセ ラ ミス ト・ミーテ ィング in 中 四国, p31–32, Okayama, **2011**-12-10.

[2] 馮旗, 孔新剛, **胡登衛**, 石川善恵, 田中康弘, ソルボサンマルソフト化学法による配向性$Ba_{1-x}(Bi_{0.5}K_{0.5})_xTiO_3$板状粒子の合成と評価, 日本セラミックス協会第24回秋季シンポジウム, p304, 札幌, 2011-09-07～09.

[3] **D. Hu**, X. Kong, Y. Ishikawa, Q. Feng Synthesis of $Ba_{0.5}(Bi_{0.5}Na_{0.5})_{0.5}TiO_3$ plate-like mesocrystal particles by solvothermal soft chemical process, *The 50th Anniversary Symposium in Basic Science of Ceramics*, p94, Tokyo, **2012**-01-12～13.

[4] Xingang Kong, **Dengwei Hu**, Yoshie Ishikawa, Qi Feng, Solvothermal process for synthesis and particle morphology control of potassium niobates from soluble potassium Hexaniobate, *The 50th Anniversary Symposium in Basic Science of Ceramics*, p91, Tokyo, **2012**-01-12～13.

[5] **Dengwei Hu,** Qi Feng, Solid state topotactic transformation reaction from layered titanate to bismuth sodium titanate and its application to orientated ceramics. *The 4th Kagawa University-Chiang Mai University Joint Symposium*, p 35, Kagawa, **2012**-09-19-21.

[6] **Dengwei Hu**, Yasuhiro Tanaka, Qi Feng, Topotactic synthesis of $bi_{0.5}na_{0.5}tio_3$ mesocrystal plate-like particles from layered titanate, *The 51st Anniversary Symposium in Basic Science of Ceramics*, p207, Sendai, **2013**-01-09～10.

[7] **Dengwei Hu**, Yasuhiro Tanaka, Qi Feng, Formation of platelike TiO_2 mesocrystals from protonated titanate based on topochemical nanocrystal conversion mechanism, *The 3rd Joint Workshop between Kagawa University and Hanbat National University*, p12–14, Kagawa, **2014**-01-06.

[8] **Dengwei Hu**, Yasuhiro Tanaka, Qi Feng, Synthesis of plate-like TiO_2 mesocrystals with different orientations from layered titanate, *The 52nd Anniversary Symposium in Basic Science of Ceramics*, p152, Nagoya, **2014**-01-09～10.

[9] **Dengwei Hu,** Yasuhiro Tanaka, Shunsuke Nakanishi, Qi Feng, Plate-like anatase-rutile mesocrystalline nanocomposites derived from nanocrystals conversion of metastable TiO_2(B) twinnings, *The 5th International Congress on Ceramics*, Beijing, **2014**-08-17～21.

Acknowledgment

I would like to express my very sincere thanks and gratitude to my research supervisor, Prof. **Qi Feng**, for his kind guidance, cultivatation, and continuous supervision, excellent advice and continuous encouragement towards the completion of this present research successfully in time. He exhibits realistic and pragmatic research attitude which is very worth my study in life. I am also very grateful that he gave me a very precious opportunity to enhance and pursue advanced studies, and he well pays attention to our future development. And the same sincere thanks and gratitude are to Associate Prof. Lin Yu (Okayama Shoka University), for her much supports on my research supervisor team, for her precious guidance and perspectives on my daily life and values.

I would like to express my sincere thanks also to my vice supervisors Associate Prof. Yasuhiro Tanaka and Associate Prof. Takafumi Kusunose for their kind advice, valuable suggestion, necessary support, and enthusiastic assistances to my Ph. D study. I am also very grateful to them.

Grateful acknowledgements are to Prof. Kazunari Shinagawa, Prof. Shunsuke Nakanishi, Prof. Hisao Kakegawa, Lecturer Shinobu Uemura, Prof. Satoshi Wada (University of Yamanashi), Dr. Xingang Kong (Shaanxi University of Science and Technology), Associate Prof. Yong Fan (Jilin University), Prof. Yaohua Xu (Jilin University), Prof. Lifang Zhao (Baoji University of Arts and Science), Prof. Jianying Miao (Baoji University of Arts and Science), Prof. Puhong Wen (Baoji University of Arts and Science), Senior Engineer Hongke Guo (Baoji University of Arts and Science), for their valuable suggestions and enthusiastic assistances.

I would like also expressing my sincere thanks to Ms. Ayami Nishioka (Faculty of Engineering, Kagawa University) for her kindly helpful TEM and FE-SEM(EDS)-experimental skills, Mr. Toshitaka Nakagawa (Faculty of medicine, Kagawa University) for his kindly helpful FE-SEM-experimental skills, and Mr. Hisao Higa (Faculty of Engineering, Kagawa University) for his enthusiastically helpful

AFM/PRM-experimental skills.

My sincere appreciations also extend to Dr. Akinari Sonoda (National Institute of Advanced Industrial Science and Technology (AIST), Shikoku) for providing me a good chance in my expanding practice study on uptake of lithium from salt lake, and teaching me some knowledge in controlling separation technique.

I wish to thank Kagawa University for offering me this PhD position. And thanks to the Japan Society for the Promotion of Science for the funding for research. Appreciates also give to Kuraoka Shogakukai Foundation ((公財)倉岡奨学会), Japan, for providing scholarship.

I am one of the lucky dogs being allowed to study in Kagawa University, so I should thank my leaders from Baoji University of Arts and Science for offering me such a precious opportunity.

I also owe my sincere gratitude to my friends and fellow classmates in our research group, who gave me many helps and much pleasures on life and study.

Lastly, I would like to acknowledge my family for their love, understanding and support throughout my research.

Dengwei Hu

Feng Lab, Department of Advanced Materials Science, Faculty of Engineering

Kagawa University, Kagawa, Japan

September, 2014